Attosecond metrology of optical field emission from tungsten nanotips

Hee-Yong Kim

München 2022

Attosecond metrology of optical field emission from tungsten nanotips

Hee-Yong Kim

Dissertation
an der Fakultät für Physik
der Ludwig–Maximilians–Universität
München

vorgelegt von
Hee-Yong Kim
aus Yongin, Südkorea

München, den 09.02.2022

Erstgutachter: Prof. Dr. Jörg Schreiber
Zweitgutachter: Prof. Dr. Eleftherios Goulielmakis
Tag der mündlichen Prüfung: 20.04.2022

Abstract

Over the last decades, attosecond physics has allowed access into the dynamics of electrons inside matter and has provided new methodologies for probing and controlling the strong field interaction of light and matter at ever shorter time scales. On a parallel front, studies of the light-induced emission of electrons in metallic nanostructures have suggested that under intense laser fields the underlying mechanisms of ionization and dynamics in these systems have strong analogies to these in atoms. Scientists in both research fronts have recognized the intriguing possibilities that could emerge by bridging the gap between these two areas of study. Indeed, the extension of attosecond physics from atoms to nanostructured solids can be arguably considered a major next milestone in ultrafast science, not only because the solid state offers a broad platform for fundamental study, but also because many ideas and concepts could eventually yield practical applications in nanophysics. The tremendous advances in nanotechnology over the last years offer completely new opportunities of control of the light matter interaction at the mesoscopic scale.

This thesis attempts an essential step towards unification of these two areas of study. Light pulses that are confined to and controlled within a fraction of a single laser field cycle are used to induced optical field emission from sharp tungsten nanotips. Generated electron pulses are backscattered at the surface of the nanotip with energies that are well within the range of modern low-energy electron diffraction microscopies. Owing to the extreme temporal confinement of the driving pulse the emission and back-scattering of electrons from the nanotip is confined into a sub-femtosecond window. This exciting possibility, however, can be only verified and used for practical applications, if the emission of electrons can be tracked in real-time. In atoms this possibility has been enabled using attosecond techniques to track the temporal structure of high harmonics that emerge when the electron pulses rescatter off the parent ion. However, this concept cannot be directly transferred to metallic nanostructures, because high harmonic emission is hitherto absent.

In this thesis I develop and apply a new methodology which allows probing of the dynamics of the electron emission in solids directly on the electron domain. Inspired by earlier works in gas phase attosecond physics a weak replica of the same pulse that drives emission is used to gate the electron release. A variation of the delay between the pulse driving the emission and its weak replica allows the composition of spectrograms which embody critical information of the emission dynamics. I extend semiclassical concepts of strong field physics to develop an analysis framework that can be used to reconstruct these spectrograms. Analysis of experimentally recorded spectrograms revealed the generation

of electron pulses whose intensity envelope is confined to 53 ± 5 as. The retrieved spectral and temporal properties of the attosecond electron pulse firmly establish the validity of the recollision picture in optical field emission from metal nanostructures. More importantly it opens the route to endowing electron-based microscopes with attosecond resolution and provides a new PHz scale metrological tool for probing laser induced electric currents on the nanometer scale.

Zusammenfassung

In den letzten Jahrzehnten hat die Attosekundenphysik den Zugang zur Dynamik von Elektronen im Inneren von Materie ermöglicht und neue Methoden zur Untersuchung und Kontrolle der Starkfeld-Wechselwirkung von Licht und Materie auf immer kürzeren Zeitskalen bereitgestellt. Parallel dazu haben Untersuchungen der lichtinduzierten Emission von Elektronen in metallischen Nanostrukturen gezeigt, dass die zugrundeliegenden Mechanismen der Ionisierung und Dynamik in diesen Systemen unter intensiven Laserfeldern starke Analogien zu denen in Atomen aufweisen. Wissenschaftler beider Forschungsrichtungen haben die faszinierenden Möglichkeiten erkannt, die sich aus der Überbrückung zwischen diesen beiden Forschungsbereichen ergeben könnten. In der Tat kann die Erweiterung der Attosekundenphysik von Atomen auf nanostrukturierte Festkörper als ein wichtiger nächster Meilenstein in der ultraschnellen Forschungsbereichen angesehen werden. Nicht nur, weil der feste Zustand eine breite Plattform für die Grundlagenforschung bietet, sondern auch, weil viele Ideen und Konzepte schließlich zu praktischen Anwendungen in der Nanophysik führen könnten. Die enormen Fortschritte in der Nanotechnologie in den letzten Jahren bieten völlig neue Möglichkeiten der Kontrolle der Licht-Materie-Wechselwirkung auf der mesoskopischen Skala.

In dieser Dissertation wird ein wesentlicher Schritt zur Vereinheitlichung dieser beiden Forschungsbereiche unternommen. Lichtpulse, die auf einen Bruchteil eines einzelnen Laserfeldzyklus begrenzt und kontrolliert sind, werden verwendet, um optische Feldemission von scharfen Wolfram-Nanospitzen zu induzieren. Die erzeugten Elektronenpulse werden an der Oberfläche der Nanospitze mit Energien zurückgestreut, die innerhalb des Bereiches moderner Mikroskope mit niederenergetischer Elektronenbeugung liegen. Aufgrund der extremen zeitlichen Begrenzung des Antriebspulses ist die Emission und Rückstreuung von Elektronen aus der Nanospitze auf ein Sub-Femtosekunden-Fenster beschränkt. Diese spannende Möglichkeit kann jedoch nur dann verifiziert und für praktische Anwendungen genutzt werden, wenn die Emission von Elektronen in Echtzeit verfolgt werden kann. In Atomen wurde diese Möglichkeit mit Hilfe von Attosekundentechniken geschaffen, um die zeitliche Struktur der hohen Harmonischen zu verfolgen, die entstehen, wenn die Elektronenpulse vom Mutterion zurückgestreut werden. Dieses Konzept lässt sich jedoch nicht direkt auf metallische Nanostrukturen übertragen, da die Emission hoher Harmonischer bisher nicht vorhanden ist.

In dieser Arbeit entwickle und verwende ich eine neue Methode, die es ermöglicht, die Dynamik der Elektronenemission in Festkörpern direkt auf der Elektronendomäne zu

untersuchen. Inspiriert von früheren Gasphasen-Attosekundenphysik Arbeiten wird ein schwaches Replikat des Pulses, der die Emission antreibt, verwendet, um die freigesetzten Elektronen zu steuern. Eine Variation der Verzögerung zwischen dem Puls, der die Emission antreibt, und seinem schwachen Replikat ermöglicht die Erstellung von Spektrogrammen, die wichtige Informationen über die Emissionsdynamik enthalten. Ich erweitere semiklassische Konzepte der Starkfeldphysik, um einen Analyserahmen zu entwickeln, mit dem diese Spektrogramme rekonstruiert werden können. Die Analyse der experimentell aufgezeichneten Spektrogramme zeigt die Erzeugung von Elektronenpulsen, deren Intensitätseinhüllende auf 53 ± 5 as beschränkt ist. Die ermittelten spektralen und zeitlichen Eigenschaften des Attosekunden-Elektronenpulses bestätigen die Gültigkeit des Bildes der Rekollision bei der optischen Feldemission von Metall-Nanostrukturen. Noch wichtiger ist, dass dies den Weg zu elektronenbasierten Mikroskopen mit Attosekunden-Auflösung ebnen und ein neues messtechnisches Werkzeug für die Untersuchung laserinduzierter elektrischer Ströme auf der Nanometerskala im PHz-Bereich bieten.

Contents

Introduction

I see, I know, I believe, I am undeceived.
-Pierre Corneille

In the microcosm, the laws of quantum mechanics dictates physical phenomena to unfold within extremely short time scales. In molecules and solids, atoms are vibrating at the scale of picoseconds (1ps = 10^{-12}s) and femtoseconds (1fs = 10^{-15}s) [1, 2]. Deeper, inside atoms, electron motion dominates the dynamics, and it is even faster. An electron in the lowest quantum orbit of the Bohr atom takes approximately ∼150 attoseconds (1as = 10^{-18}s) to revolve around the nucleus [3].

Microscopic electron motion underlies a vast range of physical phenomena and their macroscopic manifestations. For instance, the polarization of the electron cloud, is directly related to optical properties of materials such as refraction, reflection, absorption, and emission of light [4, 5]. At the same time, the microscopic transport of electrons in semiconductors determines their electric properties and therefore their capability to process electronic signals. An important question that naturally arises is: how can we "see/observe" electron motion in the microcosm?

Scientific interrogation of physical phenomena is based on measurements, and therefore the development and advancement of measurement tools/techniques is essential for scientific progress. One of the best tools to investigate the microscopic motion of electrons is the electromagnetic wave. Primarily through its electric field component, an electromagnetic wave can apply direct forces on electrons to probe their status inside a system. For phenomena that evolve extremely fast, for instance electrons in an atom, a molecule or a solid, it is of great importance that the electromagnetic fields are confined to time scales shorter or comparable to the characteristic time scales of the electron motion.

The invention of the laser in 1960 [6] enabled for the first-time coherent sources of visible light to reach the table-tops of experimental physicists and opened the door for generating electromagnetic fields with advanced measurement capabilities. After this essential milestone in optical sciences the duration of laser pulses became gradually shorter with a tremendous pace. Only two years later, the Q-switching technique [7] made the generation of nanosecond pulses possible, and picosecond pulses were realized with mode-locked lasers in 1964 [8]. Mode-locking drove further advancements reaching femtosecond resolution in the 80's. The combination of femtosecond laser with pump-probe techniques allowed the

exploration of the dynamics of chemical bond through the field of femtochemistry [9, 10].

When the field of laser pulses is not strong enough to significantly modify the electrostatic potential in atoms, molecules or crystals, nonlinear optics is typically referred to as perturbative nonlinear optics. The action of a laser pulse on quantum systems can be described as a small perturbation on the field-free system. In this regime, the nonlinearity can be best understood as a result of anharmonic electronic motion in a binding potential, and much of its description can be based on phenomenological models [5].

Nonlinear optics has not only emerged by the availability of lasers but has also followed the rapid pace of advancement of laser technology. It has dramatically profited from the capability of lasers to confine light into ultrashort time windows and thus to boost the intensity of the electric fields to extraordinary magnitudes, comparable to these that valence electrons experience inside matter. Indeed, right after the invention of the laser, harmonic generation [11] was discovered. Light control based on nonlinear phenomena such as saturable absorption and Kerr effects have in fact been instrumental for light oscillator mode-locking [12, 13, 14] which has, in turn lead to the generation of pulses whose intensity envelope is confined to only a few femtoseconds. Today, synthesis techniques allow the confinement of visible light to sub-femtosecond windows [15, 16].

Advanced laser technology, based on mode-locked lasers and chirped pulse amplification technique (CPA) [17] made possible high power, table-top laser systems, wherein the peak field strength of the generated pulses can exceed the Coulombic binding field inside atoms, molecules and crystals. The interaction of matter with such high-intensity laser fields revealed new phenomena that cannot be described within the framework of perturbation theory. This regime of light-matter interaction is referred to as "strong-field regime" or "non-perturbative" regime. On exposure to strong laser fields the atomic potential can be significantly distorted, and electrons can be set free from the outermost orbitals of atoms or molecules via tunneling through the potential barrier. In turn, the dynamics of the liberated photoelectrons is governed by the ultrafast swings of the driving field. Depending on the release time of electrons from atoms, the photoelectrons are brought back to recombine with the parent ion and emit high harmonics. The photoelectrons can also rescatter from the atomic core leading to above threshold ionization. The above simple picture is broadly known as the three-step model [18].

The three-step model has provided scientists an intuitive picture to describe an inherently complex process. As such it has opened the door to several advances in ultrafast science and attosecond physics. The tunneling processes confine the electron emission to a very short time window around a field crest. In turn, the generated electron wavepacket or electron pulse can be driven to recollide with the atomic core within a fraction of the field-half-cycle. Under an optical driving field whose oscillation period is $\sim$2 fs, the recollision event is intrinsically confined to a sub-femtosecond temporal window. Correspondingly, the coherent radiation of high harmonics emerging during recollision shall be also confined to attosecond time intervals.

Strong field phenomena are sensitive to instantaneous field rather than the cycle-averaged intensity of the driving pulse. Harnessing of the full potential of strong field phenomena called for additional advancement on the control of light. Pulses that emerge

from an ordinary laser cavity do not carry identical field waveforms under the intensity envelope. As a result, the processes of tunneling and recollision which are sensitive to the field evolution could not be controlled. This fact introduced a fundamental limitation on controlling the strong field processes. In this context, the control of the field waveform is essential for the research in strong-field physics. For example, the variation of the carrier-envelope phase (CEP) modulates the waveform of an ultrashort laser pulse while still maintaining the same envelope and consequently, the physical quantities in a strong-field light-matter interaction can be coherently controlled [19, 20, 21, 22, 23, 24]. Therefore, the stabilization and control of the phase from one pulse to another in a pulse train arose as an important factor of strong-field physics.

The possibility to generate reproducible light fields has been attained via the frequency comb technique [25, 26]. With these tools and hand at the beginning of the new millennium, scientists utilized high harmonic generation (HHG) in noble gases to generated isolated attosecond pulses in the extreme ultraviolet part of the spectrum opening the field of attosecond science [27, 28, 29, 30, 31]. Thanks to the ultrashort duration of attosecond pulses, pump-probe schemes in which at least of one of the two pulses is an attosecond EUV pulse have shown the possibility to probe matter with significantly higher temporal resolution in comparison to any previous light-based metrologies of dynamical phenomena in matter. Attosecond experiments can now offer direct access to the physics of strong field ionization, the absolute time of emission in gases and solids [32, 33, 34, 35], the excitation and measurement of valence electron coherences [36, 37, 38, 39] and the possibility to trace the relaxation dynamics of core-excited excitons in solids [16, 40]. In recent years the advancement of attosecond technology has made it possible to confine also visible fields into sub-cycle [37, 41] and even sub-femtosecond windows [15, 16]. This capability has enabled new ways of probing ultrafast phenomena in real-time [15, 16, 42].

Electrons as tools to explore the microcosm in space and time

The matter-wave duality of quantum mechanics suggests that an electron of an energy E has a corresponding wavelength ($\lambda = h/\sqrt{2m_eE}$) typically referred to as *de Broglie* wavelength. An electron of energy of say ∼30 eV corresponds to a wavelength of ∼2.23 Å. Because the spatial resolution of an electron in diffraction is directly associated with its wavelength, it is clear that for the same energy, electron waves can offer dramatically higher spatial resolution for probing the microcosm than electromagnetic waves. The spatial resolution of high energy electrons underlies important microscopy techniques such as transmission (TEM) [43, 44] or scanning (SEM)[45] electron microscope which are nowadays widely used in a broad range of research disciplines.

The efforts to introduce temporal resolution to electron diffraction and microscopy techniques led to the development of new methodologies that could enable the temporal confinement of electrons to very short times (electron pulse) [2, 46, 47, 48, 49]. Modern techniques are based on a post modulation of electron pulses generated from an electron gun using microwaves or terahertz fields to compress the pulse to as short duration as possible [50, 51, 52]. Such kind of sources can now reach single-electron pulse durations of

a few femtoseconds, and furthermore, attosecond pulse trains by modulating the envelope of a femtosecond electron pulse [53, 54].

Another school of thought relies on the idea that attosecond electron pulses can be generated/controlled and used within a strong-field process. The recolliding electron wavepacket in a strong-field process is, in fact, an electron pulse that probes its parent system. Moreover, from generation to recollision an electron wavepacket undergoes a tiny amount of dispersion. Under this notion an electron pulse can probe both dynamics and structure under the right circumstances. In atomic physics, this aspect is currently gaining significant momentum [55, 56, 57, 58, 59].

Certainly, the extension of these capabilities to solids will offer the possibility to study structural dynamics with attosecond resolution for a much broader range of systems. Experiments over the last years have shown that the photoemission from nanotips or nanospheres under intense laser fields shows characteristics that are closely related to these in atoms. These include the linear cutoff law with intensity and the sensitivity of the emission to the carrier-envelope phase of the driving pulse. The experiments have also shown unique characteristics of the emission related to these systems such as the local field enhancement near a nanotip or effects of plasmons on the electron emission. Yet, the direct connection of the optical field emission from this system and the attosecond confinement of electrons remains circumstantial. In other words, no direct measurement of the electron pulses has been so far possible.

In this thesis, I used single-cycle pulses to confine the emission of electrons from a nanotip to merely a single energetic attosecond electron pulse. I developed the theoretical framework that allows the direct measurement of these pulses in the electron domain and have used to demonstrate electron pulses of energy > 30 eV and a confinement to $\sim$50 attoseconds.

High harmonic generation in solids

There has been an immense interest to extend strong field, attosecond physics to condensed matter. The processes that I discussed in the previous section could allow probing the surface of solids with attosecond resolution. Yet, bulk materials cannot be studied this way. Since the first observation of high harmonic generation (HHG) in zinc oxide (ZnO) [60] in 2011, a tremendous attention to the underlying physics has emerged. Could high harmonics from solids allow access to structural properties of solids in new ways? This question can be answered firmly only if the mechanism of emission is understood. Over the last years, experimental studies on the HHG in solids have been reported in a broad range of driving frequencies including tera-hertz [61, 62], mid-infrared [60, 63, 64] and visible [65, 42], and in various materials with very different bandgaps such as ZnO [60, 63], SiO_2 [65, 42], GaSe [61, 62], and also graphene [66]. Up to this moment, the mechanism of emission or what is the simplest mechanism to describe the phenomenon is still debated. Is the mechanism the same as high harmonics in atoms? Are interband transitions in the solid important or is the emission a result of the motion of electrons in the non-parabolic profile of bands?

We recently presented a new picture in which the phenomenon can be described as a simple scattering problem between a laser driven electron and its binding potential. Under this assumption, it is possible to visualize the electron potential and the electron density of valence electrons by measuring the emission of harmonics versus intensity and the angle between laser polarization and the direction of the crystal [67]. I will discuss in this thesis how this picture could possibly emerge under strong fields and conduct phase measurements of the high harmonic emission that support this perspective.

The structure of this thesis is as following:

- **Chapter 1** offers a brief introduction to strong-field phenomena in light-matter interactions. It also provides the physical and mathematical foundation which will be extensively used in the next chapters.

- **Chapter 2** discusses the experimental setup and methodology which will be used for the studies in the chapters following.

- **Chapter 3** presents an experimental study of the optical field emission from metallic nanotips. Using single-cycle optical fields of precisely characterized waveforms the study has the goal to attempt a detailed comparison of the properties of the optical field emission with those predicted by atomic semiclassical theories of emission earlier developed for atoms. Associated publication [P1].

- **Chapter 4** introduces the theoretical foundation for a new attosecond steaking technique which can allow the characterization of attosecond electron pulses. The technique is called "Homochormic attosecond streaking (HAS)". HAS allows the characterization of attosecond electron bursts from systems where the recollision does not yield detectable high harmonic radiation, for instance in metals. Associated publications [P1, C1]

- **Chapter 5** presents the experimental implementation of HAS and the analytical framework used to characterize attosecond electron pulses generated by single-cycle laser pulses in a nanotip. The technique will allow us to characterize (a) the local laser fields, as these are enhanced by the presence of the nanostructure, (b) the duration and chirp of the recolliding attosecond electron pulse, (c) the detailed comparison of atomic and solid state recollision models in the time domain. Associated publications [P1,C1]

- **Chapter 6** introduces a new perspective for high harmonic generation in solids. In this new interpretation, high harmonic generation is understood as radiation emerging from the nonlinear electron motion induced by its scattering from the periodic potential of a crystal. This approach has recently enabled us to probe valence potential and electron density of a solid under a new technique dubbed as "Laser picoscopy". Here, I will introduce the first steps that show how under strong laser fields harmonic

emission can be understood not as transition between bands but as a scattering of an electron with the crystal potential. Associated publications [P2, C2].

- **Chapter 7** presents a detailed study of phase phenomena on high harmonic generation in dielectrics. Since the phase of EUV radiation embodies critical information about the mechanism of high harmonic generation, we will argue that at least in these systems high harmonic generation cannot be explained by semiclassical models developed for atoms. We show that scattering based models such as the intraband picture or the potential scattering model can account for the experimental findings. Associated publication [P3]

List of publication in the context of the work presented in this thesis

[**P1**] **H. Y. Kim**, M. Garg, S. Mandal, L. Seiffert, T. Fennel and E. Goulielmakis, *Attosecond field emission* in preparation (2022).

[**P2**] H. Lakhotia*, **H. Y. Kim***, M. Zhan, S. S. Meng and E. Goulielmakis, *Laser picoscopy of valence electrons in solids*, Nature **583**, 55-59 (2020).

[**P3**] M. Garg, **H. Y. Kim** and E. Goulielmakis, *Ultimate waveform reproducibility of extreme-ultraviolet pulses by high-harmonic generation in quartz*, Nat. Phot. **12**, 291-296 (2018).

Conference contributions in the context of this dissertation

[**C1**] **H. Y. Kim**, M. Garg and E. Goulielmakis, *Measurement of attosecond electron pulses emitted from metallic nanotips*, 7th International Conference on Attosecond Science and Technology (ATTO 2019), July 2019, Szeged, Hungary. (Poster)

[**C2**] H. Lakhotia, **H. Y. Kim**, M. Zhan, S. Hu, S. Meng and E. Goulielmakis, *Reconstruction of valence electron density in solids using optical laser fields*, 7th International Conference on Attosecond Science and Technology (ATTO 2019), July 2019, Szeged, Hungary. (Oral presentation)

* These authors equally contribute to this work.

Chapter 1

Strong Field phenomena

The only way to discover the limits of the possible is to go beyond them into the impossible.
-Arthur C. Clarke

This chapter offers a brief introduction to basic theoretical concepts that will be essential for the detailed understanding of the chapters in which the key research elements of this thesis are presented: the phenomenon of ionization under strong field and the phenomenon of high harmonic generation in atoms and bulk solids.

1.1 Strong-field emission of photoelectrons

1.1.1 Multiphoton ionization (MPI) and Above-threshold ionization (ATI)

Ever since the experimental observation of the photoelectric effect from metals in 19^{th} century [68] the light-induced ionization has been a central element in research of light-matter interactions. The photoelectric effect is typically described by Einstein's interpretation [69]: a photon whose energy ($\hbar\omega_L$) is greater than the work function (W) of a metal $\hbar\omega_L > W$ ejects an electron. The ionization of a metal under these circumstances is a linear process, in the sense of that a single photon releases an electron, and therefore the current is linear to the intensity (number of photons) of the impinging field, $\Gamma(I) \propto I$. The invention of laser opened a new era of research in photoionization of matter that goes beyond Einstein's interpretation of photoelectric effect. Even if a light field is carried at a photon energy lower than the binding potential energy (I_p) or the work function of a metal, an electron can be ejected from an atom, a molecule or a metal by the absorption of multiple photons under irradiance by a strong field. This ionization process is now nonlinear, and it is typically referred to as multiphoton ionization (MPI) [70] (Fig. 1.1). The nonlinearity of the ionization rate is well described by lowest order perturbation theory (LOPT) in a form of a power law [71],

$$\Gamma_{MPI}(I) = \sigma I^n \tag{1.1}$$

where σ is the cross-section associated with the dipole element involved in transition, I is the intensity of the impinging field, and n is an integer number of photons minimally required to overcome the potential barrier I_p (or W), $n = \lceil I_p/(\hbar\omega_L) \rceil$ (black arrows in Fig. 1.1).

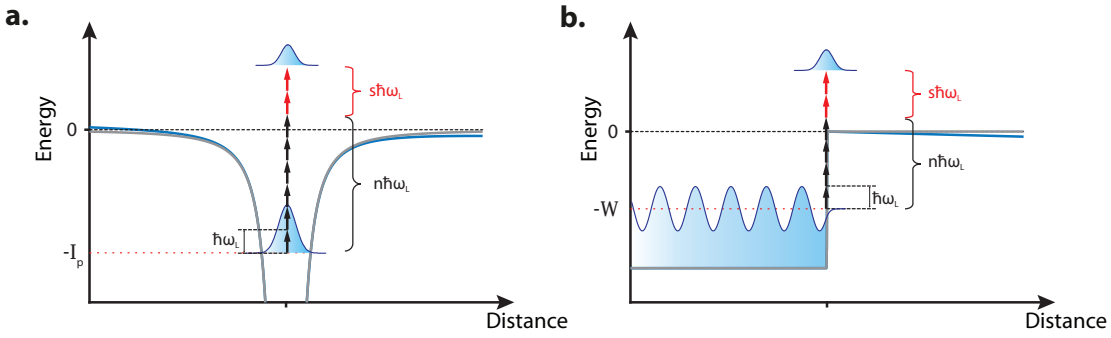

Figure 1.1: **Schematic illustration of multiphoton ionization (MPI) and Above-threshold ionization (ATI).** Multi-photon ionization (black arrows) and above-threshold ionization (red arrows) in an atom (**a**) and in a metal (**b**).

In the presence of a strong electric field, higher order perturbations significantly contribute to the process, and the emission occurs via the absorption of a number of photons even higher than those required to overcome the potential barrier (n) (red arrows in Fig. 1.1), as shown by an experimental observation in 1979 [72].

The above phenomenon is known as above-threshold ionization (ATI). The emission rate also follows a power law, $\Gamma_{ATI}(I) = \sigma I^{(n+s)}$, where s is an integer number of additionally absorbed photons. This results in characteristic harmonic peaks in the photoelectron spectrum separated by $\hbar\omega_L$. ATI can also be understood in the time-domain as a result of the interference between consecutive electron wavepackets that are generated every one-cycle of the driving laser pulse.

An essential difference in the photoemission from atoms and metals (that will become central in this thesis) is related to the geometry of these systems. An atom can be conveniently described by an isotropic Coulomb potential (Fig. 1.1 a). On the expose to an electromagnetic field, an electron will be ejected in both directions along the polarization vector of the driving field. By contrast, the potential that an electron experience at the interface of a metal and vacuum is half-sided. Such a potential is best described by a jellium model (Fig. 1.1 b), where the electronic states of the system are strongly bound on one side of space. This potential in metals dictates that electron emission will only occur in the metal to vacuum direction, that is, when the electron is driven away from the surface and not into it.

1.1.2 Keldysh parameter and tunnel-ionization

In the presence of a strong laser field, the binding potential of electron in an atom, a molecule or a solid can be significantly suppressed. This allows electrons to tunnel through the potential barrier. In 1965, Keldysh was among the first to propose a theoretical picture of ionization under strong laser fields [73]. In his picture, the release of an electron under multiphoton absorption and tunneling can be considered as two distinct paths of ionization. He suggested that the dominant ionization process can be identified by evaluating the relative ratio of the tunneling time (T_{tun}) and laser period (T_L) [74], which can be described as a parameter γ involving ionization energy, laser intensity (I) and frequency (ω_L),

$$\gamma = \frac{T_{tun}}{T_L} = \sqrt{\frac{I_p}{2U_p}} \tag{1.2}$$

where U_p, is the cycle-averaged quiver energy of an electron in the laser-field,

$$U_p = \frac{e^2E^2}{4m_e\omega_L^2} = \frac{e^2}{2c\varepsilon_0 m_e}\frac{I}{\omega_L^2} \tag{1.3}$$

Here, c, ε_0 and m_e are the speed of light, the vacuum permittivity and the electron mass, respectively. When the Keldysh parameter is $\gamma \gg 1$, the potential barrier is not sufficiently suppressed, and hence the distance for electrons to tunnel the barrier is long. As a result, time required for tunnel ionization is longer than the laser period ($T_{tun} \gg T_L$). In this case, the multiphoton ionization is dominant. By contrast, if $\gamma \ll 1$, the electron tunneling time is much shorter than the laser period, and the emission is dominated by the tunneling processes (Fig. 1.2).

The ionization mechanisms under strong static as well as periodic fields have not only been of interest in the study of atoms and molecules but also in metals. One of the earliest studies of ionization of metals under strong static fields is that of Fowler and Nordheim [75]. By inserting a triangular potential barrier into the WKB approximation, one can express the electron ionization rate under a strong static field (E) in the following form [76, 77, 78]:

$$\Gamma_{FN} \propto E^2 \exp\left[-\frac{2}{\hbar}\int_0^{\Delta x_t} dx\sqrt{2m_e(I_p - eEx)}\right] = E^2 \exp\left[-\frac{4\sqrt{2m_e}I_p^{3/2}}{3\hbar e|E|}\right] \tag{1.4}$$

Keldysh obtained the same exponential dependence of long-time-averaged tunnel ionization probability (under low frequency waves) with an additional factor in front of the exponent in the limit of $\gamma \ll 1$. The field-ionization rate has further been developed by many theorists [79, 80, 81, 82], for example Ammosov, Delone and Krainov (known as ADK-rate) [83]. Although the ADK rate is basically a cycle-average concept, it is also widely used for instantaneous field emission by replacing the field, $E \to E(t)$:

$$\Gamma_{ADK}(t) \propto N(Z, n^*, l, m)\sqrt{\frac{3\hbar eE(t)}{2\pi\sqrt{2m_e}I_p^{3/2}}}\left(\frac{4\sqrt{2m_e}I_p^{3/2}}{\hbar eE(t)}\right)^{2n^*-|m|-1}\exp\left[-\frac{4\sqrt{2m_e}I_p^{3/2}}{3\hbar eE(t)}\right] \tag{1.5}$$

where $N(Z, n^*, l, m)$ is a constant for a given atomic charge Z, effective quantum number $n^* = Z/(2I_P)^{1/2}$ (in atomic unit), orbital (l) and magnetic (m) quantum numbers.

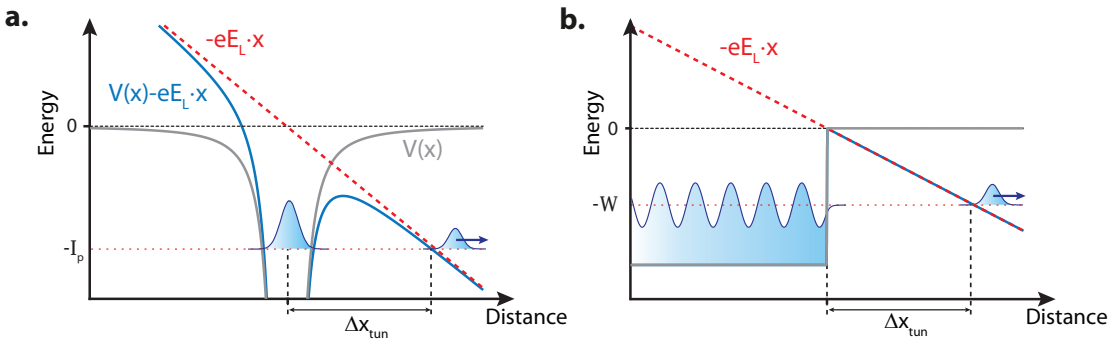

Figure 1.2: **Tunnel ionization of electrons in atoms and metals.** Tunnel ionization in the presence of a strong field E_L in an atomic potential (**a**) and the metal-vacuum interface (**b**). The binding potential ($V(x)$, grey curve) is suppressed by the strong field (red dashed line), and the wavefunction of the ground state tunnels through the barrier at a distance of $\Delta x_{tun} = I_p/eE_L$.

1.2 Dynamics of electron in intense laser fields

The electrons released in the free space by ionization are subsequently driven by the strong laser field. Fig. 1.3 illustrates classical dynamics of electrons under an intense linearly polarized light field. When the applied field is so strong that the Coulombic attraction from the parent ion or metallic surface can be considered negligible, the kinematics of the photoelectrons are purely governed by the driving laser field. This approximation is known as "Strong field approximation" (SFA). Furthermore, since the wavelength of the optical driving field (hundreds of nm) is much larger than the size of an atom (hundreds of pm), the driving electric field can be safely considered spatially homogeneous in the interaction area, known as "dipole approximation".

1.2.1 Classical kinematics of electrons under strong laser fields

A classical method, so-called the three step model (TSM) offers an intuitive understanding of the dynamics of a photoelectron after the ionization from its parent ionic core. A classical description of strong field dynamics starts with the ionization of an atom by a strong field $E_L(t)$ at an instance t_b. The liberated electron is treated as a point charge ($-e$, $e > 0$) and experiences the electric force from the oscillating laser field. The kinematics of a photoelectron starting from its birth time t_b is described by Newton's 2$^{\text{nd}}$ law as:

$$F(t) = -eE_L(t) = m_e \frac{d^2x(t)}{dt^2} \text{ for } t > t_b \tag{1.6}$$

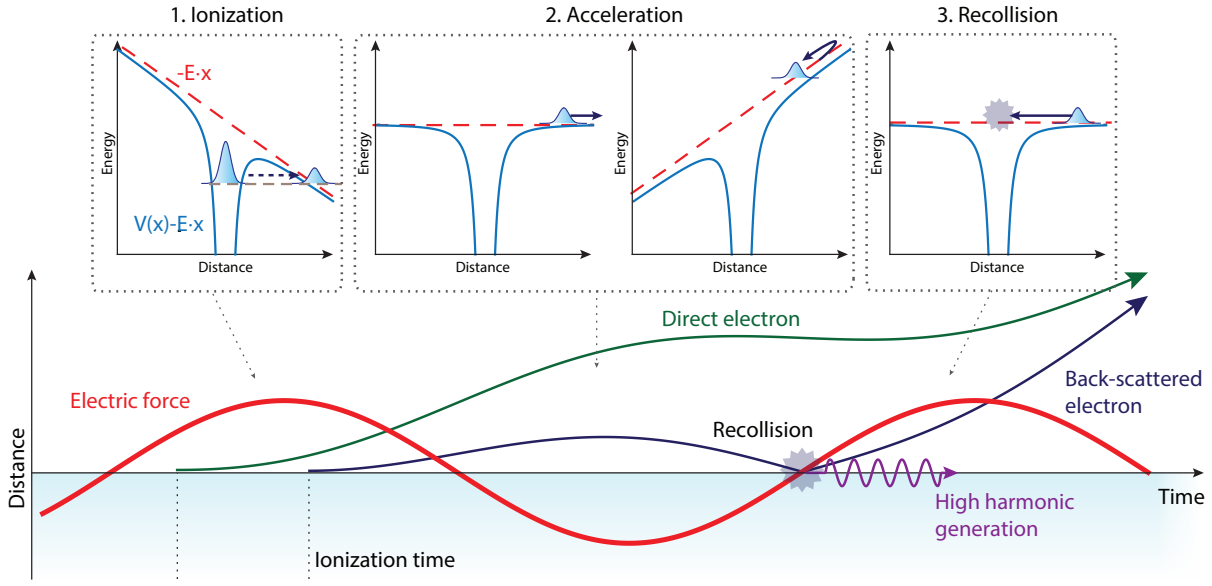

Figure 1.3: **Schematic illustration of the semiclassical three step model.** 1. Ionization: the laser electric field (red curve) ionizes the atom, and electrons are set free. 2. Acceleration: a released electron is accelerated by the electric field in vacuum. The electrons which are not driven back to the surface (green curve) are referred to as "direct electrons". 3. recollision: The photoelectrons ionized around the peak of the field are driven back to the parent ion or the surface of a metal and recollide. The back-scatted electron from the surface (dark blue) is further accelerated by the driving field. At the recollision moment, a recombination to the parent ion leads to radiative emission at harmonic frequencies of the laser field (purple). Harmonics from metals under the above mechanism have not yet been observed.

The velocity $v(t)$ and the excursion $x(t)$ of the photoelectron can be evaluated by the integration of the acceleration in time with the initial conditions, $x(t_b) = 0$ and $v(t_b) = 0$. The velocity and accordingly the momentum are expressed by the integration of the electric field, which can be casted into the vector potential $A(t)$,

$$v(t, t_b) = -\frac{e}{m_e}\int_{t_b}^{t} dt E_L(t) = -\frac{e}{m_e}[A(t_b) - A(t)] \tag{1.7}$$

Depending on the phase of the electric field at the electron birth time t_b, the emitted photoelectrons can be classified into two types: direct (green in Fig. 1.3) and back-scattered (dark blue in Fig. 1.3). For the sake of simplicity, a continuous wave (CW) laser field can be considered as $E_L(t) = -E_0 \sin(\omega_L t)$, and the solution of the above differential equation (Eq. 1.6) can be written as:

$$x(t, t_b) = -\frac{eE_0}{m_e\omega_L^2}[\sin(\omega_L t) - \sin(\omega_L t_b)] + \frac{eE_0}{m_e\omega_L}(t - t_b)\cos(\omega_L t_b) \tag{1.8}$$

This expression consists of temporally oscillating and linear terms, the first and second term, respectively on the right hand side of Eq. 1.8. Depending on the ionization time t_b, the contribution of the linear term is modulated by a sinusoidal function. Now, one can consider the solution for a trajectory that brings the electron back to the origin, *i.e.*, $x(t; t > t_b) = 0$. The equation can be solved numerically and has a solution only if $\omega_L t_b > \pi/2$. This implies that the electrons generated at the leading edge of an electric field crest, within the time range from $\omega_L t_b = 0$ to $\omega_L t_b = \pi/2$, do not revisit the origin during their excursion, *i.e.*, $x(t > t_b) > 0$. Photoelectrons generated within this time window are usually referred to as direct electrons. The momentum accumulated by the direct electrons until their detection is proportional to the vector potential of the light waveform at the time of their birth $A(t_b)$. The maximum terminal kinetic energy (referred to as "cutoff" energy) of the direct electron $E^{(d)}_{cutoff}$ is related to the maximum of the vector potential of the laser pulse as:

$$E^{(d)}_{cutoff} = \frac{1}{2m_e}(e \max[A(t_b)])^2 \approx 2U_p \tag{1.9}$$

In contrast to direct electrons, the solution for an electron generated at the trailing edge of a field half cycle ($\omega_L t_b > \pi/2$) predicts return of the electron to its parent ion or metallic surface, $x(t_r, t_r > t_b) = 0$. These electrons (can) elastically rebounce at the origin $x = 0$. This effect is incorporated into the model as a change of the direction of their velocity, $v(t_r) \rightarrow -v(t_r)$. These electrons are referred to as "back-scattered electrons". The back-scattered electrons accumulate further momentum under the laser field until the end of the laser pulse. The singularity of the back-scattering event leads to an increase of the electron energy. The maximum momentum of the back-scattered electron is, $\max(p) = e \max(2A(t_r) - A(t_b))$, and correspondingly its cutoff energy $E^{(bs)}_{cutoff}$ is given by [84],

$$E^{(bs)}_{cutoff} \approx 10U_p \tag{1.10}$$

In this thesis, the term "release time" is occasionally used to refer to the recollision moment when discussing back-scattered electrons.

The above formalism has been developed under CW laser fields. However, a more realistic consideration is that the driving fields are generally pulsed, and one can expect differences. Especially at the limit of single-cycle pulses used in the experiments in this thesis, the electron trajectory highly depends on the waveform of the driving field. The ionization rate and time, as well as the release time for each type of the photoelectrons (direct of back-scattered) are modified by the incident electric field waveform.

For recolliding electrons, a further classification based on their classical trajectories is possible. Depending on their excursion time and energy profile, we refer to them as long and short trajectories. Long trajectories are of those electrons that are ionized earlier in time and recollided later, *i.e.*, with a longer excursion time than short trajectories resulting in descending recollision energy profile in time. The recollision events happen within a sub-half cycle ($< T_L/2$) time window. For optical fields whose period is $T_L \sim 2$ fs, this implies a sub-femtosecond time scale.

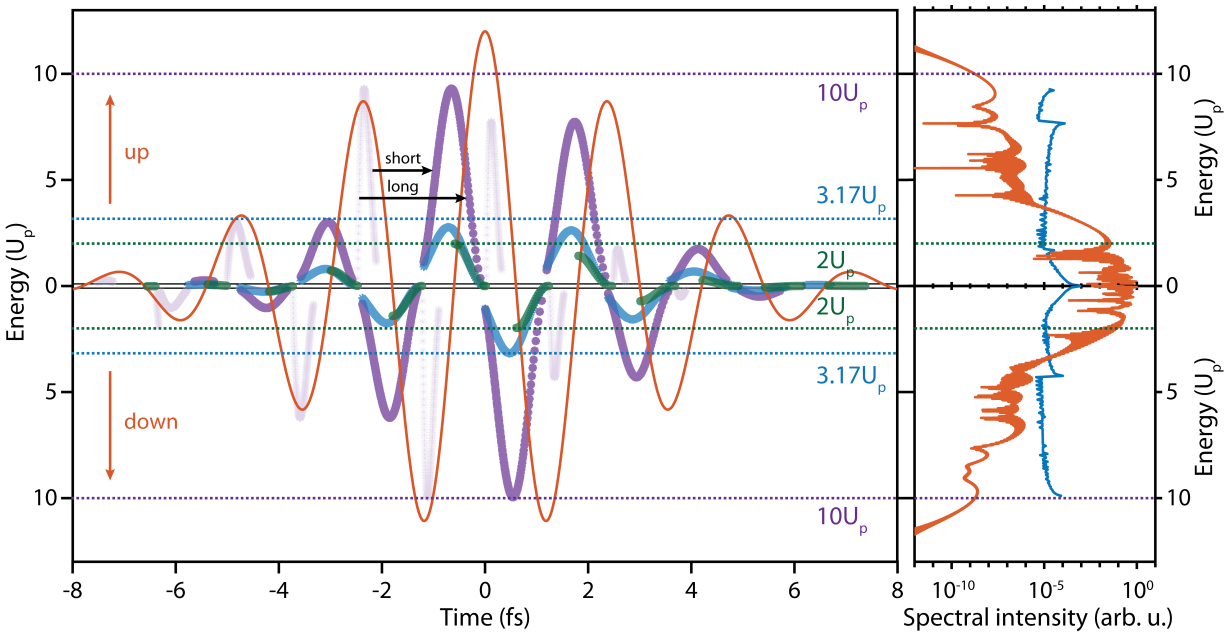

Figure 1.4: **Kinetic energy of back-scattered and direct electrons.** Terminal kinetic energies of back-scattered (purple) and direct (green) photoelectron under a strong electric field pulse (central energy of 1.7 eV, duration of 5 fs and intensity of 5×10^{14} W/cm^2). The red curve denotes the electric field force ($-eE_L(t)$). The cyan points denote the kinetic energy at the moment of the recollision (recollision energy). Upper and lower sides correspond to electrons detected in these directions of the field force (red arrows). The dimmed purple points indicate the terminal kinetic energy of the back-scattered electrons as a function of the ionization time. Long and short trajectories are classified by the excursion time from ionization to recollision (black arrows). The spectra of photoelectron from xenon atom calculated by TDSE (red) and TSM (blue) are shown in the right panel.

1.2.2 Quantum mechanical description

Numerical approach

For the quantum mechanical description of ionization and the ensuing dynamics in the presence of a strong field of a laser pulse, one can consider the time-dependent Schrödinger equation (TDSE) in one dimension [85, 86].

$$i\frac{\partial\psi(x,t)}{\partial t} = \hat{H}\psi(x,t) \tag{1.11}$$

where the Hamiltonian is given by a superposition of laser-free, $\hat{H}_0 = \frac{1}{2}\frac{\partial^2}{\partial x^2} + V(x)$, and laser-driven dipolar interaction, $\hat{H}_{int} = -E(t)x$ terms in the length gauge,

$$\hat{H} = \hat{H}_0 + \hat{H}_{int} = \frac{1}{2}\frac{\partial^2}{\partial x^2} + V(x) - E(t)x \tag{1.12}$$

Atomic units ($e = \hbar = m_e = 1$) is used in this discussion. The atomic potential $V(x)$ is typically represented by a Coulombic potential. However, because of the singularity of a Coulomb potential $V(x) \propto 1/x$ at the origin, $x = 0$, a modified Coulomb potential known as the soft-core potential is widely used in atomic physics, $V(x) \propto -1/\sqrt{x^2 + a^2}$, with the core size of a [87, 85]. The core size can be chosen to fit the ionization energy of the considered atom. For instance, the ionization energy calculated with a soft-core size of $\sim$1.19 (atomic units) predicts well that of argon, $\sim$15.7 eV. A solution of the TDSE is typically obtained numerically. There the initial state of the system is the ground state of an electron in the atomic potential and can be calculated by imaginary time propagation or by diagonalization of the Hamiltonian utilizing finite differences. From the ground state, the time propagation of the wavepacket can be numerically calculated by the split-step Fourier method [88]. A detailed description of numerical process is summarized in Appendix A.

A TDSE calculation of the photoelectron spectra in xenon is shown in the Fig. 1.4, and it is compared with the results of the three-step model. The quantum mechanical results produce a slightly higher cutoff energy than the semiclassical calculation under the same parameters. This difference can be understood as an effect of quantum tunneling and diffusion effect of the electronic wavefunction [89].

Analytical approach

The possibility of a quasi-analytical description of the strong field emission is essential for developing a new time-resolving technique that allows the measurement of attosecond electron pulses (Chapter 4 and 5). In this section therefore we review previous works on strong field emission [90, 91, 92], and therewith provide a firm background for the theoretical framework discussed later in Chapter 4.

Generally, the wavefunction of electrons can be described as a coherent superposition of the ground state $|0\rangle$ and the unbounded continuum states $|p\rangle$,

$$\psi(t) = \left[|0\rangle + \int d^3p \chi(p,t)|p\rangle\right] e^{iI_p t} \tag{1.13}$$

where I_p is the ionization energy of the system, and $\chi(p,t)$, represents the complex transition amplitude from the ground to the continuum state, $|0\rangle \rightarrow |p\rangle$ at a detection time t. Since we are interested in the temporal characteristics of the electron wavepacket, only the temporal component of the wavefunction is considered. As described in Eq. 1.13, the transition amplitude is related to both the spectral and temporal characteristics of the electron wavepacket. Therefore, the primary subject of this section is the theoretical formalism of the transition amplitude $\chi(p,t)$ and its analytical expression.

As in the classical description of the strong field emission, the dynamics of an electron are classified based on whether it undergoes a back-scattering event or not. Similarly, the transition amplitude can be considered as composition of two different contributions: direct $\chi_{dir}(p,t)$ and back-scattered $\chi_{sc}(p,t)$ amplitudes,

$$\chi(p,t) = \chi_{dir}(p,t) + \chi_{sc}(p,t) \tag{1.14}$$

Because the direct electron does not undergo back-scattering, the transition amplitude at the detection time is simply the ionization probability amplitude after the electron propagation from the ionization time to the detection time. Analytically, this is given by a superposition of the probability amplitude $E(t')d(p + A(t'))$ with a phase accumulation during the propagation following the ionization time t' as:

$$\chi_{dir}(p,t) = i\int_{-\infty}^{t} dt' E(t') d(p + A(t')) \exp\left[-i\int_{t'}^{t} dt \frac{1}{2}[p + A(t)]^2 \right] \tag{1.15}$$

where $E(t)$ and $A(t)$ are electric field and vector potential, respectively, and $d(p+A(t'))$ is the dipole element which is associated with the transition from the bound to the continuum states, $d(p + A(t')) = \langle p + A(t')|r|0\rangle$. In this derivation, the strong field approximation is used; the dynamics of the electron is governed purely by the strong electric field, *i.e.*, without considering the Coulomb potential of the ion. The phase term in the exponent is the accumulated phase during the time from t' to t which is the semiclassical action also known as Volkov phase [93],

$$S(p, t_2, t_1; A(t)) = \int_{t_1}^{t_2} dt' \frac{1}{2}[p + A(t')]^2 \tag{1.16}$$

In contrast to the direct electron, a formalism of the transition amplitude for the back-scattered electron calls upon inclusion of the scattering process. The back-scattering process can be introduced by a scattering transition matrix $g(p)$ associated with the momentum component p. Now we can split the process into two steps before and after the back-scattering time t_r: 1) from ionization (t') to back-scattering (t_r) time 2) from back-scattering (t_r) to detection time (t). In the first step 1), the electron wavepacket at the back-scattering time $\psi_{bs}(t_r)$ can be expressed as a coherent superposition of all momentum components of the ionization and scattering amplitudes with the Volkov phase accumulated:

$$\psi_{bs}(t_r) = \int_{-\infty}^{t_r} dt' \int d^3p' E(t_r) g[p' + A(t_r)] E(t') d[p' + A(t')] \exp[-iS(p', t_r, t'; A(t))] \tag{1.17}$$

In analogy to the case of the direct electron (Eq. 1.15), $E(t')d[p' + A(t')]$ describes the ionization amplitude at time t'. The back-scattering amplitude is expressed by $E(t_r)g[p' + A(t_r)]$ at time t_r. The phase propagation from the ionization to back-scattering time is given by the Volkov phase $S(p, t_r, t'; A(t))$. After the back-scattering event, in the step 2), the electron wavepacket $\psi_{bs}(t_r)$ propagates to the detector. Hence, the electron spectral amplitude at time t can be easily obtained by an integration of the back-scattered wavepacket with the Volkov phase over time,

$$\chi_{sc}(p,t) = -\int_{-\infty}^{t} dt_r \psi_{bs}(t_r) \exp[-iS(p, t, t_r; A(t))] \tag{1.18}$$

The detection time is virtually the time after the end of the transient electric field ($t \to \infty$). Eq. 1.15 and 1.18 can be now simplified as $\chi(p, t = \infty) = \chi(p)$ (referred to as "terminal

amplitude"). The electron spectrum of the strong field emission is then give by

$$I(p) = |\chi(p)|^2 = |\chi_{dir}(p) + \chi_{sc}(p)|^2 \tag{1.19}$$

The formalism of Eq. 1.18 clearly shows that the spectral amplitude $\chi_{sc}(p)$ is linked with the back-scattered electron wavepacket at its release time, $\psi_{bs}(t_r)$. It implies that the electron pulse $\psi_{bs}(t_r)$ can be characterized, if the complex spectral amplitude $\chi_{sc}(p)$ is known, and the electric field and back-scattering time are precisely known in order to evaluate the Volkov phase. A realization of this idea will be presented in Chapter 4 and 5.

1.3 High harmonic generation

1.3.1 Three-Step model: High harmonic generation in gaseous media

High harmonic generation (HHG) in atoms shares the same mechanism as that of strong field photoemission. The electron recombines with the parent ion in its ground state and emits radiation. In other words, the recombination event leads to a conversion of the kinetic energy of the recolliding electron to coherent radiation. The highest energy of the coherent radiation is thus directly related to the maximum kinetic energy of photoelectron at the recollision time t_r. The highest momentum at the recollision instance can be evaluated as $\max(p) = e\max(A(t_r) - A(t_b))$, and the corresponding cutoff energy of the radiation $E^{(HH)}_{cutoff}$ is given by [18, 94, 95]

$$E^{(HH)}_{cutoff} \approx 3.17U_p + I_p \tag{1.20}$$

The extension of the high harmonic generation process from the semiclassical to the quantum mechanical description was introduced by Lewenstein *et. al.* [89]. In this model, high harmonics generation is described as the time-dependent electronic dipole under the strong field approximation. Fig. 1.5 shows simulated high harmonic spectra based on the Lewenstein model (blue) and the semiclassical three step model (red). Higher cutoff energy is observed in the Lewenstein model compared to the three step model, which is once again attributed to quantum properties, *i.e.*, quantum tunneling and diffusion.

The probability of recombination of electrons with the parent ion is highly related to the scattering cross-section of the electronic wavepacket and the parent ion. The electron wavepacket is naturally broadened in space during its excursion due to dispersion. The short trajectory electron is less broadened and therefore, a larger scattering cross-section than that of the long electron trajectory is anticipated. This fact implies that high harmonic radiation from atoms is primarily dictated by the physics of the short trajectories. Consequently, its temporal properties are related to the recolision times of the short trajectory such as positive chirp. For the same reasons, the wavelength of the driving fields plays a key role in the conversion efficiency. A driving field of a longer wavelength can provide higher ponderomotive energy, but the excursion time to recollision is longer. Therefore,

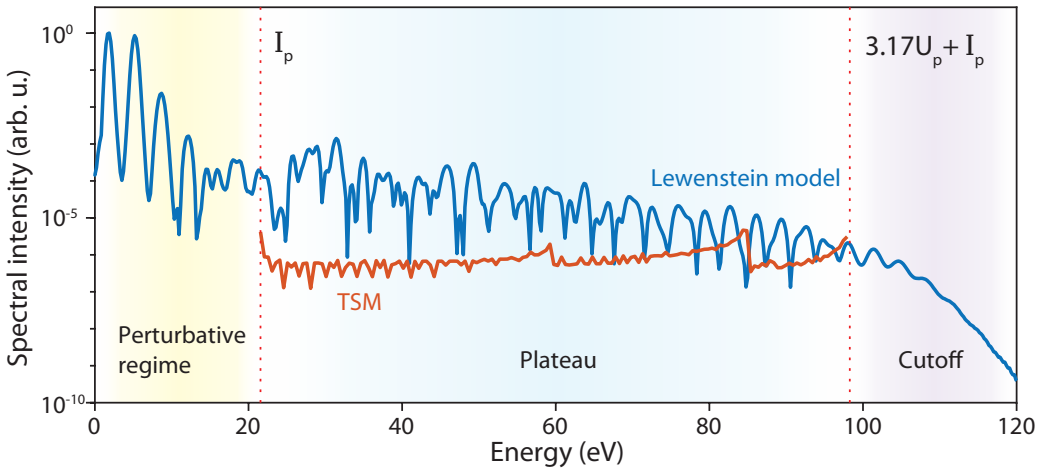

Figure 1.5: **High harmonics in atoms.** High harmonic spectra in neon calculated by the Lewenstein (blue) and the three step (red) models under the identical conditions as used for Fig. 1.4.

lower energy conversion efficiency is to be expected [96, 97]. High harmonic emission takes place at each consecutive half cycle of the driving field. Due to inversion symmetry, only odd harmonics are produced and are manifested in the spectrum as peaks separated by $2\hbar\omega_L$. High harmonic bursts from many half cycles of similar intensity spectrally interfere and create the plateau of the harmonic spectrum (blue shaded area in Fig. 1.5). Around the cutoff regime of the spectrum (purple shaded area in Fig. 1.5), a continuum can be observed due to the isolation of the highest energy components.

1.3.2 High harmonics and EUV attosecond pulses

In high harmonic generation, the recollision process occurs within a half-cycle of driving field. This implies that high harmonic generation provides a route for generating EUV attosecond pulse bursts. To better understand this aspect, a time-resolved simulation based on the Lewenstein model [89] is once again considered. In the simulation, a Gaussian laser pulse is used with a peak intensity of $I = 6 \times 10^{14}$ W/cm^2 and a central wavelength of 700 nm. As shown in Fig. 1.6 a, the EUV emission occurs at every half cycle of the driving field, that is, a sub-femtosecond window. The highest photon energy, $\sim$ 80 eV under the considered parameters (Fig. 1.6 b), is released around the zero transition of main half-field-cycle, as shown in the time-frequency analysis (Gabor transformation) of the EUV burst in Fig. 1.6 c.

The temporal isolation of EUV attosecond pulses is crucial for their use in time-resolved measurements. Over the last decades, different types of gating approaches that allow the temporal isolation of the EUV attosecond pulse have been invented such as polarization

gate [98, 99], double optical gate [100], amplitude gate [29, 22] and ionization gate [101, 102]. In the AS beamline of this group, the amplitude gate is the method of choice. I will therefore briefly discuss this technique. Because a few or single cycle pulse has high contrast in field strength of consecutive cycles and therefore the energy variation of adjacent EUV burst around highest energy is large enough to have a wide bandwidth for an attosecond scaled pulse duration, a spectral filtering around cutoff regime (blue curves in Fig. 1.6 b and c) is able to provide single isolated attosecond EUV burst (Fig. 1.6 d). Metallic filter for the amplitude gating must be chosen by its characteristic transmission and the cutoff energy under laser parameters.

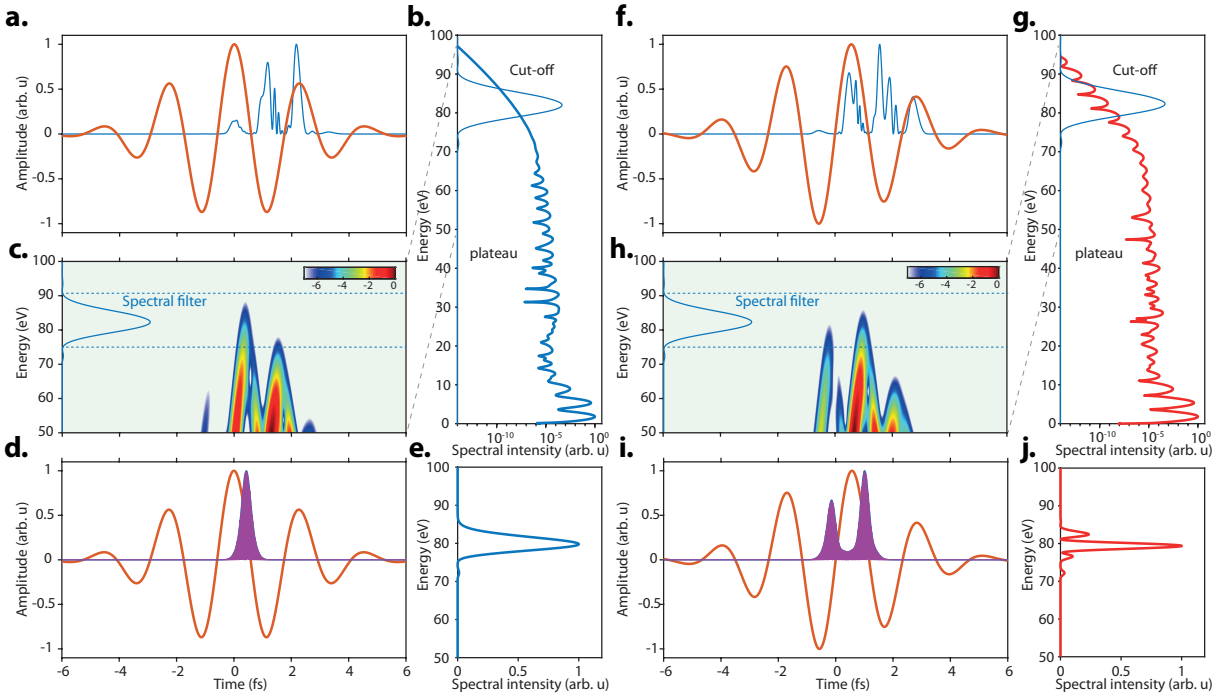

Figure 1.6: **High harmonic generation in gaseous media and temporal isolation of an attosecond EUV pulse.** **a** and **b**, The EUV high harmonic emission calculated using the Lewensteim model (blue) under a strong incident field ($I = 6 \times 10^{14}$ W/cm^2) at central wavelength of 700 nm (red) in time domain (a) and its spectrum was computed by the Fourier transform (b). **c**, Time-frequency analysis of the radiated EUV is shown for energies above ∼50 eV. The blue curve in panel b and c is shows the application of a spectral filter (Zr foil and a customized EUV multilayer mirror used in AS beamline). The dashed lines indicate the margins of the filter. **d** and **e**, Spectrally filtered EUV pulse (d) and its spectrum (e). **f-j**, The EUV radiation under identical condition but with a 0.5π CEP shifted waveform.

Just as in strong field ionization, high harmonic generation is a field-waveform sensitive process. As a result, a carrier-envelope phase (CEP) variation of the driving pulse can control the temporal and spectral characteristics of the generated EUV bursts. A simulation under identical conditions as used in Fig. 1.6 a-e, but with a CEP shifted by 0.5π illustrates this effect. For a CEP of 0, a single energetic bust of radiation emerges around the cutoff energy, whereas for a CEP 0.5π there are multiple EUV bursts (2 bursts in the single-cycle pulsed case) as shown in the time-frequency analysis (Fig. 1.6 h). The appearance of discrete harmonics in the cutoff region indicates a clear spectral signature of the multiple pulses in the time domain (Fig. 1.6 g and j). Therefore, only spectral filtering of the cutoff radiation is not sufficient to isolate a single attosecond pulse but also the appropriate carrier-envelope phase setting of the pulse.

1.3.3 High harmonic generation in bulk solids

The extension of the non-perturbative optics from atom to condensed matter was limited by the irreversible structural damage of solids under extreme fields. This obstacle was overcome by the advancement of laser pulses to short durations and towards infrared carrier frequencies. Ever since the first report on the high harmonic generation in ZnO in 2011 [60], the properties of high harmonics emerging from bulk solid have been at the research focus of several research groups. Typical studies include field scaling of the cutoff energy [60, 62, 65, 103], nonlinearity of harmonic yield versus the driving field strength [60, 62, 65], field waveform sensitivity of the harmonic spectra [65, 104, 105], temporal confinement and distribution of the emerging EUV pulses [61, 42, 104]. Many distinct characteristics of the solid-state high harmonics which are in contrast to those in atom have been reported. Experiments focused on the spectral characteristics of the high harmonics in solids revealed a linear scaling of the cutoff energy to the field strength [60, 62, 65, 103]. This is in contrast to the high harmonics in atoms where the cutoff energy exhibits a quadratic scaling of field. This feature has been observed in diverse solids from semiconductors (ZnO [60], GaSe [62]) to wide band-gap dielectrics (SiO_2 [65], Ai_2O_3 [103]) under incidence of broad range of the central frequency, THz [62, 61], mid-infrared [60] and up to visible range [65, 42]. However, despite this feature, a mechanism that can describe the temporal characteristics of solid-state harmonics is still under debate, because of contradicting experimental observations. For example, experimental reports on measurements with ZnO [63, 106] revealed chirped harmonics, which can be understood by a mechanism similar to the recollision picture, while experiments with SiO_2 using a time-resolving technique [42] and an interferometry technique [107] revealed synchronization of harmonic pulse with the peak of the driving field and a zero-chirp, which are supporting non-recollisonal pictures such as the intraband scattering.

Since a part of this thesis is concerned with the electron dynamics and associated high harmonic radiation in dielectrics, in this section I will briefly summarize the current models for HHG in solid which have been developed in the strong-field physics community.

Quantum mechanical description: Semiconductor Bloch equation (SBE)

In the band picture of solids, electron dynamics in solids are directly linked to the time evolution of populations involving transition among different electronic bands and the transportation of charge carriers within individual band. Within the premises of this model, the fully occupied bands of a semiconductor or a dielectric cannot yield an electronic current. However, in the presence of a strong-laser field transitions of electron population from fully occupied valence bands to unoccupied conduction bands give rise to partially filled bands, *i.e.*, by creating a vacancy on valence bands (holes) and electron in the conduction bands. The polarization by the motion of the electron-hole pair is typically referred to as interband polarization. In parallel to the interband motion of electrons, the electrons and holes are simultaneously driven on underlying bands, and this gives rise to a second current which is typically referred to as intraband current. Inter- and intraband motion evolves in a coupled manner over time. A quantum mechanical treatment of the electron dynamics can be understood as an extension of optical Bloch equation [108]: semiconductor Bloch equation (SBE) [109, 110, 111]. The SBE describes the time evolution of polarization (p_k) and population (f_k^λ) of electrons and holes as:

$$i\hbar\frac{\partial}{\partial t}p_k = \left[\epsilon_k^\lambda + \epsilon_k^{\lambda'} - i\frac{1}{T_d}\right]p_k - d_k E(t)(1 - f_k^\lambda - f_k^{\lambda'}) + ieE(t)\nabla_k p_k \tag{1.21}$$

where λ is an index for electron and hole, $\lambda = e, h$. The first term stands for the phase evolution including the dephasing ($1/T_d$) of wavepacket. The second term represents the transition rate dictated by the dipole (d_k), and the last term has a meaning of the transportation of polarization in the momentum space k. The time evolution of population of electrons and holes is given by:

$$\hbar\frac{\partial}{\partial t}f_k^\lambda = -2Im[d_k E(t)p_k^*] + eE(t)\nabla_k f_k^\lambda \tag{1.22}$$

The total interband polarization $P(t)$ is expressed by a coherent superposition of polarization contributions, $P(t) = \sum_k d_k p_k$, while the total intraband current is given by a summation of group velocity, $v_g(k) = \hbar^{-1}\nabla_k\epsilon_k$, of holes and electrons on all populated bands, $J(t) = \sum_k[\sum_h f_k^\lambda \nabla_k \epsilon_k^h + \sum_e f_k^\lambda \nabla_k \epsilon_k^e]$. The amplitude of high harmonic radiation is proportional to the time variation of the total current, $E_{HH}(t) \propto \frac{d}{dt}\left[\frac{dp}{dt} + J(t)\right]$, and hence its spectrum can be expressed as

$$I_{HH}(\omega) \propto |\omega^2 P(\omega) + i\omega J(\omega)|^2 \tag{1.23}$$

The first and second terms on the right hand side denote the spectral contribution from interband and intraband motions, respectively.

Semiclassical description of intraband motion

The harmonics originated from intraband current can be more intuitively understood within the concept of Bloch oscillations of an electron on the conduction bands of a solid

(or a hole on a valence band) in the semiclassical approach [74, 65]. In this approach, the transition of an electron from a valence band to a conduction band is not considered, but the electronic wavepacket is treated as being pre-existing before the incidence of the field. Furthermore, the population of the band is assumed to remain constant in time without any depletion. The acceleration theorem describes the equation of electron motion with the laser field, $E_L(t) = E_0 \cos(\omega_L t)$, as $\hbar \frac{dk}{dt} = -eE_L(t)$. The time dependent momentum is given by a description with the vector potential, $A(t) = \int_t^\infty dt' E_L(t') = \frac{E_0}{\omega_L} \sin(\omega_L t)$ as,

$$k(t) = k_0 + \frac{e}{\hbar} A(t) = k_0 + \frac{eE_0}{\hbar\omega_L} \sin(\omega_L t) \tag{1.24}$$

The time evolution of the electron momentum distribution g(k,t) is given by the Boltzmann transport equation,

$$\frac{\partial g(k,t)}{\partial t} = \frac{\partial g(k,t)}{\partial k} \frac{dk}{dt} \tag{1.25}$$

It is important to note that this is the same equation as Eq. 1.22 but without the term that accounts for the population variation of the band in time (the first term). The analytical solution of the Boltzmann's equation results in a translation of the initial momentum distribution from k_0 to the instantaneous momentum, $k(t) = k_0 + A(t)$.

$$g(k_0, t) = g(k_0 + A(t), t_0) \tag{1.26}$$

The laser induced intraband current is given by the weighted group velocity over the electron distribution within the Brillouin zone, $J(t) = e\hbar^{-1} \int dk \nabla \epsilon_i(k) g(k,t)$. In the one-dimensional tight-binding model, the energy dispersion of a band $\epsilon_i(k)$ can be described as the superposition of harmonics as a Fourier series, $\epsilon_i(k) = Re[\sum_m \tilde{\varepsilon}_{i,m} \exp(imkd)]$ where i and m are indices of the band and reciprocal harmonics, respectively, and d is the lattice constant of the crystal lattice. For the simple case of a system having inversion symmetry, the band dispersion consists of cosine functions with real valued coefficients, $\epsilon_i(k) = \sum_m \varepsilon_{i,m} \cos(mkd)$. With an assumption of the initial central momentum of, $k_0 = 0$ and the delta-function-like initial momentum distribution, the current density reads

$$J(t) \propto \nabla_k \epsilon_i(k)|_{k=A(t)} = \sum_m md\varepsilon_{i,m} \sin\left(m \frac{eE_0 d}{\hbar\omega_L} \sin(\omega_L t)\right) \tag{1.27}$$

Applying the Jacobi-Anger expansion to the above equation yields the current as a superposition of harmonics of the laser field with an amplitude of odd order 1$^{\text{st}}$ kind Bessel function J_N,

$$J(t) \propto 2 \sum_m md\varepsilon_{i,m} \sum_N J_N\left(m \frac{eE_0 d}{\hbar\omega_L}\right) \sin(N\omega_L t) \tag{1.28}$$

where N is odd integer number. The N$^{\text{th}}$ order harmonic intensity can thus be derived as,

$$I_N \propto \left| N\omega_L \sum_m md\varepsilon_{i,m} J_N\left(m \frac{eE_0 d}{\hbar\omega_L}\right) \right|^2 \tag{1.29}$$

Owing to the fact that the Bessel function is maximized approximately when the argument is equal to its order, the cutoff energy of high harmonics is scaled with the highest order of significant Fourier component of the band dispersion (n_{cutoff}),

$$E_{cutoff}^{HH} = \left(n_{cutoff} \frac{eE_0 d}{\hbar\omega_L} \right) \hbar\omega_L \tag{1.30}$$

The cutoff energy of high harmonics from solids exhibits linear dependence to the field strength rather than intensity. This property is one of distinct contrasts to harmonics in atomic gases.

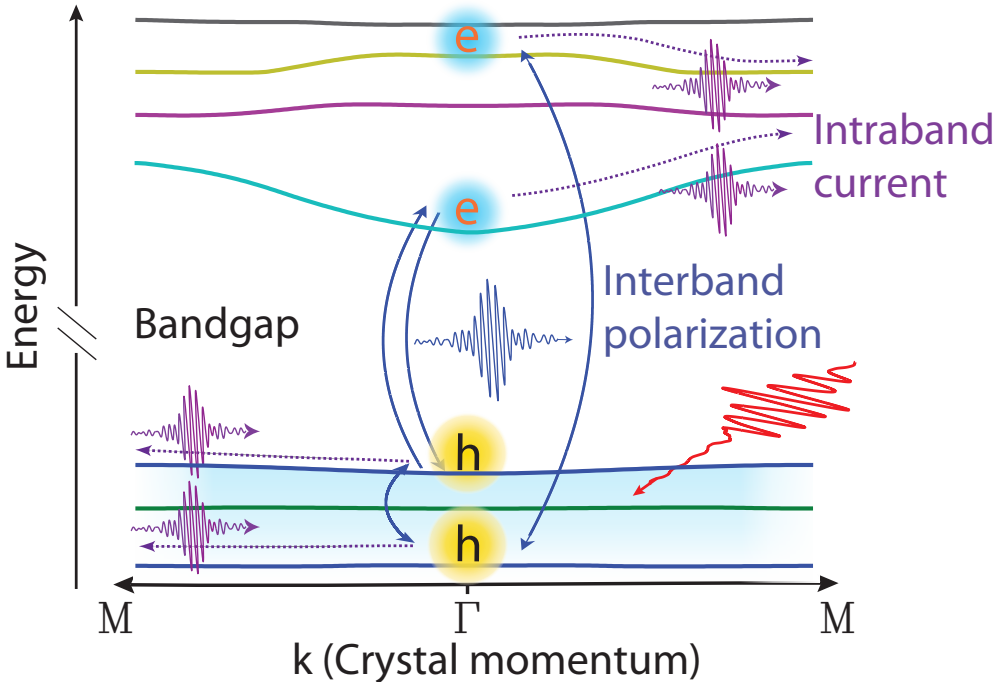

Figure 1.7: **Interpretation of HHG in solids in the band picture.** Interband polarizations (blue arrows) and intraband currents (purple dotted arrows) of electrons (cyan) and holes (yellow) play a key role as sources of the coherent radiation of high harmonics (blue and purple pulses, respectively) in the presence of a strong laser field (red pulse). Figure adapted from ref. [42].

Chapter 2

Experimental tools

Nicht Kunst und Wissenschaft allein, Geduld will bei dem Werke sein.
-Johann Wolfgang von Goethe

All the experiments presented in this thesis were conducted in the AS beamline of our group. In this chapter we will explore the most advanced features of the beamline which will facilitate a comprehensive understanding of the details of the experiments reported in this thesis. Along with the introduction of the beamline, founding bricks of ultrafast optics as well as attosecond metrology will be reviewed to enable an independent reading of this thesis. Further details of individual experiment will be introduced in the associated chapters.

2.1 Light source of the AS Beamline

2.1.1 Laser system: Kerr-lens Mode locked (KLM) oscillator and Chirped Pulse Amplification (CPA) system

The laser system of the AS beamline can be mainly divided into two parts, the oscillator and the amplifier, a widely used configuration of laser systems in the ultrafast optics. The laser source is a commercial Kerr-lens mode locked (KLM) oscillator (Rainbow, Femtolaser Gmbh) shown schematically in Fig. 2.1. A Titanium-doped Sapphire crystal (Ti:Sa) is used as a gain medium, and it is pumped by a continuous wave laser at a wavelength of $\sim$532 nm (Verdi V6, Coherent) and a power of $\sim$3W, giving a gain spectrum centered at $\sim$800 nm. The oscillator provides ultrashort pulse trains with a duration of $\sim$6 fs and an energy of $3 \sim 4$ nJ per pulse at a repetition rate of 78 MHz. In the next step, the pulse-train delivered from the oscillator is boosted to $\sim$1 mJ of energy, and the repetition rate is reduced to $\sim$3 kHz by the amplifier (Femtopower, Femtolaser). The amplifier is implemented based on the chirped pulse amplification (CPA) principle which consists of 3 steps: stretching, amplification and compression. CPA allows avoiding optical damage

to the optical components, resulting from a high peak intensity of the pulses during the amplification process. This is possible by stretching the pulse in time domain, resulting in a reduction of the peak intensity of the pulses. In our system, the seeded pulses (∼6 fs) are temporally stretched to ∼25 ps before the amplification process using highly dispersive materials (SF57). The stretched pulse trains are amplified in a Ti:Sa crystal during the first 4 passes and are picked (3 kHz) by a Pockels cell. The picked pulses are further amplified by additional 5 passes. A total of 9 amplification passes gives rise to pulses with an energy in excess of ∼1 mJ.

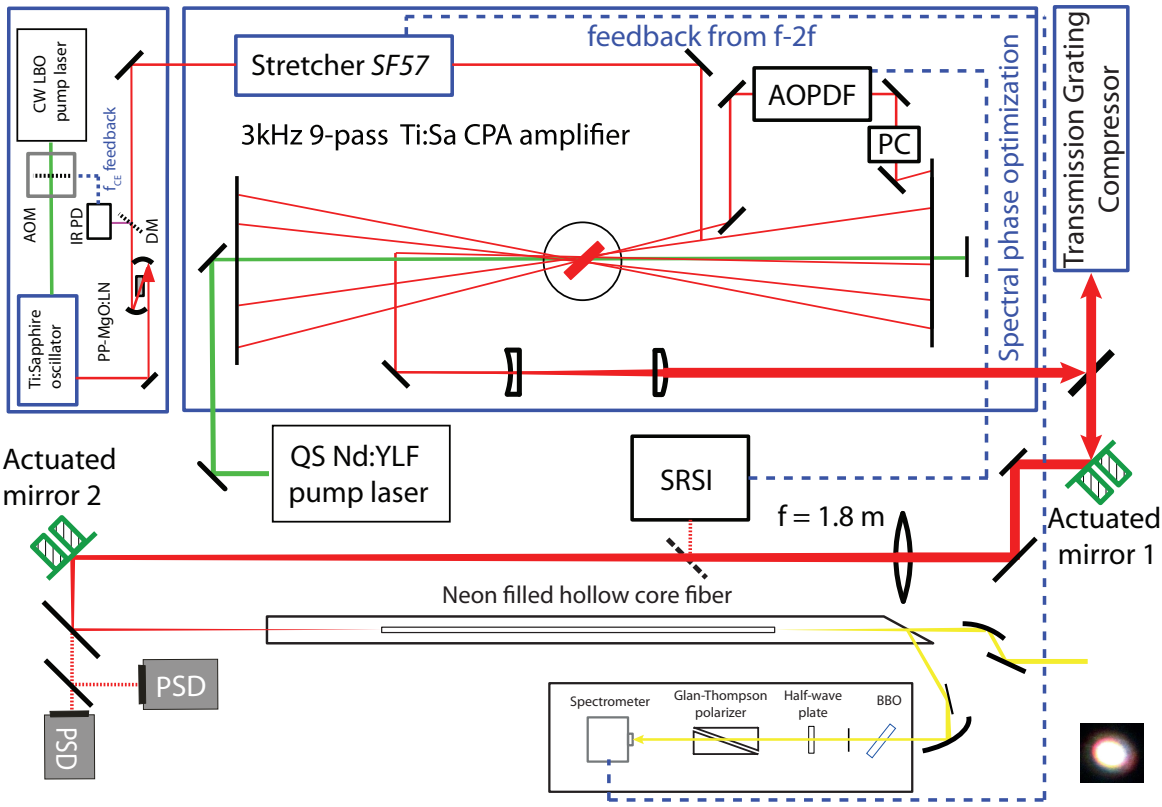

Figure 2.1: **Schematic of the laser source.** At the front end, the Kerr-lens mode-locked (KLM) oscillator delivers a train of pulses with duration of ∼6 fs at a repetition rate of 78 MHz. These pulses are temporally stretched by passing through a highly dispersive material, SF57. The stretched pulses are amplified pass by pass in the Ti:Sa crystal, which is optically pumped by Q-switched Nd:YLF laser (532nm). After the 4^{th} pass, pulses are picked from the train by a Pockels cell (PC) at a repetition rate of 3 kHz. An AOPDF (Dazzler) is employed to compensate for gain narrowing effects and to shape the spectrum of the amplified pulse. After the 9^{th} pass, the amplified pulses are enlarged by a telescope and are sent to a transmission grating compressor which reduces their duration down to ∼23 fs. Figure adapted from ref. [112]

In order to overcome gain narrowing, an acousto-optic, programmable, dispersive filter (AOPDF, commercially available as Dazzler from Festlite)[113, 114] which can shape the spectrum of the pulses is utilized. In such way at the end of amplification, a quasi-flat-top spectrum is attained. After the 9^{th} pass the beam size of the amplified pulses is enlarged to $\sim$25 mm such as to prevent damage of the optics in the compression stage, the last step of CPA. A transmission grating compressor temporally compresses the pulses down to $\sim$23 fs. A diagnostic device based on the Self-Referenced Spectral Interferometry technique (SRSI, commercially available as Wizzler from Festlite) [115] is utilized to measure the temporal characteristics of the amplified pulses. The Wizzler gives a feedback to the Dazzler to compensate high order chirp up to 4^{th} order. The amplified pulses are delivered with a pulse-to-pulse intensity stability better than 1%.

2.1.2 Spectral broadening

To generate single cycle pulses, a spectrum spanning at least one-octave is required according to the time-bandwidth product, $\Delta t \Delta\omega \geq 2\pi$. An established method for spectral broadening is exploiting the physics of self-phase-modulation (SPM) via the Kerr effect. In the presence of a strong field, the refractive index exhibits a nonlinearity which is proportional to the intensity of the driving pulse, $n(t, I) = n_0 + n_2 I(t)$ [5, 116], where n_0 and n_2 indicate linear and nonlinear refractive index, respectively. If the propagation of a laser pulse, whose intensity profile is $I(t) = I_0 \exp(-t^2/\tau^2)$, in a nonlinear medium of thickness L is considered, the temporal phase variation induced by the nonlinear refractive index n_2 is given by $\Delta\varphi(t) = n_2 I_0 L \exp(-t^2/\tau^2)$. The instantaneous frequency of the laser pulse undergoing SPM can be calculated by the time derivative of the temporal phase as:

$$\omega(t) = \omega_L - 2n_2 I_0 L t \exp\left(-\frac{t^2}{\tau^2}\right) \tag{2.1}$$

Around the central frequency of the incident laser pulse ω_L, new frequency components are generated depending on the slope of the intensity envelope. As connoted in Eq. 2.1, the spectral width of the new frequencies is linear to the peak intensity I_0, and therefore, a good efficiency in frequency conversion can be assured by a good compression of the input pulse.

Gaseous medium such as neon filled hollow-core fiber (HCF) is one of the best options for the spectral broadening of intense pulses. One of the key advantages of using hollow-core fibers, other than the efficient generation of a broad coherent spectrum, is the quality of the beam profile. A good matching of an incident laser beam size and the fiber diameter results in a rather pure TEM00 spatial eigenmode at the exit of the capillary. The near Fourier limited pulse delivered from the laser compressor is gently focused by a thin convex lens with focal length of $\sim$1.8 m onto the entrance of the hollow core fiber (Fig. 2.2 a). To avoid spatial instability for the coupling, a PID control-based beam stabilization system (Aligna4D from TEM) consisting of two mirror actuators and position sensitive diodes (PSD) is employed in the system (marked in green in Fig. 2.1). In the AS beamline, a 1.1 m long hollow-core fiber of a core-size of $\sim$250 μm is used. It is encapsulated in a tube

filled with neon at a pressure of ∼2 bar. An AR-coated entrance window at the front and a Brewster window (0.5 mm thick at ∼ 57°) at the exit ensure minimal energy and spectral losses. The Brewster window is used not only for minimizing the reflection loss but also for selecting a weak portion of the beam which is in turn used for the CEP measurement of the pulses.

With our laser parameters (central wavelength of 800 nm, duration of ∼23 fs and ∼1 mJ pulse energy), SPM in neon at a pressure of ∼2 bar provides ∼2.5-octave broadband spectrum extending from 250nm to 1100 nm (Fig. 2.2 b). The corresponding Fourier limited pulse duration is ∼0.9 fs, connoting the possibility of an optical attosecond pulse generation [15, 16]. To maintain a consistent efficiency of spectral broadening and beam profile, the temporal compression and spatial beam profile at the focus is frequently optimized for long term applications.

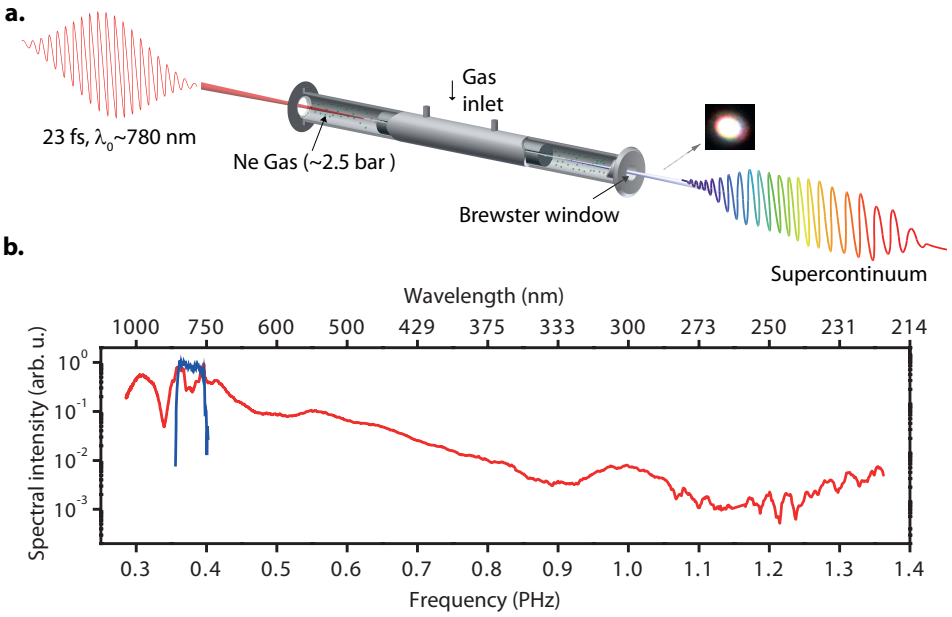

Figure 2.2: **Spectral broadening in neon filled hollow core fiber.** **a**, Intense laser pulses are focused onto a neon-filled hollow core fiber to generate a spectrum of ∼2.5 octaves. **b**, Spectrum of the supercontinuum spanning from ∼250nm to 1100nm (red curve). The blue curve is the spectrum of the incident laser to the fiber. Figure adapted from ref. [41].

2.1.3 Carrier-Envelope Phase (CEP) and stability control

In few-cycle and in single-cycle pulses, the control and stabilization of the carrier-envelope phase (CEP) from pulse to pulse is essential for research of field-sensitive phenomena. This is because the waveform under the pulse envelope is drastically affected by the variation of CEP. An instability of CEP from pulse to pulse can causes incoherent superposition of measurable quantities in strong-field phenomena resulting in a smearing of key observables. Technically, the CEP variation of consecutive pulses emerging from an oscillator is a result of the difference between the group and phase velocities inside the laser resonator [25, 26]. For each round trip in a cavity with a length l, the consecutive pulses exiting the laser cavity have a phase difference of

$$\Delta\varphi_{CEP} = \frac{2\pi l}{T_c}\left(\frac{1}{v_g} - \frac{1}{v_p}\right) \tag{2.2}$$

where T_c, v_g and v_p are laser period, group velocity and phase velocity, respectively.

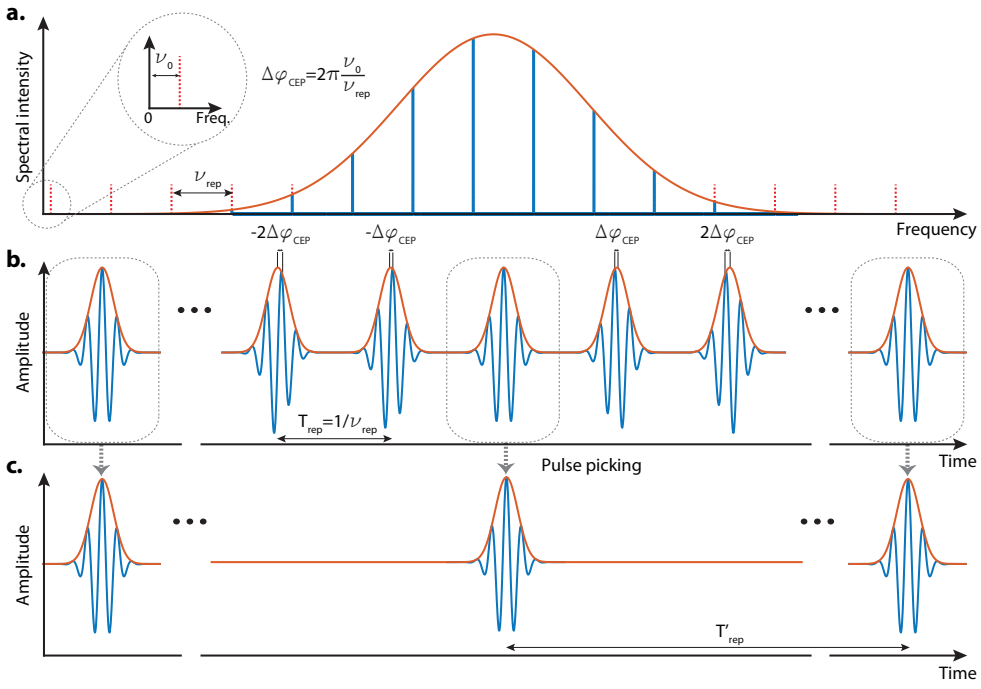

Figure 2.3: **Principles of carrier-envelope phase (CEP) stabilization. a** and **b**, A spectrum consisting of frequency combs describes a pulse train in the time domain (a). The comb spacing is directly related to the repetition rate of the pulses ν_{rep}. An offset of the frequency comb from the zero frequency ν_0 results in a CEP variation of consecutive pulses (b). **c**, A pulse-picking process by a Pockels cell inside the amplifier enables selection of pulses with the same CEP.

The phase shift can be well understood in the spectral domain. A pulse train is analytically described by the multiplication of a continuous spectrum and a comb of frequencies that correspond to the laser longitudinal modes (Fig. 2.3 a). Pulse-to-pulse CEP differences can be understood as a result of an onset ν_0 of the frequency comb (inset in Fig. 2.3 a), referred to as carrier-envelope offset (CEO). The comb frequencies are located at $\nu_m = \nu_0 + m\nu_{rep}$, where m is an integer as depicted by vertical solid lines in Fig. 2.3 a. The inverse Fourier transform shows that the frequency offset introduces a constant phase shift between two adjacent pulses in the time domain which amounts to (Fig. 2.3 b),

$$\Delta\varphi_{CEP} = 2\pi\frac{\nu_0}{\nu_{rep}} \tag{2.3}$$

If ν_0 is set to be an integer fraction (1/n) of the repetition frequency of ν_{rep}, *i.e.*, $n\nu_0 = \nu_{rep}$, the above equation dictates that every n^{th} pulse has an identical phase, when $\Delta\varphi_{CEP}$ returns to 2π. Pulses with the same phase are obtained by a Pockels cell pulse picking in the amplifier as illustrated in Fig. 2.3 b and c. The timing of the Pockels cell is adjusted such that pulses with the same CEP are selected. As one can notice from the comparison of Eq. 2.2 and 2.3, the frequency offset is a result of the difference between the group and phase velocities which are characteristics directly related to the properties of the laser cavity. Random noise impacting on the laser cavity, typically originating from thermal or mechanical drifts of the optical elements results in a jitter of the CEO and consequently a pulse-to-pulse phase instability. The stabilization of the CEO can be attained by a fast active feedback loop whose speed is comparable to the repetition rate of the laser.

For the feedback to the oscillator, a continuous detection of the CEO is required. The CEO is detected by the f to 0 interferometric method. The pulse train at the exit of the oscillator is focused on a periodically poled magnesium-oxide-doped lithium niobate (PP-MgO:LN) crystal (See Oscillator in Fig. 2.1). Difference frequency generation (DFG) in PP-MgO:LN eliminates the CEO in the DFG frequencies, which results in multiple of ν_{rep} *i.e.*, $\nu_{DFG} = k\nu_{rep}$, where k is an integer. Detection of the beating between fundamental and DFG modes gives access to the CEO, whose frequency is $\nu - \nu_{DFG} = \nu_0$. The beating frequency signal is captured by an avalanche photodiode (APD) following a low-pass filtering at radio-frequencies. The shift of the beating frequency directly indicates the shift of the CEO, and it is used to provide feedback to an acousto optical modulator (AOM). The AOM controls the intensity of the pump laser of the Ti:Sa oscillator, and CEP stabilization is attained by controlling the phase induced by the Kerr-effect in the gain medium.

Long-term instability of the phase (tens of Hz range) is introduced during the propagation of the pulses in the laser system including amplification. To overcome this issue a second stabilization stage referred to as "slow-loop", is also important. In the slow-loop, a small portion of the white light generated in the hollow-core fiber is routed to a f-2f interferometer [117]. In this device, the laser beam is focused by an off-axis parabolic-mirror onto a β-BBO crystal to generate its second harmonic. The phase of the second harmonic is double than that of the fundamental pulse, $E_{SHG}(t) = \exp(2i\omega t + 2i\varphi_{CEP})$. A spectral overlap of the fundamental and the second harmonic (time delayed by Δt) gives rise to a spectral interference, $I(\omega) = |E_{fund}(\omega)|^2 + |E_{SHG}(\omega)|^2 + 2E_{fund}E_{SHG}\cos(\omega\Delta t + \varphi_{CEP})$.

Variation of the fringe pattern directly enables tracing of the CEP variation and provides a signal for corrections. A piezoelectric stage driven by a PID-control based active-loop adjusts the distance of a pair of SF57 prisms in the stretcher of the amplifier to compensate the CEP variation and stabilize the long-term CEP. The capability of controlling the phase by the above method also allows setting a desirable CEP. A pulse-to-pulse CEP stabilization of less than 100 mrad can be achieved with this system [117, 41].

2.1.4 Light field Synthesizer

The light field synthesizer provides us the possibility to shape the electric field of pulses with a higher degree of freedom in comparison to ordinary CEP control. It is based on a very intuitive working principle as shown in Fig. 2.4. The coherent broadband light delivered from the hollow-core fiber is spectrally and spatially divided into 4 channels (NIR: 700∼1100nm, VIS: 500∼700nm, VIS-UV: 350∼500nm, and UV-DUV: 270∼350nm) by broadband dichroic beam-splitters (DBS).

6 custom-designed chirped mirrors (CM) installed in each channel compress the corresponding pulses. The sequence of channels is designed to minimize dispersion of pulses by arranging more dispersive wavelengths (DUV, UV-VIS, VIS and NIR in sequence) first such as to avoid their extensive propagation through dispersive optics. At the exit of the apparatus, all four channels are coherently recombined using identical DBSs as for spectral division. The temporal profiles of the pulses in each channel are typically characterized by a transient grating frequency-resolved optical gating (TG-FROG) [118]. Thin fused-silica wedges introduced in the beam path of each channel enable fine tuning of the dispersion of each pulse. The pulse duration of constituent pulses is compressed to nearly their Fourier limit, NIR: ∼8 fs, VIS: 6-7 fs, VIS-UV: 6-7 fs, and UV-DUV: 6-7 fs. The spatial superposition of the beams of the constituent pulses is one of the essential parameters for synthesis. Each beam is carefully aligned by adjusting the corresponding beam splitters via observation of beam profile in the near and far-field. A desirable electric field waveform is synthesized by tuning the relative delay among the channels using piezo-electric stages. The fine precision of piezoelectric stages down to 10 nm provides a capability of controlling the timing among the channels with accuracy better than ∼80 as. In order to avoid thermal drifts which hinder the long term spatial and temporal accuracy of the synthesized pulses, a passive water-cooling system under the metallic base of the synthesizer is implemented. Additionally, for the stability of the temporal synchronization, a PID-control based active loop is implemented. At the exit of the apparatus, a small fraction of the synthesized beam is sent to a spectrometer to trace the interference pattern in the spectral region where neighboring channels overlap. The interferometric pattern is used to provide a feedback to the active-loop which in turn adjusts the delay to compensate for the drifts. In total, an interferometric stability better than 50 mrad can be achieved [41]. The synthesized waveforms are completely characterized by EUV attosecond streaking measurement [29, 119] as discussed in the next section.

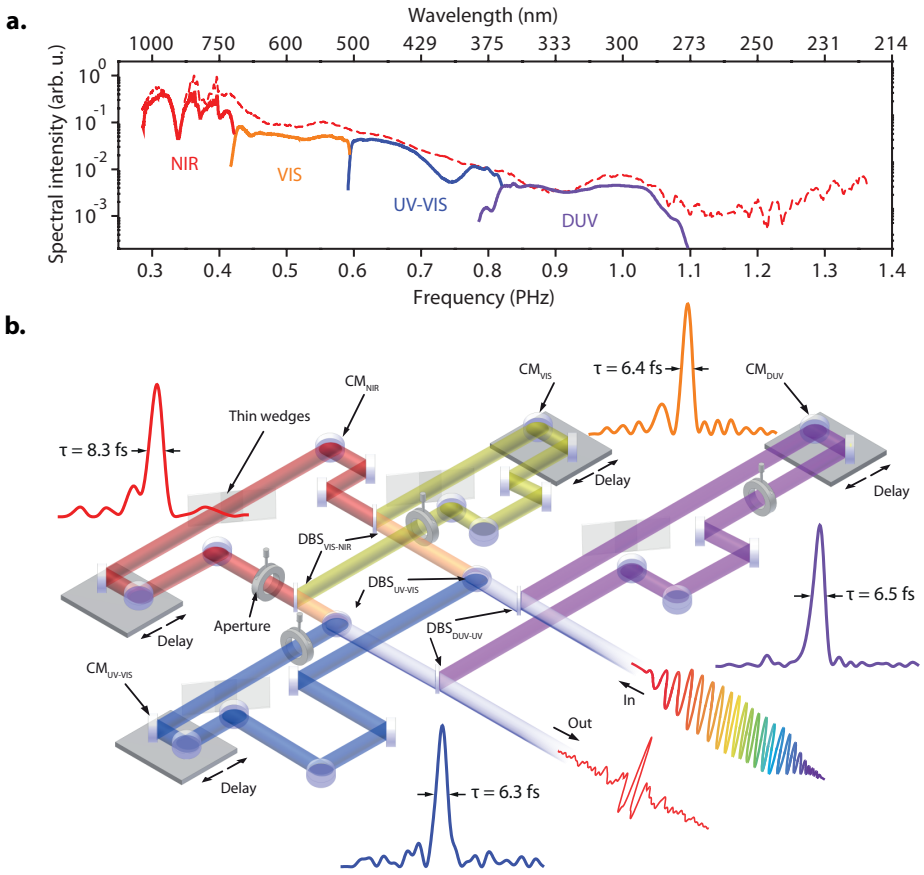

Figure 2.4: **Light field Synthesizer. a**, A coherent multi-octave supercontinuum pulse delivered from the HCF (red dashed curve) is spectrally divided into 4 channels, NIR (red), VIS (yellow), UV-VIS (blue) and DUV (purple) by dichroic beam splitters (DBS). **b**, Schematic of the second-generation light field synthesizer. The pulses in each channel are temporally compressed down to their Fourier limit by 6 reflections off broadband chirped mirrors designed for their corresponding bandwidths. At the exit of the apparatus, all constituent pulses are spatially and temporally superimposed. By controlling the timing among these pulses with piezoelectric stages introduced in the path of each channel, custom waveforms reaching also the optical attosecond domain can be attained. Figure adapted from ref. [41]

2.2 Attosecond metrology

2.2.1 AS beamline

A schematic drawing of the AS beamline is shown in Fig. 2.5. The experimental setup is in a series of high vacuum chambers, which consists of two main chambers, referred to

as "HHG" and "experimental" chambers. At the core of the beamline stands the EUV attosecond streaking technique. High harmonic generation in noble gas is implemented in the first chamber, the HHG chamber. A strongly focused synthesized laser field is shone to a gas nozzle filled with a noble gas (neon or argon). The generated high harmonics which extend to the EUV range (blue beam in Fig. 2.5 a) collinearly propagate with the optical laser beam (red beam in Fig. 2.5 a). An adjustable iris controls the intensity of the optical pulse by clipping the outer rim of the beam. A spatial isolation of the EUV pulse from the optical pulse is possible by using a free-standing ultrathin (< 100 nm) metallic filter (Al, Zr, In and etc.) placed at the center of the beam. The filter holder is attached on a transitional stage which can change the type of filter on demand. The co-propagating inner EUV and outer optical beams are reflected off a dual concave mirror assembly (inset in Fig. 2.5 a) with a focal length of 12.5 cm. The inner mirror whose size matches with that of the EUV pulse beam is mounted on a piezo stage. The time-delay between inner and outer beams which is an essential ingredient for measurements in pump-probe schemes is given by the optical path difference introduced by the piezoelectric stage. A time-of-flight electron spectrometer (TOF) which is mounted on the top of the experimental chamber, allows the measurement of photoelectron spectra. A number of ports on the experimental chamber permits installation and use of several measurement instruments such as EUV spectrometers, beam profiler and etc.

2.2.2 EUV attosecond streaking

The term, "EUV attosecond streaking" generally refers to a technique used for the temporal characterization of EUV attosecond pulses as well as optical driving pulses. The EUV pulse instantaneously ionizes atoms and releases photoelectrons through a single-photon absorption process. The temporal and the corresponding spectral structure of the EUV attosecond pulse is directly transferred to the photoelectron pulse.

Under a classical perspective, a photoelectron released by an EUV pulse is driven in free space by the weak optical field (gate field), following the classical equation of motion. The momentum gained by the electron from its ionization time (t_b) to the end of the pulse ($t = \infty$) can be mathematically treated as integration of the acting electric force $-eE_L(t)$ within that time window. Using the definition of the vector potential $A(t)$, the momentum change imparted to the electron by the optical gate field can be expressed as:

$$\Delta p = -e \int_{t_b}^{\infty} dt E_L(t) = e \int_{t_b}^{\infty} dt \frac{dA}{dt} = -eA(t_b) \tag{2.4}$$

Accordingly, the terminal kinetic energy of the electron at the end of the optical pulse ($t = \infty$) is given as a function of the delay (τ) between EUV and optical gate pulses:

$$E(\tau) = \frac{(p_0 + \Delta p(\tau))^2}{2m_e} = \frac{1}{2m_e}\left(p_0^2 + 2p_0\Delta p(\tau) + (\Delta p(\tau))^2\right) \approx \frac{p_0^2}{2m_e} + \frac{p_0 \Delta p(\tau)}{m_e} \tag{2.5}$$

If the optical field is sufficiently weak, so that the momentum variation is negligible compared to the initial momentum of the electron, $\Delta p \ll p_0$, the term $(\Delta p(\tau))^2$ in Eq. 2.5 can

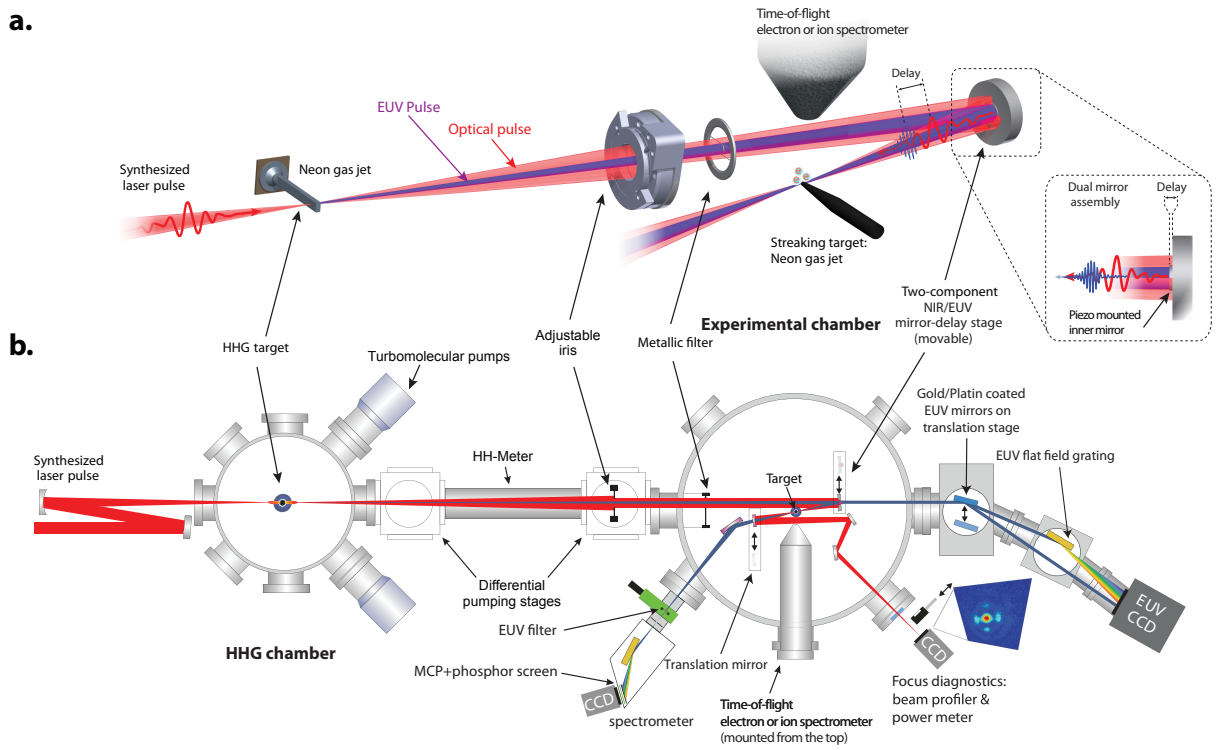

Figure 2.5: **AS Beamline.** **a**, A schematic of the experimental configuration of EUV attosecond streaking measurement. Optical driving pulses (red pulse) from the light field synthesizer are tightly focused onto a neon gas jet to generate EUV pulses. A metallic filter (for example, Zr) filters out the optical frequency from the inner beam to spectrally and spatially separate EUV and optical pulses. Concentrically propagating EUV and optical pulses are reflected off the inner and outer mirrors of the dual mirror assembly, respectively. Both the inner and outer mirrors having a short focal length (12.5 cm) focus the EUV and optical pulses onto the streaking gas target. The inner mirror has a high reflectivity in the EUV range centered at ∼85 eV. A Piezo-electric transitional stage carrying the inner mirror enables a time-delay of EUV pulse with respect to the optical pulse (inset). Spectrum of photoelectrons released by the EUV pulses and perturbed by the optical pulses is recorded by a time-of-flight electron spectrometer (TOF). **b**, Overview of AS beamline with all the essential equipment used in experiments discussed in this thesis. Figure adapted from ref. [120]

be neglected, and the energy modulation by the optical gate field can be approximated as a linear function of the vector potential, $\Delta E(\tau) = E(\tau) - p_0^2/(2m_e) \approx -eA(t_b + \tau)p_0/m_e$.

The vector potential of the optical gate pulse can be directly extracted by tracing the centroid of the spectrogram. The phase information of the photoelectron pulse emitted by the EUV pulse is also embodied in the spectrogram in accordance to the principles shown

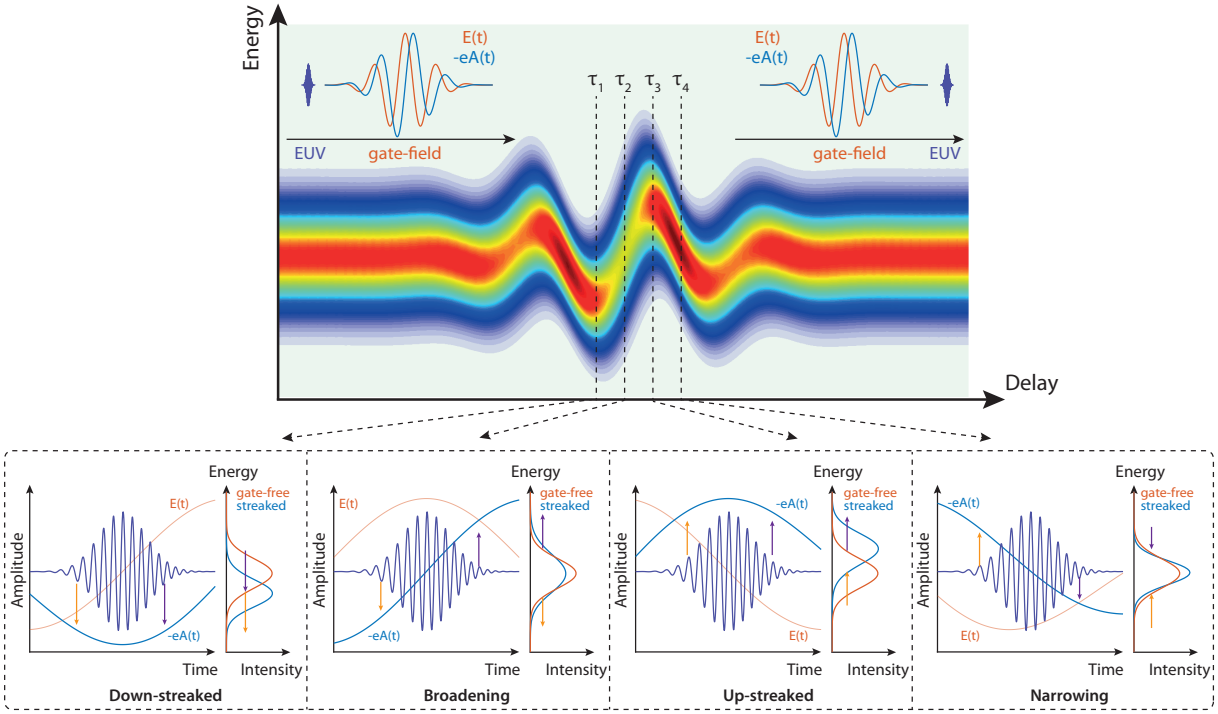

Figure 2.6: **EUV attosecond streaking principle.** A simulated EUV attosecond streaking spectrogram for a positively chirped EUV pulse. EUV pulse (purple) and vector potential of optical gate field (blue) for different delay instances (black vertical dashed lines in top panel) are shown in bottom panels. The arrows (red and purple) indicate the momentum variation introduced by the vector potential to the released photoelectrons. The photoelectron spectrum is shown at the right side at each delay instance. The red curves indicate the gate-free photoelectron spectrum, while the blue curves denote the photoelectron spectrum streaked by the optical gate field.

in Fig. 2.6.

How the vector potential of the gate pulse probes the time structure of the released electron pulse can be best understood based on the schematics of bottom panels in Fig. 2.6. At a delay for which the electron pulse is released within a negative half cycle of the vector potential (τ_1), the overall electron pulse wavepacket loses momentum resulting into a reduction of terminal kinetic energy (down-streaked). When the electron pulse is released within a positive half cycle of the vector potential (τ_3), the overall energy of the wavepacket is increased (up-streaked). The detailed shape of the spectrogram depends on the chirp of the photoelectron pulse. This is clearly shown, when the photoelectron pulse is synchronized with the zero transition of the vector potential (τ_2 and τ_4). At a positive slope of the vector potential, the front tail of electron pulse loses kinetic energy, while its end tail gains kinetic energy. For a positively chirped electron pulse, the low energy

constituents of the electron pulse at its leading edge lose kinetic energy, while the high energy constituents at its trailing edge gain kinetic energy. This effect is manifested by a broadening of the photoelectron spectrum (τ_2). On the negative slope (τ_4), the situation is the opposite, resulting in a narrowing of the spectrum. Similarly, a spectrogram with a negatively chirped EUV pulse and a corresponding photoelectron pulse exhibits opposite effects: spectral narrowing on the positive slope and broadening on the negative slope of the vector potential.

Theoretical description of EUV attosecond streaking

A formal description of an attosecond streaking spectrogram as a frequency resolved optical gate(FROG) spectrogram was introduced in ref. [121, 122]. In this picture, the electronic wavepacket can be described as a coherent superposition of the ground state $|0\rangle$ and the unbounded continuum states $|p\rangle$ as Eq. 1.13 discussed in chapter 1, $\psi(t) = [|0\rangle + \int d^3p\chi(p,t)|p\rangle]e^{iI_p t}$. The transition amplitude $\chi(p,\tau)$ from the ground state to a continuum state via the photons of the EUV pulse under a weak optical gate field is described by the dipole transition without consideration of the Coulomb potential of the parent ion, that is, in the strong field approximation (SFA). In the velocity gauge, the complex transition amplitude is given by

$$\chi(p,\tau) = -i\int_{-\infty}^{\infty} dt d_p(t) E_{XUV}(t) \exp[-i\Delta S(p,t,\tau)] \exp\left[i\left(\frac{p^2}{2} + I_p\right)t\right] \tag{2.6}$$

where the phase introduced by the optical gate field is described by the Volkov phase $\Delta S(p,t,\tau)$. $A(t)$ is the vector potential of the gate field.

$$\Delta S(p,t,\tau) = \int_t^{\infty} dt' \left[pA(t'+\tau) + \frac{A(t'+\tau)^2}{2}\right] \approx \int_t^{\infty} dt' pA(t'+\tau) \tag{2.7}$$

The square term of the vector potential $A(t'+\tau)^2$ can be ignored, when the central momentum of the wavepacket is much higher than the momentum gained by the weak gate field in analogy to the expression in Eq. 2.5. Under the assumption that the EUV pulse promotes the electron wavepacket from the ground state to the continuum state by a single photon absorption, the dipole matrix element can be approximated by $d_p(t) \approx 1$. This assumption has a meaning that the electronic wavepaket probed by the streaking pulse has the same temporal structure as the EUV pulse. The Volkov phase has a dependence on the electron momentum p. However, under the assumption that the bandwidth of the electron wavepacket momentum (accordingly energy) is narrow, so that the central momentum can represent all momentum components of the wavepaket, the momentum variable can be replaced by the constant central momentum, $p \to p_c$,

$$\Delta S(p,t,\tau) \approx \Delta S_{CMA}(t,\tau) = p_c \int_t^{\infty} dt' A(t'+\tau) \tag{2.8}$$

This approximation simplifies the reconstruction problem by reducing the number of coordinates, widely known as "Central momentum approximation" (CMA) in the research field

of attosecond physics. Finally, the two-dimensional spectrogram as a function of energy (E) and delay (τ) is given by the absolute-square of the transition amplitude,

$$I(E,\tau) = \left| \int_{-\infty}^{\infty} dt d_p(t) E_{XUV}(t) \exp[-i\Delta S_{CMA}(p,t,\tau)] \exp\left[i\left(\frac{p^2}{2} + I_p\right)t\right]\right|^2 \tag{2.9}$$

The attosecond spectrogram described in Eq. 2.9 has the same form as that of the ordinary frequency resolved optical gating (FROG),

$$I(\omega,\tau) = \left| \int_{-\infty}^{\infty} dt P(t) G(t+\tau) e^{i\omega t}\right|^2 \tag{2.10}$$

The EUV field $E_{EUV}(t)$ plays a role of a pump, $P(t)$ in the FROG form, and the exponent of the Volkov phase corresponds to the gate, $G(t-\tau)$. The Volkov phase does not influence the amplitude of the spectrogram but only the phase. This kind of gate is called "phase gate" to distinguish from the case where the gate modulates the intensity of the spectrogram known as "amplitude gate".

Reconstruction of EUV attosecond streaking spectrogram

The temporal and corresponding spectral information of the pump $P(t)$ and gate $G(t)$ field is embodied in the 2D spectrogram. However, it is difficult to analytically retrieve two unknown functions $P(t)$ and $G(t)$, because the spectrogram is recorded in intensity (the absolute square of the complex amplitude), which eliminates the phase information of the product of $P(t)$ and $G(t+\tau)$. Therefore, a reconstruction algorithm is required to find the unique solution for pump and gate pulses. For more than a decade, reconstruction algorithms particularly for the FROG-like form have been developed by taking inspiration from those used in image processing: the generalized projection algorithms (GPA). Many algorithms such as principal components (PCGPA) [123, 124], Least-squares (LSGPA) [125] and Volkov-transform (VTGPA) [126] are based on this idea.

I briefly discuss the most common algorithm, PCGPA. The PCGPA starts with an initial guess for the unknown functions. A matrix representing a solution, is generated by the outer product of $P(t)$ and $G(t)$, *i.e.*, $O = P(t)G(t)^T$, in the grid of the time axis. A time-shift process for the delay of the gate vector (which is represented by row vectors) can be performed by circularly shifting the row vector of the outer-product matrix O, so that each column vector represents $P(t)G(t+\tau)$ at each delay point. Fourier transform, column by column, results in a complex amplitude of the spectrogram, so-called signal matrix $S(\omega,\tau)$. The projection process in PCGPA is one the main steps for the reconstruction. By projecting the intensity of the measured spectrogram $I(\omega,\tau)$ ("target") onto the signal matrix, the complex amplitude of the signal matrix is driven to converge towards that of the target spectrogram, *i.e.*, $S'(\omega,\tau) = \sqrt{I(\omega,\tau)}\exp\left[i\ \mathrm{ang}(S(\omega,\tau))\right]$. The projected signal matrix $S'(\omega,\tau)$ is inverse-Fourier transformed back to the time domain, and the inverse circular shifting of the row vectors creates a new outer-product matrix O'. The singular value decomposition (SVD) of O' provides the new optimized solution set of $P(t)$

and $G(t)$ at each iteration of the process. An example reconstruction of experimental data recorded in the AS beamline is shown in Fig. 2.7. Iteratively, the solution (Fig. 2.7 b) efficiently converges to the target spectrogram (Fig. 2.7 a). The gate electric field is completely characterized, including its absolute strength and phase (dashed white curves in Fig. 2.7 b). The attosecond EUV pulse is also retrieved both in amplitude (blue) and phase (red), in both spectral and temporal domains (Fig. 2.7 c and d, respectively).

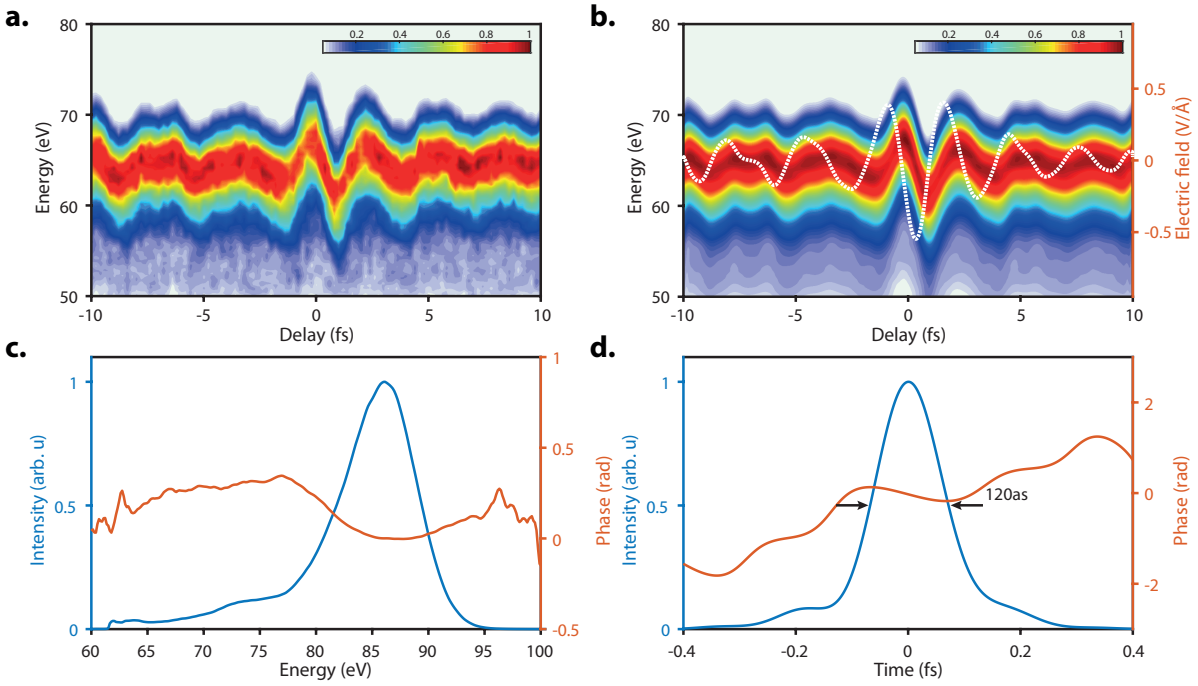

Figure 2.7: **Experimental attosecond streaking and its reconstruction.** **a** and **b**, Measured EUV attosecond spectrogram (a) and its reconstruction by PCGPA (b). The retrieved optical gate pulse (white dashed curve) is superimposed on the reconstructed spectrogram in panel b. **c** and **d**, The retrieved spectral (c) and temporal (d) structure of EUV attosecond pulse. The blue and red curves denote intensity and phase, respectively.

Chapter 3

Optical-field emission from tungsten nanotips at the single-cycle limit

The summit is what drives us, but the climb itself is what matters.
-Conrad Anker

This chapter presents spectral studies of photoemission from a tungsten nanotip under intense singe-cycle pulses. An essential advance in comparison to previous studies is the use of single-cycle pulses of precisely characterized fields. As we will see bellow, this capability allows a detailed examination of the validity of semiclassical strong-field pictures in describing the process. The conclusions of this chapter will set the stage for the complete characterization of the optical field emission in real time in the chapters that follow.

3.1 Strong field emission from nanotips at the single-cycle limit

3.1.1 Experiment

Conically shaped nanotips with an apex radius of ∼35 nm and a full opening angle of ∼ 15° (Fig. 3.1 a) were used in this study. They were mounted on a controllable, three-dimensional positioning stage and were placed ∼3 mm below the entrance aperture of a time-of-flight electron spectrometer (TOF). The orientation of the tip was along the polarization direction of the driving field vector. To avoid charge accumulation, both the nanotip as well as its carrier stage were electrically connected to the ground of the system.

The linearly polarized single-cycle pulses were produced in the light field synthesizer apparatus presented in chapter 2 and were characterized by EUV attosecond streaking as shown in Fig. 3.1 b. Other than the field waveform, important characteristics of the pulses are: the central energy ∼1.8 eV and the duration τ ∼1.9 fs.

A concave nickel mirror (f=12.5 cm) was used to focus the pulses at the apex of the

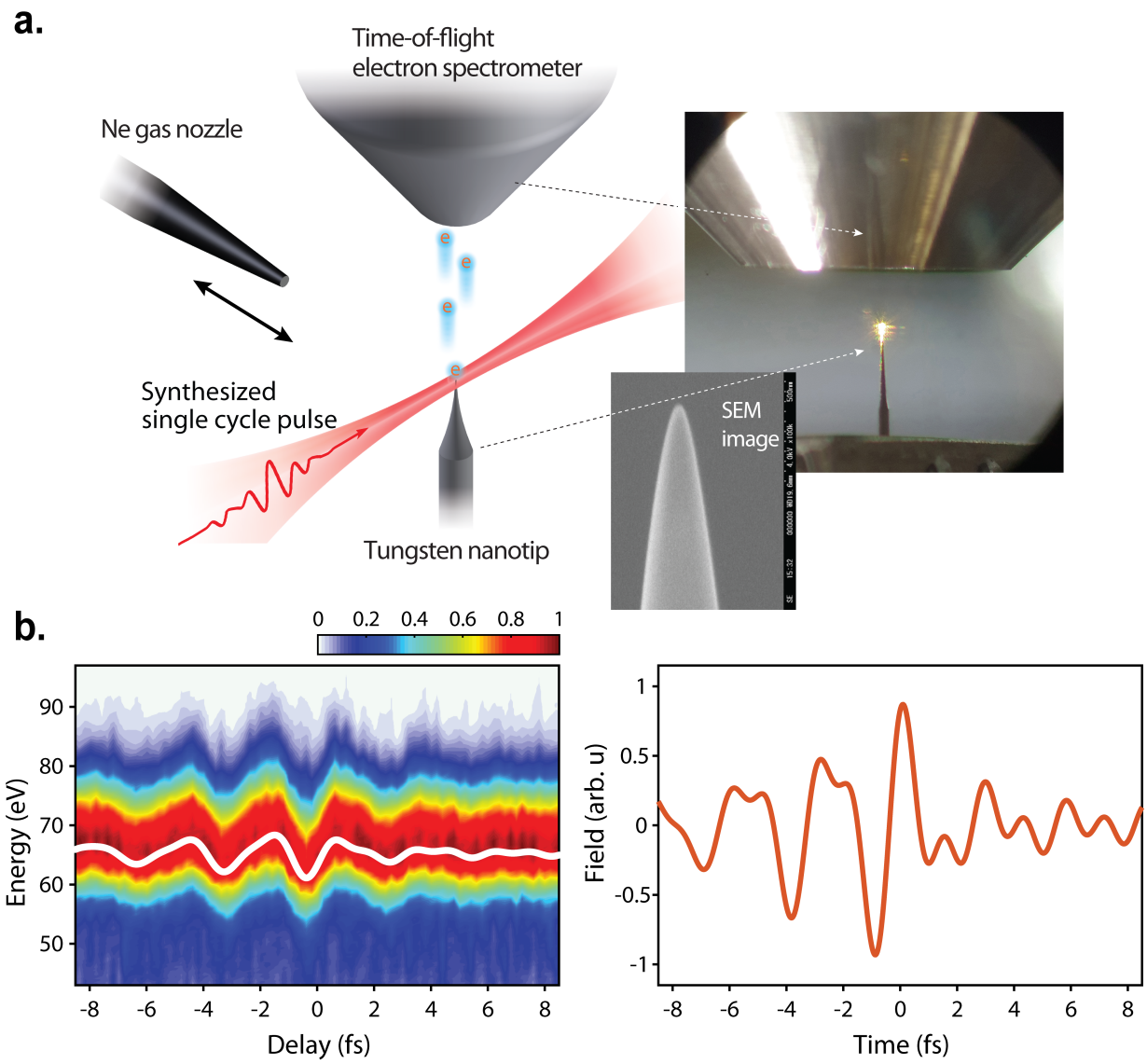

Figure 3.1: **Experimental setup for single-cycle optical field emission. a**, Strong, single-cycle optical pulses were shone on a sharp tungsten nanotip. The photoelectrons released from the nanotip (cyan cloud) were captured, and their spectra were recorded by a TOF electron spectrometer. The tungsten nanotip and the neon gas nozzle were mounted on a 3D Piezo-electric stage, so that they can be promptly swapped under demand. The insets show a photo of the nanotip in the experimental chamber as well as a scanning electron microscope (SEM) image provided by the tip manufacturer (Unisoku, Japan). **b**, The optical single-cycle pulses used in the experiment were characterized by EUV attosecond streaking measurement. The left panel shows the recorded attosecond streaking spectrogram, and the right panel displays the retrieved electric field waveform.

nanotip. The emitted photoelectrons were collected by a time-of-flight spectrometer with an acceptance angle of ∼6 deg. A digital oscilloscope with a sampling rate of 10 Gs/s, (Waverunner 610Zi, Teledyne LeCroy) was used to record the photoelectron spectra.

In a first set of measurements, electron spectra were recorded as a function of the peak intensity of the incident laser driving pulse (Fig. 3.2). The intensity range of this study was from ∼5 TW/cm^2 to ∼40 TW/cm^2 and was precisely controlled by a motorized iris. Damage of the nanotips was observed at a peak intensity of ∼ 45 TW/cm^2.

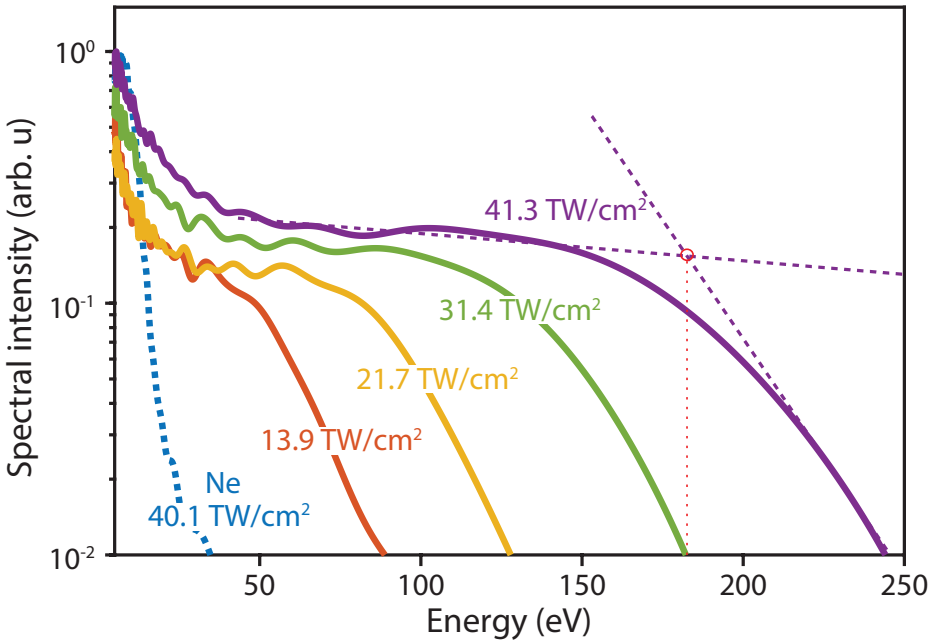

Figure 3.2: **Photoelectron spectra from tungsten nanotip under single-cycle optical pulses.** Electron spectra from the tungsten nanotip recorded at peak intensities, 13.9, 21.7, 31.4 and 41.3 TW/cm^2 are shown in red, yellow, green and purple solid curves, respectively. The blue dashed curve displays the electron spectrum recorded with neon at an intensity of ∼40.1 TW/cm^2. Figure adapted from ref. [127]

To precisely calibrate the intensity of the pulses at each iris setting the following procedure was taken. Using the motorized iris the intensity of the beam was adjusted to a level for which an ordinary EUV attosecond streaking in neon can be conveniently performed. At this aperture setting the peak intensity and the field waveform can be accurately characterized. Because the adjustment of the iris aperture not only modifies the energy in the focus but also the focal spot size, an imaging system based on a set of lenses and a CCD camera was used to record both the focal spot size and the laser power at the focus. With the help of these measurements an absolute calibration of the intensity for each aperture setting was possible. Fig. 3.2 shows photoelectron spectra emerging from the tungsten nanotip for gradually increasing peak intensity of the incident single-cycle pulse. For the

highest peak intensity, the cutoff energy reaches approximately 180 eV. Note that the cutoff energy is defined as the energy beyond which the electron yield exponentially drops (see dashed lines in Fig. 3.2).

Even though the electric field of the driving pulse is already characterized, a direct comparison at this point with semiclassical theory is not possible, because the local field enhanced at the apex of the tip is not trivially accessible. We can however perform the same experiment with an atomic system under the same driving field to acquire an estimation of the field enhancement in the vicinity of the nanotip. To this end, the tungsten nanotip was replaced by a neon gas jet, and photoelectron spectra were recorded under the identical experimental conditions. A comparison of the tungsten spectra (purple curve in Fig. 3.2) to the neon spectra (blue dashed curve in Fig. 3.2) at a similar peak intensity reveals an increase of the cutoff energy by a factor of ~ 12. To understand the origin of this dramatic difference it is important at this stage to introduce the concept of field enhancement.

3.1.2 Near-field enhancement

When a nanostructured metal is shone by an electromagnetic field, the discontinuity of the dielectric constant at the interface between vacuum and the material gives rise to a rearrangement of charges. Such rearrangement leads to a spatial concentration of charge on the surface of the metal and thus results in a local field enhancement of the incident pulse. In the case of a nanotip, the charge concentration and consequently the field enhancement factor intrinsically depend on the geometrical characteristics of the structure, such as the apex radius and the opening angle [128, 129, 130]. A sharper nanotip generally exhibits higher local field enhancement due to a higher local charge confinement. This effect is also known as "lightning rod effect" in the broad field of nano-optics [130, 131, 132]. Moreover, plasmonic effects under a resonance condition also results in a strong local field enhancement [133, 134, 132]. Therefore, one can expect strong optical-field enhancement in materials like gold and silver which have a negative permittivity in the visible and near-infrared [130, 135]. For the case study here, tungsten does not exhibit plasmonic effects in the optical frequency range. As a result, the geometry of the nanostructure has a leading role in describing field enhancement.

In order to quantify the enhancement factor in the vicinity of our tungsten nanotip we performed a numerical simulation based on the three dimensional Maxwell equations using a commercially available software (COMSOL). This Maxwell solver is based on the finite-difference time-domain (FDTD) method [136], which solves the finite differential equation by leapfrog integration in time and space. The boundary conditions, which are essential in solving the Maxwell equation, were dictated by the geometry of the given nanotip. As we were primarily interested in the field enhancement very close to the apex of the tip, geometry was modeled as a hemisphere of radius $\sim$35nm on a cone with an opening angle of $\sim 15^\circ$, in accordance with the properties of the tip used in experiments. The simulation was carried out with a single-cycle laser pulse carried at an energy of $\sim$1.8 eV. The spatial distribution of the local field enhancement factor based on this simulation is shown in Fig. 3.3. The field-enhancement factor, which is the ratio between the enhanced and impinging

near-field strengths, was estimated to ∼4 on the apex of the tip. It smoothly decreases with distance from the metal surface and reduces by a factor of two at a distance of ∼20 nm. This result also agrees well with values reported in the previous works [130, 137, 23, 132] for similar tips.

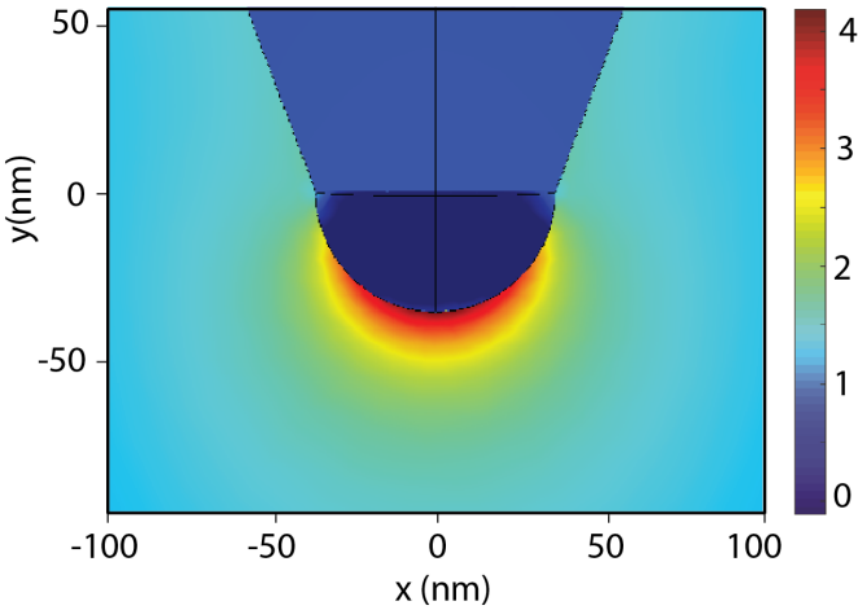

Figure 3.3: **Simulated field-enhancement in the vicinity of the tungsten nanotip.** Utilizing a Maxwell solver based on FDTD, the field enhancement factor of a tungsten nanotip was computed within a range of ±100 nm from the tip apex. The geometry of the nanotip in the simulation was chosen to mimic this in the experiment (apex radius of 35 nm, opening angle of 15°). Figure adapted from ref. [127]

In one dimension, the spatial distribution of the enhanced near-field can be expressed analytically. It can be expressed as a power-law with a dipolar distance dependence. Assuming a Gaussian distribution of the laser intensity in the focus, the near-field enhancement factor as a function of the distance (z) from the tip apex is given by [138].

$$f(z) = \left[(f_0 - 1)\left(\frac{r_0}{z + r_0}\right)^3 + \exp\left[-\frac{2\log 2z^2}{(2w_{foc})^2}\right]\right] \tag{3.1}$$

where f_0 is the field enhancement factor on the surface, *i.e.*. when $z = 0$, and r_0, w_foc are the radius of the tip apex and the beam waist of the laser, respectively. The enhanced near-field in space and time can now be expressed as a multiplication of the incident field and the enhancement factor as: $E_{near}(z,t) = f(z)E_L(0,t)$. Fig. 3.4 b plots the enhancement factor as a function of distance z. This analytical description is useful in accounting for

the space dependent near-field in numerical simulations of semiclassical trajectories in the vicinity of the nanotip surface as presented in the next section.

3.1.3 Quiver and sub-cycle motion

In the previous section, we have shown that the photoelectrons emerging from metallic nanostructures experience inhomogeneous near-field enhancement in space, and as a consequence, its dynamics is expected to be generally different from this in free space. To explore the relevance of this effects in our experiments, we consider the electron motion in the presence of a monochromatic electric field with an amplitude of E_0 and an angular frequency of ω_L. The electron quivers in space with an amplitude of $l_q = eE/m_e\omega_L^2$. Considering that the field enhancement monotonically declines versus distance from the apex of the nanotip one can define a characteristic distance l_f as the (1/e)-decay length from the apex. The comparison between the quiver length of the electron and the decay length can be used to quantify the effect of the spatial distribution of the near-field enhancement on the dynamics [138, 139, 140]. An adiabaticity parameter is then defined as:

$$\delta = \frac{l_f}{l_q} \tag{3.2}$$

If the quiver length is shorter than the decay length ($\delta > 1$), the excursion of electron takes place within a slowly varying near-field. In this case, it can be safely assumed that the electron experiences a nearly homogeneous near-field, and its kinetic energy is simply scaled by the enhancement factor. This regime is known as "quiver regime". However, in the opposite case ($\delta < 1$, known as sub-cycle regime) which occurs for driving fields of long wavelength, the electron experiences a drastic variation of the local field along its excursion. In this case, the total momentum accumulated from the field is less than that under a homogenous field, and the back-scattering process is quenched. This fact results in a suppression of the electron kinetic energy under the inhomogeneous near-field as experimentally observed by Herink *et. al.* [138]. Extending the above discussion to the case study of our experiments the decay length of the near-field is ∼29.9 nm. This is much longer than the quiver length of the ponderomotive motion, ∼1.3 nm, giving rise to an adiabaticity parameter of δ ∼23. Therefore, we can expect that under our experimental condition the emitted electron experiences a quasi-homogeneous field with negligible quenching effects in the back-scattering process.

To better understand the kinematics of electrons in the space-dependent field enhancement as well as to introduce the calculation methodology used later on in this thesis, a semiclassical simulation of electron trajectories was conducted by utilizing the three step model under the experimental conditions. In the simulation a single-cycle optical pulse with a peak intensity of 25 TW/cm^2 and a central energy of 1.8 eV was used. The electron trajectories were traced by solving the classical equation of motion (Fig. 3.4 a) in the presence of a spatially varying enhanced near-field, $m_e(d^2z_i/dt^2) = -ef(z_i)E(t)$, where m_e, e and z_i are mass, charge and position of the i$^{\text{th}}$ electron, respectively. The simulation was performed in the single electron limit, *i.e.* interaction among the electrons was ignored.

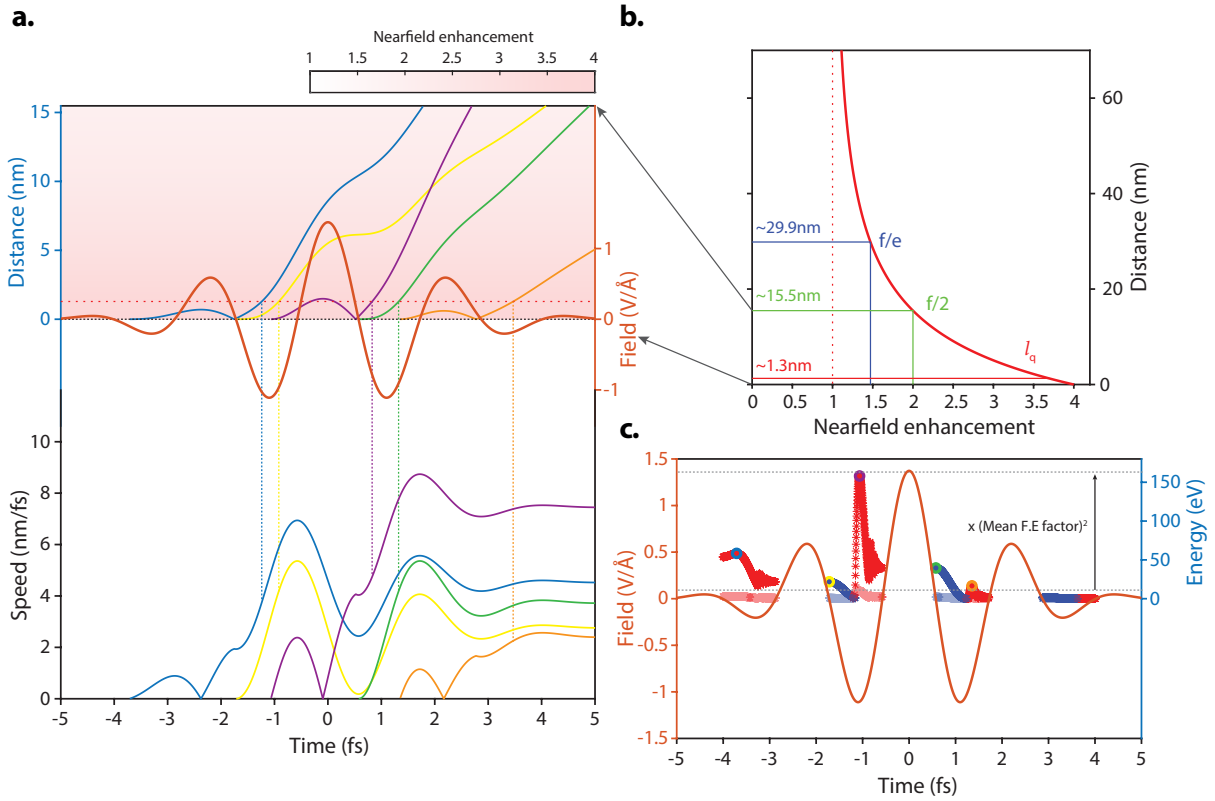

Figure 3.4: **Electron dynamics in spatially inhomogeneous near-field.** **a** and **b**, Photoelectron trajectories (top in panel a) and their speed (bottom in panel a) calculated semiclassically under a single-cycle electric field (red curve) and a spatial distribution of the field enhancement as described by Eq. 3.1 (b). The field enhancement factor was calculated using parameters relevant to the experiments, $f_0 = 4$, $r_0 = 35$ nm and w_{foc}=15 μm. The red solid line shows the quiver length, while the lines in green and blue denote the half and the 1/e-decay length of the field enhancement factor, respectively. The red dotted vertical line displays an unitary number that represents the incident field. **c**, The terminal energies of photoelectron as a function of the ionization time. The red and blue colors indicate the back-scattered and direct electron energy, respectively. The shadowed plots display the electron energy calculated in the absence of field-enhancement. The color of the circles superimposed on the plot is associated with the corresponding electron trajectories shown in the panel a.

The propagation of the trajectories was performed by the Verlet propagation method which allows us to account for the position dependent field-enhancement. The spatial distribution of the field enhancement was modeled according to Eq. 3.1 with the nanotip and laser parameters ($r_0 = 35$ nm, w_{foc} =15μm and $f_0 = 4$) as displayed in Fig. 3.4 b.

Fig. 3.4 a shows the simulated electron excursions and velocities as a function of time

in the top and bottom panels, respectively. We can observe that the electron excursion remains within the half-maximum length of the field enhancement factor (marked as green line in Fig. 3.4 b) for the entire duration of the driving pulse. Furthermore, the electron momentum (velocity) reaches more than the half of the terminal value within the quiver length as marked by the red dashed and solid line in Fig. 3.4 a and b, respectively. This fact highlights that the field-electron interaction and the consequent electron momentum accumulation mostly occur within a range where the near-field is quasi-constant. Therefore, the enhancement factor can be effectively considered homogeneous during the interaction.

Because the energy scales linearly with the local field intensity, the terminal electron energy is accordingly enhanced (Fig. 3.4 c). In our simulation, we obtained an enhancement factor of $\sim 3.85^2$ which is close to that on the surface $(f_0 = 4)^2$. Energy enhancement of exact f_0^2 can be obtained only with a fully homogeneous field-enhancement factor. For a better approximation concerning the spatial effects, one can define a space-averaged field enhancement factor covering the range from the origin to the quiver length.

$$\bar{f} = \frac{1}{l_q} \int_0^{l_q} dz f(z) \tag{3.3}$$

In our simulation, the space-averaged value of $\bar{f} = 3.82$ was obtained, which is in excellent agreement with the value from the semiclassical calculation, ~ 3.85. This fact further supports the notion that the electron dynamics under our experimental conditions can be effectively considered to occur under a homogeneous near-field with enhancement of $\bar{f}$.

3.2 Energetic features of photoelectron emitted from a tungsten nanotip

3.2.1 Extendibility of the recollision physics from atom to nanostructured metals

To best visualize the relation between intensity and cutoff energies in our experiments, a 2D plot is considered (Fig. 3.5). Fig. 3.5 a and b show electron spectra from neon gas and tungsten nanotip versus peak pulse intensity, respectively. In both cases, a linear relationship between the electron cutoff energy and the intensity is apparent, and it is highlighted by the experimentally evaluated points on the plot and their linear fitting (dash lines). The dramatic difference, however, in the slopes is also apparent, and this can provide information about the field enhancement in the vicinity of the metal nanotip.

The cutoff energy slope in Ne was evaluated by a linear fit (black dashed line in Fig. 3.5 a) of the measured data (black points), $s_{Ne}^{(exp)} = dE_{Ne}^{(exp)}/dI = 0.446 \pm 0.016$ eV/(TW $\cdot$ cm^{-2}). This slope is compatible with a relation of $E_{Ne}^{(exp)} \propto (9.88 \pm 0.343)U_p$. where U_p is the ponderomotive energy of the electron in the driving field. This result is in excellent agreement with well-established semiclassical theory (see also Chapter 1). A precise calculation based on the experimental field-waveform yields a relation between the

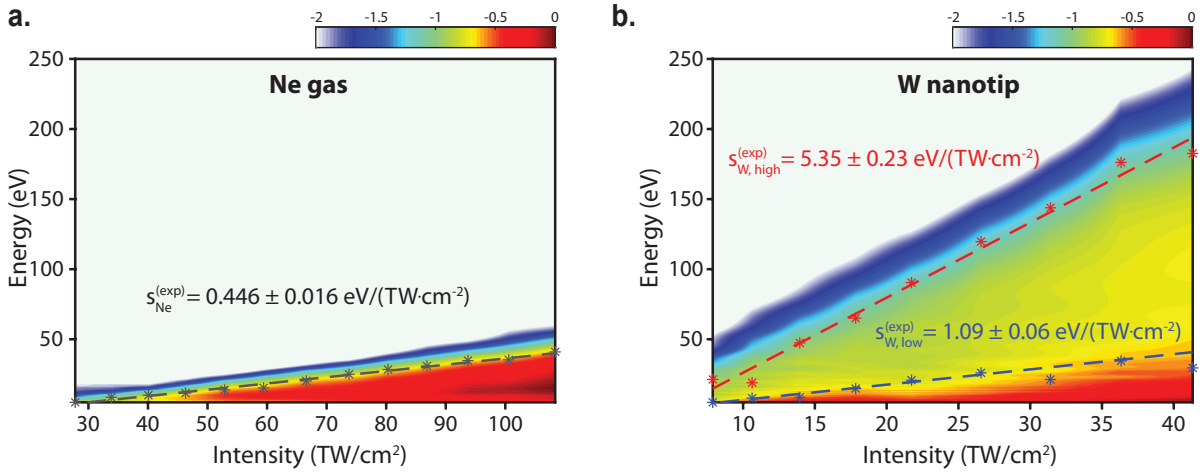

Figure 3.5: **Experimental photoelectron spectra.** Recorded photoelectron spectra emerging from Ne gas (**a**) and tungsten nanotip (**b**). The points on the plot denote the evaluated cutoff energy, while the dashed lines show its linear fit. Figure adapted from ref. [127]

cutoff energy and the ponderomotive energy: $E^{(theo)}_{Ne} \propto 10.8U_p$. Note that $10U_p$ is strictly correct under a CW driving light field, and it is slightly modified at the limit of single-cycle pulses.

The dramatic difference in the photoemission properties between neon and tungsten nanotip targets can best be understood quantitively by comparing the corresponding cutoff energy slopes. The slope of the highest energy cutoff in tungsten is (red dashed line in Fig. 3.5 b) $s^{(exp)}_{W,high)} = 5.35 \pm 0.23$ eV/(TW $\cdot$ cm^{-2}), and it is by factor of ∼12 "steeper" in comparison to that of neon. At energies below 50 eV, the tungsten spectra show a second cutoff energy bearing a slope of $s^{(exp)}_{W,low} = 1.09 \pm 0.06$ eV/(TW $\cdot$ cm^{-2}) (blue dashed line in Fig. 3.5 b). The relative ratio between the high and low energy cutoffs in the tungsten tip is $s^{(exp)}_{W,high}/s^{(exp)}_{W,low} = 4.91 \pm 0.35$ and agrees well with the theoretically expected value of $10U_p/2U_p \sim 5$ in the semiclassical single-electron model. This observation supports the notion that the potential space charge effects do not play a significant role in the kinematics of electrons in our experiments.

Under this consideration, we can now process to evaluate the field-enhancement factor in the vicinity of the nanotip from the ratio of the slopes of the high energy cutoffs in neon gas and tungsten nanotip as, $\bar{f} = \sqrt{s_W/s_{Ne}}$. We obtained a factor of $\bar{f} \sim 3.46 \pm 0.10$ which is in reasonable agreement with the calculated value of 3.82 in the previous section with less than 10% of discrepancy.

The evaluated field enhancement factor and the incident electric pulse waveform precisely measured by EUV attosecond streaking allow us to conduct a complete semiclassical simulation (Fig. 3.6) to investigate the temporal and spectral properties of the emission.

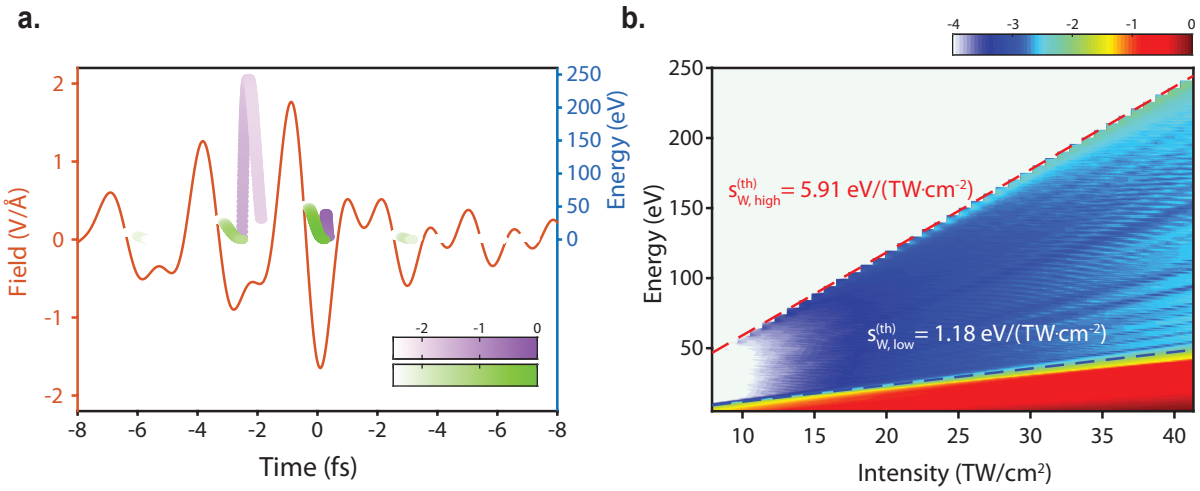

Figure 3.6: **Semiclassical simulation of the optical field emission in tungsten nanotips. a**, Terminal electron energy was simulated by the recollision model and plotted on the axis of ionization time. The waveform of the driving pulse was precisely characterized by EUV attosecond streaking (red curve). In the simulation, the field enhancement factor of 3.46 evaluated from the slope comparison in Fig. 3.5 was used. The purple and green colors denote the back-scattered and direct electrons, respectively, and the logarithmic color scale stands for the ionization probability. **b**, Simulated photoelectron spectra as function of the intensity of the driving pulse. Red and blue dashed lines display theoretically evaluated cutoff energies. Figure adapted from ref. [127].

The theoretically evaluated features in the electron spectrum match well with those in the experimental observation. These include the linear slopes of the cutoff in the high (5.91 eV/(TW $\cdot$ cm^{-2}), red dashed line) and the low (1.18 eV/(TW $\cdot$ cm^{-2}), blue dashed line) energy electron spectra and the absence of electrons at the intermediate energies between the two cutoffs. This good agreement between the experimental and theoretical results suggests that the single-electron recollision physics, well established in atomic physics, can be successfully extended to the dynamics of field-emitted electrons from solids.

3.2.2 Optical field emission and electron yield

The relation between photoelectron yield and the driving pulse peak intensity is a useful observable that can allow the understanding of the ionization regime. In the previous section, we have made the tacit assumption that tunneling ionization is dominant in our experiments. We have also based our semiclassical simulations on this assumption. Yet, extracting this information from experiments is essential for utilizing theoretical models in order to interpret the experimental data and to derive useful physical properties of the system. To figure out the dominant emission process under our experimental conditions, a measurement of the photoelectron yield (total number of electrons) under the variation

of driving pulse intensity was conducted.

Since the TOF spectrometer can record photoelectrons only within a limited solid emission angle (∼6°) and is more sensitive to energies higher than ∼ 20 eV, a method to capture all emitted electrons was considered. To this end a thin metallic electrode plate was introduced ∼2 mm above the tungsten nanotip (Fig. 3.7). Like all other instruments in this setup the metallic plate can be inserted and removed in the setup on demand. This allows spectral and total electron count measurements under the identical conditions.

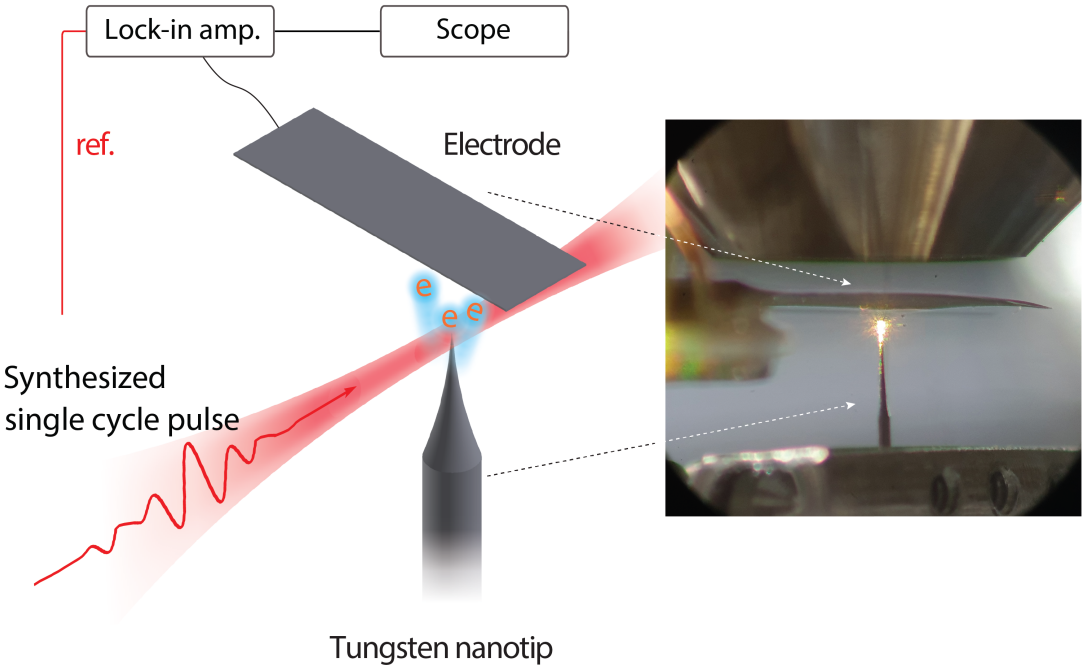

Figure 3.7: **Experimental module for the measurement of the total photoelectron yield.** Experimental configuration for a measurement of photoelectron yields. A thin metallic electrode was placed ∼2 mm above the tungsten nanotip. The photoelectrons generated from the metallic nanotip were collected by the electrode, and the induced voltage was measured by a lock-in amplifier.

The metallic electrode, whose size is approximately 5 × 5 mm, was sufficiently large to capture photoelectrons emerging from the tip in solid angles higher than 100°. The electrode was connected to a high gain lock-in amplifier that allowed the precise determination of the induced current. According to its operational principles the lock-in amplifier selectively amplifies the frequency components of the voltage at the reference frequency, which in our case was the repetition rate (3 kHz) of the laser source. In this way a great deal of noise can be eliminated. The photocurrent was evaluated by Ohm's law, *i.e.*, by dividing the measured voltage by the system impedance (10 MΩ). In a next step, the number of electrons per pulse was evaluated by dividing the photocurrent with the laser repetition rate.

In the experiment, the photoelectron yield was recorded as a function of the laser intensity. A linear fit of the measured data points reveals a slope of $\sim 1.18 \pm 0.09$ (Fig. 3.8). Because the minimum number of photons (energy of ~1.8 eV) required to release electrons under a multiphoton process is, $\lceil W/\hbar\omega_L \rceil = 3$ where W denotes the workfunction of tungsten, we can safely conclude that under the experimental conditions the processes is in the tunneling or optical-field emission regime [141, 142].

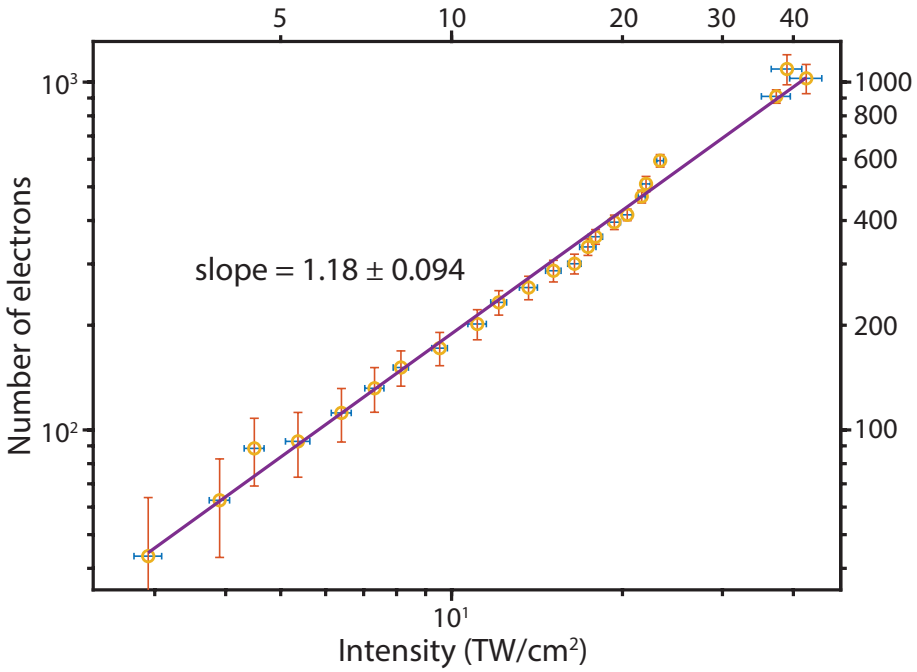

Figure 3.8: **Optical field emission and the total electron yield per pulse.** The evaluated photoelectron counts released per laser shot is mapped as a function of the incident intensity of driving laser pulse in log-log scale. Figure adapted from ref. [127]

At this stage it is also useful to evaluate the Keldysh parameter of the system and to investigate if the above conclusion is in good accordance. Here the Keldysh parameter is:

$$\gamma = \sqrt{\frac{W}{2U_p}} \tag{3.4}$$

where W denotes the work-function of the metal. With the work-function of tungsten (W=4.55 eV for polycrystalline tungsten [143]) and the laser parameters used in the experiment such as the enhanced local intensity of $f^2I = 3.46^2 \times 25$ TW/cm^2 and central energy of $\hbar\omega_L$=1.8 eV, the Keldysh parameter is evaluated to γ ~0.41, indicating once again that the ionization process is in the tunneling regime.

In the measurement, the maximum electrons per pulse observed was ~1000 at an intensity of $\sim$ 40 TW/cm^2. This number is lower compared to previous reports even at lower

intensities [142, 144]. This fact can be attributed to a lower number of cycles of laser field (∼1.2 cycle) as well as a reduced area of the tip (∼35 nm) used in our measurement.

3.2.3 Field sensitivity of the optical field emission

The sensitivity of the emission to the driving field waveform is often considered as another important criterion for identifying the onset of the strong field regime, for instance in atoms [20]. Such field-sensitivity and–controllability supports the notion that the electron emission is localized to half-cycles of the driving field. Several studies on this feature in photoelectron spectra with a variation of carrier-envelope phase (CEP) have earlier suggested the possibility of attosecond control of the photoelectron emission [23, 24]. However, these studies were conducted at much lower driving intensities and consequently electron energy remained lower compared to our study. It is therefore important to also investigate this aspect here, before we advance to the next chapter and introduce methods that allow us to directly probe the dynamics of the electron pulse emerging from the system.

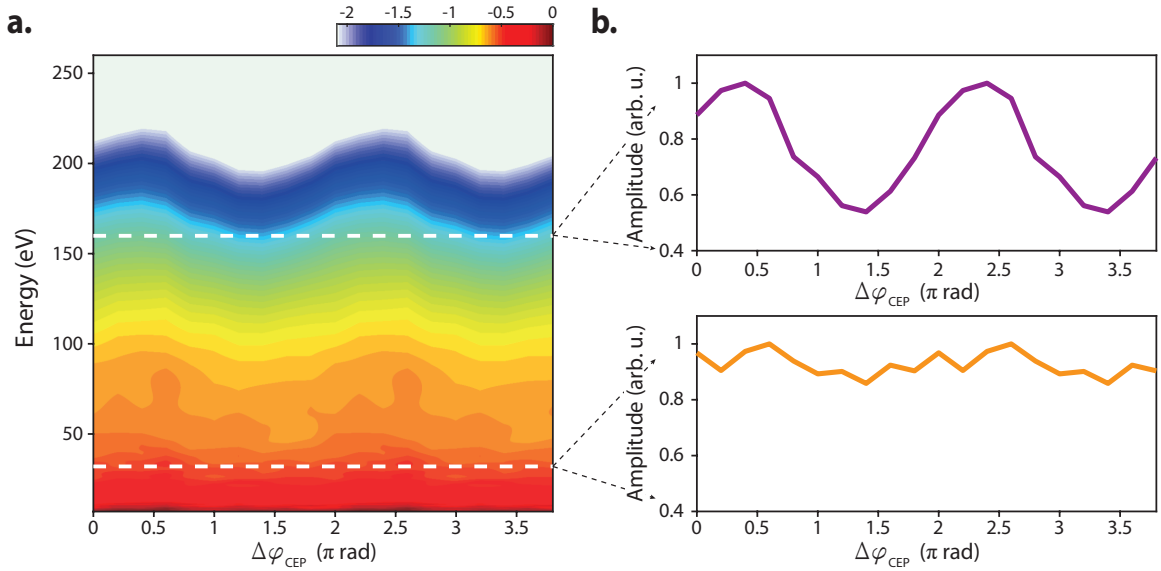

Figure 3.9: **Single-cycle CEP control of the optical field emission.** **a**, Photoelectron spectra emerging from the tungsten nanotip as a function of the CEP of the driving pulse at a peak intensity of ∼ 35 TW/cm^2. **b**, The variations of the photoelectron yield at high (∼160 eV) and low (∼32 eV) cutoff energies (white dashed lines in panel a) are shown in top and bottom panels, respectively.

To this end, we recorded photoelectron spectra versus the CEP of the driving pulse at a peak intensity of $I \sim 35$ TW/cm^2. A conspicuous modulation of the cutoff energy with a 2π periodicity was observed (Fig. 3.9 a). Near the higher cutoff energy (∼160 eV, upper white line) of the spectra, the spectral yield modulation is higher than 50% (Fig. 3.9 b

top panel). At energies lower than 50 eV (∼32 eV, lower white line) the contrast in the yield variation is dramatically reduced to ∼10% (Fig. 3.9 b bottom panel). The fact that the higher cutoff energy has a dramatically higher contrast can be understood (in close analogy to high harmonic emission in atoms [20, 21, 22]) as a result of the confinement of electron pulse emerging at these energies to within the main half-cycle of the driving field (see Fig. 3.6 a). By contrast, the lower energy emission comprises a mixture of several electron pulses emerging from different half-cycles of the driving pulse, and this results in a reduction of the sensitivity to the half-cycle variation of the field.

Chapter 4

Homochromic Attosecond Streaking (HAS): The principles

An artist makes a work of art because it is not there.
-Carl Andre

In the previous chapter, the general features of the strong field electron emission in metallic nanotips were explored: cutoff laws, nonlinearity of the photoelectron yield and sensitivity to the carrier-envelope phase of the driving pulse. Despite the large number of emitted electrons, the analysis of the energetic characteristics of the electron emission suggests a close relation to strong field ionization in atoms without notable deviations. As such, it is logical to anticipate that attosecond electron bursts must be also generated in the optical field emission in metals. However in analogy to previous works, a spectral domain or time-integrated study only offers circumstantial evidence for the generation of these pulses. To understand the physics of the optical field emission from metal nanostructures under a strong ultrafast optical field and to explore its potential applications in spectroscopy and microscopy, a characterization technique for the emitted electron pulse in real time is essential.

The attosecond streaking technique summarized in the previous chapters is one of the most essential temporal characterization techniques in ultrafast optics. A key characteristic of EUV attosecond streaking is that the optical pulse acting on the photoelectrons released by an EUV attosecond pulse does not influence ionization. This optical pulse is often referred to as a "phase gate". If a strong pulse is used to release electrons, the introduction of a phase gate is not that trivial, but efforts over the last decade have shown that in atoms this approach is possible [29, 119, 22]. Whereas in atoms the electron emission can be directly probed in time by inspecting the properties of the emerging high harmonics, in metals this is not possible as high harmonic generation has not been so far observed. In this chapter, I will introduce an extension of the streaking technique by utilizing the optical phase gate onto strong field emitted photoelectron from a metallic nanotip. The technique allows probing the dynamics of the electron emission directly in the electron

spectral domain.

4.1 Homochromic attosecond streaking (HAS): Concept

To characterize the time structure of an electron pulse emerging from an optically driven solid, the concept of the optical phase gate, as used in the EUV attosecond streaking technique, needs to be extended. This is because the EUV pulse is now replaced by a strong optical pulse (pump pulse) which serves not only as a "photoelectron generator" but also as a "free-space driver" to the released photoelectrons, while the weak replica of the pump field (gate pulse) introduces a gentle perturbation to the final energy distribution. Spectral measurements as a function of the time delay between the pump and gate pulses composes a temporally and spectrally resolved spectrogram. Since the two pulses are spectrally identical, this new technique will be referred to as "Homochromic attosecond streaking (HAS)" hereafter to distinguish from the conventional EUV attosecond streaking technique. Thanks to the reduced nonlinearity of the photoelectron emission versus pump field, the weak gate field, intensity of which is ~ 2 order less than that of the pump pulse, is expected to act only on the kinetic energy of the photoelectrons with marginal variation of photoelectron counts. In other words, it serves only as a phase gate to the photoelectron pulse generated by the pump field rather than an amplitude gate.

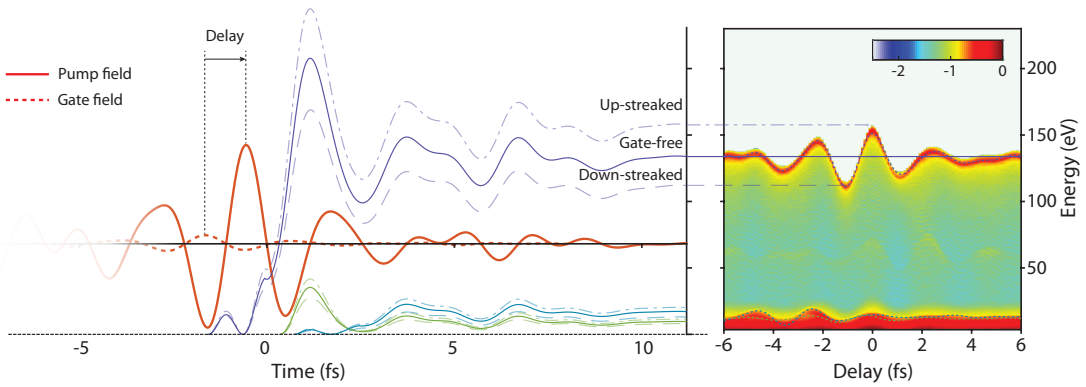

Figure 4.1: **Illustration of the concept of Homochromic attosecond streaking (HAS).** A strong pump pulse (red solid pulse) generates and drives electrons to compose a photoelectron spectrum. A weak replica of the gate field (red dashed pulse) leads a small perturbation on the photoelectron energy. The gate-free energy trajectories are shown as thin solid lines, while up- and down streaked trajectories are shown in dot-dashed and dashed curves, respectively. The energy spectrum of the streaked photoelectron is calculated at each delay point between pump and gate field and are used to compose a 2D spectrogram.

The conceptual illustration of HAS is shown in Fig. 4.1. In the absence of a gate (gate-free case), the strong optical pump pulse (red solid pulse) generates and accelerates the photoelectrons. A portion of generated electrons are driven back to the surface of the nanotip and back-scatters (blue solid curve). These back-scattered electrons gain more energy (> 100 eV) than the direct electrons which do not undergo scattering (green solid curve) as discussed earlier. In the presence of an additional weak gate field, the gate (red dashed pulse) energetically perturbs the electron trajectories in comparison to those of the gate-free case. The distribution of the terminal electron energy is up- or down-streaked depending on the time delay of the gate with respect to the pump. The up and down-streaked trajectories are shown in dot-dashed and dashed curves, respectively. This spectrally and temporally resolved measurement encrypts temporal information of the strong field electron emission in a 2D HAS spectrogram (right in Fig. 4.1).

4.2 Theoretical description of the Homochromic Attosecond Streaking (HAS)

4.2.1 Phase gate of HAS

Just as in the previous techniques that are based on pump and probe fields of the same color [145, 146], HAS relies on the utilization of an optical gate which is sufficiently weak to perturb the momentum (energy) of a released electron pulse but without contributing to the strong field emission from an atom, a molecule or a solid. In this sense, HAS bears similarities to EUV attosecond streaking. However, a great difference between the two is that in HAS the final kinetic energy of the photoelectrons (terminal energy) develops along with the strong pump driving field before and after the back-scattering event, whereas that of photoelectron in EUV attosecond streaking is instantly transferred from EUV pulse at the release of photoelectrons. Hence, in HAS the phase accumulation after a back-scattering event is the result of both pump and gate. The goal of this section is to derive an analytical description of the concept of HAS as an extension of that in the strong field emission described in Chapter 1 (section 1.2.2). As verified in the previous chapter, the strong field emission under our experimental conditions exhibits a reduced nonlinearity. For instance, based on the measurements shown in Fig. 3.8, a 5% of variation of the laser intensity results in a marginal change of $\sim 6\%$ in the photoelectron yield. This suggests that a sufficiently weak gate pulse in comparison to the pump will marginally affect the ionization and thus could be approximated as a pure phase gate which acts solely on the momentum of the strong field-emitted electrons. In HAS, since the highest energetic back-scattered electron has an essential role for the gate field characterization (see Fig. 4.1), and moreover in future applications of the electron pulses for instance in low energy electron diffraction, the temporal characteristics of the high energetic electron is more central than those of low energy electrons. Therefore, the theoretical framework that we put together here primarily focuses on the properties of back-scattered electron rather than the direct electrons.

As a first step, we revisit the analytical description of the complex terminal amplitude of the back-scattered electron once again (see Eq. 1.17 and 1.18). The term, "terminal" electron wavepacket or amplitude in this context will refer to the back-scattered electron at the end of the driving pulse ($t = \infty$), when the development of its kinetic energy under the field terminates. The term "back-scattered electron" will be used hereafter to refer to the electron at the recollision instance to distinguish from the other. In the gate-free case, *i.e.*, when only the pump pulse is acting on the system, the complex amplitude of the terminal electron $\chi_{tr}^{(0)}(p)$ in the electron momentum space (p) is written as an integration of the back-scattered electron wavepacket amplitude $\psi_{bs}^{(0)}(t_r)$ with the phase accumulation from the recollision moment to the detection $S^{(0)}(p, t = \infty, t_r; A_p(t))$ over all recollison time (t_r):

$$\chi_{tr}^{(0)}(p) \propto i \int_{-\infty}^{\infty} dt_r \psi_{bs}^{(0)}(t_r) \exp[-iS^{(0)}(p, t = \infty, t_r; A_p(t))] \tag{4.1}$$

Note that the superscript (0) is used to denote the gate-free quantities to distinguish from the quantities altered by the gate pulse field. The accumulation of phase introduced by the pump field within the time window from t_1 to t_2 is expressed by the Volkov phase as:

$$S^{(0)}(p, t_2, t_1; A_p(t)) = \int_{t_1}^{t_2} dt \frac{1}{2}[p + A_p(t)]^2 = \int_{t_1}^{t_2} dt \frac{p^2}{2} + \int_{t_1}^{t_2} dt \left[pA_p(t) + \frac{A_p^2(t)}{2} \right] \tag{4.2}$$

where $A_p(t)$ is the vector potential of the pump pulse. Henceforth, atomic units ($\hbar = e = 1$) are used for simplicity. Since the first term on the right hand side of Eq. 4.2 represents a plane wave basis, one can define a "terminal electron wavepacket" $\psi_{tr}^{(0)}(t_r)$ on the basis of continuum states (plane waves) by merging the back-scattered electron wavepacket and the phase term introduced by the field (second term on the right hand side of Eq. 4.2).

$$\chi_{tr}^{(0)}(p) \equiv \int_{-\infty}^{\infty} dt_r \psi_{tr}^{(0)}(t_r) \exp\left[i \frac{p^2}{2} t_r \right] \tag{4.3}$$

The terminal electron wavepacket here $\psi_{tr}^{(0)}(t_r)$ represents the terminal state of the back-scattered electron, the phase of which is modulated by the driving pump pulse, *i.e.*, the final energy distribution. The resulting spectrum of the electron at the detector is then given by the absolute square of the complex amplitude of the terminal electron wavepacket as:

$$I^{(0)}(\omega = p^2/2) = \left| \chi_{tr}^{(0)}(\omega = p^2/2) \right|^2 \tag{4.4}$$

Now we move on to the case where a weak gate time-delayed by (τ) is added to the pump, and we scrutinize how the terminal wave is affected. To do so we simply replace the terms of the electric field and the vector potential with the superposition of pump and gate, *i.e.*, $E_p(t) \to E_p(t) + E_g(t+\tau)$ and $A_p(t) \to A_p(t) + A_g(t+\tau)$. Now the Volkov phase (Eq. 4.2)

can be rewritten as,

$$S(p,t_2,t_1;A_p(t)+A_g(t+\tau)) = \int_{t_1}^{t_2} dt \frac{1}{2}[p+A_p(t)+A_g(t+\tau)]^2$$
$$\approx \underbrace{\int_{t_1}^{t_2} dt \frac{1}{2}[p+A_p(t)]^2}_{=S^{(0)}(p,t_2,t_1;A_p(t))} + \underbrace{\int_{t_1}^{t_2} dt[p+A_p(t)]A_g(t+\tau)}_{\equiv \Delta S(p+A_p(t),t_2,t_1;A_g(t+\tau))} \quad (4.5)$$

Since the gate is very weak in intensity compared to the pump field, $|A_p(t)|^2 \gg |A_g(t)|^2$, the contribution of the squared term of the gate vector potential is negligible in comparison to the others and can be safely ignored in Eq. 4.5. The Volkov phase can now be decomposed into two terms, the gate-free Volkov phase ($S^{(0)}$) and the additional phase introduced by the weak gate (ΔS).

First, we will have a close look on the phase variation of the back-scattered electron wavepacket $\psi_{bs}(t_r)$ under the addition of the weak gate. The gate-free back-scattered electron wavepacket described by Eq. 1.17 is now rewritten with the gate field terms as following:

$$\psi_{bs}(t_r) = \int_{-\infty}^{t_r} dt' \int d^3p' [E_p(t_r)+E_g(t_r+\tau)] g(p'+A_p(t_r)+A_g(t_r+\tau))$$
$$\times [E_p(t')+E_g(t'+\tau)] d(p'+A_p(t')+A_g(t'+\tau)) \exp[-iS(p',t_r,t';A_p(t)+A_g(t+\tau))] \quad (4.6)$$

The assumption of the phase gate leads to an approximation under which the dipole element is not affected by the weak gate, *i.e.*, it remains constant along the delay, $[E_p(t)+E_g(t+\tau)]d(p+A_p(t)+A_g(t+\tau)) \approx E_p(t)d(p+A_p(t))$. This approximation also applies to the scattering transition matrix g, so that it is also assumed to be invariant under the condition, $[E_p(t)+E_g(t+\tau)]g(p+A_p(t)+A_g(t+\tau)) \approx E_p(t)g(p+A_p(t))$. Under these circumstances the effect of the weak gate on the back-scattered electron is dictated by the variation of the Volkov phase in Eq. 4.7.

$$S(p',t_r,t';A_p(t)+A_g(t+\tau)) \approx S^{(0)}(p',t_r,t';A_p(t)) + \Delta S(p'+A_p(t),t_r,t';A_g(t+\tau)) \quad (4.7)$$

By inserting Eq. 4.7 into Eq. 4.6, one can derive the perturbed back-scattered electron wavepacket in the form of a gate-free back-scattered electron wavepacket with an additional phase as:

$$\psi_{bs}(t_r) \approx \int_{-\infty}^{t_r} dt' \int d^3p' E_p(t_r) g(p'+A_p(t_r)) E_p(t') d(p'+A_p(t')) \exp[-S^{(0)}(p',t_r,t';A_p(t))]$$
$$\times \exp[-i\Delta S(p'+A_p(t),t_r,t';A_g(t+\tau))] \quad (4.8)$$

As alluded to earlier, the weak gate field contributes an additional phase ΔS to the gate-free back-scattered electron wavepacket. Since the strong pump in terms of $A_p(t)$ of the

gate-free Volkov phase $S^{(0)}$ dominantly contributes to the momentum, the momentum $p' + A_p(t)$ in the additional phase ΔS can be replaced by the momentum of the gate-free back-scattered electron p_s in the integral over the momentum p' of Eq. 4.8.

Furthermore, in the time integration over t' of Eq. 4.8, we assume that the additional phase can be effectively replaced with its time average over the excursion time $|\Delta t|$,

$$\overline{\Delta S}(p_s, t_r; A_g(t+\tau)) = \frac{1}{|\Delta t|}\int_{t_r+\Delta t}^{t_r} dt' \Delta S(p_s, t_r, t'; A_g(t+\tau)) \tag{4.9}$$

Note that Δt denotes the time difference from the back-scattering (t_r) to the ionization (t_i) events, $\Delta t = t_i - t_r < 0$. Using the property of the definite integral, $\int_{t'}^{t_r} \cdots = -\int_{t_r}^{\infty} \cdots + \int_{t'}^{\infty} \cdots$, one can decompose ΔS into two terms according to the t' dependence as,

$$\Delta S(p_s, t_r, t', A_g(t+\tau)) = \int_{t'}^{t_r} dt p_s A_g(t+\tau) = -\int_{t_r}^{\infty} dt p_s A_g(t+\tau) + \int_{t'}^{\infty} dt p_s A_g(t+\tau) \tag{4.10}$$

and the averaged phase described by Eq. 4.9 can be expressed in the following form:

$$\begin{aligned}\overline{\Delta S} &= -\int_{t_r}^{\infty} dt p_s A_g(t+\tau) + \int_{t_r}^{\infty} dt p_s \left[\frac{1}{|\Delta t|}\int_{\Delta t}^{0} dt'' A_g(t+t''+\tau)\right] \\ &= -\int_{t_r}^{\infty} dt p_s \left[A_g(t+\tau) - \bar{A}_g^{(b)}(t+\tau)\right]\end{aligned} \tag{4.11}$$

where $\bar{A}_g^{(b)}(t+\tau)$ is defined as,

$$\bar{A}_g^{(b)}(t+\tau) = \frac{1}{|\Delta t|}\int_{\Delta t}^{0} dt'' A_g(t+t''+\tau) \tag{4.12}$$

Eq. 4.11 implies that the time-averaged phase ($\overline{\Delta S}$) is equivalent to the additional phase effectively introduced by the vector potential of $A_g(t+\tau) - \bar{A}_g^{(b)}(t+\tau)$, *i.e.*, $\overline{\Delta S} = -\Delta S(p_s, t=\infty, t_r; A_g(t+\tau) - \bar{A}_g^{(b)}(t+\tau))$. The time-averaged perturbing phase term is acting on the momentum constituents of the gate-free back-scattered electron wavepacket independently from the ionization time t'. Therefore, we can plug the gate-free back-scattered electron wavepacket and the perturbing phase independently into the spectral amplitude of the terminal electron under the consideration of the phase inversion due to the back-scattering ($\overline{\Delta S} \to -\overline{\Delta S}$) and the canonical momentum ($p_s \to p + A_p(t)$). In other words, the back-scattered electron wavepacket in Eq. 4.1 can be replaced by $\psi_{bs}^{(0)}(t_r) \to \psi_{bs}^{(0)}(t_r)\exp[-i\Delta S(p + A_p(t), t=\infty, t_r; A_g(t+\tau) - \bar{A}_g^{(b)}(t+\tau))]$ to yield:

$$\begin{aligned}\chi_{tr}(p,\tau) \approx i\int_{-\infty}^{\infty} dt_r \psi_{bs}^{(0)}(t_r)\exp[-iS(p, t=\infty, t_r, A_p(t) + A_g(t+\tau)] \\ \times \exp[-i\Delta S(p + A_p(t), t=\infty, t_r; A_g(t+\tau) - \bar{A}_g^{(b)}(t+\tau))]\end{aligned} \tag{4.13}$$

Time integration of the phase terms S and ΔS are performed over the same time window from t_r to $t = \infty$. Therefore, they can be effectively merged into a single phase term, and the transition amplitude can be rewritten as:

$$\chi_{tr}(p,\tau) \propto i \int_{-\infty}^{\infty} dt_r \psi_{bs}^{(0)}(t_r) \exp[-iS'(p, t=\infty, t_r, \tau)] \tag{4.14}$$

where the effective Volkov phase by the gate field is expressed as

$$S'(p, t=\infty, t_r, \tau) = \int_{t_r}^{\infty} dt \frac{1}{2}[p + A_p(t) + A_{eff}(t+\tau)]^2 \tag{4.15}$$

and the effective HAS vector potential $A_{eff}(t+\tau)$ is now given by

$$A_{eff}(t+\tau) = 2A_g(t+\tau) - \bar{A}_g^{(b)}(t+\tau) \tag{4.16}$$

The HAS spectrogram is the absolute square of the streaked complex amplitude,

$$I(p,\tau) = \left|\chi_{tr}(p,\tau)\right|^2 \propto \left| \int_{-\infty}^{\infty} dt_r \psi_{bs}^{(0)}(t_r) \exp[-iS'(p, t=\infty, t_r, \tau)] \right|^2 \tag{4.17}$$

The HAS spectrogram described in Eq. 4.17 now has a form similar to that of a frequency resolved optical gating (FROG) [147]. Importantly, we note that under a variation of the time delay the modulation of the electron momentum follows the effective HAS vector potential which is closely linked to that of the incident gate pulse. The delay dependent effective Volkov phase is acting therefore as a phase gate on the back-scattered electron wavepacket at its release time, and hence the temporal characteristics of the wavepacket is imprinted in the delay-energy spectrogram like in a conventional EUV streaking spectrogram.

Fig. 4.2 a illustrates the effects of the phase gate in HAS. In the gate-free case, the momentum distribution of the back-scattered electron pulse $|\chi_{bs}^{(0)}(p)|^2$ (orange) is transferred to the terminal distribution $|\chi_{tr}^{(0)}(p)|^2$ (blue) by the vector potential of the pump field $-eA_p(t_r)$ (red curve in Fig. 4.2 a) at its moment of release. The gate-field (yellow dashed curve) introduces an additional momentum shift of $-eA_{eff}(t_r+\tau)$ and gives rise to a spectral modulation of the photoelectron spectrum. As the delay τ varies it gives rise to a streaked spectrum as a function of its delay, $|\chi_{tr}(p,\tau)|^2$ (purple). In order to see how the temporal features of the back-scattered electron are manifested in a HAS spectrogram, simulations based on Eq. 4.17 were performed for three different kinds of chirp of the back-scattered electron pulse: chirp-free, positive group delay dispersion (GDD), and third order dispersion (TOD). As shown in Fig. 4.2 b, the different types of chirp manifest themselves as conspicuous shifts of intensity modulation in the spectrogram along the energy and time delay axes. This fact suggests that an analysis and reconstruction of a HAS spectrogram can offer attosecond measurement of the back-scattered electron pulse, if the pump/gate fields and their relative timing are precisely known.

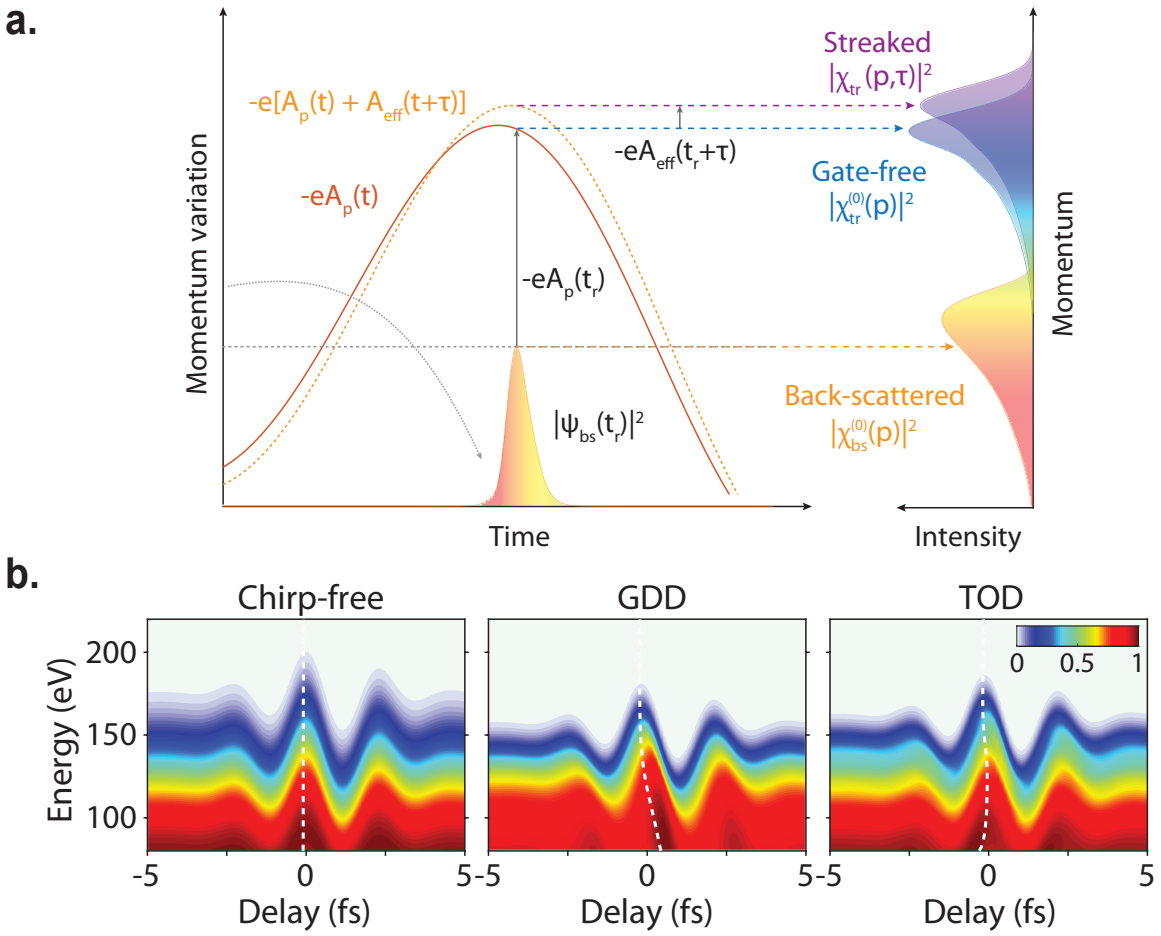

Figure 4.2: **Phase gate on a back-scatted electron wavepacket.** **a**, An electron pulse at the back-scattering instance $|\psi_{bs}^{(0)}(t_r)|^2$,and its momentum distribution $|\chi_{bs}^{(0)}(p)|^2$ are shown as their intensity envelope. In the absence of the gate, the momentum of the photoelectron further evolves by the vector potential of the pump field $A_p(t)$ (red curve) after the back-scattering instance and forms a terminal momentum distribution $|\chi_{tr}^{(0)}(p)|^2$ (blue). An applied gate field with a time delay (τ) with respect to the pump pulse effectively modulates the momentum distribution by a shift of $-eA_{eff}(t+\tau)$ and results in a streaked spectrum $|\chi_{tr}(p,\tau)|^2$ (purple). **b**, HAS spectrograms simulated under different types of chirp of the back-scattered electron pulse, chirp-free (left), positive GDD (middle) and TOD (right). The white dashed curves are guides for eye and highlight the intensity modulation in the spectrograms. From ref. [127]

HAS spectrogram in terminal energy

Similarly as in Eq. 4.7, the effective Volkov phase in Eq. 4.15 can be decomposed into gate-free and gate-associated terms as:

$$S'(p, t=\infty, t_r, \tau) \approx S^{(0)}(p, t=\infty, t_r; A_p(t)) + \Delta S(p + A_p(t), t=\infty, t_r; A_{eff}(t+\tau)) \quad (4.18)$$

The back-scattered electron wavepacket $\psi_{bs}^{(0)}(t_r)$ and the gate-free Volkov phase $S^{(0)}$ in the integration of Eq. 4.14 can be merged to create a terminal electron wave $\psi_{tr}^{(0)}(t_r)$ under the assumption that the back-scattered electron pulse is reasonably confined in time so that the variation within the time window is small in the second term in Eq. 4.18.

$$\begin{aligned}\chi_{tr}(p,\tau) &\approx i\int_{-\infty}^{\infty} dt_r \psi_{bs}^{(0)}(t_r) \exp[-iS^{(0)}(p, t=\infty, t_r; A_p(t))] \exp[-i\Delta S(p + A_p(t), t=\infty, t_r; A_{eff}(t+\tau))] \\ &\approx i\int_{-\infty}^{\infty} dt_r \psi_{tr}^{(0)}(t_r) \exp[-iS(p, t=\infty, t_r; A_{eff}(t+\tau))]\end{aligned} \quad (4.19)$$

Correspondingly, the HAS spectrogram (Eq. 4.17) can be now expressed in terms of the terminal electron pulse as:

$$I(p,\tau) = |\chi_{tr}(p,\tau)|^2 \propto \left| \int_{-\infty}^{\infty} dt_r \psi_{tr}^{(0)}(t_r) \exp[-iS(p, t=\infty, t_r; A_{eff}(t+\tau))] \right|^2 \quad (4.20)$$

Compared to Eq. 4.17, the above equation provides a practical advantage in the reconstruction of a HAS spectrogram (see next chapter), because the spectrum of the terminal electron is directly accessible by a photoelectron spectral measurement, and therefore the reconstruction problem can be reduced to a search for the corresponding spectral phase.

4.2.2 Relation between effective HAS and incident gate vector potentials

As shown in Eq. 4.16, the effective HAS $A_{eff}(t)$ and incident gate $A_g(t)$ vector potentials are closely linked by a time average. Now we interrogate the explicit relation between them. The time averaged term (the second term in Eq. 4.16) can be best analyzed in the Fourier space. Using the Fourier transform of the incident vector potential:

$$A_g(t) = \int_{-\infty}^{\infty} d\omega \tilde{A}_g(\omega) e^{i\omega t} \quad (4.21)$$

the effective HAS vector potential can be rewritten with the Fourier components of the incident gate vector potential as:

$$\begin{aligned}A_{eff}(t+\tau) &= 2\int_{-\infty}^{\infty} d\omega \tilde{A}_g(\omega) e^{i\omega(t+\tau)} - \frac{1}{|\Delta t|}\int_{\Delta t}^{0} dt' \int_{-\infty}^{\infty} d\omega \tilde{A}_g(\omega) e^{i\omega(t+t'+\tau)} \\ &= \int_{-\infty}^{\infty} d\omega \underbrace{\tilde{A}_g(\omega)\left[2 - \frac{i}{\omega|\Delta t|}(e^{i\omega\Delta t} - 1)\right]}_{=\tilde{A}_{eff}(\omega)} e^{i\omega(t+\tau)}\end{aligned} \quad (4.22)$$

The Fourier components of the effective gate vector potential $\tilde{A}_{eff}(\omega)$ can be linked to those of the incident gate vector potential $\tilde{A}_g(\omega)$:

$$\tilde{A}_{eff}(\omega) = \tilde{A}_g(\omega)\left[2 - \frac{i}{\omega|\Delta t|}(e^{i\omega\Delta t} - 1)\right] \equiv \tilde{A}_g(\omega)\tilde{m}(\omega) \tag{4.23}$$

where the multiplier $\tilde{m}(\omega)$ (hereafter referred to as "gate multiplier") connects $\tilde{A}_{eff}(\omega)$ to $\tilde{A}_g(\omega)$, and it is defined as:

$$\tilde{m}(\omega) = \left[2 - \frac{i}{\omega|\Delta t|}(e^{i\omega\Delta t} - 1)\right] \tag{4.24}$$

The factor of 2 in the gate multiplier (first term in Eq. 4.24) corresponds to $2A_g(t+\tau)$ in Eq. 4.16, while the exponent (second term) expresses $\bar{A}_g^{(b)}(t+\tau)$ in the spectral domain. If the time window for the average is appropriately chosen, the multiplier is a function of the frequency regardless of the detailed waveform of the driving pulse. In order to verify the concept of the effective HAS gate, a numerical calculation was conducted by using the semiclassical three-step model. Since the numerical simulation is performed without any a-priori assumptions about the HAS gate introduced in the analytical derivation, the comparison of the gate in the derivation with one revealed in the simulation verifies the validity of our assumptions.

Fig. 4.3 displays a semiclassical HAS simulation performed with single-cycle laser pulses centered at 1.8 eV. The effective HAS vector potential (black curve) was directly evaluated from the incident field using Eq. 4.23. For the time window, Δt in the average, 0.85 of the driving field period was chosen, since it is the excursion time of classical trajectory for electron having more than half of the maximum back-scattering energy, where the electron pulse is mostly confined to. As clearly shown in Fig. 4.3, the cutoff energy variation of the simulated HAS spectrogram agrees with the calculated effective HAS vector potential (black curve). This excellent agreement strongly supports the validity of the assumptions used in the theoretical framework.

The effective HAS vector potential $A_{eff}(t+\tau)$ is very close to the double of the incident vector potential $2A_g(t+\tau)$ (red dashed curve). However, a small discrepancy in waveform can be observed behind the zero-delay as marked in green circles in Fig. 4.3 a. This observation can be interpreted as that the gate vector potential at the ionization time $\bar{A}_g^{(b)}(t+\tau)$ contributes to the effective HAS vector potential, when the main half-cycle of the vector potential is placed around the ionization time. This is also apparent by the evaluation of the gate multiplier (Fig. 4.3 b). Its amplitude and phase are frequency dependent functions of small oscillation centered at 2 and 0, respectively, which reflect that $2A_g(t+\tau)$ dominantly contributes to $A_{eff}(t+\tau)$, while $\bar{A}_g^{(b)}(t+\tau)$ results in a relatively small discrepancy. The gate multiplier is independent from the phase of the incident vector potential. This implies that the gate multiplier can be generally used regardless the phase of the incident field, such as the carrier-envelope phase. This aspect was numerically verified by simulations at different CEPs of the incident gate field (Fig. 4.3 a).

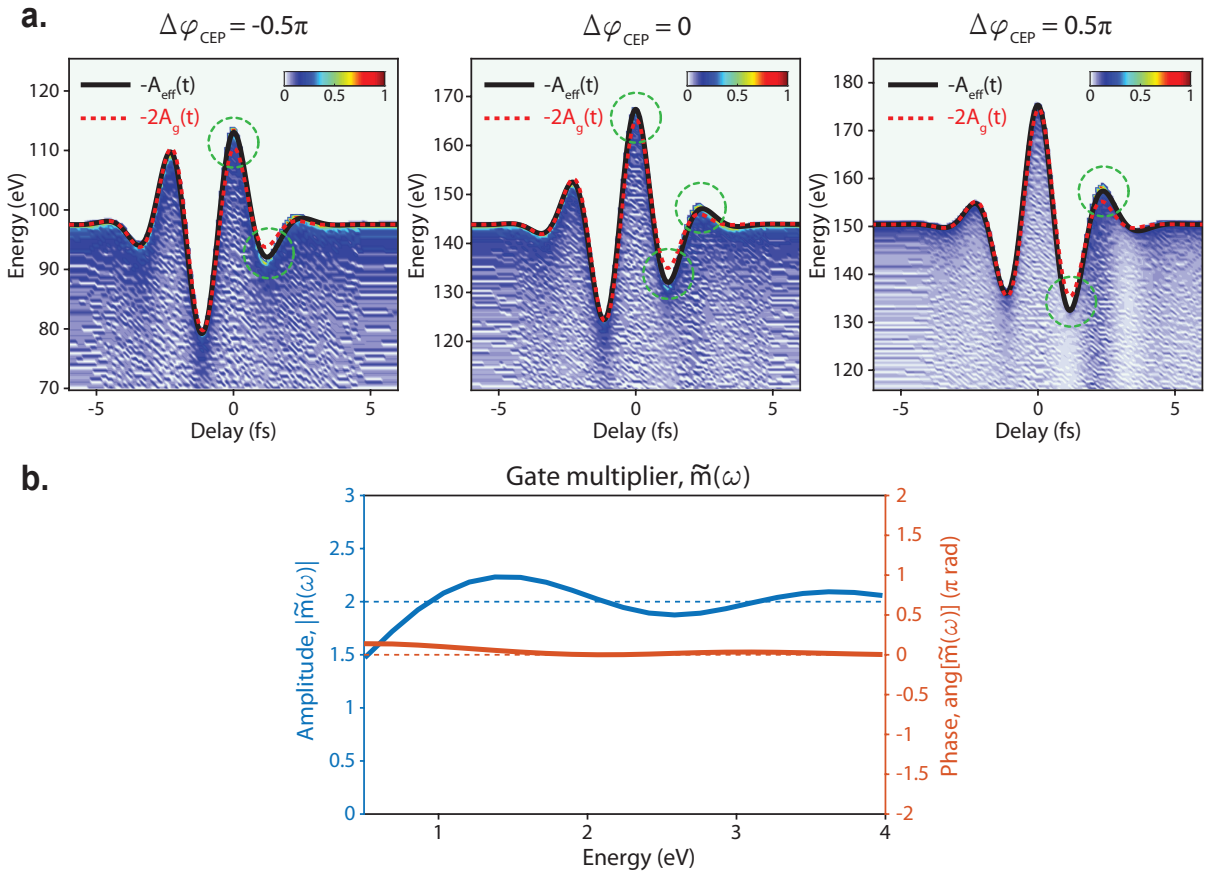

Figure 4.3: **The effective vector potential for the phase gate of HAS. a**, A semiclassically simulated HAS spectrogram. The black curve displays the effective HAS gate vector potential calculated by Eq. 4.23, and the red dashed curve shows the double of the incident vector potential $2A_g(t)$ for comparison. The green dashed circles mark a notable discrepancy between the incident and effective HAS vector potentials. **b**, The spectral amplitude and phase of the gate multiplier $\tilde{m}(\omega)$ are shown in red and blue curves, respectively.

Chapter 5

Measurement of attosecond electron pulses in the optical field emission

Ein Nachmittag im Labor kann leicht eine Woche in der Bibliothek ersparen.
-Hartmut Schröder

The Homochromic attosecond streaking (HAS) methodology introduced in the previous chapter holds promise for applications aiming at the measurement of strong field generated electron pulses from nanostructured metals. In this chapter, I will present the experimental implementation of the HAS technique and will discuss the retrieved temporal characteristics of these pulses.

5.1 Experiments using the Homochromic Attosecond Streaking technique (HAS)

5.1.1 Experimental implementation of HAS

The experimental implementation of HAS bears obvious analogies to ordinary EUV attosecond streaking with the difference that the photoemission by an attosecond EUV is replaced by that by an intense field (Fig. 5.1). Single-cycle electric pulses delivered from the light field synthesizer at a central energy of 1.8 eV (red-colored laser beam in Fig. 5.1) were reflected off a nickel coated, dual concave mirror assembly. The incident laser pulse is spatially divided into a strong inner and a weak outer beam (inset in Fig. 5.1). The inner and outer beams play the role of the pump and gate fields, respectively as introduced in the previous chapter. In other words, the pulse carried by the strong inner optical beam generates and drives electron bursts, while the pulse of the weak outer beam gently perturbs their phase. The inner mirror is attached onto a piezo-electric transitional stage to manipulate the time delay with respect to the outer beam with attosecond precision. Both optical beams were focused onto the sharp tungsten nanotip. The nanotip is oriented

along the laser polarization direction and points towards the entrance of the time-of-flight spectrometer. Just as in the experiments described in Chapter 3, the electric grounding of the nanotip rapidly eliminated charges between consecutive pulses and thereby identical electro-static conditions were ensured for each laser shot. Poorly grounded nanotips give rise to charge accumulation on the tip which results in energy shifts of the recorded photoelectron spectra. The time-of-flight electron spectrometer (TOF) was used once again, to record photoelectron spectra as a function of the time delay between the pump and gate pulses.

An essential first step in the path of utilizing the principles introduced in the previous chapter is an experimental benchmarking of their validity. This is especially important in the case that approximations are taken to simplify the mathematical formulation of these principles. A potential way to do so is to contrast findings in HAS with the ones acquired by an already established technique.

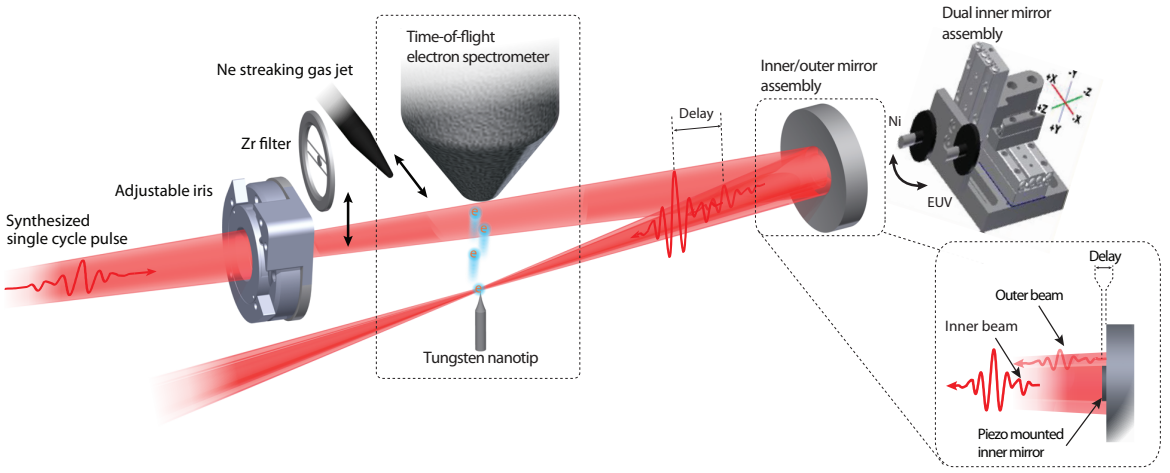

Figure 5.1: **Experimental setup for Homochromic Attosecond Streaking (HAS).** The strong pump and weak gate optical fields were spatially divided by a nickel-coated inner/outer concave (f=12.5 cm) mirror assembly (inset). For the implementation of HAS, the intense inner beam serves as a pump which generates and drives the electron from metallic nanotip, while the outer plays a role of a gate which alters the electron energy distribution. A time delay between the pump and gate pulses was introduced by a piezo controlled inner mirror. The dual inner mirror assembly provides the possibility to swap between a Ni-coated and EUV multilayer inner mirrors. By controlling the motorized iris, the strength of the gate pulse can be adjusted. The Zr-foil and the Ne gas jet are inserted for the EUV attosecond streaking measurements.

5.1.2 The phase gate of HAS and benchmarking with EUV attosecond streaking

The theoretical study in the previous chapter has suggested that the energy variation of the photoelectron imprinted in a HAS spectrogram is directly associated with the effective HAS vector potential which is explicitly related to the incident weak gate vector potential in the spectral domain as:

$$\tilde{A}_{eff}(\omega) = \tilde{A}_g(\omega) \underbrace{\left[2 - \frac{i}{\omega|\Delta t|}(e^{i\omega\Delta t} - 1)\right]}_{\equiv\tilde{m}(\omega)} \tag{5.1}$$

This relation suggests that the characterization of the effective HAS vector potential also allows the measurement of the real vector potential of the incident gate near-field. As a first step, a HAS measurement was performed with a pump pulse of a peak intensity of ~ 25 TW/cm^2. The cutoff energy of the electron spectrum reached approximately 140 eV. A weak gate whose intensity was $\sim 6.3 \times 10^{-3}$ lower than that of the pump pulse was used. The HAS spectrogram was recorded as a function of the time delay between pump and gate (Fig. 5.2 a).

The effective HAS vector potential $A_{eff}^{(raw)}(t)$ can be directly extracted by the cutoff energy variation (red dashed curves in Fig. 5.2 a and b). The gate multiplier $\tilde{m}(\omega)$ is an evaluable function under the assumption of the effective excursion time of $\sim$ 0.85T, where T the centroid optical period of the driving pulse as discussed in the section 4.2.2. The spectral amplitude of the incident gate vector potential $\tilde{A}_g(\omega)$ can be obtained by multiplication of the inverse of the gate multiplier $\tilde{m}(\omega)^{-1}$ (Fig. 5.2 c) to the effective HAS vector potential in the Fourier space (Fig. 5.2 d.), $\tilde{A}_g(\omega) = \tilde{A}_{eff}(\omega)\tilde{m}(\omega)^{-1}$. In the Fourier analysis, zero-padding was used for interpolation of the intermediate points within the measured time delay points, keeping the spectral and its corresponding temporal properties of the waveform intact. Moreover, since the bandwidth of the laser pulse used in the experiment is a-priori known, the frequency components outside this bandwidth, which are primarily the result of experimental noise, can be safely filtered out by applying a hyper-Gaussian filter (grey dashed curve in Fig 5.2 d). The noise filtered effective HAS $A_{eff}(t)$ and the incident gate $A_g(t)$ vector potential are shown as red and blue solid curves in Fig. 5.2 b, respectively.

In order to set the theoretical framework of HAS on a firm ground, an experimental verification of the above conclusions is needed. Since EUV attosecond streaking is an established technique for directly accessing the vector potential of a laser pulse [119], a benchmarking of HAS with the EUV attosecond streaking can straightly verify (or disprove) its validity. For the implementation of the EUV attosecond streaking the nickel inner mirror was replaced by an EUV multilayer inner mirror of the same focal length.

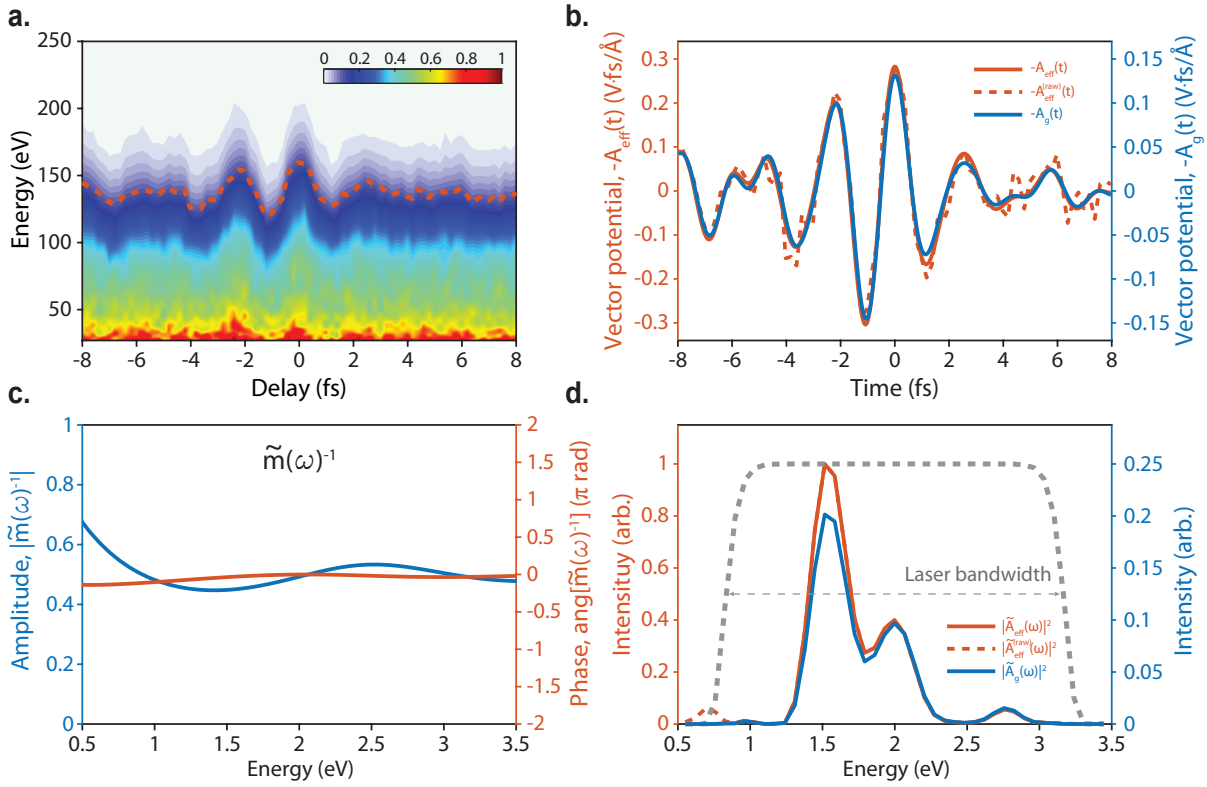

Figure 5.2: **HAS spectrogram and phase gate. a**, HAS measurement performed under the incidence of a strong optical pump and a weak gate pulse. The peak intensity of the pump pulse was ~ 25 TW/cm^2, and a gate/pump intensity ratio of $\sim 6.3 \times 10^{-3}$ was used. The evaluated cutoff energy variation is plotted as a red dashed curve. **b**, The red dashed, and solid curves display the effective HAS vector potential that was directly sampled from the spectrogram $A_{eff}^{(raw)}(t)$ and the Fourier-analyzed one $A_{eff}(t)$, respectively. The blue curve shows the retrieved vector potential of the incident gate near-field $A_g(t)$. **c**, The inverse of the gate multiplier ($\tilde{m}(\omega)^{-1}$) was evaluated with an excursion time of 0.85 driving field period. **d**, The spectral amplitude of the incident gate vector potential was evaluated by multiplication of the inverse of the gate multiplier, *i.e.*, $\tilde{A}_g(\omega) = \tilde{A}_{eff}(\omega)\tilde{m}(\omega)^{-1}$. Blue and red curves show the spectral intensity of the effective HAS, $|\tilde{A}_{eff}(\omega)|^2$ and incident gate, $|\tilde{A}_g(\omega)|^2$ vector potentials, respectively. To suppress the noise, a hyper-Gaussian Fourier filter in the spectral area of laser bandwidth (grey dashed curve) was used.

The process of the mirror replacement is completely automatized in this setup. In practice, two inner mirrors, a Ni-coated and an EUV multilayer, are attached onto a 3D Piezo-electric transitional stage, and on experimental demand they can be instantly swapped on site without any further modification of the experimental setup (Fig. 5.1). In both measurements, the focal spot of the gate pulse was recorded by an 1-to-4 imaging system. This allows one to accurately obtain the relative ratio of the gate pulse-intensities used in HAS and EUV attosecond streaking measurements. The EUV attosecond streaking was consecutively performed after the completion of the HAS measurement (left Fig. 5.3 a) under the identical experimental conditions (middle Fig. 5.3 a). The vector potential waveforms evaluated by the two techniques are compared in Fig. 5.3 a (right).

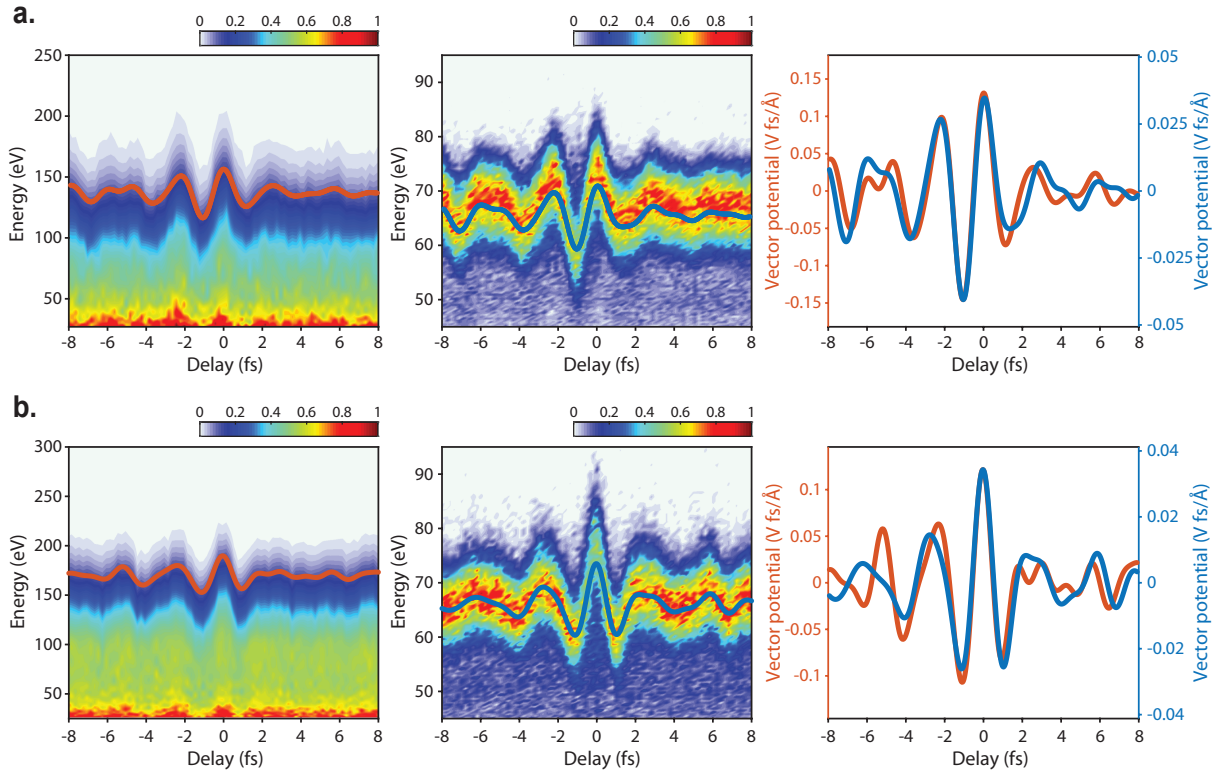

Figure 5.3: **Comparison between HAS and EUV attosecond streaking.** **a**, HAS spectrogram recorded using a single-cycle, optical pump pulse of a peak intensity of $\sim$ 25 TW/cm^2 and a weak gate pulse whose intensity is $\sim 6.3 \times 10^{-3}$ times that of the pump (left). The EUV attosecond streaking measurement of the field waveform was consecutively conducted under the identical conditions (middle). The right panel displays the comparison of waveforms evaluated from the cutoff energy variation in the HAS spectrogram (red curve) and EUV attosecond streaking (blue curve). **b**, A second experiment for a different driving pulse waveform at an incident peak intensity of $\sim$ 31 TW/cm^2, and gate/pump ratio of $\sim 3.6 \times 10^{-3}$. Adapted from ref. [127]

A potential metric to evaluate how close two waveforms are, is the degree of similarity which can be defined as the normalized cross-correlation among the two waveforms as:

$$S = \frac{1}{\sqrt{N}}(f \star g)(\tau) = \frac{1}{\sqrt{N}} \int_{-\infty}^{\infty} dt f(t) g(t+\tau) \tag{5.2}$$

where N is the normalization factor, $N = [(f \star f)(0) \times (g \star g)(0)]$. A perfect similarity (identical waveforms) corresponds to a normalized cross correlation of 1. By comparing the waveforms retrieved from HAS and EUV attosecond streaking, a value of $S \sim 0.95$ was obtained. A second set of measurements based on a different waveform is shown in Fig. 5.3 b. In this set the pump pulse intensity was ~ 31 TW/cm^2, and the gate/pump intensity ratio was $\sim 3.6 \times 10^{-3}$. Once again, a good degree of similarity for the waveforms of $S \sim 0.93$ was obtained. The study in this section, therefore, offers first concrete experimental evidence that the cutoff energy variation in a HAS spectrogram is directly associated to vector potential of the gate pulse as discussed in the theoretical foundations of HAS in the previous chapter. This fact suggests the feasibility of a direct and complete characterization of the near-field of the light pulse. Furthermore, the precise measurement of the field enhancement factor is also possible by evaluating the ratio between the retrieved and the incident amplitudes of the gate pulse. A detailed discussion on this aspect of HAS is given in section 5.2.

5.1.3 Effect of the gate field strength on a HAS spectrogram: identifying safe limits

HAS assumes that the gate pulse is weak such as to be considered a pure phase gate on the released electron pulse waveform. The previous section showed that this notion is supported by the experiments under the stated conditions. However, one can raise the question: how can we identify a safe limit for which this assumption is correct in various systems? One way to do so is theoretically. Yet this is only possible, if the ionization mechanisms are well understood, which is not really the case for metals under intense laser fields. Alternatively, a potential collapse of the pure phase gate assumption under a high gate intensity can be experimentally investigated by the direct comparison of the gate waveforms extracted from HAS and EUV attosecond streaking for various field strengths of the gate. This is the aim of the study described in this section.

Fig. 5.4 displays HAS spectrograms measured at four different gate/pump pulse intensity ratios ranging from $\sim 4.5 \times 10^{-3}$ to $\sim 1.4 \times 10^{-1}$. A first observation on these plots is that the contrast of the amplitude variation along the time delay axis increases with the gate intensity. This observation suggests that an intense gate pulse significantly affects the ionization processes.

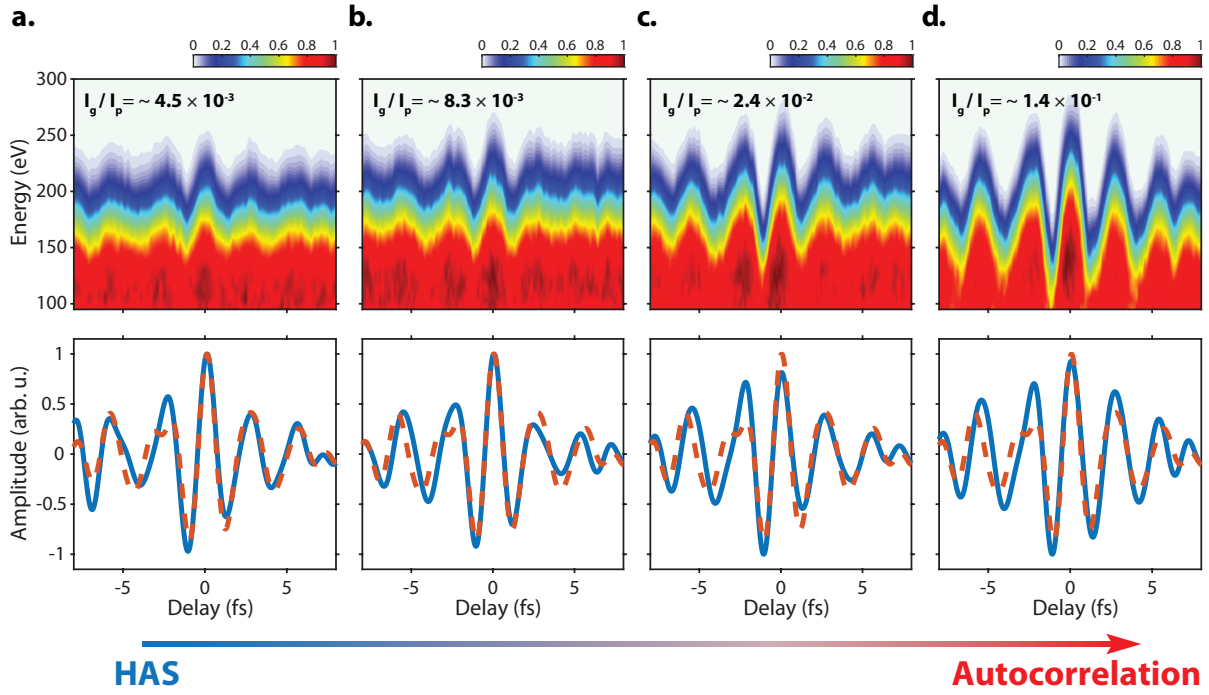

Figure 5.4: **Exploring the working range of HAS.** HAS spectrograms recorded for different ratios of gate/pulse intensity, 4.5×10^{-3} (**a**), 8.3×10^{-3} (**b**), 2.4×10^{-2} (**c**), and 1.4×10^{-1} (**d**). Bottom panels display the comparisons of gate pulse waveforms retrieved from HAS (blue solid curves) and EUV attosecond streaking measurement (red dashed curves). Adapted from ref. [127]

To take a more detailed look at the effects of a strong gate on the electron dynamics and the deviation from the perfect phase gate, we compared the vector potential evaluated from the HAS spectrogram of Fig. 5.4 with that of the waveform characterized by the EUV attosecond streaking measurements. At a low gate/pump intensity ratio, $< 10^{-2}$, the vector potential evaluated in HAS (blue curves in bottom panels of Fig. 5.4 a and b) is in good agreement with that evaluated from EUV attosecond streaking (red dashed curve). In contrast, for higher gate/pump ratios the disagreement between the two is gradually increasing (bottom panels of Fig. 5.4 c and d). This observation indicates that an increasing ratio of gate/pump drives a HAS spectrogram towards ordinary, spectrally resolved, autocorrelation of the two pulses. This set of experiments therefore offers a guidance for identifying the appropriate gate/pulse ratio in experiments. The results of Fig. 5.4 suggest us that HAS measurements should be performed at a gate/pump ratio lower than 10^{-2}.

5.1.4 Relative timing of pump and gate pulses in HAS measurements

Not only in HAS, but also in conventional EUV-based attosecond streaking as well as in other ultrafast measurement techniques that are based on pump-probe schemes, a spectrogram is recorded on a time delay axis between the two pulses. This delay axis is arbitrarily defined in the experiment. Of course, the absolute zero-delay between two waveforms can be defined only if they are identical. Pump and gate pulses used in HAS are indeed identical in terms of the details of the waveforms, because they are spatially divided from the same pulse beam.

Identifying the absolute delay between the pump and the gate pulses is important in HAS. This is because the determination of an absolute time axis allows one to clock the emission of photoelectrons under the waveform of the pump field. In other words, it can allow us to say at which moment of time under the pump field waveform the electron pulse is formed. This is also useful because the vector potential at the time of release determines the momentum accumulation of the released electron following the back-scattering instance. Therefore, it plays a vital role for accessing the temporal properties of the electron pulse at the back-scattering. One way to identify the absolute delay between pump and gate pulses is by utilizing a nonlinear autocorrelation scheme with pump and gate pulses of commensurate peak intensities. However, at the zero-delay of an autocorrelation scheme, the peak intensity resulting from the coherent superposition of two pulses can easily exceed the damage threshold of the metallic specimen, and the damage can prevent subsequent HAS measurements under identical experimental conditions.

Nonetheless, also in a HAS spectrogram itself it is possible to identify the zero-delay of pump and gate pulses. This is because, despite the large contrast in pump and gate pulse intensities, a weak variation of the total photoelectron yield versus time delay will inevitably be present, and this is sufficient to identify the absolute timing between two pulses with reasonable accuracy.

In a HAS spectrogram the variation of the total electron yield can be evaluated by the spectral integration over the photoelectrons energy (Fig. 5.5). The delay offset which represents the zero-delay on the experimental delay axis can now be identified as the delay point at which the electron yield undergoes the maximum variation (red dashed line in Fig. 5.5).

One may think that the accuracy of timing here is dictated by the step size of the delay used in the experiment $\sim$ 200 as. Yet, the data of Fig. 5.5 does not represent a single point measurement but an ensemble of different delay points. To take all measurements into account one needs to switch to the Fourier domain, since the Fourier components of the electron yield variation emerges from all sampled points in the time delay. In the Fourier analysis, the zero-padding method at a size factor of 100 was used to determine the delay offset value with an accuracy better than $\sim$ 2 as (inset in Fig. 5.5).

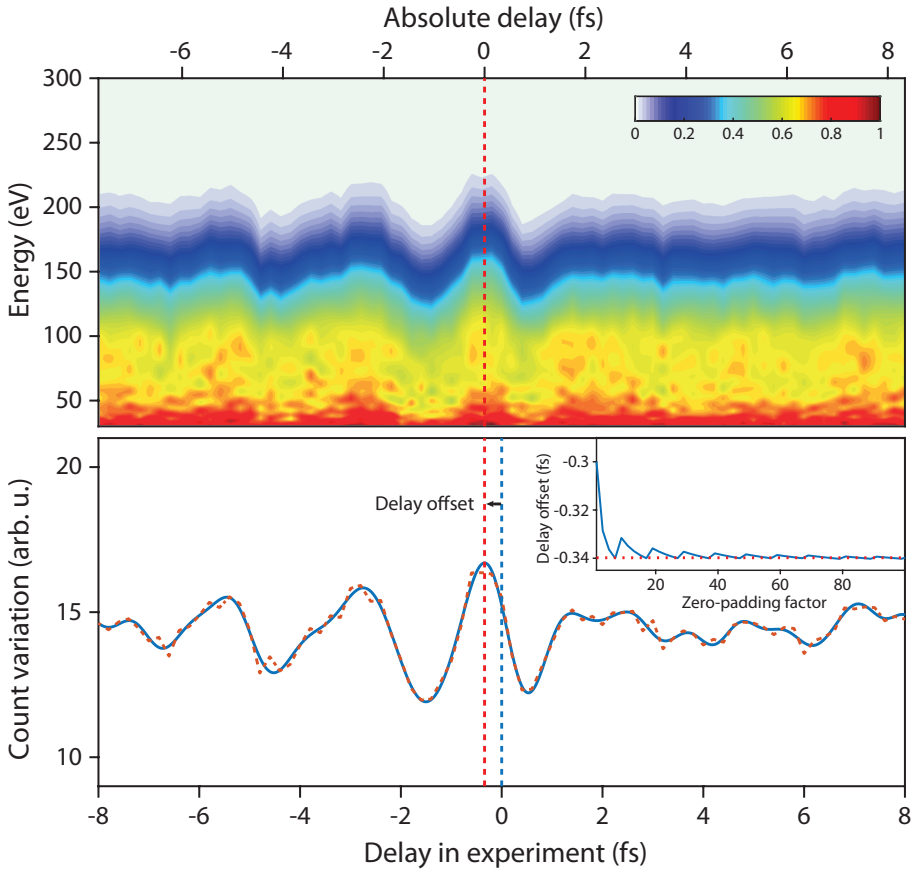

Figure 5.5: **Absolute timing between pump and gate pulses.** A measured HAS spectrogram (top) and the total electron yield variation versus time delay between pump and gate (bottom). The red-dashed curve indicates the directly sampled electron yield variation, while the blue curve denotes the Fourier-analyzed one. The red dashed vertical line marks the delay at which the maximum count variation occurs and which indicates the absolute zero-delay point on the experimental delay axis, while the blue dashed vertical line denotes the zero of the experimental delay axis. The inset in the bottom panel displays the delay offset evaluation as increasing the zero-padding size factor in the Fourier analysis. The red horizontal dashed line marks the converged value of the delay offset.

5.2 Measurements of optical near-fields

5.2.1 Measurement of near-field using a HAS spectrogram

Based on the experimental verification presented in the previous section, the trace of the cutoff energy variation in a HAS spectrogram provides a way to measure the vector potential of the near-field of the gate pulse (blue curve in Fig. 5.6 a). The complete characterization of the gate near-field can be obtained by the time derivative of the vector

potential, $E_g(t) = -dA_g(t)/dt$. Equivalently in the Fourier space, the spectral amplitude of the near-field can be evaluated as $\tilde{E}_g(\omega) = -i\omega\tilde{A}_g(\omega)$ as shown in Fig. 5.6 b.

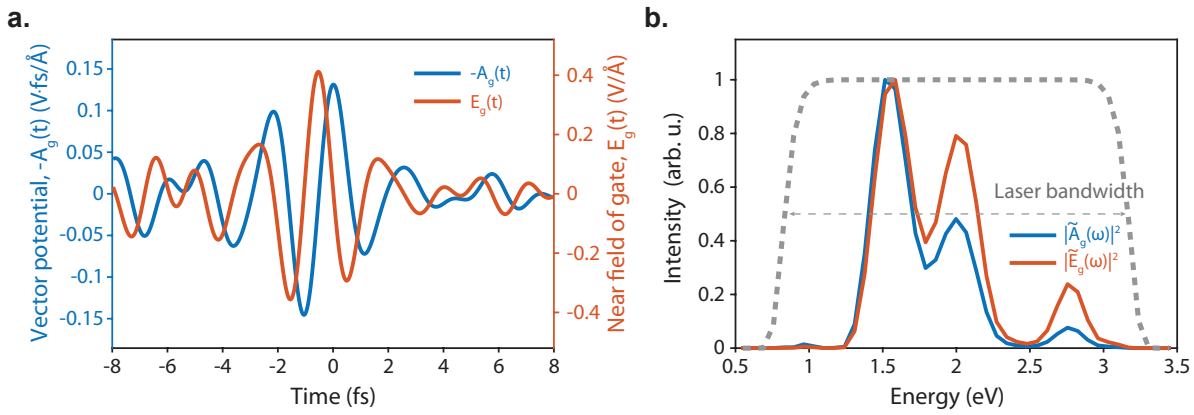

Figure 5.6: **Near-field measurement based on the vector potential of the gate pulse. a**, The near-field of the gate pulse (red curve) was evaluated as the time derivative of the gate vector potential (blue curve) extracted from the HAS spectrogram, $E_g(t) = -dA_g(t)/dt$. **b**, Spectral intensity of the near-field and vector potential are shown in red and blue curves, respectively.

Field enhancement factor

The direct comparison of the retrieved near-field by HAS to the incident field characterized by the EUV attosecond streaking provides a precise way to measure the field enhancement factor in the vicinity of the tungsten nano-tip used in our experiment.

Note that a higher gate strength was used for the EUV attosecond streaking measurement compared to HAS in order to sample the waveform in the gas target accurately. The incident gate field strength for HAS was evaluated by scaling of intensity ratio measured in the focal images of the optical gates used in both measurements. The peak field ratio obtained is 3.74 ± 0.25 as shown in Fig. 5.7. In our study, we have obtained a field enhancement factor in the range from 3.46 to 3.76. The deviation of the measured field enhancement factor and the discrepancy with the theoretically calculated value of ~ 3.82 can be attributed to the geometry of the nano-tip, which is difficult to be precisely controlled in manufacturing.

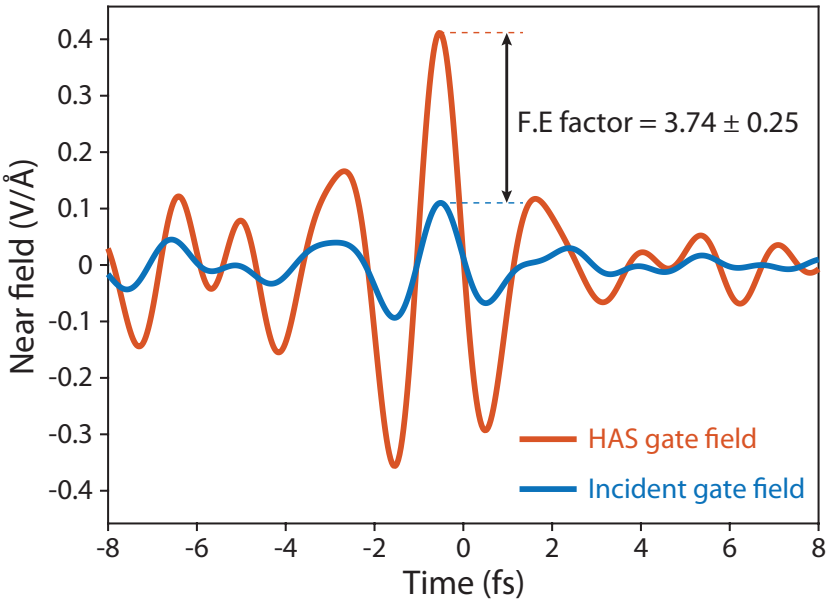

Figure 5.7: **Measurement of the field enhancement factor.** The enhanced near-field of the gate pulse (red curve) was retrieved from the HAS spectrogram (fig. 5.2 a). The blue curve shows the incident gate field characterized by the EUV attosecond streaking. The ratio of peak field strengths between the two waveforms allows the evaluation of the field enhancement factor of 3.74 ± 0.25.

Near-field strength of the pump pulse and the cutoff law

The electron cutoff energy is linearly related to the incident intensity of the pump pulse. However, the so-called $10U_p$ law is difficult to be verified without precise knowledge of the pump near-field enhanced by the nanostructure. Yet, the near-field of the gate is a measurable quantity by the method discussed in the previous sections, and one can also obtain the intensity ratio between the pump and gate by comparing their peak intensities by analyzing their focal images. In this way, one can finally gain access into the absolute strength of pump near-field in a HAS measurement.

Once HAS is verified as an accurate method, the ratio of the pump and gate fields can also be evaluated directly by the data of the HAS spectrogram without the need of additional experimental data. Since the pump (E_p) and gate (E_g) fields have identical waveforms but differ only in their strength (with a relative ratio, $E_g/E_p = 1/r$), at the zero-time delay in the HAS spectrogram the spectrum can be considered as a result of a single pump field whose intensity is multiplied by $(1+1/r)^2$. Based on the zero-delay identification method discussed earlier, the spectrum of the zero-delay can be easily identified in a HAS spectrogram. In turn, it can be compared with the gate-free spectrum. Owing to the linear relationship between the cutoff energy and the intensity, the cutoff energy difference

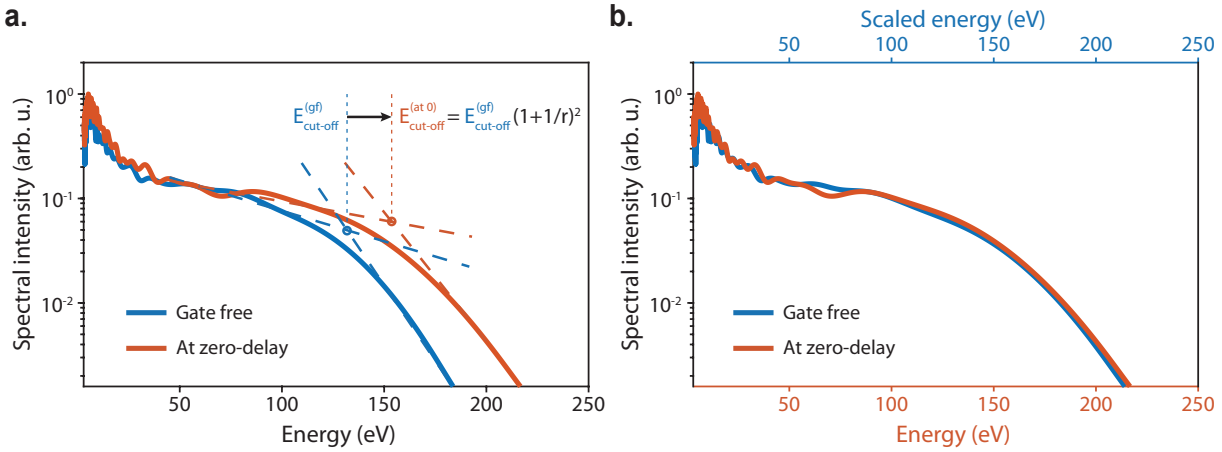

Figure 5.8: **HAS photoelectron spectra at zero-delay with and without gate field.** **a**, The gate-free and at-zero photoelectron spectra in HAS shown in fig. 5.2 a. The vertical lines indicate the cutoff energy evaluated in both cases. **b**, The spectrum at zero-delay (red curve) is superimposed with the gate-free spectrum mapped in an energy axis scaled by $(1 + 1/r)^2$ (blue curve).

between gate-free and at-zero-delay spectra directly offers the relative ratio of gate and pump field (Fig. 5.8 a). Similarly, it can also be verified by the excellent agreement of the zero-delay spectrum with the gate-free spectrum mapped on an energy axis scaled by a factor of $(1 + 1/r)^2$ (Fig. 5.8 b). These findings suggest that HAS can serve as a stand-alone metrology to characterize both pump and gate fields. Accurate knowledge of the enhanced near-field of the pump pulse allows the evaluation of the multiplication factor for the electron cutoff energy. The multiplication factor $E_{cutoff}/U_p^{(enh)}$ was evaluated to be 10.13 ± 0.22 and agrees well with the classical estimation in the single-electron approximation. It also reflects that multi-electron effects which could influence the energy scaling are negligible in this study.

5.2.2 Carrier-envelope phase (CEP) effects on HAS spectrograms

Up to this point we have seen that HAS is a field-sensitive technique which allows the complete characterization of the gate field waveform. In other words, we anticipate that a variation of field waveform, for instance, through a carrier-envelope phase (CEP) change should be clearly imprinted in a HAS spectrogram. In order to experimentally explore if this is indeed the case, HAS measurements were performed for three different CEP settings of the driving field as shown in Fig. 5.9.

At each CEP setting, the cutoff energy variation versus the delay (white curves in top panels), which is associated with the vector potential of the gate field as well as the corresponding retrieved near-field (red curves in bottom panels) exhibits a significant phase variation of their waveform under the envelope (red dashed curve). To better visualize the

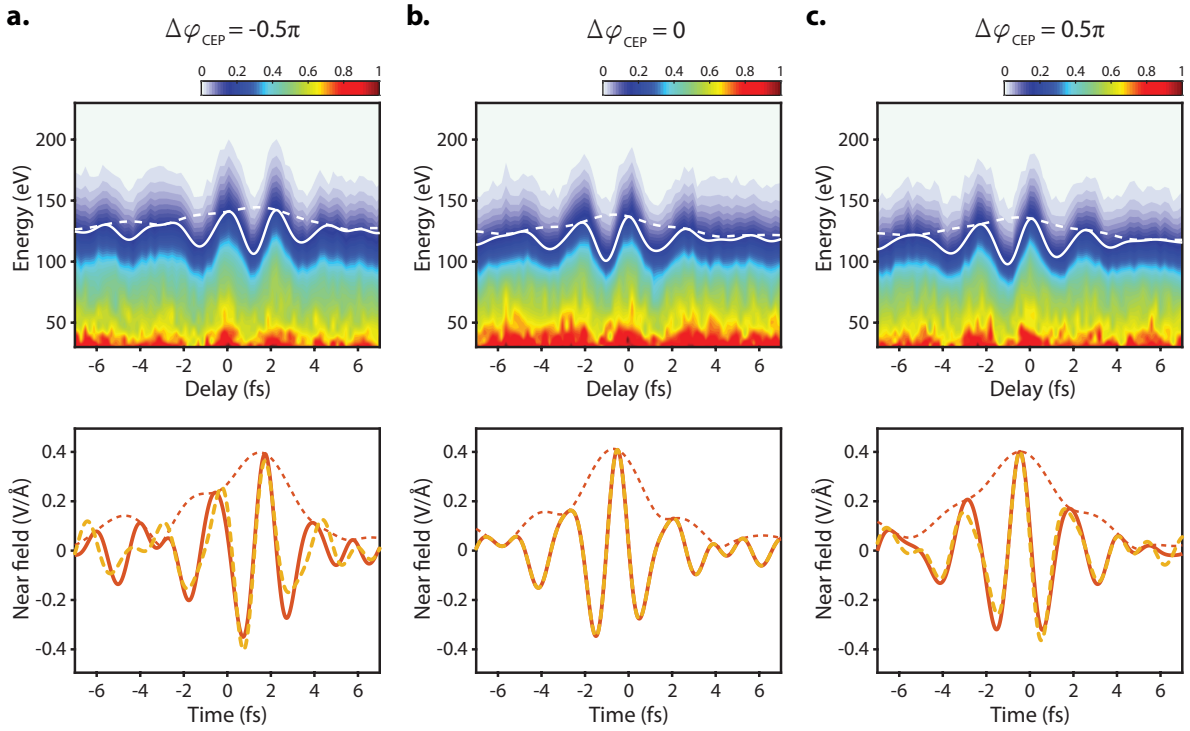

Figure 5.9: **Homochromic attosecond streaking at various CEPs.** HAS spectrograms recorded at three different CEP settings of the driving pulse, -0.5π (**a**), 0 (**b**) and 0.5π (**c**), respectively. The white solid lines superimposed on the spectrogram denote the extracted vector potential from the cutoff energy trace (top). The near-fields retrieved by the temporal-derivative of the vector potential are shown in red solid curves (bottom). The yellow dashed curves display the waveforms calculated (anticipated) via a CEP variation of the waveform of the shown in panel b.

fact that the experimentally retrieved gate waveforms are indeed compatible with the corresponding CEP variation, the predicted waveforms were calculated by the addition of a relative phase to the waveform extracted in panel b ($\Delta\varphi_{CEP} = 0$) and compared with the individual case, as shown in bottom panels of Fig. 5.9. The comparison shows an excellent matching between the experimentally measured (red solid) and calculated (yellow dashed) waveforms, and hence, once again verifies the field sensitivity of the HAS technique and its capacity to attain complete characterization of near-fields. Notably, one can observe a delay-shift in the spectrogram at different CEPs. For example, the HAS spectrogram at -0.5π (Fig. 5.9 a) is delay-shifted compared to the case of 0 (Fig. 5.9 b). This can be attributed to the fact that the generation of the highest energetic photoelectrons is one-cycle shifted in time due the variation of the CEP.

5.3 Temporal characteristics of photoemission revealed in a HAS spectrogram

The complete characterization of the near-fields of pump and gate pulses, including the waveform and its amplitude provides the complete information required to perform a faithful simulation of the dynamics. A theoretical simulation on HAS can offer a better understanding of the temporal properties of electron kinematics via the direct comparison between experimental and theoretical spectrograms. Utilizing the semiclassical three-step model as described in the previous chapter, a simulation of a HAS spectrogram was conducted and compared with the experimental result as shown in Fig. 5.10. To mimic the experimental conditions other than the field waveform, the parameters were used as close as possible to the experimental: work-function of 4.55 eV for polycrystalline tungsten, apex radius of 35 nm. The spatial field distribution was modeled as Eq. 3.1. For the ionization, the Fowler-Nordheim equation (Eq. 1.4) was used to weight individual trajectories for composing an electron spectrum.

One can notice that the modulation of the cutoff energy versus delay in the simulated spectrogram excellently matches the effective HAS vector potential (black dashed curves in Fig. 5.10 b). This fact, once again, is in support of the theoretical description of the phase gate introduced in Eq. 4.14. It is also discernible that the simulated cutoff energy is in good agreement with that in the recorded HAS spectrogram, reflecting that the method of the near-field evaluation is accurate. Furthermore, one can observe that the same cutoff modulation timing with respect to the zero-delay in both simulation and experiment. It supports the identifying method of the zero-delay, since the theoretical simulation provides absolute relative timing of streaking traces without any assumption.

The HAS spectrogram offers direct information on the time-structure of the photoemission. Based on the comparison between experiment and theory, we can conclude that the highest cutoff energy trace is isolated within the energy from ~ 60 to ~ 140 eV, whereas the lower energy region below 50 eV consists of two major contributions: one from direct electron released around t =0.3 fs (green in Fig. 5.10 c) and another from back-scattered electron released around t =2.5 fs (purple Fig. 5.10 c). Both the electron bursts overlap spectrally, and thus the spectrogram in the low energy can be seen as a hybridized trace with two different timings (purple and green dashed curves in Fig. 5.10 b). Therefore, the waveform evaluated from the low energy cutoff trace does not match that from the highest energy cutoff trace as well as that characterized by EUV attosecond streaking. There is one more electron burst anticipated by the simulation in the intermediate energy range around ~ 60 eV. However, its amplitude is negligibly small, ~ 2 orders of magnitude lower than the other electron bursts, because the ionization yield at the leading half-cycle of the pump pulse is low. Therefore, it does not notably contribute to the spectrum and dynamics imprinted in the HAS spectrogram.

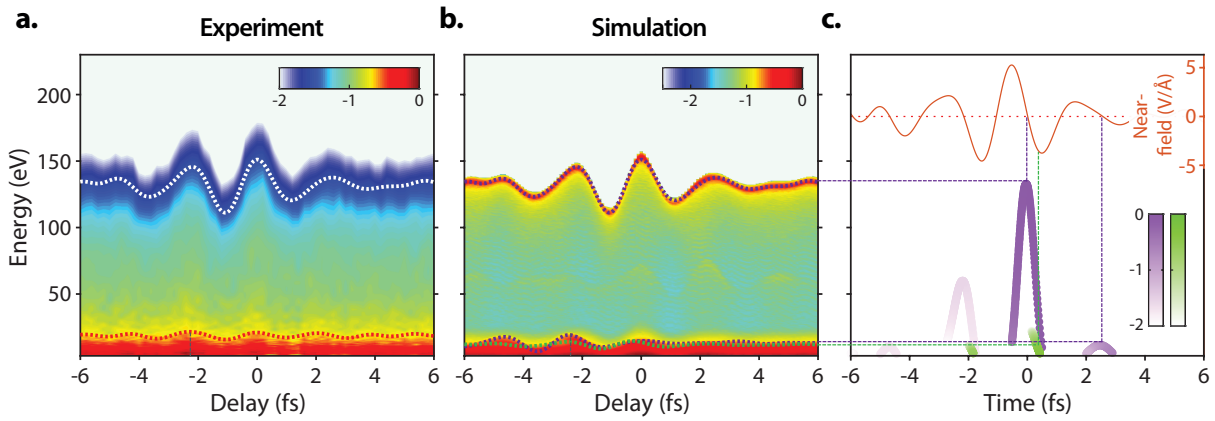

Figure 5.10: **Comparison between experimental and simulated HAS spectrograms. a** and **b**, HAS spectrogram measured (a) and simulated semiclassically (b) under the pump and gate pulses of the experiments. The white and black dashed curves superimposed on the spectrograms are effective HAS vector potential $A_{eff}(t)$. **c**, The gate-free terminal energy was calculated with the experimental pump field (red curves) and is plotted on the back-scattering time. The color code of the curves represents the ionization probability (in logarithmic scale) as calculated by the Fowler-Nordheim equation. The purple and green colors indicate back-scattered and direct electrons, respectively. Adapted from ref. [127].

5.4 Attosecond measurement of strong-field emitted photoelectron pulses

The HAS spectrogram embodies both the temporal and spectral properties of back-scattered electron pulse. As suggested in the analytical description in Chapter 4, these characteristics can now become accessible by a reconstruction of a HAS spectrogram with precisely retrieved gate and pump fields and the timing between the pump pulse and terminal electron pulse. In this section, the reconstruction strategy will be presented step by step and at the end of the chapter, the retrieved characteristics of the back-scattered electron pulse will be evaluated.

5.4.1 A quick comparison between HAS and EUV attosecond streaking spectrogram

Like other techniques that are based on frequency resolved gating methods, a reconstruction algorithm is essential to retrieve the spectral and temporal properties of the electron pulse from a HAS spectrogram. Although a HAS spectrogram has the form of a frequency resolved optical gating (FROG) trace, there are a few aspects in which hinder the direct

application of conventional FROG reconstruction algorithms such as PCGPA [123, 124], LSGPA [125]. To address the reconstruction of the spectrogram of the new technique and relevant algorithms, first I stress the differences between HAS and the conventional streaking technique.

1. **Incompleteness of spectral isolation.** In contrasts to an EUV attosecond streaking spectrogram, an isolated spectrum of low and high energies is not present in a HAS spectrogram. We cannot filter a part of the photoelectrons to characterize them as we do in EUV streaking with ordinary thin metal foils. Therefore, one has to find ways to accurately reconstruct specific energy ranges of the HAS spectrogram.

2. **Coexistence of pump and gate fields after the back-scattering event of the electron wavepacket.** In the HAS measurement, both pump and gate fields are acting on the back-scattered electron wavepacket. This is different from the ordinary EUV attosecond streaking, where only the gate is acting on the electrons liberated by EUV. Therefore, a separation of the roles of the two fields is needed.

Reconstruction strategy

The complete characterization of the pump and gate pulses based only on the cutoff energy variation analysis and the absolute timing from total yield variation dramatically reduce the number of free variables for a HAS spectrogram reconstruction. In other words, the gate is known in advance, and this simplifies the reconstruction problem to finding only the properties of the electron pulse. The spectral amplitude of the terminal electron can be directly obtained by the gate-free spectrum. This implies that the reconstruction of the terminal electron wavepacket requires only the retrieval of the spectral phase rather than both amplitude and phase. This fact leads us to consider a reconstruction of the terminal electron pulse as the first step towards the retrieval of the back-scattered electron pulse. The contribution of pump pulse to the photoelectron spectrum after the back-scattering event is already part of the terminal electron wavepacket as described in Eq. 4.19. Hence, only the gate will be needed for the reconstruction of the spectrogram. This fact allows overcoming the "coexistence problem" of the pump and gate pulses. In this stage, one can set a spectral interested area in a HAS spectrogram to address the issue of the spectral isolation. The back-scattered electron is linked by Volkov phase introduced by the pump pulse (Volkov propagation), and the Volkov basis can be constructed with the precisely measured pump pulse on the back-scattering time axis. Therefore, in the next step, we can consider the inverse Volkov propagation of the terminal electron pulse to obtain the back-scattered electron pulse.

5.4.2 Retrieval of the terminal electron pulse in HAS

In this section, the reconstruction of the terminal electron pulse is primarily discussed. At this stage, it is worth to highlight, how a HAS spectrogram directly reveals the presence of chirp of the terminal electron pulse.

Manifestation of atto-chirp of terminal electron pulse in a HAS spectrogram

In the EUV attosecond streaking technique, the atto-chirp is manifested as spectral broadening and narrowing of the spectrum at the time delays, especially when the electron wavepacket is released close to an extreme (maximum or minimum) of the gate field. This bandwidth modulation by the gate field in EUV attosecond streaking is a result of the time-shift of the different spectral components in an isolated spectrum. Differently from the conventional EUV attosecond streaking, the HAS spectrogram has a wide bandwidth and does not exhibit clear spectral isolation. Therefore, the bandwidth variation of electron spectrum is not directly applicable to observe the atto-chirp in HAS. This fact calls upon a new "eye" to examine the atto-chirp. To better understand this with a clear visualization, HAS spectrograms were simulated utilizing Eq. 4.20 with different kinds of dispersion, zero-chirp, GDD of 2×10^3 as^2 and TOD of 5×10^4 as^3 of the terminal electron wavpacket (top panels in Fig. 5.11). As shown in the simulation, the chirp of the terminal electron wavepacket is manifested in a HAS spectrogram as a modulation of the spectral intensity versus delay. In the case of a positive GDD (Fig. 5.11 b), the high energetic component of the spectrogram is linearly shifted to a negative delay (white dashed line). This can be intuitively attributed to the linear group delay among the different energy constituents of the electron wavepacket. The direction of the shift is defined by the sign of chirp, *i.e.*, for a negative GDD the direction of the spectral intensity shift is opposite to that shown in Fig. 5.11 b. In the case of TOD (Fig. 5.11 c), the shift exhibits a quadratic curve which indicates a quadratic group delay in energy (white dashed curve). In order to increase the visibility of such spectral intensity shift in time delay, we can evaluate the differential map $D(E, \tau)$ of the spectrogram $S(E, \tau)$ (bottom panels in Fig. 5.11). The differential map is evaluated by consecutively taking a partial derivative and integration along the time delay (τ) at each energy point (E).

$$D(E, \tau) = \int d\tau \frac{\partial S(E, \tau)}{\partial \tau} \tag{5.3}$$

In such a way, the unmodulated spectrum along with the delay axis is eliminated by the derivative, and only the spectral variation clearly appears in the integration at each energy component of the terminal electron wavepacket. The modulations visible in the differential map are periodic and oscillate with the central frequency of the gate pulse. As in the interferometric methods, the amount of the delay shift in the differential map can be evaluated by tracing the phase of the principal frequency component in the Fourier space along the energy axis. This phase extraction intuitively offers information about the direction and the type of chirp of the terminal electron pulse (white curves in bottom

panels, Fig. 5.11). Although it does not provide a direct evaluation of the chirp of the electron pulse, it vividly offers distinct features of the spectral phase of electron pulse which can be helpful in the final reconstruction.

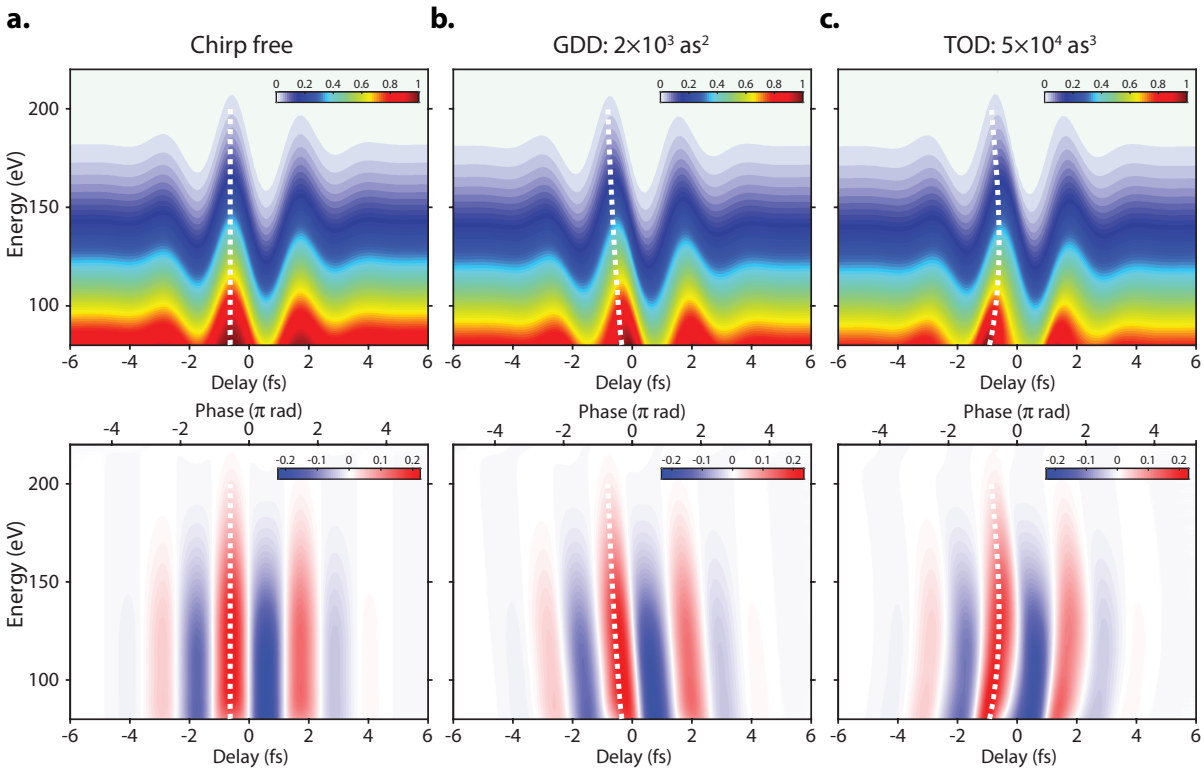

Figure 5.11: **Simulated HAS spectrogram with different chirps of the terminal electron wavepacket.** HAS spectrograms were simulated with a terminal electron wavepacket of atto-chirp, zero-chirp (**a**), GDD of 2×10^3 as^2 (**b**) and TOD of 5×10^4 as^3 (**c**), respectively. Bottom panels display the differential maps derived from the spectrograms shown in the top panels. The phase of the differential map was evaluated by the interferometric method (white dashed curves).

Retrieval of the terminal electron wavepacket

For the reconstruction of the terminal electron wavepacket, we select a part of the gate-free spectrum (HAS-AOI) around the cutoff energy as shown in Fig. 5.12 (marked in red). The bandwidth is chosen such that the lower edge of the back-scattered electron pulse is higher than 20 eV. The purpose to set the lower edge at 20 eV is dictated by future applications of the electron diffraction experiments. However, since the lower edge of the spectrogram in HAS-AOI is in influences of up-streaked electrons at even lower energy, the gate-free spectrum in a wider range (marked in yellow) was used to generate a signal matrix of the

spectrogram in the reconstruction, such that the up-streaked spectral components can be well captured in the HAS-AOI (Fig. 5.12).

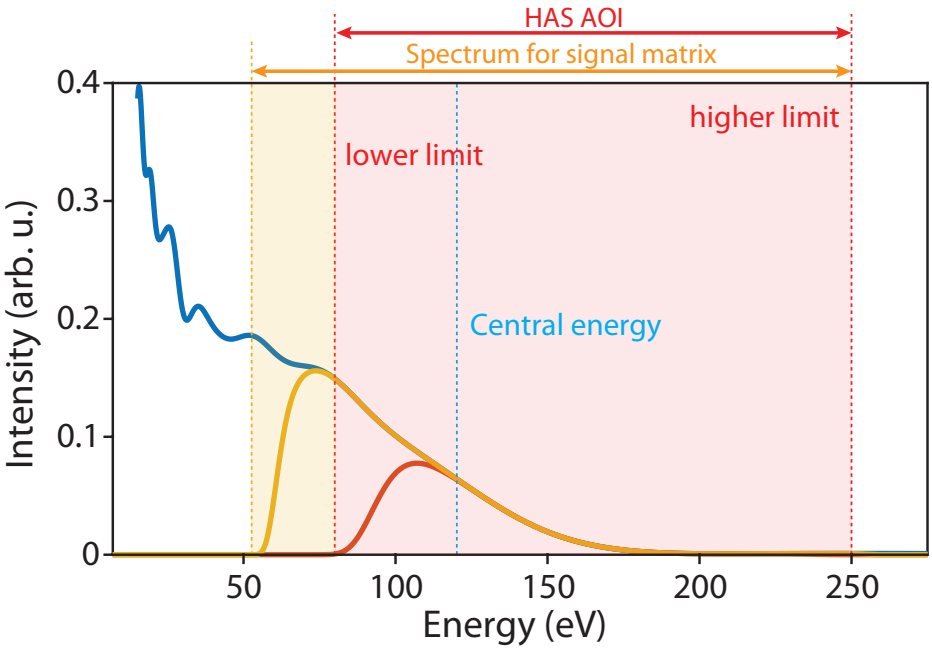

Figure 5.12: **Spectral selection in a HAS reconstruction.** Portion of gate-free spectrum as well as HAS spectrogram selected for the reconstruction is marked by the spectral area of interest (AOI, red colored area). The portion of the spectrogram is selected by a hyper-Gaussian filter covering the AOI. For the signal matrix of the spectrogram, the gate-free spectrum was selected in a wider window than the AOI, such that the up-streaked spectral components can be properly considered in the AOI (yellow colored area).

Since the gate-free spectrum provides the spectral amplitude $|\chi_{tr}^{(AOI)}(\omega)|$, the terminal electron pulse associated with the spectral components in the AOI is given in the energy domain ($\omega = p^2/2$ and $d\omega = pdp$) as:

$$\psi_{tr}^{(AOI)}(t) = \int_{-\infty}^{\infty} d\omega |\chi_{tr}^{(AOI)}(\omega)| e^{-i\varphi(\omega)} e^{i\omega t} \tag{5.4}$$

where $\varphi(\omega)$ is the spectral phase. In this reconstruction problem, the unknown variable is the spectral phase in the bandwidth of the AOI. The phase of the terminal electron wavepacket is important for the reconstruction, because it contains the spectral phase of the back-scattered electron together with the Volkov phase introduced by the pump pulse after the back-scattering moment, as discussed in Chapter 4.

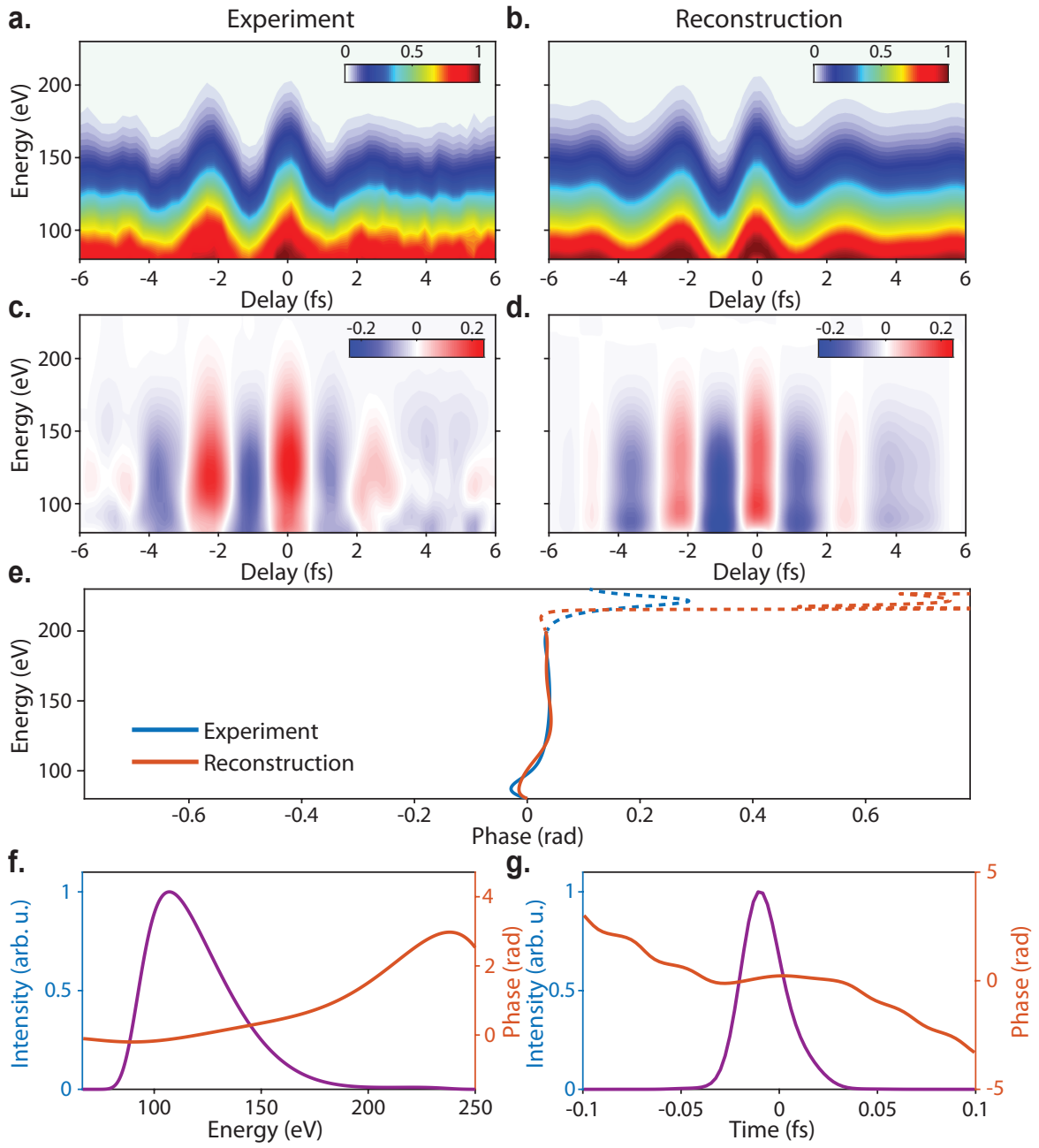

Figure 5.13: **Reconstruction of the terminal electron wavepacket.** **a** and **b**, Measured (a) and reconstructed (b) HAS spectrograms in the spectral area of interest from 80 to 230 eV. **c** and **d**, Differential maps evaluated from the measured (c) and reconstructed (d) spectrograms. **e**, Phase shifts in the experimental and reconstructed HAS spectrograms along the energy axis are shown in blue and red, respectively. **f** and **g**, Retrieved electron pulse in spectral (f) and temporal (g) domains. Intensity and phase are displayed in purple and red, respectively. Adapted from ref. [127].

The reconstruction is based on a least-square fitting algorithm. The spectral phase $\varphi(\omega)$ is modeled as a polynomial series composing up to the 6^{th} order:

$$\varphi(\omega) = \sum_{n}^{6} D_n(\omega - \omega_c)^n \tag{5.5}$$

where D_n denotes the n^{th} order dispersion, and ω_c is the central angular frequency in the spectral area of interest (cyan dashed line in Fig. 5.12). We observed that terms higher than the 6^{th} order do not yield any difference in the reconstruction of the spectrogram. Since the differential map embodies (indirect) information of the group-delay with a large contrast, the fitting target includes the original HAS spectrogram as well as the phase extracted from the differential map. Both are normalized to their maximum value and are equally weighted for the reconstruction.

Since at energies above 200 eV the spectral intensity is low, the phase extracted from the differential map is not accurate. Hence, the phase information provided by the differential map at energies above 200 eV was not used in the reconstruction (marked as dashed curve in Fig. 5.13 e). The HAS spectrogram used for the reconstruction is the one presented in Fig. 5.2 a, and the pump and gate pulse were evaluated from the cutoff analysis as shown in Fig. 5.6. As an initial gauss, a zero-chirped (chirp-free) pulse was used. The reconstruction algorithm converged iteratively to the result shown in Fig. 5.13 b.

5.4.3 Temporal characteristics of the electron pulse at the back-scattering instance

The reconstruction of a HAS spectrogram retrieves the terminal electron pulse wavepacket in the spectral area of interest (Fig. 5.13). The terminal electron wavepacket is linked to the back-scattered electron pulse via the Volkov basis (Eq. 4.1). Now the Volkov basis can be constructed by the well characterized pump field and the absolute timing of the electron pulse with respect to it. Therefore, the back-scattered electron pulse can be obtained by the inverse Volkov propagation of the terminal electron wavepacket,

$$\psi_{bs}^{(AOI)}(t) = \int_{-\infty}^{\infty} dp \chi_{tr}^{(AOI)}(p) \exp[iS^{(0)}(p, \infty, t; A_p(t))] \tag{5.6}$$

Fig. 5.14 a and b show the back-scattered electron wavepacket as retrieved by the back-propagation of the Volkov phase in both spectral and time domains, respectively. The spectrum of the back-scattered electron pulse spans from ~ 20 to ~ 80 eV, and the spectral phase exhibits a little amount of positive 2^{nd} and 3^{rd} order chirp. Correspondingly, the duration of the pulse is $\sim 53 \pm 5$ as measured at the full width half maximum. This result is very close to the Fourier-limited duration associated with the corresponding spectrum, ~ 52 as. This negligible degree of chirp can be understood on the basis of the recollision model at near cutoff energies as discussed later.

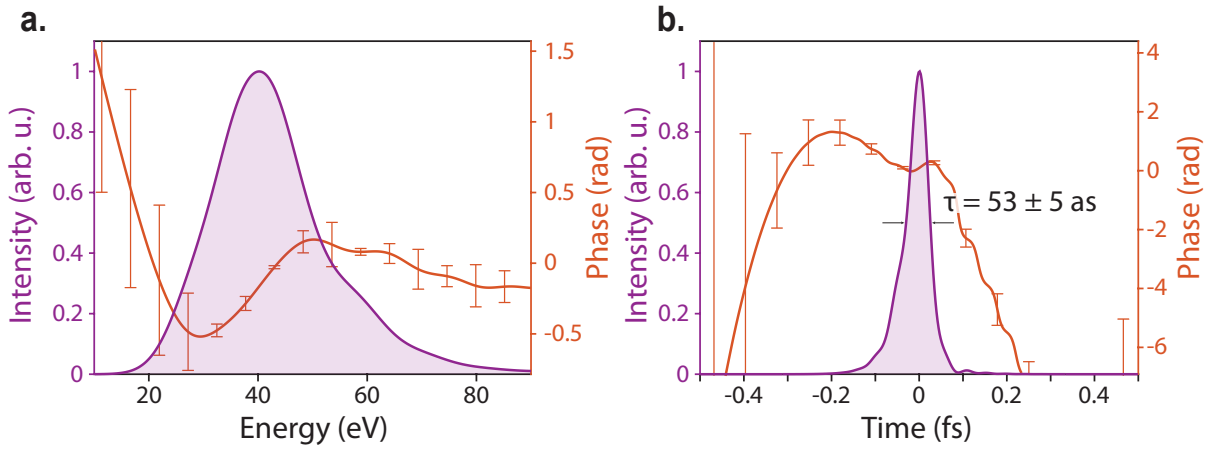

Figure 5.14: **Retrieved back-scattered electron pulse in the optical field emission.** Retrieved back-scattered electron pulse in spectral (**a**) and temporal (**b**) domains. The shaded purple curves are the intensities, and the red curves show the phase in both domains. Adapted from ref. [127].

Fig. 5.15 a elaborates on the relative timing of the pump pulse waveform and the release of the back-scattered electron pulse. One can observe that the release of the electron pulse occurs $\sim$ 0.1 fs earlier than the zero-crossing of the driving electric field. This fact and along with a positive 2^{nd} order chirp implies that the back-scattering process is slightly more weighted on the short-trajectories than the long-trajectories. A similar behavior has been also observed in high harmonic generation in atoms, which is attributed to the spatial and temporal broadening of the wavepacket during the propagation, resulting in reduction of the scattering cross-section of long trajectories.

To better visualize the time-structure of the electron pulse, a time-frequency analysis (Gabor transform) was performed. A Gaussian temporal window whose full width half maximum is 200 as was used in the analysis (Fig. 5.15 b). The width of the window was chosen such that at least one cycle of the lowest energy component, $\sim$ 20 eV, can be captured by the Gaussian gate, *i.e.*, $h/20$ eV $\sim$ 200 as such as to avoid numerical artifacts in the Fourier transform. The instantaneous energy of the back-scattered electron pulse in the time-frequency analysis (black curve in Fig. 5.15 b) shows a good agreement with that calculated by the semiclassical model (red dashed curve). This result supports once again the validity of the recollision picture in the study of ultrafast phenomena in photoemission.

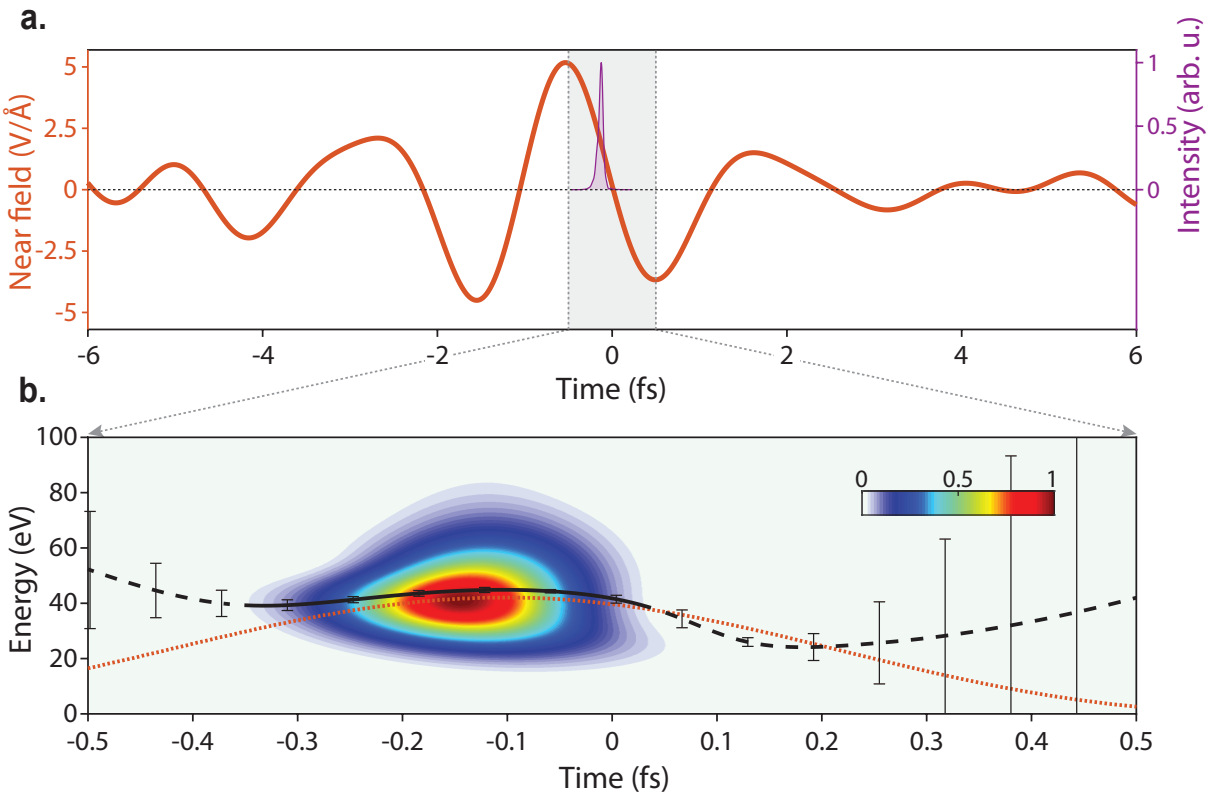

Figure 5.15: **Time-frequency analysis of the retrieved electron pulse.** **a**, Timing of the retrieved back-scattered electron pulse (purple) and the pump field (red). **b**, Time-frequency analysis of the retrieved back-scattered electron pulse. The black curve represents the group delay of the retrieved pulse, while the red dashed curve stands for semiclassically calculated group delay based on the recollision model. Adapted from ref. [127].

Error analysis

The error shown in Fig. 5.14 were derived based on the discrepancy in the intensity of the reconstructed and experimental spectrograms. A measured spectrogram can be considered as a statistical ensemble of individually measured spectra but at different delay points [22, 148], and the final result of the retrieved complex spectral amplitude is the principal value of this ensemble. The discrepancy in the spectral intensity between the experiment and reconstruction, which is inevitable due to the absence of an intensity projection process in the algorithm, was transferred to the spectral phase error in the retrieved electron pulse.

In order to evaluate the error, the reconstructed amplitudes (modulus of the complex amplitude) at each time delay was substituted by that of the experimental spectrogram,

and then an inverse Volkov propagation was performed to obtain a set of spectral complex amplitudes of the back-scattered electron pulse for all delay points as displayed in the curves of Fig. 5.16 a. The error bar shown in Fig. 5.14 is the standard error from the principal value. The error in phase is high at the low spectral intensity regions, in energies below $\sim$ 20 eV and above 60 eV due to the low statistics in these areas. The temporal intensity computed from the individual complex amplitude at each delay point is shown in Fig. 5.16 b. The standard deviation of the pulse duration of the ensemble is $\sim$ 5 as.

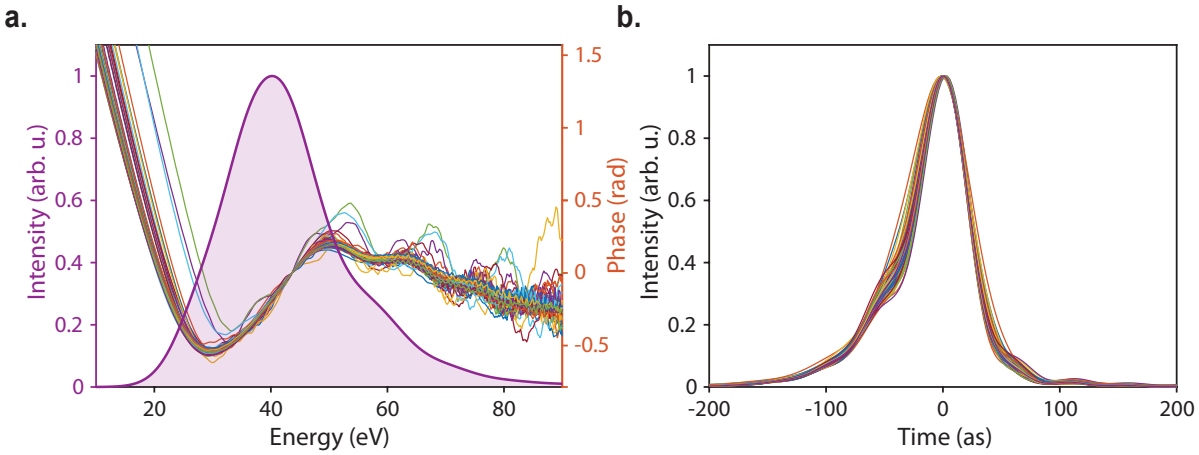

Figure 5.16: **Error analysis in the retrieval of the back-scattered electron pulse.** **a**, The phase of each delay point in the reconstructed spectrogram. **b**, The temporal intensity of the electron pulse calculated from the individual complex amplitudes shown in the panel a. The duration of the pulse has a standard deviation of $\sim$ 5 as with respect to the principal value.

Chapter 6

Scattering perspective of high harmonic generation in bulk solids

It's beyond imagination until you actually get up and see it and experience it and feel it.
-William C. McCool

In strong field atomic and molecular physics, electrons are liberated via tunneling to vacuum states (continuum states). In the framework of a quasi-free electron the dynamics are primarily dictated by the laser field and less by the binding potential of the system. This perspective has not only allowed an intuitive way for describing high harmonic generation in gases but also supported the development of new methodologies for probing the electronic orbitals of molecules via observing high harmonics scattered from them [56, 58].

One could imagine the extension of this idea to condensed matter. However, in terms of the most popular understanding of high harmonic generation in solids, namely via interband and intraband transitions, a coupling between bound and free states is not apparent. Here I present first steps that open the way to such an understanding.

6.1 Scattering perspective of high harmonic generation in solids

6.1.1 Potential suppression: interpretation based on the Floquet-Bloch theory

It has long been discussed that an intense electric field modifies the potential electrons experience in atoms, molecules and crystal lattices. In atomic and molecular physics, the phenomenon of atomic stabilization is best described in the language of a bounding atomic potential suppressed by an intense electric field [149, 150, 151]. With the potential suppressed, the electron motion is fully dominated by the driving field. Also in solid-state physics, at least in theory, it has been predicted that the band gap of semiconductors

and dielectrics can collapse under a periodic intense field [152, 153]. As a result, one can anticipate that the field-free band structure will be severely affected, if the fields are strong enough. Such modifications can be best described within the concept of the Floquet-Bloch theory which provides solutions based on dressed states including both the spatial periodicity of the potential and the temporal periodicity of the external driving electric field [154, 155, 156, 157]. Using the Floquet method, Tzoar and Gersten in 1975 [154] have explicitly shown that the band structure of a crystalline solid will be modified by an intense laser field. In this section, we will follow that work in order to understand how strong fields relevant to modern high harmonic generation experiments in solids alter the band structure and how the modified band can provide clues for the applicability of a scattering approximation for describing high harmonics.

The electronic motion in a periodic potential and under a periodic electric field can be described by the time-dependent Schrödinger equation. In this section the atomic units ($e = \hbar = 1$) are used for the sake of simplicity.

$$i\frac{\partial\psi(t)}{\partial t} = \hat{H}(t)\psi(t) \tag{6.1}$$

The laser field, $E_L(t) = -E_0 \sin(\omega_L t)$, is linearly polarized and satisfies the periodic condition, $E_L(t+T) = E_L(t)$, where T is its period. The potential satisfies the spatial periodic condition, $V(r+d) = V(r)$, where d represents the lattice constant of the crystal. The Hamiltonian of the electronic system can be written on the basis of the canonical momentum $p + A(t)$ as,

$$\hat{H} = \frac{1}{2}[p + A(t)]^2 + V(r) \tag{6.2}$$

where $A(t)$ denotes the vector potential of the field which is also periodic, $A(t+T) = A(t)$. A canonical transformation to the reference frame of the moving electron driven by the applied field allows one to simply the Schrödinger equation by inserting the Volkov phase, $\psi = \exp\big(-i\int dtp \cdot A(t) - i\int dt\frac{A(t)^2}{2}\big)\phi$,

$$\left(\frac{p^2}{2} + U(r,t)\right)\phi = i\frac{\partial\phi}{\partial t} \tag{6.3}$$

where the spatio-temporally periodic and field-coupled potential, $U(r,t)$ can be expressed as:

$$U(r,t) = V\left(r + \int dtA(t)\right) \tag{6.4}$$

The periodic potential $V(r)$ can be expanded as a Fourier series, $V(r) = \sum_G V_G e^{iG\cdot r}$, with discrete reciprocal vectors $G = mG_0$, where G_0 is the unit vector $G_0 = 2\pi/d$ and m is an integer. The vector potential of the driving field is given by $A(t) = -E_0/\omega_L \cos(\omega_L t)$. Using these facts, the spatio-temporally periodic potential (eq 6.4) can be expressed as harmonics of the driving field whose amplitude takes the form of the Bessel functions of the first kind. Essential laser parameters appear in the argument of the Bessel function.

$$U(r,t) = \sum_{n,G} V_G J_n\left(\frac{GE_0}{\omega_L^2}\right)e^{i(G\cdot r - n\omega_L t)} \tag{6.5}$$

By taking a close look at Eq. 6.5 we observe that the field-coupled potential can be divided into two major terms, the time-independent zeroth-order where $n = 0$, $U_0(r) = \sum_G V_G J_0\big(\frac{GE_0}{\omega_L^2}\big)e^{iG\cdot r}$, referred to as effective crystal potential and the rest time-dependent terms containing harmonics of the driving field, $U_n(r,t) = \sum_{n\neq 0,G} V_G J_n\big(\frac{GE_0}{\omega_L^2}\big)e^{i(G\cdot r - n\omega_L t)}$.

$$U(r,t) = \underbrace{\sum_G V_G J_0\left(\frac{GE_0}{\omega_L^2}\right)e^{iG\cdot r}}_{=U_0(r)} + \underbrace{\sum_{n\neq 0,G} V_G J_n\left(\frac{GE_0}{\omega_L^2}\right)e^{i(G\cdot r - n\omega_L t)}}_{=U_n(r,t)} \tag{6.6}$$

The above implies that the Hamiltonian can be also expressed as the sum of two terms according to their time-dependence:

$$H_c = H_{c0} + H_{cn}, \text{where } H_{c0} = \frac{p^2}{2} + U_0(r) \text{ and } H_{cn} = U_n(r,t) \tag{6.7}$$

The studies of Shirley [158], Tzoar and Gersten [154] have suggested a Floquet theory based solution of the Hamiltonian which can be expressed as a multiplication of a spatio-temporal periodic function, $u(r,t)$ and a plane wave, $e^{i(kr-\varepsilon t)}$,

$$\phi(r,t) = e^{i(kr-\varepsilon t)}u(r,t) = \sum_{n,G} c_{n,G}e^{i[(G+k)r-(\varepsilon+n\omega)t]} \tag{6.8}$$

One can easily notice that the above solution is another form of the Bloch solution with the addition of the dimension of time. Inserting the Eq. 6.8 into the new Hamiltonian, Eq. 6.7 leads us to an eigenvalue problem written as a secular equation as following:

$$(\varepsilon + n\omega_L)c_{n,G} = \underbrace{\left[\frac{1}{2}(k+G)^2\right]c_{n,G} + \sum_{G'} V_{G-G'}J_0\left(\frac{(G-G')E_0}{\omega_L^2}\right)c_{n,G'}}_{H_{c0}} + \underbrace{\sum_{n',G'} V_{G-G'}J_{n-n'}\left(\frac{(G-G')E_0}{\omega_L^2}\right)c_{n',G'}}_{H_{cn}} \tag{6.9}$$

A Floquet state ϕ is written in two independent spaces represented by n and G which are reciprocal space of time and real-space, respectively. The Floquet state consists of sub-space vectors $[\chi_n]$, where the index of n denotes the number of photons dressed with the sub-state. In a vector form, ϕ can be expressed as:

$$\phi = \begin{bmatrix} \vdots \\ [\chi_{-1}] \\ [\chi_0] \\ [\chi_1] \\ \vdots \end{bmatrix} \text{ and sub space } [\chi_n] = \begin{bmatrix} \vdots \\ c_{n,-1} \\ c_{n,0} \\ c_{n,1} \\ \vdots \end{bmatrix} \tag{6.10}$$

where the n$^{\text{th}}$ row element represents the sub-space vector $[\chi_n]$. The secular equation (Eq. 6.9) can be more intuitively understood in the matrix form with the basis of $[\chi_n]$. The

Hamiltonian matrix is given by a block matrix,

$$H_{c0} = \underbrace{\begin{bmatrix} \ddots & \vdots & \vdots & \vdots & \iddots \\ \cdots & [T_{-1}] & 0 & 0 & \cdots \\ \cdots & 0 & [T_0] & 0 & \cdots \\ \cdots & 0 & 0 & [T_1] & \cdots \\ \iddots & \vdots & \vdots & \vdots & \ddots \end{bmatrix}}_{p^2/2} + \underbrace{\begin{bmatrix} \ddots & \vdots & \vdots & \vdots & \iddots \\ \cdots & [U_0] & 0 & 0 & \cdots \\ \cdots & 0 & [U_0] & 0 & \cdots \\ \cdots & 0 & 0 & [U_0] & \cdots \\ \iddots & \vdots & \vdots & \vdots & \ddots \end{bmatrix}}_{U_0} \text{ and } H_{cn} = \underbrace{\begin{bmatrix} \ddots & \vdots & \vdots & \vdots & \iddots \\ \cdots & 0 & [U_1] & [U_2] & \cdots \\ \cdots & [U_{-1}] & 0 & [U_1] & \cdots \\ \cdots & [U_{-2}] & [U_{-1}] & 0 & \cdots \\ \iddots & \vdots & \vdots & \vdots & \ddots \end{bmatrix}}_{U_n} \tag{6.11}$$

where the sub-matrices T_n and U_n denote the kinetic energy operator, $[T_n]_{ij} = \delta_{ij}\left[\frac{1}{2}(k-(i-j)G_0)^2\right]$ and the potential energy operator, $[U_n]_{ij} = V_{i-j}J_n\left(\frac{(i-j)G_0E_0}{\omega_L^2}\right)$, respectively. These sub-matrices are written in the space of the reciprocal vector G with indices of i and j. The time-independent Hamiltonian (H_{c0}) is a diagonal matrix, and the electrostatic states of the system can be completely described by its eigen Floquet states. Hence, the off-diagonal Hamiltonian (H_{cn}) can be understood as the matrix responsible for the transitions among the eigen Floquet states of H_{c0} with absorption or emission of harmonic photons of the driving laser. Because the eigenstates of H_{c0} are dictated by the effective crystal potential U_0, the electronic motion induced by the laser can be understood in the framework of U_0. The effective crystal potential is identical in form to the so-called "cycle-averaged" or "Kramers-Henneberger" (KH) potential [159, 150, 151]. Importantly, a compelling point of the above equation is that the strength of the effective potential depends on the 0^{th} order Bessel function with the argument of laser field parameters, field strength and frequency. In other words, the applied field modifies the strength and shape of the effective potential, and therefore the band structure of the system is altered with laser parameters. This means that by observing how the band structure is modified, we can gain an insight into the relevance of quasi-free scattering concept under strong field conditions.

6.1.2 The band structure of the field-suppressed valence potential

A first step for getting the relevant insight is by investigating the band structure $\varepsilon_0(k)$ associated with the effective potential U_0. For a clear visualization of the field-dependent effective crystal potential, we consider a potential with the dominant Fourier component V_1 at $G = G_0 = 2\pi/d$, *i.e.*, $V(r) = 2V_1\cos(G_0r)$ giving the effective potential of $U_0(r) = 2V_1J_0\left(\frac{G_0E_0}{\omega_L^2}\right)\cos(G_0r)$. Recalling the Hamiltonian H_{c0}, the band structure can be found by solving the secular equation like a standard diagonalization problem in the Bloch theorem,

$$\left[\frac{1}{2}(k+G)^2 - \varepsilon_0(k)\right]c_{0,G} + \sum_{G'} V_{G-G'}J_0\left(\frac{(G-G')E_0}{\omega_L^2}\right)c_{0,G'} = 0 \tag{6.12}$$

One can notice that at a specific field strength E_c for a given laser frequency the 0^{th} order Bessel function has a zero value $J_0\left(\frac{G_0E_c}{\omega_L^2}\right) = 0$, and the secular equation has a trivial solution of $\varepsilon_0(k)$ as a free electron dispersion, the parabolic band structure. This finding

suggests that the onset of quasi-free electron motion will take place nearby field strengths and frequencies for which the above condition is met.

A calculation of the effective potential and the associated band structure with increasing field strength is shown in Fig. 6.1 a and b, respectively. For this calculation, a lattice constant of 4.65 Å and a central laser energy of 2 eV were used to mimic MgF_2 crystal and the experimental conditions reported in ref. [67]. At a weak field (0.1V/Å), the effective valence potential (magenta in Fig. 6.1 a) is marginally changed from the original bare potential (black curve in Fig. 6.1 a) and therefore the band structure is virtually identical to the original one (magenta in Fig. 6.1 b). As the potential is further suppressed by increasing field strength, the band dispersion is getting closer to the parabolic dispersion of the free electron. Importantly, around the critical field ($E_0 \approx 0.94$V/Å) the 0^{th} order Bessel function becomes zero and results in the complete suppression of the crystal potential (yellow curve in Fig. 6.1 a). The band dispersion becomes totally parabolic and the bandgap collapses as predicted by previous studies [152, 153] (yellow curve in Fig. 6.1 b). A further increase of the field beyond the critical point (between 1^{st} and 2^{nd} roots of the 0^{th} order Bessel function), the crystal potential as well as the bandgap and the band structure are restored toward the original in accordance with the oscillatory behavior of the Bessel function, as shown in the case of 1.4 V/Å in Fig. 6.1 a, b. Such effects are however difficult to be observed in experiments as materials damage at fields slightly higher than 1 V/Å.

To illustrate the above findings better, it is useful to relate those with the effective mass, $[m_i^*(k)]^{-1} = \frac{d^2\varepsilon_i(k)}{dk^2}$, where i represents the index of a band. When the electron is simultaneously occupying several bands, the reduced effective mass defined as a harmonic mean of the effective masses, is a more appropriate metric to quantify the effects of the strong field on the band structure.

$$\mu(k) = N\left[\sum_i \frac{1}{m_i^*(k)}\right]^{-1} \tag{6.13}$$

The reduced effective mass represents a ratio of the expectation value of total electron velocity in a crystal with respect to that of free electrons. In our simulations, the reduced masses were evaluated by taking the two highest valence bands and the two lowest conduction bands shown in Fig. 6.1 b for each field strength (Fig. 6.1 c.).

At a low field strength (0.1 V/Å), the effective mass remains virtually unaffected (dashed line). However, in the vicinity of the critical field, $\sim$ 0.95 V/Å the value of the reduced effective mass nears that of the free electron ($\mu \sim 1$) over the entire k-space. Beyond the critical field, the effective mass gradually revives. The sharp peaks of the reduced effective mass around the zone boundary represent the restoration of the Bragg reflection condition. Based on the effective mass shown in the Fig. 6.1 c, the velocity ratio of crystal electron to that of free electron was evaluated in the presence of a Gaussian electric pulse with a pulse duration of 5.5 fs and a carrier frequency of 2 eV (Fig. 6.1 d). For this calculation it is assumed that the initial momentum distribution is a Gaussian centered at $k = 0$ with momentum bandwidth of $\pi/5d$ (FWHM). This assumption is not quantitatively accurate, however good enough to capture the essential features of this pic-

ture. At the low field strength, the velocity ratio asymptotically converges to the relative effective mass, while it approaches to unity around the critical field strength. Beyond the critical field strength, the velocity ratio rapidly reduces. This can be attributed to the restoration of the Bragg reflection at these fields.

In the above discussion the velocity ratio was used for the comparison of crystal electron motion with that of a free electron, since the velocity is more adequate to describe the picture intuitively. However, the amplitude of the harmonic radiation is proportionally related to the acceleration of the electric motion in a crystal rather than the velocity. Therefore, the comparison of acceleration is more relevant for the harmonic generation. As considered before, the quantum mechanical description can be linked to classical observables via the Ehrenfest theorem. The expectation value of acceleration can be expressed as $\langle a \rangle = eE_L/m^*$, where m^* is the effective mass, and E_L is the field. Therefore, a comparison between the acceleration of a crystal electron and that of a free electron is equivalent to the ratio of effective mass m^* to bare electron mass m_e.

$$\frac{a_{cry}}{a_{free}} = \frac{m_e}{m^*} \tag{6.14}$$

Similarly to the acceleration, the velocity can be written with the momentum given by the field, which is in turn the vector potential A,

$$\langle v \rangle = \frac{A}{m^*} = \frac{E_L}{\omega_L^2 m^*} \tag{6.15}$$

The expectation value of the velocity additionally has a frequency dependency compared to the acceleration. However, the dynamics of the crystal electron is dictated by the laser field, and the nonlinear motion introduced by the crystal potential can be considered as a small perturbation. Therefore, it can be safely assumed that the harmonic signal is negligible compared to the fundamental, and this allows one to approximate the velocity ratio as the ratio of the effective mass to the bare electron mass:

$$\frac{v_{cry}}{v_{free}} \approx \frac{m_e}{m^*} = \frac{a_{cry}}{a_{free}} \tag{6.16}$$

Therefore, we can conclude here that the velocity ratio also represents a comparison between crystal electron motion and free-electron motion.

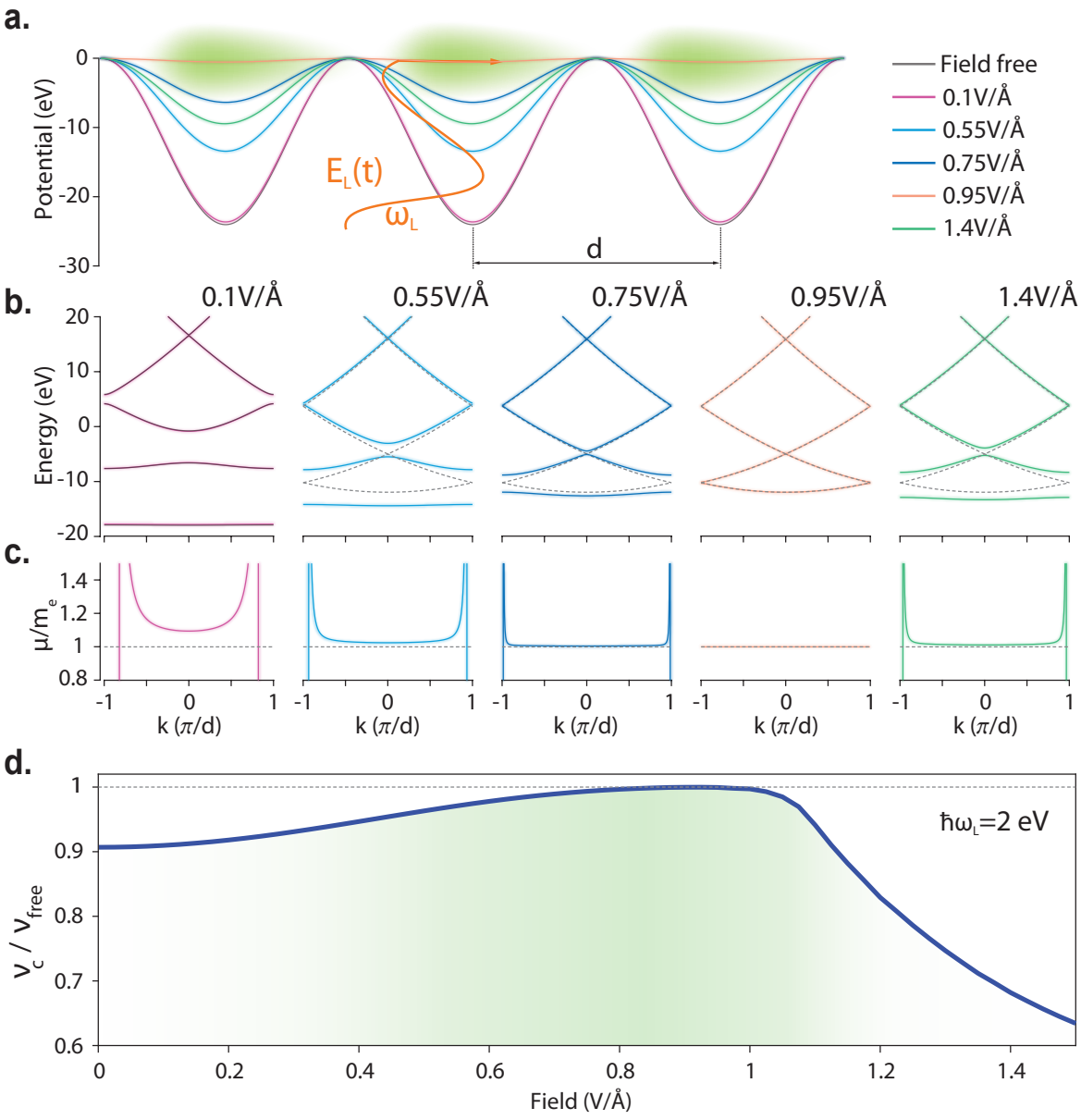

Figure 6.1: **Effective band structure and electron dynamics in a crystal exposed to a strong optical field.** **a**, Effective valence potential (lattice constant of 4.65 Å) in the presence of optical fields at $E_0 = 0.1$ (pink), 0.55 (cyan), 0.75(blue), 0.95(yellow), and 1.4 V/Å(green) with a carrier energy of $\hbar\omega_L = 2$ eV. The black curve denotes the valence potential in the absence of an optical field. **b**, The band-structure associated with the suppressed valence potential at different field strengths denoted by the same color as in panel (a). The grey dashed curves in (b) represent the free electron dispersion. The black curve is the unmodified band structure in the absence of an optical field. **c**, The ratio of effective mass to the bare electron mass calculated from the band dispersion shown in panel (b). The grey dashed horizontal line represents the unitary value. **d**, The ratio of the maximum velocity of the crystal electron based on the above calculated band dispersion to that of the free electron. Adapted from ref. [67]

6.1.3 *Ab initio* simulation: Time-dependent density functional theory

Ab initio simulations employing the time-dependent density functional theory (TDDFT) performed by our collaborators, S. Hu and S. Meng at Chinese Academy of Science in China, support the above picture. The simulations were conducted assuming a linearly polarized few-cycle laser pulse (∼5.5 fs pulse duration) carried at ∼2 eV. The system of choice was crystalline MgF_2 (bandgap of $E_g = 12$ eV and lattice constant of $d = 4.65$ Å). The laser polarization vector was aligned with the [100] direction of the crystal. The velocity of the total electron motion inside the crystal was computed from the current density operator, $\hat{v}(t) = V_{cell}^{-1} \sum_{l,G,k,\sigma} Im[\langle\psi(t)|\nabla|\psi(t)\rangle]$. Further details on the TDDFT calculation can be found in 'method' section in ref. [67].

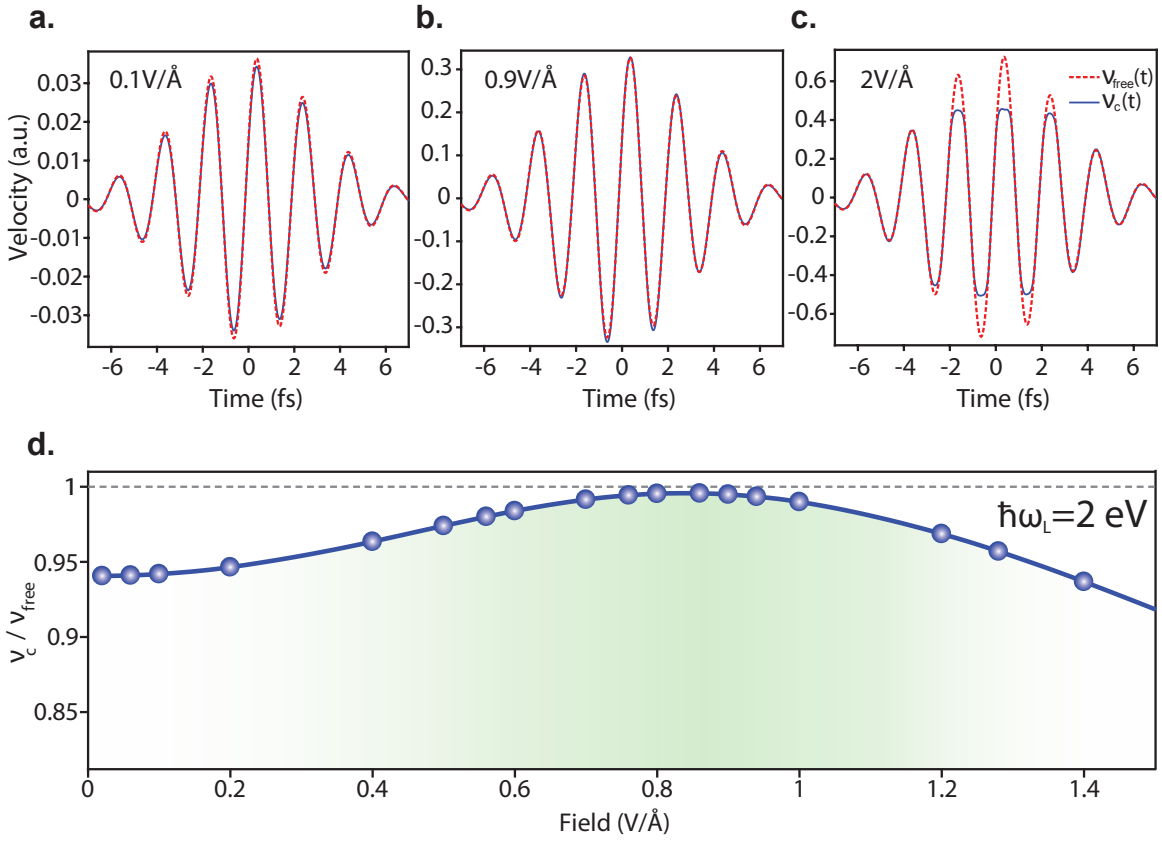

Figure 6.2: **Electron dynamics calculated in TDDFT. a-c**, Crystal (blue solid curve) and free-electron (red dashed curve) velocities along [100] direction of crystalline MgF_2 were calculated by TDDFT in the presence of a laser field with a strength of 0.1 (a), 0.9 (b) and 2.0 V/Å(c) and a carrier energy of $\hbar\omega_L = 2$ eV. **d**, The ratio of maximum of crystal velocity to free-electron velocity is plotted as a function of the field strength of the driving laser pulse. Figure adapted from ref. [67]

Like the results obtained under the field-suppressed band structure, at a low field strength ($E_0 = 0.1$ V/Å, Fig. 6.2 a), the crystal velocity (blue curve) is lower compared to the free electron velocity (red dashed curve) which can be attributed to the presence of the effective mass, $\mu/m_e \sim 0.95$. Near the critical field strength, $E_0 = 0.9$ V/Å the crystal velocity is virtually identical to the free-electron velocity (Fig. 6.2 b). At the higher field ($E_0 = 2$ V/Å, Fig. 6.2 c), the velocity drops again. The ratio of the maximum velocity in the crystal and that of the free electron motion is plotted as a function of the peak field strength of the driving field in Fig. 6.2 d. Once again in the TDDFT simulation, it is verified that a quasi-free electron motion can be anticipated around the critical field strength.

6.2 Linking high harmonic radiation to the valence potential of solids

6.2.1 Crystal potential scattering model

The description of electron dynamics on the basis of a quasi-free electron leads to a possible treatment of high harmonic generation within the framework of scattering. In the scattering perspective, the emission of harmonics stems from the perturbation of the electron acceleration, *i.e.*, temporal variation of current arising from the scattering of a driven electron by the valence potential as depicted in Fig. 6.3. Because the potential can be expressed as a superposition of its spatial Fourier components, $V(r) = \sum_G V_G e^{iGr}$, the electron motion is sensitive to each Fourier component V_G, and the accompanying harmonics are consequently linked to each other as illustrated in Fig. 6.3 b and c. In other words, measurement of a harmonic implies simultaneous probing of several Fourier components. Under an intense laser field, $\mathbf{E_L}(t) = E_0 \sin(\omega_L t)\mathbf{e}_\parallel$ with a polarization direction denoted by $\mathbf{e}_\parallel$, the temporal variation of current can be written in the form of an equation of motion (in SI units).

$$\frac{\partial \mathbf{J}}{\partial t} \propto e\nabla V(r) - e\mathbf{E_L}(t) \tag{6.17}$$

The first term on the right-hand side of the equation expresses the acceleration or deceleration by the valence potential, and the second term describes those by the laser field. Since motion is driven by the laser field, the second term gives rise to a linear response to the field at the fundamental frequency only. The high harmonic response of the system stems from the valence potential. In the semiclassical limit [160], the expectation value can be expressed as:

$$\langle -e\nabla V(\mathbf{r}(t))\rangle = -e\nabla V(\langle \mathbf{r}(t)\rangle) \tag{6.18}$$

Once again, just as in the previous treatment we can change the reference frame by inserting $\langle \mathbf{r}(t)\rangle = \frac{eE_0}{(m_e\omega_L^2)} \sin(\omega_L t)\mathbf{e}_\parallel$ into the above equation. For simplicity, here we consider a symmetric potential, $V(r) = \sum_G V_\mathbf{G} \cos(\mathbf{G}\cdot\mathbf{r})$. Using the derivative of the potential

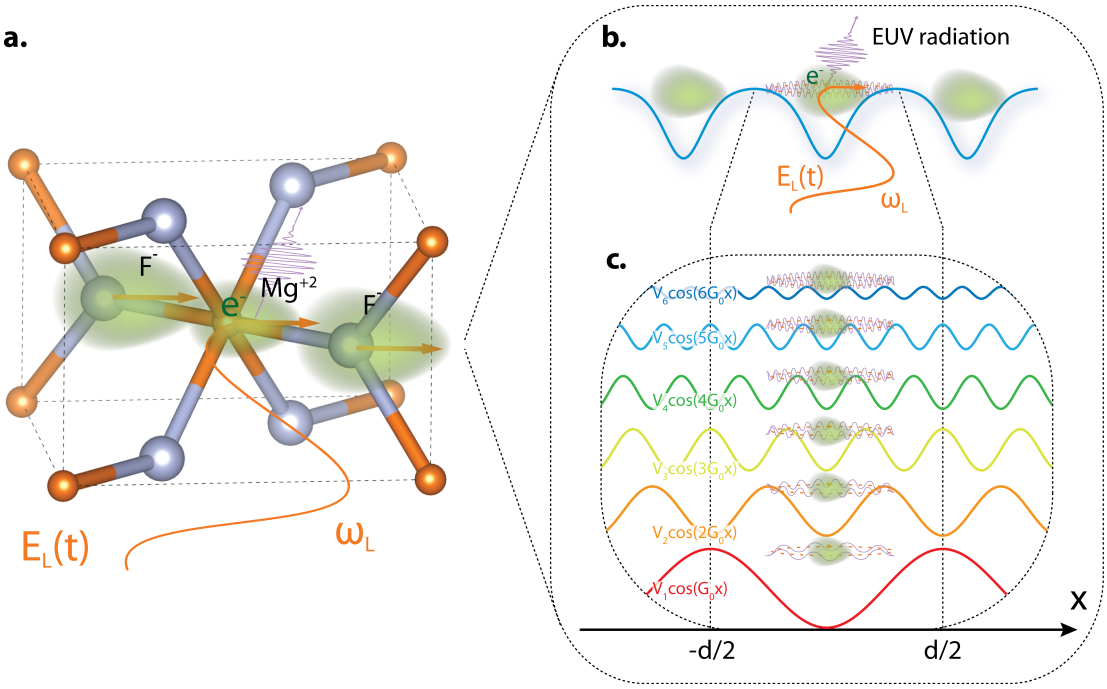

Figure 6.3: **Illustration of scattering in real space.** **a**, A crystal (here for example MgF_2) is illuminated with a strong laser field $E_L(t)$ with its carrier frequency ω_L. **b**, The electron wavepacket experiences contour of potential (1D slice) along the polarization direction of the field, and the electron current leads to radiation of high harmonics in the EUV range. **c**, The 1D slice potential can be decomposed into Fourier series with spatial frequency components V_G. Scattering of the Fourier components of the potential gives rise to coherent EUV radiation.

(force) which is given by the Fourier series, $\nabla V(r) = -\sum_G \mathbf{G} V_\mathbf{G} \sin(\mathbf{G}\cdot\mathbf{r})$, the Eq. 6.17 can be rewritten as:

$$\frac{\partial \mathbf{J}}{\partial t} \propto \underbrace{-\sum_{\mathbf{G}} (\mathbf{G}\cdot\mathbf{e}_\parallel)\mathbf{e}_\parallel V_\mathbf{G} \sin\left(\mathbf{G}\cdot\mathbf{e}_\parallel \frac{eE_0}{m_e\omega_L^2}\sin(\omega_L t)\right)}_{=\frac{\partial \mathbf{J}_\parallel}{\partial t}} \underbrace{-\sum_{\mathbf{G}} (\mathbf{G}\cdot\mathbf{e}_\perp)\mathbf{e}_\perp V_\mathbf{G} \sin\left(\mathbf{G}\cdot\mathbf{e}_\parallel \frac{eE_0}{m_e\omega_L^2}\sin(\omega_L t)\right)}_{=\frac{\partial \mathbf{J}_\perp}{\partial t}} \tag{6.19}$$

The current variation in time consists of two directional components, parallel $\frac{\partial \mathbf{J}_\parallel}{\partial t}$ and perpendicular $\frac{\partial \mathbf{J}_\perp}{\partial t}$ to the laser polarization vector. Since our experimental studies in ref. [67] are limited to radiation polarized along the laser polarization axis, we will closely scrutinize the parallel components only. A detailed derivation and a further discussion of high harmonic generation in the general case including asymmetric potentials as well as the response of the perpendicular component of the harmonics can be found in the Appendix C.

By applying the Jacobi-Anger expansion, the sinusoidal term can be decomposed into a superposition of odd harmonics of the driving laser field with their corresponding amplitude as the 1st kind Bessel function with the laser parameters and spatial Fourier components of the potential,

$$\frac{\partial \mathbf{J}_{\parallel}}{\partial t} \propto \sum_{\mathbf{G}} \sum_{N} \mathbf{G} \cdot \mathbf{e}_{\parallel} V_{\mathbf{G}} J_N \left(\mathbf{G} \cdot \mathbf{e}_{\parallel} \frac{eE_0}{m_e \omega_L^2} \right) \sin\left(N\omega_L t\right) \tag{6.20}$$

where N denotes odd harmonic orders. Note that even harmonic generation is possible only in asymmetric potentials. Because the coherent radiation emerging from the system is proportional to the acceleration, the harmonic spectrum can be expressed through the Fourier transformation of the current variation $\frac{\partial \mathbf{J}_{\parallel}}{\partial t}$.

$$I_N(E_0, \omega_L, \mathbf{e}_{\parallel}) \propto \left| \sum_{\mathbf{G}} \mathbf{G} \cdot \mathbf{e}_{\parallel} V_{\mathbf{G}} J_N \left(\mathbf{G} \cdot \mathbf{e}_{\parallel} \frac{eE_0}{m_e \omega_L^2} \right) \right|^2 \tag{6.21}$$

By summing over the perpendicular direction of the reciprocal vector, Eq. 6.21 can be rewritten with the concept of the projection of V_G, and it is simplified to a problem in 1D projected space as:

$$I_N(E_0, \omega_L, \mathbf{e}_{\parallel}) \propto \left| \sum_{G_{\parallel}} G_{\parallel} V_{proj} J_N \left(G_{\parallel} \frac{eE_0}{m_e \omega_L^2} \right) \right|^2 \tag{6.22}$$

where $V_{proj} = \sum_{G_{\perp}} V_{\mathbf{G}}$ are the Fourier components of the potential projected along polarization vector of the electric field. The projected Fourier component V_{proj} is directly linked to a slice of the potential in the real space, according to the Fourier slice theorem [161] as illustrated in Fig. 6.4 a. The N$^{\text{th}}$ harmonic is dictated by the N$^{\text{th}}$ order of the Bessel function. Therefore, in order to interrogate the relationship between harmonic yields and the Fourier components, understanding the behavior of the Bessel function is essential. Fig. 6.4 b displays different order Bessel functions $J_N\left(G\frac{eE_0}{m_e\omega_L^2}\right)$ in the reciprocal space of G. Differently from the sinusoidal functions, the amplitude of the Bessel function decreases, and the first half-cycle has the highest amplitude. The dominant oscillating cycle of the Bessel function is acting on the Fourier components and plays a role of a "gate" in G-space. As shown in Fig. 6.4 b, a higher order Bessel function reaches its maximum further in the G-space compared to the lower orders. This implies that the higher harmonics have more sensitivity to the higher Fourier components of the potential. This behavior is physically logical in the sense that in a unit time, electrons experience fast potential modulations from the high spatial frequency components of the potential.

The harmonic yields are not only sensitive to the amplitude of the Fourier components of the potential but also their relative phase. This is because each harmonic is produced by a range of Fourier components under the dominant cycle of Bessel function in reciprocal space. A variation in either the amplitude or the phase of the Fourier components of the potential gives rise to a variation of the harmonic signals. This characteristic provides a

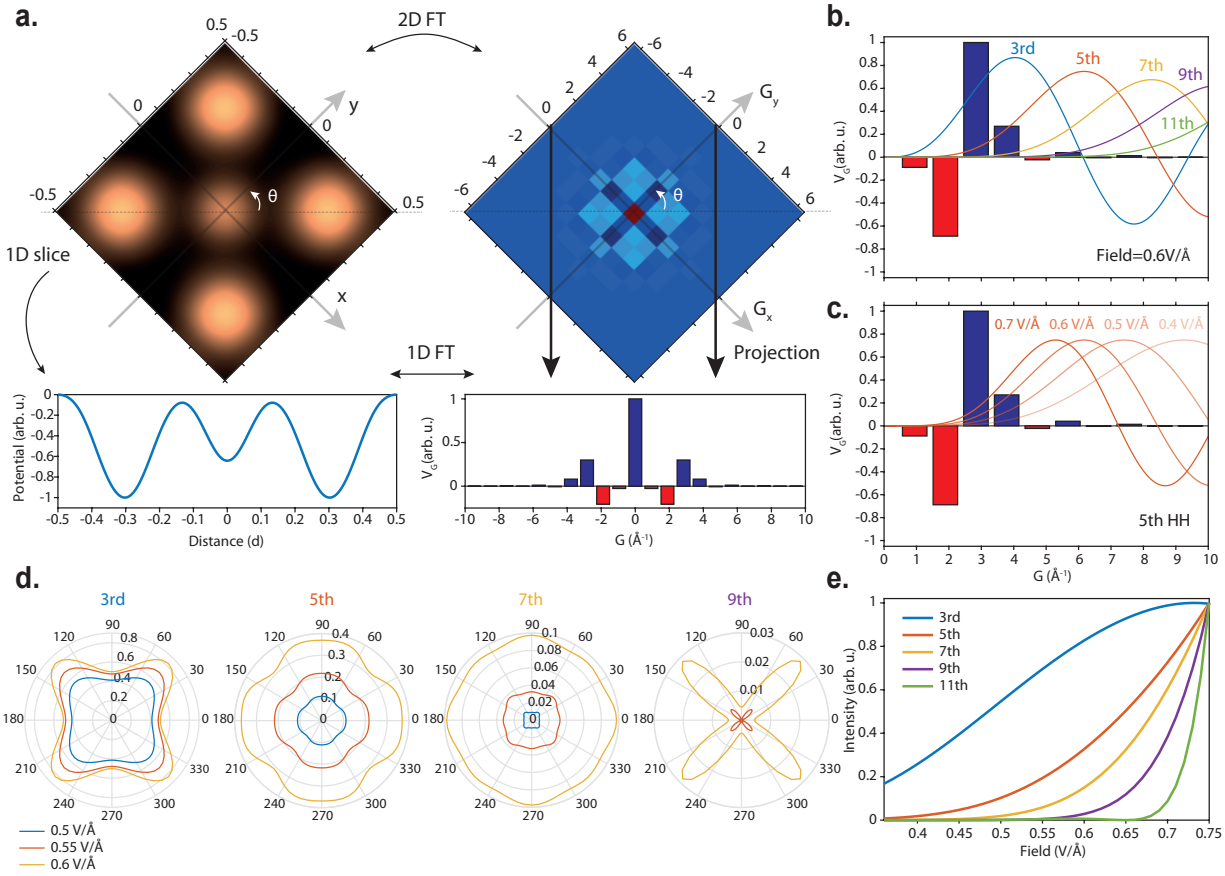

Figure 6.4: **High harmonic generation in solids.** **a**, The potential landscape in a plane of MgF_2 probed by the laser field (left) and its Fourier components in the reciprocal space (right). A linear slice of the potential along the laser polarization vector at an angle (θ) is linked to the 1D Fourier transformation of the projected Fourier components along the same direction (Fourier slice theorem). d and G denote the lattice constant and reciprocal vector, respectively. **b**, Behavior of different order (from 3^{rd} to 11^{th}) of Bessel function at a field strength of 0.6 V/Å. Each color represents a different harmonic order. **c**, 5^{th} order Bessel function at different field strengths from 0.4 to 0.7 V/Å. **d**, Orientation dependence of high harmonic yields calculated at different field strengths (blue for 0.5 V/Å, red for 0.55 V/Å, and yellow for 0.6 V/Å), with the potential shown in panel a. **e**, Field strength dependence of harmonic yields at $\theta = 45°$. The same color code is used as in panel b.

great advantage in accessing the phase relation among Fourier components of the valence potential, in contrast to conventional X-ray diffraction techniques where the probing signal is the absolute-square of the individual Fourier components, thereby loosing the phase information [162].

The dependence of high harmonics on the driving field strength can now be intuitively understood by the overlap of the Bessel function on the Fourier components of the potential

in the reciprocal space. With increasing driving field strength, the Bessel function is compressed to low Fourier components in the reciprocal space as shown in Fig. 6.4 c. Typical Fourier components of a crystal potential undergo an exponential drop with the reciprocal vector G. As a result, a higher harmonic yield is expected when the Bessel function is mostly overlapped with the lower order of Fourier components, implying the obvious result that higher harmonic intensity is generated at higher driving field strengths. Fig. 6.4 e shows the intensity of various harmonics as varying the driving field strength. By a variation of the orientation, the electrons experience a different potential landscape resulting in the angle-dependent harmonic yields as shown in Fig. 6.4 d.

6.2.2 Characteristics of high harmonic emission in the scattering model

Cutoff energy of high harmonics

One of the experimentally observed distinct characteristics of harmonics from solids is the linear dependence of the cutoff energy to the peak strength of the driving field. The high harmonic cutoff energy can be deduced from the Eq. 6.22. The highest energy of the harmonics can be expected when the Bessel function is applied on the highest order of the significant Fourier component of the valence potential at G_m. From the approximation that the Bessel function is maximized when its argument is approaching its order, the maximum harmonic order N_{max} can be estimated as $N_{max} \approx \frac{G_m e E_0}{m_e \omega_L^2}$. Then the cutoff energy is given by

$$E_{cutoff} = N_{max} \hbar \omega_L = \hbar \frac{G_m e E_0}{m_e \omega_L} \tag{6.23}$$

The scattering model exhibits a linear dependence of the cutoff energy to the peak strength of the driving field as previously reported in many experimental observations [60, 62, 65, 103]. One compelling contrast with other models such as the intraband model is the wavelength dependence in the cutoff energy. This difference is a good benchmarking point of two models for future studies.

Phase variation of high harmonics with varying intensity and CEP of the driver

To investigate the temporal properties of harmonics in the scattering picture, the phase variation of the harmonics under the variation of the intensity and the carrier-envelope phase (CEP) of the driving pulse was considered. This is important for benchmarking with other HHG mechanisms previously developed, mainly based on the interpretation of the dynamics on the band structure.

As described by Eq. 6.20, the time structure of high harmonics is directly imprinted by the current variation in time. By inserting a CEP into the driving field, $E_L(t) = E_0 \sin(\omega_L t + \varphi_{CEP})$, the individual harmonic components ($\mathrm{N^{th}}$ order) in Eq. 6.20 can be

rewritten as,

$$E_{HN}(t) = -\sum_{G_\parallel} G_\parallel V_{proj} J_N\left(\mathbf{G}\cdot\mathbf{e}_\parallel \frac{eE_0}{m_e\omega_L^2}\right)\sin\left(N(\omega_L t+\varphi_{CEP})\right) \tag{6.24}$$

The above equation suggests that the field strength acts only on the amplitude of the individual harmonic through the Bessel function, but does not affect the temporal phase of emitted harmonics. In other words, the relative amplitudes of the harmonics are manipulated by the variation of the driving field strength, but the time structure of the harmonics is independent from the field strength. Furthermore, one can notice that the temporal phase of the harmonics is dictated by the CEP, but in a synchronized manner, *i.e.*, the timing of the harmonics is shifted by φ_{CEP}/ω_L, implying a synchronization with the peak of the driving field. This synchronization effect also appears in the intraband interpretation of HHG in solids, but is a distinct contrast to the HHG in atoms and the interband interpretation in solids. Detailed experimental observations of the relative phase of the harmonics in solids will be covered in the next chapter.

6.2.3 Scattering model and pulse driving fields

So far, we considered monochromatic continuous waves (CW) for investigating the scattering model. However in the laboratory, pulsed laser fields are generally used. To consider a pulsed field as the driving field, which is mathematically expressed as $E_L(t) = \int_{-\infty}^{\infty} d\omega \tilde{E}(\omega)e^{i\omega t}$, the Eq. 6.20 is modified by substituting the electron excursion with:

$$r(t) = \int_{-\infty}^{\infty} d\omega \frac{e\tilde{E}(\omega)}{m_e\omega^2}e^{i\omega t} \tag{6.25}$$

The harmonics of the current arising from the scattering now can be rewritten as:

$$\frac{\partial \mathbf{J_H}}{\partial t} \propto \sum_G V_G iG \exp\left(iG\int_{-\infty}^{\infty} d\omega \frac{e\tilde{E}(\omega)}{m_e\omega^2}e^{i\omega t}\right) \tag{6.26}$$

and its spectrum is obtained via the Fourier transformation,

$$I(E,\omega) \propto \left|\int_{-\infty}^{\infty} dt e^{-i\omega t}\sum_G V_G iG \exp\left(iG\int_{-\infty}^{\infty} d\omega \frac{e\tilde{E}(\omega)}{m_e\omega^2}e^{i\omega t}\right)\right|^2 \tag{6.27}$$

Scattering model and TDDFT: a quantitative comparison

The validation of the scattering model can be again studied via a comparison of its predictions with these in *ab initio* TDDFT calculations. Fig. 6.5 a shows the high harmonic spectra in crystalline MgF_2 along the [100] direction calculated by the scattering model (Eq. 6.27). The same potential and pulse (5.5 fs FWHM duration and central energy of $\hbar\omega_L = 2$ eV) were used to perform a set of full 3D TDDFT simulations. In the TDDFT

study (Fig. 6.2), the high harmonic spectra were calculated by the Fourier transform of time variation of the current, *i.e.*, the acceleration (Fig. 6.5 b). In Fig. 6.5 c, the spectra from the scattering model (blue curves) are in excellent agreement with those calculated in TDDFT (red curves) under the identical conditions within a broad range of field strengths. These findings offer a strong support to the scattering model.

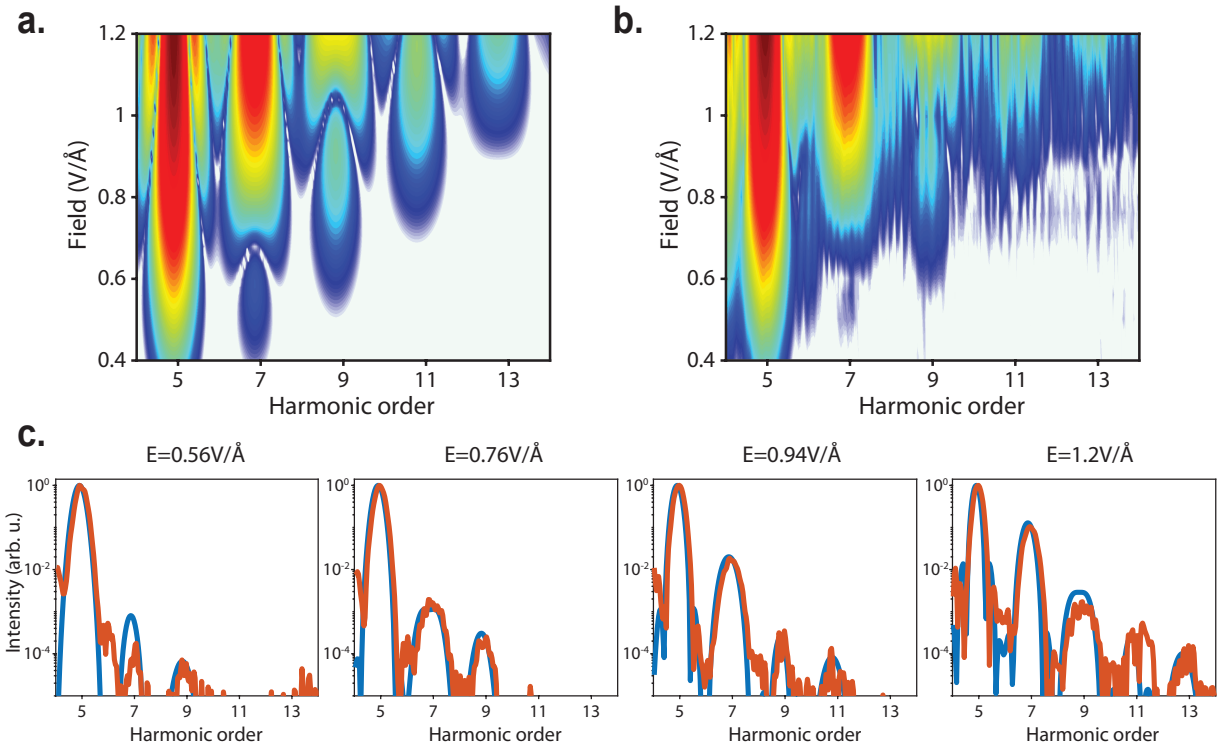

Figure 6.5: **High harmonic spectra from the scattering model and TDDFT. a**, HHG spectra from crystalline MgF_2 calculated by the scattering model with linearly polarized electric pulse (central energy of $\hbar\omega_L = 2$ eV and 5.5 fs FWHM duration) within a broad range of field strengths from 0.4 to 1.2V/Å. The polarization of the driving field is aligned along the [100] crystal orientation direction. **b**, HHG spectra from the TDDFT calculation under the identical conditions as in panel a. **c**, The comparison between high harmonic spectra from the scattering model (blue) and TDDFT (red) at different field strengths.

Chapter 7

Phase of EUV radiation in high bandgap dielectrics

Artmaking is making the invisible, visible.
-Marcel Duchamp

The characteristics of high harmonic radiation (HH) emitted from bulk solids show a range of distinct characteristics significantly different from those from atoms or molecules in the gas phase, for example, dependence of cutoff energy to the peak field strength [60, 62, 65, 103] and response of harmonic yield to the ellipticity of field [163, 66]. However, the temporal properties such as the phase and timing of harmonics radiated from solids and its underlying mechanism are still subjects under debate [63, 106, 61, 42, 104]. One way to get a deeper insight into the emission process is to study the phase of the radiated harmonics. The phase information is in general invisible in the spectral or time-integrated measurements. However, interferometric methods can help *making the invisible, visible*, where spectral phase is concerned. In this chapter, we will explore the emission phase characteristics of the harmonics arising from solids and their variation with respect to the intensity and carrier-envelope phase (CEP) of the driving laser field utilizing photoelectron interferometry.

7.1 Phase of harmonics from various models

7.1.1 Recollision model in gases

The mechanism of high harmonic generation in gaseous media is well described by the recollision model [18, 89]. In this model, the temporal characteristics of high harmonics can be explained by considering the quantum phase of electron trajectories under a driving field. The quantum phase that an electron accumulates from the moment of its ionization (t_b) to the moment of the recollision (t_r) (also discussed in chapter 1) is dictated by the

parameters of the driving laser field, $E_L(t) = E_0 \cos(\omega_L t + \varphi_{CEP})$ in the form of the Volkov phase:

$$\phi(p=0) = \int_{t_b}^{t_r} dt A(t)^2 = \frac{E_0^2}{\omega_L^2} \int_{t_b}^{t_r} dt \sin^2(\omega_L t + \varphi_{CEP}) \tag{7.1}$$

where ω_L and φ_{CEP} denote the laser frequency and CEP, respectively. The integration can be re-cast as a phase parameter $\alpha(E, \varphi_{CEP})$, which depends on the energy (E) of the harmonic emitted and the CEP of the driving field (φ_{CEP}). In this context, the phase of a harmonic $\phi_{HH}(E, \varphi_{CEP})$ can be expressed in a simple form [164, 165, 166] given by

$$\phi_{HH}(E, \varphi_{CEP}) \sim -\alpha(E, \varphi_{CEP}) \frac{I}{4\omega_L^3} \tag{7.2}$$

This relation shows that the emission phase of the harmonics scales linearly with the intensity of the driving laser field. Moreover, it depends on the CEP of the driving field, which is embodied in the phase parameter α determined by the quantum trajectories. These characteristics of the phase of the high harmonics have been intensively studied over the last decades both theoretically [167, 168] and experimentally [169, 170, 164].

7.1.2 Interband and intraband picture in bulk solids

Interband high harmonic generation

The relationship between the phase of the high harmonics arising from the interband motion of electrons/holes and the driving laser parameters is in general difficult to be explicitly expressed in an analytical form. However, we can qualitatively interrogate the relationship by examining the semiconductor Bloch equation (SBE) introduced earlier in this thesis.

We consider again the interband polarization described by the SBE in Eq. 1.21,

$$i\hbar \frac{\partial}{\partial t} p_k = \left[\epsilon_k^{\lambda} + \epsilon_k^{\lambda'} - i\frac{1}{T_d} \right] p_k - d_k E(t)(1 - f_k^{\lambda} - f_k^{\lambda'}) + ieE(t)\nabla_k p_k \tag{7.3}$$

We can see that its temporal variation intrinsically involves a transition described by the dipole element (the second term in Eq. 7.3), which is responsible for the electron-hole pair creation and annihilation (recombination of electron and hole). In the interband polarization, the radiation of high harmonics originates from the electron-hole recombination, and the phase is naturally introduced by the dipole element and the field strength. Furthermore, since the polarization is translated by the driving field in the momentum space, $k \to k + A(t)$ as described by the last term in Eq. 7.3, the electron-hole recombination also occurs at different k points during the time-evolution. Due to the band dispersion $\epsilon_k^{\lambda} - \epsilon_k^{\lambda'}$, the recombination results in the radiation of different energies at different moments in time during the interaction with the laser field. Therefore, the interband harmonics will result in a chirped high harmonic emission as reported by many different works [63, 106, 171]. In other words, the quantum-phase accumulated in the propagation of the electron-hole pair from the creation to the recombination (the first term in Eq. 7.3) is imprinted onto

the absolute phase of interband based harmonics. All the aforementioned processes within the interband polarization involve a driving field in a form of the field itself or the vector potential. Hence, the phase of the interband based harmonics inherently depends on the strength and the CEP of the driving field.

Intraband high harmonic generation

By recalling the description of the intraband motion in the semiclassical model introduced in Chapter 1 (Eq. 1.28), the induced intraband current can be expressed as a function of the driving field with a CEP, $E_L(t) = E_0 \cos(\omega_L t + \varphi_{CEP})$ by replacing the temporal phase $\omega_L t$ with $\omega_L t + \varphi_{CEP}$:

$$J(t) \propto 2 \sum_m m d \varepsilon_{i,m} \sum_n J_{2n-1}\left(m \frac{eE_0 d}{\hbar \omega_L}\right) \sin[(2n-1)(\omega_L t + \varphi_{CEP})] \tag{7.4}$$

The parameter of the driving laser intensity can be found only in the argument of the Bessel function which modulates only the amplitude of an individual harmonic without any effect on its phase. Therefore, the harmonic phase is immune to a change in the intensity of the driving laser. Moreover, the phase of the laser induced intraband is not sensitive to the variation of the CEP of the driving field other than the linear shift in time, $\Delta t = \varphi_{CEP}/\omega_L$. This temporal shift is universal for all harmonic components, implying the synchronization of the emitted harmonics with respect to the peak of the driving field, *i.e.*, all the harmonic components are in phase with the driving field. From this fact, the harmonic bursts emerging from the intraband motion exhibit no chirp in contrast to the interband based high harmonics [61, 42, 104]. Hence, we can summarize: the intraband based harmonics exhibit invariance of their absolute phase under the variation of both the intensity and CEP of the driving laser pulse in contrast to the interpretation in interband motion of electrons and holes.

Crystal potential scattering model

The phase properties of the harmonic radiation within this concept have been highlighted in the previous chapter and particularly in Eq. 6.24. In fact, the harmonic phase in the crystal scattering model shows precisely the same characteristics as in the intraband model. This similarity can be attributed to the fact that both models are founded on the "scattering" of electrons even though from a different scattering source, band dispersion (intraband model) and valence potential (potential scattering model).

7.2 Photoelectron interferometry

Here we are interested to understand how the phase of high harmonics varies under the variation of laser parameters, intensity and CEP, and therewith to attempt a more firm connection between the experiments and the above models. One of the most profound

methods to access the relative phase variation of different parts of a spectrum is interferometry. By interfering an unknown source with a reference source (whose properties remain invariable), the relative phase of the spectral components of the source is directly imprinted on a spectral interference pattern upon variation of a critical parameter that modifies the properties of the unknown source.

We employed a photoelectron based interferometry to study the properties of the high harmonics from solids. The harmonic radiation as will be shown below was spectrally confined to the VUV-EUV range (up to ∼30 eV), where the photon energy is high enough to ionize noble gases such as argon ($I_p =\sim 15.7$ eV) and to create photoelectrons. The EUV instantaneously ionizes an atom via a single photon process, and the temporal information/structure of the EUV is directly transferred to the photoelectron wavepacket as also discussed along with the concepts of the EUV attosecond streaking technique. Interferometry always requires a stable reference wave (or pulse) which must be spectrally overlapped with the pulse we desire to probe. Here, photoelectrons generated by above-threshold ionization (ATI) in atoms by a strong field were employed as the reference source.

Let us now discuss the key idea in more detail. A coherent superposition of photoelectron wavepackets released by EUV and ATI gives rise to an interference pattern which embodies the temporal phase difference between EUV and ATI photoelectrons at each energy point. The interference spectrum can be mathematically expressed by a phase difference between them as:

$$I_{EUV-ATI}(E, I, \varphi_{CEP}) = I_{ATI}+I_{EUV}+2\sqrt{I_{ATI}}\sqrt{I_{EUV}}\cos(\Delta\phi_{ATI-EUV}(E, I, \varphi_{CEP})) \quad (7.5)$$

where I_{ATI} and I_{EUV} are the spectral intensities of the ATI and EUV photoelectrons respectively. The relative spectral phase difference between the ATI and EUV photoelectrons can be expressed as

$$\Delta\phi_{ATI-EUV} = \Delta\phi_{ATI} - \Delta\phi_{EUV} \quad (7.6)$$

Technically speaking, the relative phase variation is directly extractable by tracing the shift of the interference fringes as illustrated in Fig. 7.1. The spectral interference pattern is recorded via the variation of the relevant quantity (intensity or CEP of the driving field, hereafter it will be referred to as "controlled variables x" for generality) as shown in Fig. 7.1 a.

The spectral spacing of fringes $\Delta\eta_0$ is stemming from the temporal separation, *i.e.*, the group delay (ΔT) between the two electron pulses, $\Delta\eta_0 = h/\Delta T$, where h denotes the Planck constant. The relative phase variation introduced by the control variable is represented by the fringe shift (black dashed lines in Fig. 7.1 b) with respect to the reference fringe (cyan color in Fig. 7.1 b). Since one cycle shift of an interference fringe $\Delta\eta_0$ corresponds to a 2π phase shift, the phase variation can be evaluated by its proportion:

$$\Delta\phi_{ATI-EUV}(E, I, \varphi_{CEP}) = 2\pi\frac{\Delta\eta(E)}{\Delta\eta_0} \quad (7.7)$$

At each point of the control variable x_n, the extraction of the spectral phase (Eq. 7.7) permits the mapping of the total spectral phase as a function of the control variable as

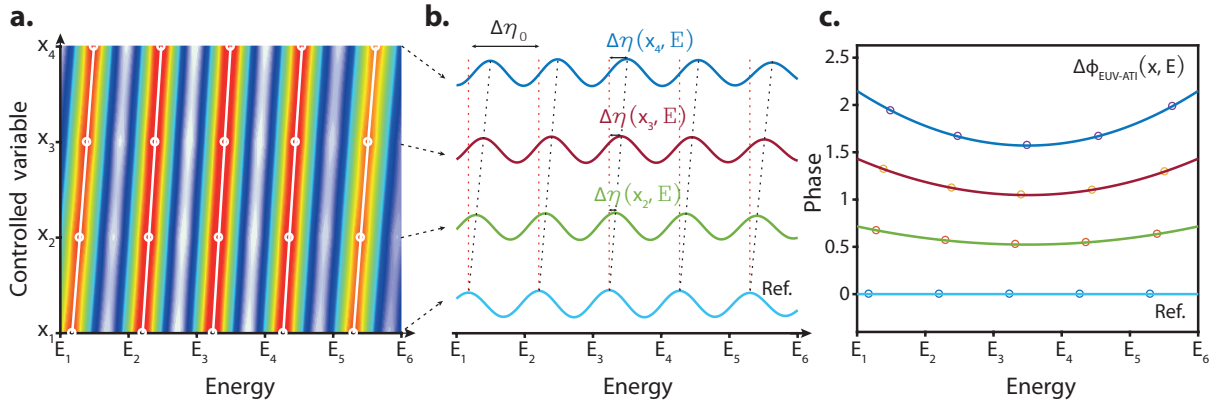

Figure 7.1: **Phase extraction from an interferogram. a**, The spectral fringe variation as a function of energy and a controlled variable x (intensity or the CEP of the driving laser field). White lines superimposed on the 2D spectra denote the shifting trend of the fringe. **b**, Trace of the fringe shift with respect to the reference (cyan) permits access to the phase variation under a controlled variable. The red vertical lines indicate the fringe maxima of the reference, while the black dotted sloped lines denote the tracing of the fringe shifts. **c**, The spectral phase plotted as a function of energy at each value of the variable carefully controlled in an experiment.

denoted by $\Delta\phi_{ATI-EUV}(x, E)$ in Fig. 7.1 c. The relative phase variation $\Delta\phi_{ATI-EUV}$ can be expressed as a polynomial series (Eq. 7.8), and its different orders of the phase involving the CEP and spectral chirp can be evaluated through a fitting of the phase with respect to the central energy $\hbar\omega_c$ as,

$$\Delta\phi_{ATI-EUV}(x,\omega) = \Delta\phi^{(0)}_{ATI-EUV} + \Delta\phi'_{ATI-EUV}(\omega-\omega_c) + \frac{1}{2!}\Delta\phi''_{ATI-EUV}(\omega-\omega_c)^2 + \cdots \quad (7.8)$$

7.3 Experiment and results

7.3.1 Experimental implementation

Single-cycle optical driving pulses delivered from the light field synthesizer (central energy of ∼1.7 eV and pulse duration of ∼2.8 fs; see technology in Chapter 2) were shone onto an ultra-thin (∼1 μm) free standing α-quartz crystal or an argon-filled gas cell (∼100 mbar at $\sim 10^{-2}$ mbar of backing pressure) to generate coherent EUV radiation as shown in Fig. 7.2.

The position of the solid and gas HHG targets was switchable at the focal spot of the driving field using a precision transitional stage. The orientation (Γ-M) of the quartz sample was aligned with the laser polarization vector to maximize the yield of high harmonics. The generated EUV and driving optical pulses were focused onto an argon gas jet to generate photoelectrons as shown in Fig. 7.2. The photoelectrons spectra were recorded by

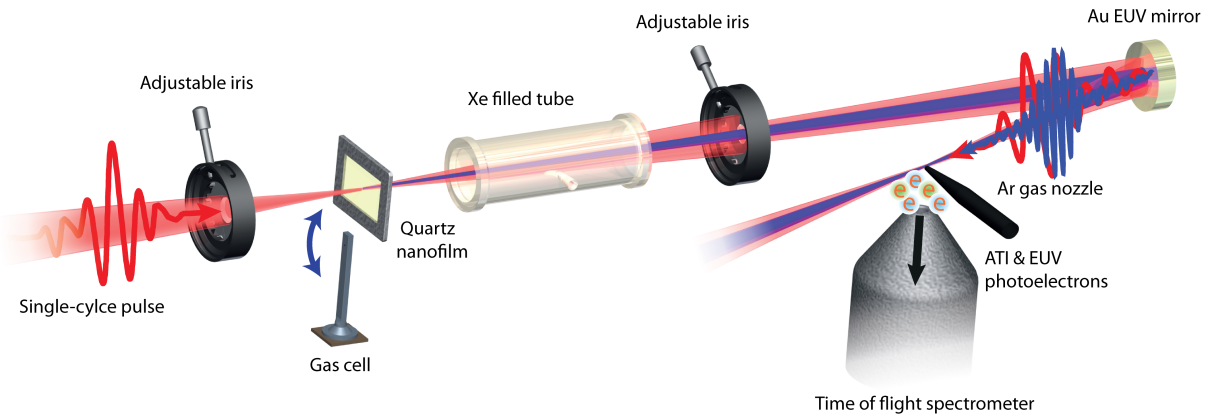

Figure 7.2: **Schematic illustration of the experimental setup for photoelectron interferometry.** Intense single-cycle optical pulses are focused onto an ultrathin ($\sim$1 μm) α-quartz sample or an Ar-filled gas cell to generate coherent EUV radiation. EUV and optical driving field collinearly propagate and are focused onto a second Ar gas jet by a gold coated concave mirror with a focal length of $\sim$12.5 cm. EUV and optical driving field release EUV (linear photoionization) and ATI photoelectrons from Ar, respectively. The spectra of photoelectrons are recorded by a time-of-flight electron spectrometer (TOF). Figure adapted from ref. [107].

a time-of-flight (TOF) electron spectrometer whose entrance was located a few mm above the argon gas jet. The pressure of the gas jet was kept constant to avoid any additional effects from gas density variations.

The ATI photoelectron generation process is well understood under the recollisional model. As a result, an amplitude variation of the driving field results in a pronounced phase change of the ATI photoelectron spectra. To ensure a stable referencing in the experiments, maintaining a constant intensity for ATI generation while varying that for EUV generation is crucial and technically demanding. To this end, we used a long focal length mirror for the EUV generation at the solid-source and a pair of adjustable apertures to control the intensity (Fig. 7.2). The intensity of the pulses generating the EUV harmonics from the quartz sample was controlled by the first adjustable aperture in front of the EUV source. Since the second iris clips only the outer rim of the optical field, regardless of the opening of the first iris, the intensity for the generation of ATI photoelectrons can be kept invariant while the intensity for EUV generation in the HHG chamber (see also Fig. 2.5) can be controlled by the opening of the first iris. Importantly, the intensity of the portion of the pulse that was generating the ATI electron spectra was carefully and continuously recorded during the measurement using a power meter and an imaging system that allowed the visualization of the focus of the beam in the experimental set-up. Owing to the much lower divergence of the EUV beam in comparison to the optical beam, the EUV radiation generated in the quartz sample could pass through the second iris without any significant

clipping.

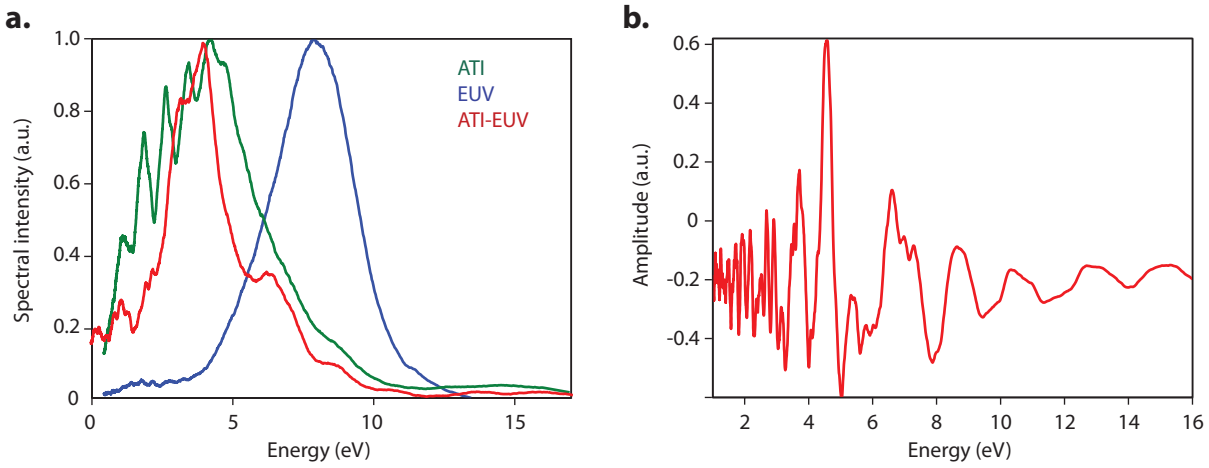

Figure 7.3: **Photoelectron interferometric measurement.** **a**, Photoelectron spectra generated by ATI (green curve), EUV (blue curve), and their interference (red-curve) were recorded by a time-of-flight (TOF) electron spectrometer. **b**, Spectral envelope removed spectrum shows a clear contrast of the interference pattern of the photoelectrons. Figure adapted from ref. [107]

Photoelectron spectra recorded by the TOF spectrometer are shown in Fig. 7.3. ATI electrons measured in the absence of EUV are denoted by the green curve. Note that prior to the EUV photoemission, the EUV pulse (blue curves) was filtered from its fundamental by a high-pass filter (150 nm thin aluminum). Yet, the interferometric measurement was carried out in the absence of the Al-filter, so that a spectral overlap is possible also at lower energies. The coexistence of ATI and EUV photoelectrons gives rise to interference in their common spectral range (red curves in Fig. 7.3 a). The subtraction of the spectral envelopes permits a clear visualization of the fringe pattern (Fig. 7.3 b). The spectral separation of the interference fringes is ∼2.2 eV, which is compatible with a recollision time of ∼1.8 fs of ATI electrons.

7.3.2 Intensity dependence of high harmonic phase in solids

As a first investigation of the phase of high harmonic radiation, the dependence of the phase of EUV emanating from quartz on the intensity of the driving laser pulse was studied and contrasted with that of EUV pulses generated in argon. ATI-EUV photoelectron interference spectra with the quartz sample were recorded as a function of the peak intensity of the driving optical pulse responsible for EUV generation, while the optical intensity for the ATI was kept constant during the measurement. The experiments were conducted within the intensity range of $\sim$ 10 TW/cm^2 up to $\sim$ 22 TW/cm^2 to avoid irreversible optical damage of the sample. As both the intensity and CEP of the optical driving

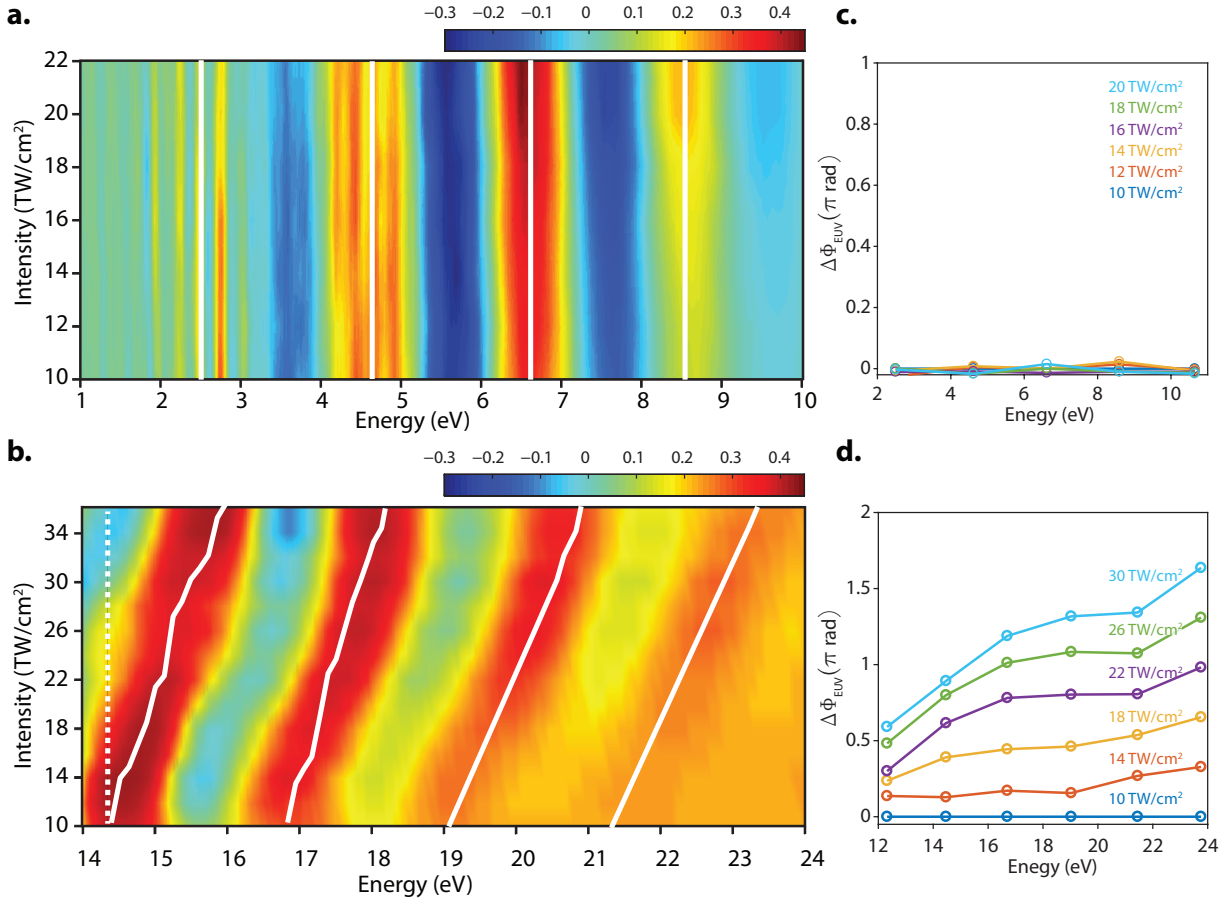

Figure 7.4: **Interferometric measurements with variation of driving optical field intensity for EUV generation.** **a** and **b**, The interference pattern between the ATI photoelectrons and the photoelectrons released by EUV emerging from quartz (**a**) and argon gas (**b**) with variation of the driving field intensity for EUV. The superimposed white curves are guides to the eye to trace the fringe shift, while the dashed vertical white line indicates the reference fringe position. **c** and **d**, The phase variation of EUV $\Delta\phi_{EUV}(E, I)$ as extracted from the data in panel (a) and (b) for quartz and argon gas, respectively. The color codes denote different intensity values used in the experiment. Figure adapted from ref. [107]

field for ATI generation were constant, the phase of the ATI photoelectrons served as a rigid reference. This ensures that the phase variation in ATI-EUV interference is purely originating from the phase variation of the EUV photoelectrons, $\Delta\phi_{ATI-EUV} = -\Delta\phi_{EUV}$. As shown in Fig. 7.4 a, a nearly invariable interference pattern of photoelectrons released by the ATI and EUV emerging in quartz was observed versus intensity.

At this stage, it is useful to contrast these findings in solids with those in gases. Our experimental setup offers directly this capability, and we therefore do not need to resort to

other experimental works. To this end, the same measurement was performed with argon gas as a source of high harmonics under the identical conditions as in the quartz case. With argon as the high harmonic nonlinear medium, a clear variation of the interference pattern versus intensity of the driving field ($\sim$ 10 TW/cm^2 to $\sim$ 35 TW/cm^2) was observed (Fig. 7.4 b). This phase observation agrees well with the predictions of the three-step model which as alluded to earlier in this chapter, predicts a linear variation of the high harmonic phase versus the peak intensity as expressed in Eq. 7.2. This comparison evidently points to a major difference in the mechanism of EUV generation in solids and gaseous media.

As an additional investigation, the total EUV phase variation was evaluated. Since the interference fringes were spaced by $\sim$2.2 eV, *i.e.*, $\Delta\eta_0 = 2.2$ eV, a tracing of the fringe shift in energy $\Delta\eta(E)$ allows evaluating the spectral phase variation of the EUV pulses $\Delta\phi_{EUV}$ as a function of laser intensity I with respect to the phase of EUV at the lowest intensity (Fig. 7.4 c and d).

$$\Delta\phi_{EUV}(E, I) = 2\pi \frac{\Delta\eta(E, I)}{2.2eV} \tag{7.9}$$

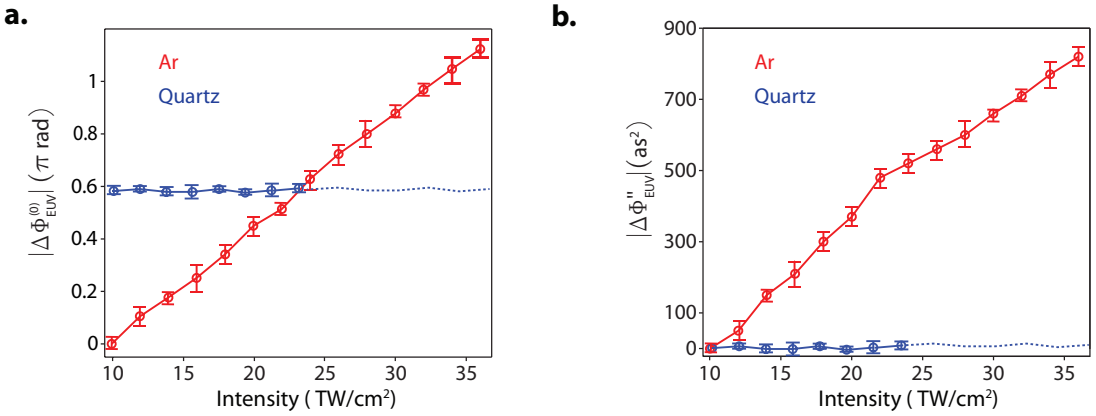

Figure 7.5: **CEP and GDD variation of the radiated EUV pulses with increasing intensity of the driving field.** Variation of CEP (**a**) and GDD (**b**) of EUV emerging from quartz (blue curve) and Ar gas (red curve), respectively extracted from the interference measured with increasing intensity of the driving field. Figure adapted from ref. [107]

The extracted phases can be fitted to a polynomial expansion around the central energy of the EUV emission ($\sim$23 eV and $\sim$34 eV for quartz and Ar, respectively) in the spectral domain for each laser intensity such to evaluate the intensity dependent CEP $\Delta\phi^{(0)}_{EUV}(I)$, group delay dispersion (GDD) $\Delta\phi''_{EUV}(I)$ and even higher order dispersion of the EUV (Fig. 7.5). The EUV pulses emerging from the quartz samples exhibit negligible variation of their CEP and GDD versus the intensity of the driving field (blue curves in Fig. 7.5), while those from Ar gas undergo a significant change (red curves in Fig. 7.5) as indicated by a slope of $\sim 5 \times 10^{-2}\pi$ (TW/cm^2)$^{-1}$ for CEP and $\sim$ 30 as^2(TW/cm^2)$^{-1}$ for GDD.

The above experiment clearly demonstrates that the phase of EUV emission from the quartz is virtually immune to the variation of the driving field intensity. This experimental observation is in good agreement with both the intraband and potential scattering models but not with the interband or the recollison picture.

Effect of the sample thickness on the spectral phase of the irradiated EUV

Due to the linear absorption of EUV light in most optically transparent materials, the high harmonic emission in the EUV range primarily takes place within few nanometers near the exit of a sample. However, the intense driving pulse undergoes a phase shift due to the Kerr nonlinearities before reaching the exit of the sample. This phase shift of the driving field acting on HHG will give an additional and undesirable phase shift to the interferometric measurement discussed above. In other words, the phase variation of EUV cannot be treated as a result of the intensity variation of the driving field only but also as a result of the intensity dependent phase variation of the driving pulse propagating in the medium. This fact suggests that a solid sample has to be properly chosen (in terms of thickness) to avoid such effects. In fact, these effects can lead to conclusions that would favor other pictures. How can we be sure that in the above experiments we are in a "safe regime"?

To explore this idea, the same intensity-dependence experiment was conducted using thicker samples, $\sim$10 μm and $\sim$20 μm. Fig. 7.6 shows significant differences in the recorded phase.

The accumulated Kerr phase variation of the driving field in the sample can be reasonably estimated by the B-integral,

$$B = \frac{2\pi}{\lambda} \int dz n_2 I(z) \tag{7.10}$$

where λ, $I(z)$ and n_2 are the central wavelength of the driver pulse, the intensity and the nonlinear refractive index of optical medium, respectively. z is the propagation length. The intensity is strictly a propagation dependent quantity which is varied by linear dispersion and self-focusing effect due to the Kerr nonlinearity. Here, given that the samples we study are rather thin, we assumed that the intensity of the beam remains constant for the entire propagation length. A simulated ATI-EUV phase variation involving the induced Kerr phase shows a reasonable agreement with the measured phase variation with thick samples (Fig. 7.6 b and c). Because of the normal incidence of light on the sample, the Fresnel reflection was taken into account for avoiding an overestimation of the intensity inside the medium. The phase shift originated by the Kerr effect amounted to $\sim 0.02\pi$ radian in the case of a 1 μm thick quartz at the highest intensity ($\sim$ 22 TW/cm^2) used in the experiment. Therefore, under the experimental conditions (1 μm quartz, intensity range from 10 to 22 TW/cm^2), the Kerr effect is negligible.

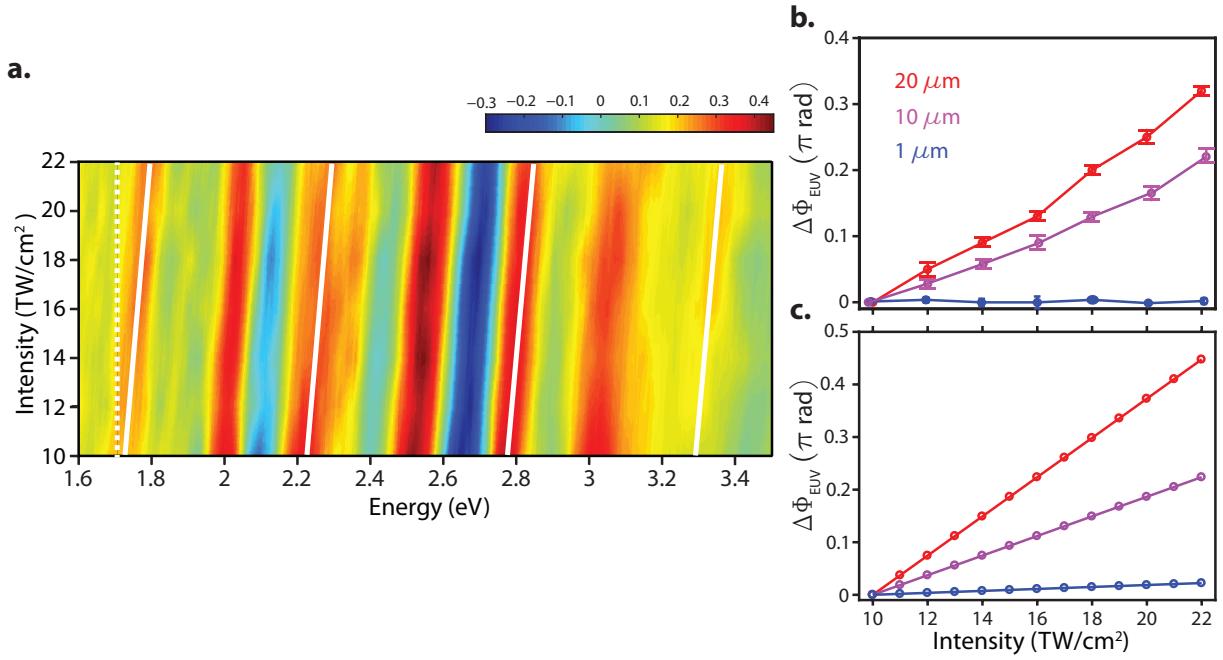

Figure 7.6: **Effect of sample thickness on the spectral phase of the emitted EUV radiation.** **a**, Interference pattern of ATI and EUV photoelectrons when the EUV is generated in a 20 μm thick quartz sample was recorded as a function of the driving field intensity. The white lines are guides for the eye and represent fringe shifts, while the white dashed vertical line indicates the reference fringe position. **b** and **c**, Measured (b) and simulated (c) ATI-EUV phase variation versus driving field intensity. The three different colors of the lines indicate different thicknesses (1, 10 and 20 μm). Figure adapted from ref. [107]

7.3.3 CEP dependence of high harmonic phase in solids

In analogy to the first set of experiments, the phase variation of EUV was also studied by varying the CEP of the driving field. Under the same experimental configuration as in the previous study, the CEP was varied, while the driving field intensity for both EUV and ATI was kept constant. The recorded ATI-EUV interference fringes as a function of the CEP of the driving field for quartz are shown in Fig. 7.7 a. Note however that in this experiment, the CEP of the driving pulse used for the ATI photoelectrons is also varied. This is due to the collinear geometry of our experiment setup. As a consequence, the ATI photoelectrons cannot anymore provide a rigid reference, as the ATI photoelectron phase $\Delta\phi_{ATI}(E, \varphi_{CEP})$ is sensitive to CEP. Therefore, it is essential to characterize the CEP dependence of ATI phase in advance. To this end, the phase variation of ATI photoelectrons was separately measured under the identical conditions (Fig 7.7 b). For the extraction of phase variation of ATI, the concept of interferometry was applied in the same manner as before. The ATI

photoelectron pulses comprise a few isolated photoelectron bursts (∼3 for a ∼1.2 cycle pulse used in the experiment) with a relative time delay of one cycle of the optical driving field. This fact was manifested by an interference pattern in the overlapping energy area. The peaks in the ATI spectra were separated by the carrier photon energy ($\Delta\eta_0 =\sim 1.7$ eV). Correspondingly, the phase of the ATI photoelectrons can be evaluated by the proportion of energy spacing between the spectral peaks as:

$$\Delta\phi_{ATI}(E,\varphi_{CEP}) = 2\pi\frac{\Delta\eta_{ATI}(E,\varphi_{CEP})}{1.7eV} \tag{7.11}$$

To isolate the EUV phase variation versus CEP (Fig. 7.7 e) was possible by subtracting the ATI phase variation (Fig. 7.7 d) from the ATI-EUV phase (Fig. 7.7 c) according to Eq. 7.6. Note that since the sampled energy points were different between the ATI-EUV and ATI interference measurement, a data interpolation was necessary for the accurate evaluation of EUV phase variation.

As one can easily notice by comparison of the measurements in Fig. 7.7 a and b, the fringe shift in the ATT-EUV interference is mainly originated from the ATI phase variation, when the EUV source is the quartz sample. The evaluated EUV phase $\Delta\phi_{EUV}(E,\varphi_{CEP})$ shows a clear invariance of the high harmonic phase under the variation of laser CEP (Fig. 7.7 e).

In order to further contrast to the recollision based harmonic generation in gaseous media, the experiment was repeated under the same conditions but with Ar gas as a harmonic source (Fig. 7.8). By contrasting Fig. 7.8 a with b, ATI-EUV relative phase shows more rapid fringe shifts (Fig. 7.8 c) than ATI interference change (Fig. 7.8 d), indicating an EUV phase variation under the changes of the driving pulse CEP (Fig. 7.8 e) in the case of Ar gas as the EUV source.

Similarly as in the previous set of experiments, the driving field CEP-dependent CEP $\Delta\phi^{(0)}_{EUV}(\varphi_{CEP})$ and GDD $\Delta\phi''_{EUV}(\varphi_{CEP})$ variation of harmonic was evaluated by the polynomial fitting for the case of quartz (blue curve) and Ar gas (red curve) as shown in Fig. 7.9. In the quartz case, the invariance of CEP and GDD was clearly observed, while there was a substantial change in those in EUV from Ar gas with slope of $\sim 1.4\pi$ for CEP and 6200 as^2 for GDD within a π shift of the driving field CEP.

The above experiments and their analysis reveal that the phase of high harmonics emitted from dielectric materials is rather insensitive to both the intensity and CEP of the driving field. The immunity of the high harmonic phase is well captured and explained by the scattering based models (intraband and potential scattering model) but not by the recollision models that dominate atomic strong field physics. The phase robustness of solid state high harmonics against the intensity and CEP variation lends high harmonic generation in solids as a stable EUV source for phase sensitive applications including EUV frequency combs.

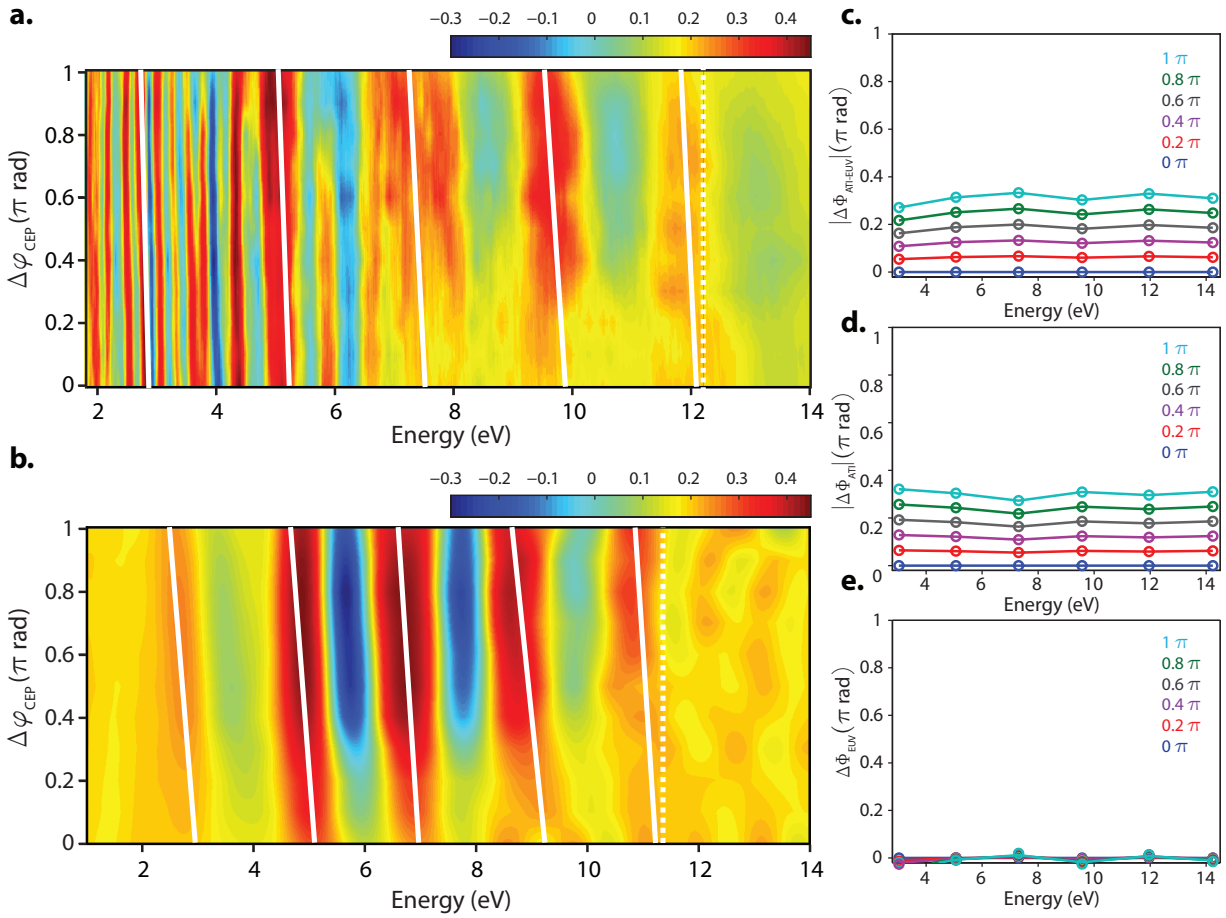

Figure 7.7: **Interferometric measurement of ATI-EUV spectra with variation of the CEP of the driving optical field in quartz. a** and **b**, The interference fringes of photoelectrons emitted by ATI and EUV emerging from quartz (a) and ATI fringes in the absence of the EUV (b) with variation of the CEP of the driving field from 0 to π rad. The white lines superimposed on the spectra are guides to indicate the fringe shift, while the white dashed vertical lines denote reference fringe position. **c**, The variation of ATI-EUV phase $\Delta\phi_{ATI-EUV}(E, \varphi_{CEP})$ extracted from the data (a). **d**, The ATI phase variation $\Delta\phi_{ATI}(E, \varphi_{CEP})$ extracted from the data (b). **e**, EUV phase variation under varying the CEP of driving field $\Delta\phi_{EUV}(E, \varphi_{CEP})$ was retrieved by the subtraction of the ATI phase variation from ATI-EUV relative phase. The color codes denote different CEP values used in the experiment. Figure adapted from ref. [107].

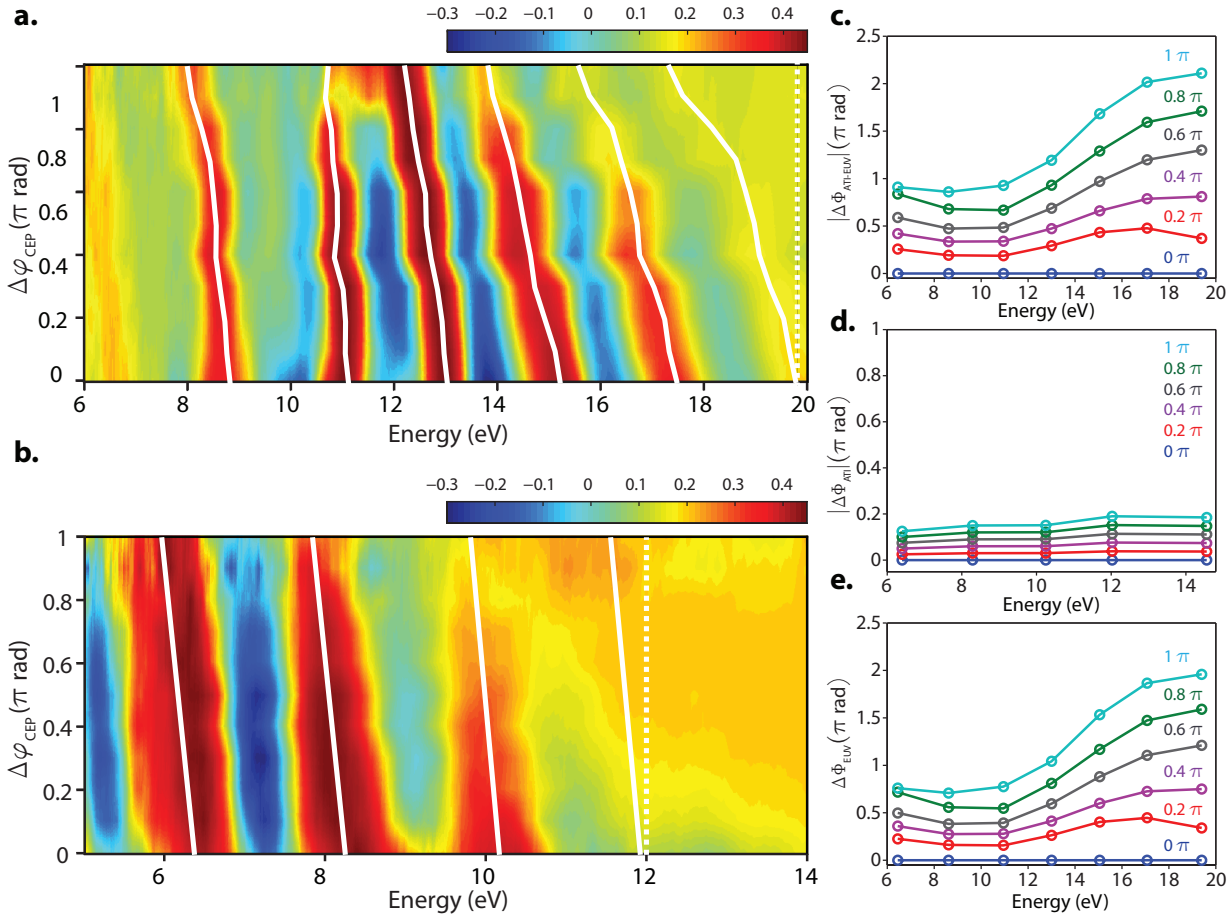

Figure 7.8: **Interferometric measurement of ATI-EUV spectra with variation of the CEP of the driving optical field in Ar.** **a** and **b**, The interference fringes of photoelectrons induced by ATI and EUV emerging from Ar (**a**) and ATI fringes in the absence of the EUV (**b**) with varying the CEP of the driving pulse from 0 to π rad. The white lines indicate the trace of fringe shift, while the white dashed vertical lines are guides for the eye to indicate the reference. **c** and **d**, The phase variation of ATI-EUV $\Delta\phi_{ATI-EUV}(E, \varphi_{CEP})$ extracted from the data (a) and that of ATI $\Delta\phi_{ATI}(E, \varphi_{CEP})$ from the data (b). **e**, By the subtraction of the ATI phase from the ATI-EUV, the EUV phase variation can be evaluated. Figure adapted from ref. [107]

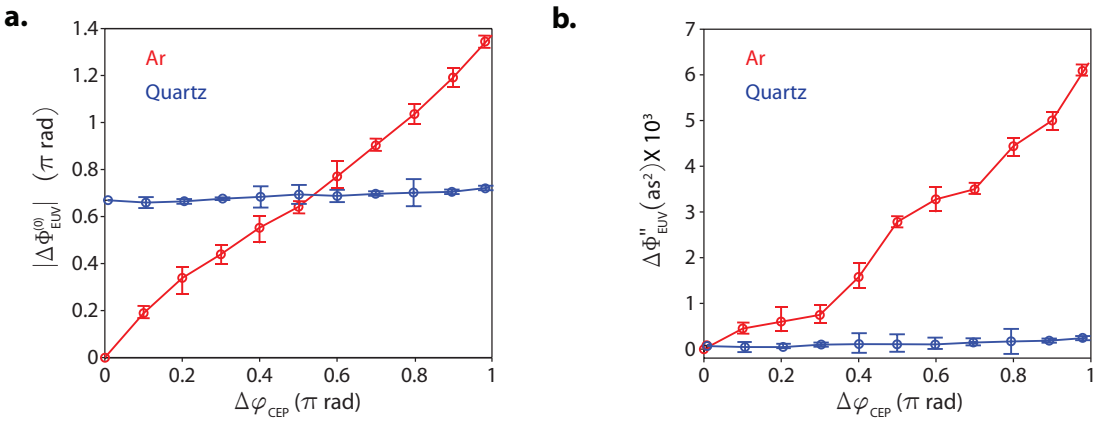

Figure 7.9: **CEP and GDD variation of EUV radiation with varying the CEP of the driving field.** Variation of CEP (**a**) and GDD (**b**) of the EUV emerging from quartz (blue curve) and Ar gas (red curve), respectively extracted from the interference measured with the CEP variation of the driving field. Figure adapted from ref. [107].

Conclusions and outlook

The important thing is not to stop questioning. Curiosity has its own reason for existing.
-Albert Einstein

In this thesis, I present experimental studies on the strong field electron emission from metallic nanotips in the single-cycle pulse limit as well as studies of high harmonic emission from bulk solids.

When single-cycle pulses are shone on nanotips, the high energy spectral emission is confined to a fraction of a half field cycle. We have seen that the energetic properties of the photoelectrons liberated from the tungsten nanotip comply with the predictions of semiclassical theories in atoms opening up new opportunities for generating ultrashort electron pulses.

To investigate the temporal characteristics of the generated attosecond electron pulses, I introduced a new approach, namely Homochromic attosecond streaking (HAS). There, a strong optical driving pulse (pump) generates and drives the photoelectron emission, and a weak (10^{-2} in intensity) replica of the same pulse probes the released photoelectron pulse in time. We have shown theoretically that a variation of the delay between pump and gate allows the composition of spectrograms which contain critical information about the attosecond electron pulse and the locally enhanced single-cycle field.

We used this method practically to measure attosecond electron pulses as short as 53 ± 5 as. The temporal confinement of the attosecond electron pulse emerging from metallic nanostructures driven by single-cycle pulses is anticipated to inspire a broad range of electron-based spectroscopy applications. First of all, the sufficient electron energy at the back-scattering (20 eV-80 eV) will allow applications of these pulses in electron based microscopy of solids. For instance, one can consider a pump-probe scheme of low energy electron diffraction (LEED) using the back-scattered electron characterized in a HAS on the same sample. Time-resolved measurements in the LEED could provide a deeper understanding of dynamic structural phenomena in solids. The generated electron pulses can be used at its full temporal resolution, if the sample that is used to create the electron pulse is also probed by the recolliding attosecond bursts. A sample in the close vicinity of the tip, typically implemented in STM could also allow probing another system without a big loss of temporal resolution. We can anticipate applications of our technique also in lightwave electronics. The field controllability of the attosecond current emitted

from the nanotip provides a possible root to the attosecond light electronics in structured metals. More specifically, PHz electron transport at the interface among different nanotips can be precisely controlled by the pump field, while its temporal characteristics could be accessed by HAS.

Strong field induced electron motion in wide band-gap materials and associated high harmonic generation were also studied. I have taken the first steps towards laying the foundation of the scattering model using the Floquet approach. Although not complete, the approach can provide an insight as to how a strong field can lead to a strong suppression of the effective valence potential and therefore, a quasi-free electron motion along with the strong driving field emerges. A potential dramatic implication of the interaction could open new ways to probing solids. The first step in this direction was the first all optical probing of the valence potential of solids [67]. Experimentally I have also focused on studies about high harmonic generation that aim at the direct measurement of phase effects on high harmonics [107]. The phase of harmonics emerging from SiO_2 was studied by utilizing photoelectron interferometry emerging from above-threshold ionization and EUV pulses originally generated from solids. We found that in contrast to the prediction of the recollision model in gases or ordinary interband models in solids, the phase of the emission appears rather insensitive to the peak field strength and CEP of the driving pulses. This observation strongly supports the scattering based models in both potential and band space.

Appendix A

Time-dependent Schrödinger equation (TDSE)

The light-electron interaction in 1D space is described by the Schrödinger equation (in atomic units),

$$i\frac{\partial\psi(x,t)}{\partial t} = \hat{H}\psi(x,t) \tag{A.1}$$

where the Hamiltonian $\hat{H}$ is given by the potential $\hat{V}(x)$ and the laser-electron dipolar interaction $-E(t)x$ in the length gauge,

$$\hat{H} = \hat{H}_0 + \hat{H_{int}} = -\frac{1}{2}\frac{\partial^2}{\partial x^2} + \hat{V}(x) - E(t)x \tag{A.2}$$

To model the atomic potential, a modified Coulombic potential (soft-core potential) is widely used to avoid the singularity of the Coulomb potential at 0 [87, 85].

$$\hat{V}(x) = -\frac{1}{\sqrt{x^2+a^2}} \tag{A.3}$$

where a is a parameter for the core size, which is chosen to fit the ionization energy of the considered system. For instance, atomic potential of argon can be modeled with $a = 1.19$ AU to fit its ionization energy, 15.7 eV.

Computation of ground state through diagonalization of Hamiltonian

The ground state of the Hamiltonian is considered as the initial state of the system. The ground state can be found by imaginary-time propagation method or diagonalization of the Hamiltonian [85, 86]. The diagonalization is computationally more expensive than the imaginary-time propagation method. However, it has the advantage of accessing all eigenstates and eigenenergies, while the imaginary propagation provides only the ground state. Here we consider only the latter.

In the finite difference approach, the second derivative in the Hamiltonian can be approximated to

$$\frac{\partial^2\psi(x,t)}{\partial x^2} = \frac{\psi(x+\Delta x,t) - 2\psi(x,t) + \psi(x-\Delta x,t)}{\Delta x^2} \tag{A.4}$$

then one can easily cast the Hamiltonian into a matrix form as,

$$\hat{H}_0 = \frac{1}{2\Delta x^2}\begin{bmatrix} -2 & 1 & 0 & \cdots & 0 \\ 1 & -2 & 1 & \cdots & 0 \\ \vdots & \ddots & \ddots & \ddots & \vdots \\ 0 & \cdots & 1 & -2 & 1 \\ 0 & \cdots & 0 & 1 & -2 \end{bmatrix} + \begin{bmatrix} V(x_1) & 0 & 0 & \cdots & 0 \\ 0 & V(x_2) & 0 & \cdots & 0 \\ \vdots & \ddots & \ddots & \ddots & \vdots \\ 0 & \cdots & 0 & V(x_{n-1}) & 0 \\ 0 & \cdots & 0 & 0 & V(x_n) \end{bmatrix} \tag{A.5}$$

The diagonalization of the above matrix gives both eigenstates and corresponding eigensenegies. The ground state is the one with the lowest energy in the set of the eigenstates.

Time propagation of wavepacket

Solving the TDSE analytically is generally difficult because it is an inhomogeneous differential equation in both time and space. However, the problem can be numerically solved by real-time propagation employing the split-step Fourier method, also known as the split-operator method [88]. From the fact that wavepacket propagation by kinetic and potential energy operator can be directly evaluated in reciprocal and real space, respectively, *i.e.*, $i\partial_t\tilde{\psi}(k,t) = -k^2\tilde{\psi}(k,t)$ for kinetic energy operator and $i\partial_t\psi(x,t) = \hat{V}_{eff}(x,t)\psi(x,t)$ for potential energy operator, where $\hat{V}_{eff}(x,t) = V(x) - E(t)x$, alternative calculations in real and reciprocal spaces enable the complete time evolution of the wavepacket. The calculation sequence is as following:

1. At an instance of time (t), the propagation of wavefunction $\psi(x,t)$ in the time step of $\Delta t/2$ is performed in real space only with the potential operator $\hat{V}_{eff}(x,t)$,

$$\psi(x,t+\Delta t/2) = \psi(x,t)\exp[-i\hat{V}_{eff}(x,t)\Delta t/2] \tag{A.6}$$

2. To solve the differential equation with kinetic operator, the propagation from t to $t+\Delta t$ is performed in the reciprocal space,

$$\tilde{\psi}(k,t+\Delta t) = \tilde{\psi}(k,t+\Delta t/2)\exp[-ik^2\Delta t], \tag{A.7}$$

   where $\tilde{\psi}(k,t)$ is the Fourier transformed wavepacket.

3. Back to the real space by inverse Fourier transform, the propagation from t to Δt is completed by evaluation of additional real space propagation with time step of $\Delta t/2$,

$$\psi(x,t+\Delta t) = \psi(x,t)\exp[-i\hat{V}_{eff}(x,t)\Delta t/2]. \tag{A.8}$$

Appendix B

Analysis of experimentally measured photoelectron spectra

B.1 Renormalization of spectra measured by time-of-flight spectrometer

The time-of-flight electron spectrometer (TOF) basically records the arriving time of the photoelectron to the detector in a uniformly spaced time axis. Due to the nonlinear relationship of energy (E) with the arriving time (t_a), the transform of the arrival time to the corresponding kinetic energy domain results in an uneven spaced energy axis, where the binning spacing is nonlinearly increasing with the energy. In other words, at a higher energy point, the photoelectron yield is counted in a broader range of energy, and it gives a rise of overestimation of high energetic spectral intensity. The spectra in two different domains must fulfill the condition,

$$\int dt_a I(t_a) = \int dE I(E) \tag{B.1}$$

Therefore, the Jacobian (dt/dE) must be used to renormalize the spectral intensity in the energy domain,

$$I(E) = I(t_a)\frac{dt_a}{dE} \tag{B.2}$$

B.2 Reduction of noise in measured photoelectron spectra

The photoelectron signal captured by the TOF is delicate enough to be easily contaminated by the noise from the measuring instruments, for instance noise from electronic resonance in the cables and interference inside the oscilloscope.

Fig. B.1 a shows noise in the domain of arrival time, measured in the absence of photoelectrons. Noise covering the energy range of our interest from ∼10 eV (red vertical

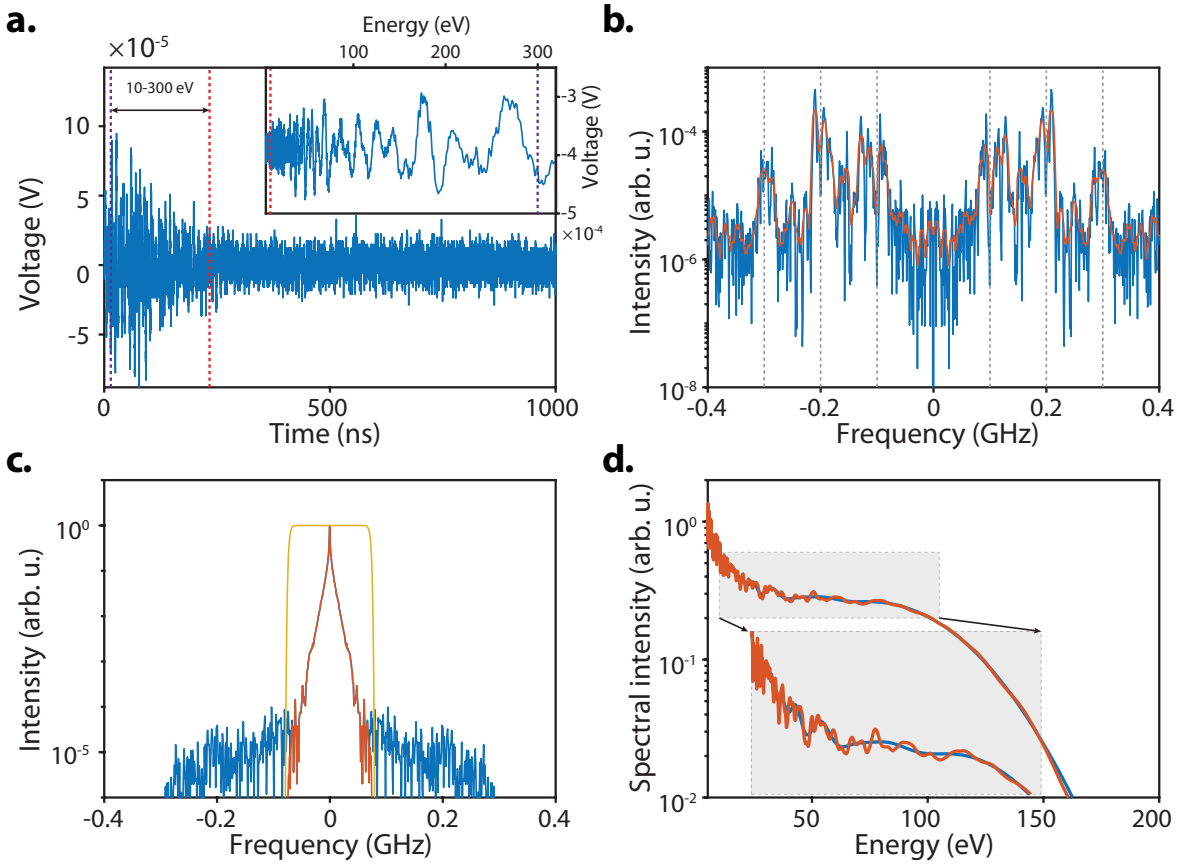

Figure B.1: **Reduction of noise in measured photoelectron spectra.** **a**, Signal-free noise originating from measuring instruments was measured in the absence of photoelectrons and plotted in the arrival time domain of the TOF. The inset displays the noise in the converted energy domain. The vertical dashed lines show the energy range of interest and its corresponding arrival time. **b**, Fourier transform of the noise provides its characteristic spectrum in the frequency of the arrival time. **c**, The signal in the frequency domain of the arrival time (blue) is filtered by a hyper-Gaussian low-pass filter (yellow) to eliminate the characteristic frequency components of the noise (> 0.1 GHz). **d**, The frequency filtered signal (red in panel c) is converted to a noise-reduced signal in the energy domain (blue). The red curve shows unprocessed signal.

line) to 300 eV (purple vertical line) is discernible. Moreover, it was observed that such noise was also amplified accordingly to the level of the signal of the photoelectrons. The noise contaminates the signal in the arrival time domain of the TOF and results in an uneven spaced oscillatory noise, which is difficult to eliminate in the energy domain (inset in Fig. B.1 a). Therefore, in order to acquire a meaningful signal of photoelectrons, the TOF signal needs to be essentially filtered in the TOF time domain before converting

to the energy domain. The signal-free noise can be used to identify its frequency for the Fourier filtering. Since the noise of our system exhibits harmonics of 0.1 GHz (blue vertical lines in Fig. B.1 b), and the bandwidth of photoelectron signal in the frequency domain is less than 0.2 GHz centered at zero (Fig. B.1 c), the noise can be safely eliminated by a hyper-Gaussian low-pass filter with its corresponding bandwidth (yellow curve in Fig. B.1 c). Through the filtering process, noise-reduced photoelectron spectrum can be obtained as shown in Fig. B.1 d.

Appendix C

Crystal potential scattering model

The general form of potential including both symmetric and asymmetric components reads,

$$V(\mathbf{r}) = Re\big[\sum_{\mathbf{G}} \tilde{V}_{\mathbf{G}} \exp(i\mathbf{G}\cdot\mathbf{r})\big] = \underbrace{\sum_{\mathbf{G}} V_{\mathbf{G}}^{(r)} \cos(\mathbf{G}\cdot\mathbf{r})}_{\text{symmetric}} - \underbrace{\sum_{\mathbf{G}} V_{\mathbf{G}}^{(i)} \sin(\mathbf{G}\cdot\mathbf{r})}_{\text{asymmetric}} \tag{C.1}$$

where the complex spatial Fourier amplitude $\tilde{V}_{\mathbf{G}}$ consists of real $V_{\mathbf{G}}^{(r)}$ and imaginary $V_{\mathbf{G}}^{(i)}$ parts, $\tilde{V}_{\mathbf{G}} = V_{\mathbf{G}}^{(r)} + iV_{\mathbf{G}}^{(i)}$. The symmetric and asymmetric components of the potential are dictated by the real and imaginary components of complex Fourier amplitude, respectively. In the presence of a strong field, $E_L(t) = E_0 \sin(\omega_L t) e_{\parallel}$, the time derivative of electron current is then given by $d\mathbf{J}/dt \propto -\nabla V(\mathbf{r})|_{\mathbf{r}=\langle\mathbf{r}(t)\rangle}$,

$$\frac{d\mathbf{J}}{dt} \propto \sum_{\mathbf{G}} \mathbf{G} V_{\mathbf{G}}^{(r)} \sin(\mathbf{G}\cdot\langle\mathbf{r}(t)\rangle) + \sum_{\mathbf{G}} \mathbf{G} V_{\mathbf{G}}^{(i)} \cos(\mathbf{G}\cdot\langle\mathbf{r}(t)\rangle) \tag{C.2}$$

High harmonics in the parallel direction of laser polarization

The current parallel to the laser polarization in Eq. C.2 is given by

$$\frac{d\mathbf{J}_{\parallel}}{dt} \propto \sum_{\mathbf{G}} \mathbf{G}_{\parallel} V_{\mathbf{G}}^{(r)} \sin(\mathbf{G}\cdot\langle\mathbf{r}(t)\rangle) + \sum_{\mathbf{G}} \mathbf{G}_{\parallel} V_{\mathbf{G}}^{(i)} \cos(\mathbf{G}\cdot\langle\mathbf{r}(t)\rangle) \tag{C.3}$$

where $\mathbf{G}_{\parallel}$ indicates the reciprocal vector parallel to the laser polarization, *i.e.*, $\mathbf{G}_{\parallel} = (\mathbf{G}\cdot\mathbf{e}_{\parallel})\mathbf{e}_{\parallel}$. The expectation value of the electron excursion reads $\langle\mathbf{r}(t)\rangle = \frac{eE_0}{m_e\omega_L^2}\sin(\omega_L t)\mathbf{e}_{\parallel}$, and Eq. C.3 can be rewritten as,

$$\frac{d\mathbf{J}_{\parallel}}{dt} \propto \sum_{\mathbf{G}} \mathbf{G}_{\parallel} V_{\mathbf{G}}^{(r)} \sin\left(\mathbf{G}\cdot\mathbf{e}_{\parallel}\frac{eE_0}{m_e\omega_L^2}\sin(\omega_L t)\right) + \sum_{\mathbf{G}} \mathbf{G}_{\parallel} V_{\mathbf{G}}^{(i)} \cos\left(\mathbf{G}\cdot\mathbf{e}_{\parallel}\frac{eE_0}{m_e\omega_L^2}\sin(\omega_L t)\right) \tag{C.4}$$

Using the Jacobi-Anger expansion,

$$\begin{aligned}\cos(z\sin(\theta)) &= J_0(z) + 2\sum_{n=1}^{\infty} J_{2n}(z)\cos(2n\theta)\\ \sin(z\sin(\theta)) &= 2\sum_{n=1}^{\infty} J_{2n-1}(z)\sin[(2n-1)\theta]\end{aligned} \tag{C.5}$$

the current variation is expanded with terms of laser harmonics,

$$\begin{aligned}\frac{d\mathbf{J}_\parallel}{dt} \propto & \underbrace{\sum_{\mathbf{G}}\sum_{n} \mathbf{G}_\parallel V_{\mathbf{G}}^{(r)} J_{2n-1}\left(\mathbf{G}_\parallel \frac{eE_0}{m_e\omega_L^2}\right)\sin((2n-1)\omega_L t)}_{\text{Odd Harmonics}}\\ & + \underbrace{\sum_{\mathbf{G}}\sum_{n} \mathbf{G}_\parallel V_{\mathbf{G}}^{(i)} J_{2n}\left(\mathbf{G}_\parallel \frac{eE_0}{m_e\omega_L^2}\right)\cos(2n\omega_L t)}_{\text{Even harmonics}} + \sum_{\mathbf{G}} \mathbf{G}_\parallel V_{\mathbf{G}}^{(r)} J_0\left(\mathbf{G}_\parallel \frac{eE_0}{m_e\omega_L^2}\right)\end{aligned} \tag{C.6}$$

As one can find in the Eq. C.6, the even harmonics are induced by the imaginary part of the potential which is responsible to the asymmetricity of the potential, linking the broken inverse symmetry to the even harmonics. The odd and even harmonic intensities are then given by

$$\begin{aligned} I_{2n-1}(E_0,\omega_L,\mathbf{e}_\parallel) &\propto \left|\sum_{\mathbf{G}} \mathbf{G}_\parallel V_{\mathbf{G}}^{(r)} J_{2n-1}\left(\mathbf{G}_\parallel \frac{eE_0}{m_e\omega_L^2}\right)\right|^2 = \left|\sum_{G_\parallel} \mathbf{G}_\parallel V_{proj}^{(r)} J_{2n-1}\left(\mathbf{G}_\parallel \frac{eE_0}{m_e\omega_L^2}\right)\right|^2\\ I_{2n}(E_0,\omega_L,\mathbf{e}_\parallel) &\propto \left|\sum_{\mathbf{G}} \mathbf{G}_\parallel V_{\mathbf{G}}^{(i)} J_{2n}\left(\mathbf{G}_\parallel \frac{eE_0}{m_e\omega_L^2}\right)\right|^2 = \left|\sum_{G_\parallel} \mathbf{G}_\parallel V_{proj}^{(i)} J_{2n}\left(\mathbf{G}_\parallel \frac{eE_0}{m_e\omega_L^2}\right)\right|^2 \end{aligned} \tag{C.7}$$

where V_{proj} refers to the projected Fourier amplitude, $V_{proj} = \sum_{\mathbf{G}_\perp} V_{\mathbf{G}}$.

High harmonics in the perpendicular direction of laser polarization

Similarly the current whose direction is perpendicular to the laser polarization can be simply derived from Eq. C.2 as,

$$\begin{aligned}\frac{d\mathbf{J}_\perp}{dt} \propto & \underbrace{\sum_{\mathbf{G}}\sum_{n} \mathbf{G}_\perp V_{\mathbf{G}}^{(r)} J_{2n-1}\left(\mathbf{G}_\parallel \frac{eE_0}{m_e\omega_L^2}\right)\sin((2n-1)\omega_L t)}_{\text{Odd Harmonics}}\\ & + \underbrace{\sum_{\mathbf{G}}\sum_{n} \mathbf{G}_\perp V_{\mathbf{G}}^{(i)} J_{2n}\left(\mathbf{G}_\parallel \frac{eE_0}{m_e\omega_L^2}\right)\cos(2n\omega_L t)}_{\text{Even harmonics}} + \sum_{\mathbf{G}} \mathbf{G}_\perp V_{\mathbf{G}}^{(r)} J_0\left(\mathbf{G}_\parallel \frac{eE_0}{m_e\omega_L^2}\right)\end{aligned} \tag{C.8}$$

where $\mathbf{G}_\perp$ denotes the reciprocal vector perpendicular to the laser polarization, $\mathbf{G}_\perp = \mathbf{G} - \mathbf{G}_\parallel$. The intensity of perpendicular harmonics is then given by

$$\begin{aligned} I_{2n-1}(E_0, \omega_L, \mathbf{e}_\perp) &\propto \left| \sum_{\mathbf{G}} \mathbf{G}_\perp V_{\mathbf{G}}^{(r)} J_{2n-1}\left(\mathbf{G}_\parallel \frac{eE_0}{m_e \omega_L^2} \right) \right|^2 \\ I_{2n}(E_0, \omega_L, \mathbf{e}_\perp) &\propto \left| \sum_{\mathbf{G}} \mathbf{G}_\perp V_{\mathbf{G}}^{(i)} J_{2n}\left(\mathbf{G}_\parallel \frac{eE_0}{m_e \omega_L^2} \right) \right|^2 \end{aligned} \tag{C.9}$$

Bibliography

[1] F. Krausz and M. Ivanov, "Attosecond physics," *Rev. Mod. Phys.*, vol. 81, pp. 163–234, Feb 2009.

[2] A. H. Zewail and J. M. Thomas, *4D Electron Microscopy*. IMPERIAL COLLEGE PRESS, 2009.

[3] N. Bohr, "I. on the constitution of atoms and molecules," *The London, Edinburgh, and Dublin Philosophical Magazine and Journal of Science*, vol. 26, no. 151, pp. 1–25, 1913.

[4] E. Hecht, *Optics*. Addison-Wesley, 4. ed., 2002.

[5] R. W. Boyd, *Nonlinear optics*. Academic press, 2003.

[6] T. Maiman, "Stimulated optical radiation in ruby," *Nature*, vol. 187, pp. 493–494, 1960.

[7] F. McClung and R. Hellwarth, "Giant optical pulsations from ruby," *Journal of Applied Physics*, vol. 33, no. 3, pp. 828–829, 1962.

[8] L. E. Hargrove, R. L. Fork, and M. A. Pollack, "Locking of he–ne laser modes induced by synchronous intracavity modulation," *Applied Physics Letters*, vol. 5, pp. 4–5, Jul 1964.

[9] M. Dantus, M. J. Rosker, and A. H. Zewail, "Real-time femtosecond probing of "transition states"in chemical reactions," *The Journal of Chemical Physics*, vol. 87, no. 4, pp. 2395–2397, 1987.

[10] A. H. Zewail, "Laser femtochemistry," *Science*, vol. 242, no. 4886, pp. 1645–1653, 1988.

[11] P. A. Franken, A. E. Hill, C. W. Peters, and G. Weinreich, "Generation of optical harmonics," *Phys. Rev. Lett.*, vol. 7, pp. 118–119, Aug 1961.

[12] A. J. DeMaria, D. A. Stetser, and H. Heynau, "Self mode-locking of lasers with saturable absorbers," *Applied Physics Letters*, vol. 8, pp. 174–176, Apr 1966.

[13] D. E. Spence, P. N. Kean, and W. Sibbett, "60-fsec pulse generation from a self-mode-locked ti:sapphire laser," *Optics Letters*, vol. 16, pp. 42–44, Jan 1991.

[14] T. Brabec and F. Krausz, "Intense few-cycle laser fields: Frontiers of nonlinear optics," *RMP*, vol. 72, pp. 545–591, Apr. 2000.

[15] M. T. Hassan, T. T. Luu, A. Moulet, O. Raskazovskaya, P. Zhokhov, M. Garg, N. Karpowicz, A. Zheltikov, V. Pervak, F. Krausz, *et al.*, "Optical attosecond pulses and tracking the nonlinear response of bound electrons," *Nature*, vol. 530, no. 7588, pp. 66–70, 2016.

[16] A. Moulet, J. B. Bertrand, T. Klostermann, A. Guggenmos, N. Karpowicz, and E. Goulielmakis, "Soft x-ray excitonics," *Science*, vol. 357, no. 6356, pp. 1134–1138, 2017.

[17] D. Strickland and G. Mourou, "Compression of amplified chirped optical pulses," *Optics communications*, vol. 55, no. 6, pp. 447–449, 1985.

[18] P. B. Corkum, "Plasma perspective on strong field multiphoton ionization," *Phys. Rev. Lett.*, vol. 71, pp. 1994–1997, Sep 1993.

[19] G. G. Paulus, F. Grasbon, H. Walther, P. Villoresi, M. Nisoli, S. Stagira, E. Priori, and S. De Silvestri, "Absolute-phase phenomena in photoionization with few-cycle laser pulses," *Nature*, vol. 414, pp. 182–184, Nov 2001.

[20] A. Baltuška, T. Udem, M. Uiberacker, M. Hentschel, E. Goulielmakis, C. Gohle, R. Holzwarth, V. S. Yakovlev, A. Scrinzi, T. W. Hänsch, and F. Krausz, "Attosecond control of electronic processes by intense light fields," *Nature*, vol. 421, pp. 611–615, Feb 2003.

[21] C. Haworth, L. Chipperfield, J. Robinson, P. Knight, J. Marangos, and J. Tisch, "Half-cycle cutoffs in harmonic spectra and robust carrier-envelope phase retrieval," *Nature Physics*, vol. 3, no. 1, pp. 52–57, 2007.

[22] E. Goulielmakis, M. Schultze, M. Hofstetter, V. S. Yakovlev, J. Gagnon, M. Uiberacker, A. L. Aquila, E. M. Gullikson, D. T. Attwood, R. Kienberger, F. Krausz, and U. Kleineberg, "Single-cycle nonlinear optics," *Science*, vol. 320, no. 5883, pp. 1614–1617, 2008.

[23] M. Krüger, M. Schenk, and P. Hommelhoff, "Attosecond control of electrons emitted from a nanoscale metal tip," *Nature*, vol. 475, no. 7354, pp. 78–81, 2011.

[24] B. Piglosiewicz, S. Schmidt, D. J. Park, J. Vogelsang, P. Groß, C. Manzoni, P. Farinello, G. Cerullo, and C. Lienau, "Carrier-envelope phase effects on the strong-field photoemission of electrons from metallic nanostructures," *Nature Photonics*, vol. 8, no. 1, pp. 37–42, 2014.

[25] T. Udem, R. Holzwarth, and T. W. Hänsch, "Optical frequency metrology," *Nature*, vol. 416, pp. 233–237, Mar 2002.

[26] D. J. Jones, S. A. Diddams, J. K. Ranka, A. Stentz, R. S. Windeler, J. L. Hall, and S. T. Cundiff, "Carrier-envelope phase control of femtosecond mode-locked lasers and direct optical frequency synthesis," *Science*, vol. 288, no. 5466, pp. 635–639, 2000.

[27] M. Drescher, M. Hentschel, R. Kienberger, G. Tempea, C. Spielmann, G. A. Reider, P. B. Corkum, and F. Krausz, "X-ray pulses approaching the attosecond frontier," *Science*, vol. 291, no. 5510, pp. 1923–1927, 2001.

[28] M. Hentschel, R. Kienberger, C. Spielmann, G. A. Reider, N. Milosevic, T. Brabec, P. Corkum, U. Heinzmann, M. Drescher, and F. Krausz, "Attosecond metrology," *Nature*, vol. 414, pp. 509–513, Nov 2001.

[29] R. Kienberger, E. Goulielmakis, M. Uiberacker, A. Baltuska, V. Yakovlev, F. Bammer, A. Scrinzi, T. Westerwalbesloh, U. Kleineberg, U. Heinzmann, M. Drescher, and F. Krausz, "Atomic transient recorder," *Nature*, vol. 427, pp. 817–821, Feb 2004.

[30] P. Agostini and L. F. DiMauro, "The physics of attosecond light pulses," *Reports on Progress in Physics*, vol. 67, pp. 813–855, may 2004.

[31] A. Scrinzi, M. Y. Ivanov, R. Kienberger, and D. M. Villeneuve, "Attosecond physics," *Journal of Physics B: Atomic, Molecular and Optical Physics*, vol. 39, no. 1, p. R1, 2006.

[32] M. Uiberacker, T. Uphues, M. Schultze, A. J. Verhoef, V. Yakovlev, M. F. Kling, J. Rauschenberger, N. M. Kabachnik, H. Schröder, M. Lezius, K. L. Kompa, H.-G. Muller, M. J. J. Vrakking, S. Hendel, U. Kleineberg, U. Heinzmann, M. Drescher, and F. Krausz, "Attosecond real-time observation of electron tunnelling in atoms," *Nature*, vol. 446, pp. 627–632, Apr 2007.

[33] A. L. Cavalieri, N. Müller, T. Uphues, V. S. Yakovlev, A. Baltuška, B. Horvath, B. Schmidt, L. Blümel, R. Holzwarth, S. Hendel, *et al.*, "Attosecond spectroscopy in condensed matter," *Nature*, vol. 449, no. 7165, p. 1029, 2007.

[34] M. Schultze, M. Fieß, N. Karpowicz, J. Gagnon, M. Korbman, M. Hofstetter, S. Neppl, A. L. Cavalieri, Y. Komninos, T. Mercouris, C. A. Nicolaides, R. Pazourek, S. Nagele, J. Feist, J. Burgdörfer, A. M. Azzeer, R. Ernstorfer, R. Kienberger, U. Kleineberg, E. Goulielmakis, F. Krausz, and V. S. Yakovlev, "Delay in photoemission," *Science*, vol. 328, no. 5986, pp. 1658–1662, 2010.

[35] L. Seiffert, Q. Liu, S. Zherebtsov, A. Trabattoni, P. Rupp, M. C. Castrovilli, M. Galli, F. Süßmann, K. Wintersperger, J. Stierle, G. Sansone, L. Poletto, F. Frassetto, I. Halfpap, V. Mondes, C. Graf, E. Rühl, F. Krausz, M. Nisoli, T. Fennel, F. Calegari, and M. . F. Kling, "Attosecond chronoscopy of electron scattering in dielectric nanoparticles," *Nature Physics*, vol. 13, pp. 766–770, Aug 2017.

[36] E. Goulielmakis, Z.-H. Loh, A. Wirth, R. Santra, N. Rohringer, V. S. Yakovlev, S. Zherebtsov, T. Pfeifer, A. M. Azzeer, M. F. Kling, S. R. Leone, and F. Krausz, "Real-time observation of valence electron motion," *Nature*, vol. 466, pp. 739–743, Aug 2010.

[37] A. Wirth, M. T. Hassan, I. Grguraš, J. Gagnon, A. Moulet, T. T. Luu, S. Pabst, R. Santra, Z. Alahmed, A. Azzeer, *et al.*, "Synthesized light transients," *Science*, vol. 334, no. 6053, pp. 195–200, 2011.

[38] F. Calegari, D. Ayuso, A. Trabattoni, L. Belshaw, S. D. Camillis, S. Anumula, F. Frassetto, L. Poletto, A. Palacios, P. Decleva, J. B. Greenwood, F. Martín, and M. Nisoli, "Ultrafast electron dynamics in phenylalanine initiated by attosecond pulses," *Science*, vol. 346, no. 6207, pp. 336–339, 2014.

[39] A. R. Beck, B. Bernhardt, E. R. Warrick, M. Wu, S. Chen, M. B. Gaarde, K. J. Schafer, D. M. Neumark, and S. R. Leone, "Attosecond transient absorption probing of electronic superpositions of bound states in neon: detection of quantum beats," *New Journal of Physics*, vol. 16, p. 113016, nov 2014.

[40] R. Géneaux, C. J. Kaplan, L. Yue, A. D. Ross, J. E. Bækhøj, P. M. Kraus, H.-T. Chang, A. Guggenmos, M.-Y. Huang, M. Zürch, K. J. Schafer, D. M. Neumark, M. B. Gaarde, and S. R. Leone, "Attosecond time-domain measurement of core-level-exciton decay in magnesium oxide," *Phys. Rev. Lett.*, vol. 124, p. 207401, May 2020.

[41] M. T. Hassan, A. Wirth, I. Grguraš, A. Moulet, T. T. Luu, J. Gagnon, V. Pervak, and E. Goulielmakis, "Invited article: Attosecond photonics: Synthesis and control of light transients," *Review of Scientific Instruments*, vol. 83, no. 11, p. 111301, 2012.

[42] M. Garg, M. Zhan, T. T. Luu, H. Lakhotia, T. Klostermann, A. Guggenmos, and E. Goulielmakis, "Multi-petahertz electronic metrology," *Nature*, vol. 538, no. 7625, pp. 359–363, 2016.

[43] E. Ruska, "The development of the electron microscope and of electron microscopy (nobel lecture)," *Angewandte Chemie International Edition in English*, vol. 26, no. 7, pp. 595–605, 1987.

[44] D. B. Williams and C. B. Carter, "The transmission electron microscope," in *Transmission electron microscopy*, pp. 3–17, Springer, 1996.

[45] D. McMullan, "Scanning electron microscopy 1928–1965," *Scanning*, vol. 17, no. 3, pp. 175–185, 1995.

[46] J. C. Williamson, J. Cao, H. Ihee, H. Frey, and A. H. Zewail, "Clocking transient chemical changes by ultrafast electron diffraction," *Nature*, vol. 386, pp. 159–162, Mar 1997.

[47] E. Fill, L. Veisz, A. Apolonski, and F. Krausz, "Sub-fs electron pulses for ultrafast electron diffraction," *New Journal of Physics*, vol. 8, pp. 272–272, nov 2006.

[48] P. Baum, D.-S. Yang, and A. H. Zewail, "4d visualization of transitional structures in phase transformations by electron diffraction," *Science*, vol. 318, no. 5851, pp. 788–792, 2007.

[49] B. Barwick, H. S. Park, O.-H. Kwon, J. S. Baskin, and A. H. Zewail, "4d imaging of transient structures and morphologies in ultrafast electron microscopy," *Science*, vol. 322, no. 5905, pp. 1227–1231, 2008.

[50] A. Gliserin, M. Walbran, F. Krausz, and P. Baum, "Sub-phonon-period compression of electron pulses for atomic diffraction," *Nature Communications*, vol. 6, p. 8723, Oct 2015.

[51] C. Kealhofer, W. Schneider, D. Ehberger, A. Ryabov, F. Krausz, and P. Baum, "All-optical control and metrology of electron pulses," *Science*, vol. 352, no. 6284, pp. 429–433, 2016.

[52] A. Ryabov and P. Baum, "Electron microscopy of electromagnetic waveforms," *Science*, vol. 353, no. 6297, pp. 374–377, 2016.

[53] P. Baum and A. H. Zewail, "Attosecond electron pulses for 4d diffraction and microscopy," *Proceedings of the National Academy of Sciences*, vol. 104, no. 47, pp. 18409–18414, 2007.

[54] A. Feist, K. E. Echternkamp, J. Schauss, S. V. Yalunin, S. Schäfer, and C. Ropers, "Quantum coherent optical phase modulation in an ultrafast transmission electron microscope," *Nature*, vol. 521, pp. 200–203, May 2015.

[55] H. Niikura, F. Légaré, R. Hasbani, A. D. Bandrauk, M. Y. Ivanov, D. M. Villeneuve, and P. B. Corkum, "Sub-laser-cycle electron pulses for probing molecular dynamics," *Nature*, vol. 417, pp. 917–922, Jun 2002.

[56] J. Itatani, J. Levesque, D. Zeidler, H. Niikura, H. Pépin, J. C. Kieffer, P. B. Corkum, and D. M. Villeneuve, "Tomographic imaging of molecular orbitals," *Nature*, vol. 432, no. 7019, pp. 867–871, 2004.

[57] S. Baker, J. S. Robinson, C. A. Haworth, H. Teng, R. A. Smith, C. C. Chirilă, M. Lein, J. W. G. Tisch, and J. P. Marangos, "Probing proton dynamics in molecules on an attosecond time scale," *Science*, vol. 312, no. 5772, pp. 424–427, 2006.

[58] S. Haessler, J. Caillat, W. Boutu, C. Giovanetti-Teixeira, T. Ruchon, T. Auguste, Z. Diveki, P. Breger, A. Maquet, B. Carré, R. Taïeb, and P. Salières, "Attosecond imaging of molecular electronic wavepackets," *Nature Physics*, vol. 6, no. 3, pp. 200–206, 2010.

[59] C. I. Blaga, J. Xu, A. D. DiChiara, E. Sistrunk, K. Zhang, P. Agostini, T. A. Miller, L. F. DiMauro, and C. D. Lin, "Imaging ultrafast molecular dynamics with laser-induced electron diffraction," *Nature*, vol. 483, pp. 194–197, Mar 2012.

[60] S. Ghimire, A. D. DiChiara, E. Sistrunk, P. Agostini, L. F. DiMauro, and D. A. Reis, "Observation of high-order harmonic generation in a bulk crystal," *Nature physics*, vol. 7, no. 2, pp. 138–141, 2011.

[61] M. Hohenleutner, F. Langer, O. Schubert, M. Knorr, U. Huttner, S. W. Koch, M. Kira, and R. Huber, "Real-time observation of interfering crystal electrons in high-harmonic generation," *Nature*, vol. 523, pp. 572–575, Jul 2015.

[62] O. Schubert, M. Hohenleutner, F. Langer, B. Urbanek, C. Lange, U. Huttner, D. Golde, T. Meier, M. Kira, S. W. Koch, *et al.*, "Sub-cycle control of terahertz high-harmonic generation by dynamical bloch oscillations," *Nature Photonics*, vol. 8, no. 2, pp. 119–123, 2014.

[63] G. Vampa, T. J. Hammond, N. Thiré, B. E. Schmidt, F. Légaré, C. R. McDonald, T. Brabec, and P. B. Corkum, "Linking high harmonics from gases and solids," *Nature*, vol. 522, pp. 462–464, Jun 2015.

[64] A. A. Lanin, E. A. Stepanov, A. B. Fedotov, and A. M. Zheltikov, "Mapping the electron band structure by intraband high-harmonic generation in solids," *Optica*, vol. 4, pp. 516–519, May 2017.

[65] T. T. Luu, M. Garg, S. Y. Kruchinin, A. Moulet, M. T. Hassan, and E. Goulielmakis, "Extreme ultraviolet high-harmonic spectroscopy of solids," *Nature*, vol. 521, no. 7553, pp. 498–502, 2015.

[66] N. Yoshikawa, T. Tamaya, and K. Tanaka, "High-harmonic generation in graphene enhanced by elliptically polarized light excitation," *Science*, vol. 356, no. 6339, pp. 736–738, 2017.

[67] H. Lakhotia, H. Y. Kim, M. Zhan, S. Hu, S. Meng, and E. Goulielmakis, "Laser picoscopy of valence electrons in solids," *Nature*, vol. 583, pp. 55–59, Jul 2020.

[68] H. Hertz, "Ueber einen einfluss des ultravioletten lichtes auf die electrische entladung," *Annalen der Physik*, vol. 267, pp. 983–1000, Jan 1887.

[69] A. Einstein, "Über einen die erzeugung und verwandlung des lichtes betreffenden heuristischen gesichtspunkt," *Annalen der Physik*, vol. 322, pp. 132–148, Jan 1905.

[70] C. J. Joachain, N. J. Kylstra, and R. M. Potvliege, *Multiphoton ionization*, p. 377–417. Cambridge University Press, 2011.

[71] C. J. Joachain, N. J. Kylstra, and R. M. Potvliege, *Perturbation theory*, p. 93–140. Cambridge University Press, 2011.

[72] P. Agostini, F. Fabre, G. Mainfray, G. Petite, and N. K. Rahman, "Free-free transitions following six-photon ionization of xenon atoms," *Phys. Rev. Lett.*, vol. 42, pp. 1127–1130, Apr 1979.

[73] L. Keldysh, "Ionization in the field of a strong electromagnetic wave," *Sov. Phys. JETP*, vol. 20, no. 5, pp. 1307–1314, 1965.

[74] M. Wegener, *Extreme nonlinear optics: an introduction*. Springer Science & Business Media, 2005.

[75] R. H. Fowler and L. Nordheim, "Electron emission in intense electric fields," *Proceedings of the Royal Society of London. Series A, Containing Papers of a Mathematical and Physical Character*, vol. 119, no. 781, pp. 173–181, 1928.

[76] E. L. Murphy and R. H. Good, "Thermionic emission, field emission, and the transition region," *Phys. Rev.*, vol. 102, pp. 1464–1473, Jun 1956.

[77] R. G. Forbes, "Simple good approximations for the special elliptic functions in standard fowler-nordheim tunneling theory for a schottky-nordheim barrier," *Applied Physics Letters*, vol. 89, p. 113122, Sep 2006.

[78] S. V. Yalunin, M. Gulde, and C. Ropers, "Strong-field photoemission from surfaces: Theoretical approaches," *Phys. Rev. B*, vol. 84, p. 195426, Nov 2011.

[79] F. H. M. Faisal, "Multiple absorption of laser photons by atoms," *Journal of Physics B: Atomic and Molecular Physics*, vol. 6, pp. L89–L92, apr 1973.

[80] H. R. Reiss, "Effect of an intense electromagnetic field on a weakly bound system," *Phys. Rev. A*, vol. 22, pp. 1786–1813, Nov 1980.

[81] A. Scrinzi, M. Geissler, and T. Brabec, "Ionization above the coulomb barrier," *Phys. Rev. Lett.*, vol. 83, pp. 706–709, Jul 1999.

[82] V. S. Popov, "Tunnel and multiphoton ionization of atoms and ions in a strong laser field (keldysh theory)," *Physics-Uspekhi*, vol. 47, pp. 855–885, sep 2004.

[83] M. V. Ammosov, "Tunnel ionization of complex atoms and of atomic ions in an altemating electromagnetic field," *Sov. Phys. JETP*, vol. 64, p. 1191, 1987.

[84] G. G. Paulus, W. Becker, W. Nicklich, and H. Walther, "Rescattering effects in above-threshold ionization: a classical model," *Journal of Physics B: Atomic, Molecular and Optical Physics*, vol. 27, pp. L703–L708, nov 1994.

[85] K. J. Schafer, *Numerical Methods in Strong Field Physics*, pp. 111–145. New York, NY: Springer New York, 2009.

[86] D. Bauer, ed., *Computational Strong-Field Quantum Dynamics: Intense Light-Matter Interactions*. De Gruyter SN - 9783110417265, 2017.

[87] J. Javanainen, J. H. Eberly, and Q. Su, "Numerical simulations of multiphoton ionization and above-threshold electron spectra," *Phys. Rev. A*, vol. 38, pp. 3430–3446, Oct 1988.

[88] M. D. Feit, J. A. Fleck, and A. Steiger, "Solution of the schrödinger equation by a spectral method," *Journal of Computational Physics*, vol. 47, pp. 412–433, Sep 1982.

[89] M. Lewenstein, P. Balcou, M. Y. Ivanov, A. L'Huillier, and P. B. Corkum, "Theory of high-harmonic generation by low-frequency laser fields," *Phys. Rev. A*, vol. 49, pp. 2117–2132, Mar 1994.

[90] M. Lewenstein, K. C. Kulander, K. J. Schafer, and P. H. Bucksbaum, "Rings in above-threshold ionization: A quasiclassical analysis," *Phys. Rev. A*, vol. 51, pp. 1495–1507, Feb 1995.

[91] D. B. Milošević, G. G. Paulus, D. Bauer, and W. Becker, "Above-threshold ionization by few-cycle pulses," *Journal of Physics B: Atomic, Molecular and Optical Physics*, vol. 39, pp. R203–R262, jul 2006.

[92] N. Suárez, A. Chacón, M. F. Ciappina, J. Biegert, and M. Lewenstein, "Above-threshold ionization and photoelectron spectra in atomic systems driven by strong laser fields," *Phys. Rev. A*, vol. 92, p. 063421, Dec 2015.

[93] D. M. Wolkow, "Über eine klasse von lösungen der diracschen gleichung," *Zeitschrift für Physik*, vol. 94, pp. 250–260, Mar 1935.

[94] A. L'Huillier, M. Lewenstein, P. Salieres, P. Balcou, M. Y. Ivanov, J. Larsson, and C.-G. Wahlström, "High-order harmonic-generation cutoff," *Phys. Rev. A*, vol. 48, pp. R3433–R3436, Nov 1993.

[95] K. J. Schafer, B. Yang, L. F. DiMauro, and K. C. Kulander, "Above threshold ionization beyond the high harmonic cutoff," *Phys. Rev. Lett.*, vol. 70, pp. 1599–1602, Mar 1993.

[96] J. Tate, T. Auguste, H. G. Muller, P. Salières, P. Agostini, and L. F. DiMauro, "Scaling of wave-packet dynamics in an intense midinfrared field," *Phys. Rev. Lett.*, vol. 98, p. 013901, Jan 2007.

[97] A. D. Shiner, C. Trallero-Herrero, N. Kajumba, H.-C. Bandulet, D. Comtois, F. Légaré, M. Giguère, J.-C. Kieffer, P. B. Corkum, and D. M. Villeneuve, "Wavelength scaling of high harmonic generation efficiency," *Phys. Rev. Lett.*, vol. 103, p. 073902, Aug 2009.

[98] P. B. Corkum, N. H. Burnett, and M. Y. Ivanov, "Subfemtosecond pulses," *Opt. Lett.*, vol. 19, pp. 1870–1872, Nov 1994.

[99] I. J. Sola, E. Mével, L. Elouga, E. Constant, V. Strelkov, L. Poletto, P. Villoresi, E. Benedetti, J.-P. Caumes, S. Stagira, C. Vozzi, G. Sansone, and M. Nisoli, "Controlling attosecond electron dynamics by phase-stabilized polarization gating," *Nature Physics*, vol. 2, pp. 319–322, May 2006.

[100] H. Mashiko, S. Gilbertson, C. Li, S. D. Khan, M. M. Shakya, E. Moon, and Z. Chang, "Double optical gating of high-order harmonic generation with carrier-envelope phase stabilized lasers," *Phys. Rev. Lett.*, vol. 100, p. 103906, Mar 2008.

[101] A. Jullien, T. Pfeifer, M. J. Abel, P. M. Nagel, M. J. Bell, D. M. Neumark, and S. R. Leone, "Ionization phase-match gating for wavelength-tunable isolated attosecond pulse generation," *Applied Physics B*, vol. 93, p. 433, Sep 2008.

[102] M. J. Abel, T. Pfeifer, P. M. Nagel, W. Boutu, M. J. Bell, C. P. Steiner, D. M. Neumark, and S. R. Leone, "Isolated attosecond pulses from ionization gating of high-harmonic emission," *Chemical Physics*, vol. 366, no. 1, pp. 9–14, 2009. Attosecond Molecular Dynamics.

[103] H. Kim, S. Han, Y. W. Kim, S. Kim, and S.-W. Kim, "Generation of coherent extreme-ultraviolet radiation from bulk sapphire crystal," *ACS Photonics*, vol. 4, pp. 1627–1632, Jul 2017.

[104] T. J. Hammond, S. Monchocé, C. Zhang, G. Vampa, D. Klug, A. Y. Naumov, D. M. Villeneuve, and P. B. Corkum, "Integrating solids and gases for attosecond pulse generation," *Nature Photonics*, vol. 11, pp. 594–599, Sep 2017.

[105] Y. S. You, Y. Yin, Y. Wu, A. Chew, X. Ren, F. Zhuang, S. Gholam-Mirzaei, M. Chini, Z. Chang, and S. Ghimire, "High-harmonic generation in amorphous solids," *Nature Communications*, vol. 8, no. 1, p. 724, 2017.

[106] G. Vampa, T. J. Hammond, N. Thiré, B. E. Schmidt, F. Légaré, C. R. McDonald, T. Brabec, D. D. Klug, and P. B. Corkum, "All-optical reconstruction of crystal band structure," *Phys. Rev. Lett.*, vol. 115, p. 193603, Nov 2015.

[107] M. Garg, H. Y. Kim, and E. Goulielmakis, "Ultimate waveform reproducibility of extreme-ultraviolet pulses by high-harmonic generation in quartz," *Nature Photonics*, vol. 12, pp. 291–296, May 2018.

[108] F. Bloch, "Über die quantenmechanik der elektronen in kristallgittern," *Zeitschrift für Physik*, vol. 52, pp. 555–600, Jul 1929.

[109] M. Kira and S. W. Koch, *Semiconductor quantum optics*. Cambridge University Press, 2011.

[110] H. Haug and S. W. Koch, *Quantum theory of the optical and electronic properties of semiconductors*. World Scientific Publishing Company, 2009.

[111] D. Golde, T. Meier, and S. W. Koch, "High harmonics generated in semiconductor nanostructures by the coupled dynamics of optical inter- and intraband excitations," *Phys. Rev. B*, vol. 77, p. 075330, Feb 2008.

[112] A. Moulet, *Attosecond Nonlinear Spectroscopy of Core-Shell Excitations in Atomic and Solid State Systems*. PhD thesis, Ludwig–Maximilians–Universität, 2015.

[113] P. Tournois, "Acousto-optic programmable dispersive filter for adaptive compensation of group delay time dispersion in laser systems," *Optics Communications*, vol. 140, pp. 245–249, Aug 1997.

[114] F. Verluise, V. Laude, J.-P. Huignard, P. Tournois, and A. Migus, "Arbitrary dispersion control of ultrashort optical pulses with acoustic waves," *J. Opt. Soc. Am. B*, vol. 17, pp. 138–145, Jan 2000.

[115] T. Oksenhendler, S. Coudreau, N. Forget, V. Crozatier, S. Grabielle, R. Herzog, O. Gobert, and D. Kaplan, "Self-referenced spectral interferometry," *Applied Physics B*, vol. 99, pp. 7–12, Apr 2010.

[116] A. Weiner, *Ultrafast optics*. John Wiley & Sons, 2009.

[117] M. Schultze, A. Wirth, I. Grguras, M. Uiberacker, T. Uphues, A. J. Verhoef, J. Gagnon, M. Hofstetter, U. Kleineberg, E. Goulielmakis, and F. Krausz, "State-of-the-art attosecond metrology," *Journal of Electron Spectroscopy and Related Phenomena*, vol. 184, pp. 68–77, Apr 2011.

[118] J. N. Sweetser, D. N. Fittinghoff, and R. Trebino, "Transient-grating frequency-resolved optical gating," *Optics letters*, vol. 22, no. 8, pp. 519–521, 1997.

[119] E. Goulielmakis, M. Uiberacker, R. Kienberger, A. Baltuska, V. Yakovlev, A. Scrinzi, T. Westerwalbesloh, U. Kleineberg, U. Heinzmann, M. Drescher, *et al.*, "Direct measurement of light waves," *Science*, vol. 305, no. 5688, pp. 1267–1269, 2004.

[120] A. Wirth, *Attosecond Transient Absorption Spectroscopy*. PhD thesis, Ludwig–Maximilians–Universität, 2011.

[121] Y. Mairesse and F. Quéré, "Frequency-resolved optical gating for complete reconstruction of attosecond bursts," *Physical Review A*, vol. 71, no. 1, p. 011401, 2005.

[122] V. S. Yakovlev, F. Bammer, and A. Scrinzi, "Attosecond streaking measurements," *Journal of Modern Optics*, vol. 52, pp. 395–410, Jan 2005.

[123] D. Kane, "Real-time measurement of ultrashort laser pulses using principal component generalized projections," *IEEE Journal of Selected Topics in Quantum Electronics*, vol. 4, no. 2, pp. 278–284, 1998.

[124] D. J. Kane, "Principal components generalized projections: a review [invited]," *Journal of the Optical Society of America B*, vol. 25, pp. A120–A132, Jun 2008.

[125] J. Gagnon, E. Goulielmakis, and V. S. Yakovlev, "The accurate frog characterization of attosecond pulses from streaking measurements," *Applied Physics B*, vol. 92, pp. 25–32, Jul 2008.

[126] P. D. Keathley, S. Bhardwaj, J. Moses, G. Laurent, and F. X. Kärtner, "Volkov transform generalized projection algorithm for attosecond pulse characterization," *New Journal of Physics*, vol. 18, p. 073009, jul 2016.

[127] H. Y. Kim, M. Garg, S. Mandal, L. Seiffert, T. Fennel, and E. Goulielmakis, "Attosecond field emission." in perparation.

[128] Y. C. Martin, H. F. Hamann, and H. K. Wickramasinghe, "Strength of the electric field in apertureless near-field optical microscopy," *Journal of Applied Physics*, vol. 89, pp. 5774–5778, May 2001.

[129] A. V. Goncharenko, J.-K. Wang, and Y.-C. Chang, "Electric near-field enhancement of a sharp semi-infinite conical probe: Material and cone angle dependence," *Phys. Rev. B*, vol. 74, p. 235442, Dec 2006.

[130] S. Thomas, G. Wachter, C. Lemell, J. Burgdörfer, and P. Hommelhoff, "Large optical field enhancement for nanotips with large opening angles," *New Journal of Physics*, vol. 17, p. 063010, jun 2015.

[131] P. Dombi, Z. Pápa, J. Vogelsang, S. V. Yalunin, M. Sivis, G. Herink, S. Schäfer, P. Groß, C. Ropers, and C. Lienau, "Strong-field nano-optics," *Rev. Mod. Phys.*, vol. 92, p. 025003, Jun 2020.

[132] S. Thomas, M. Krüger, M. Förster, M. Schenk, and P. Hommelhoff, "Probing of optical near-fields by electron rescattering on the 1 nm scale," *Nano Letters*, vol. 13, pp. 4790–4794, Oct 2013.

[133] M. I. Stockman, M. F. Kling, U. Kleineberg, and F. Krausz, "Attosecond nanoplasmonic-field microscope," *Nature Photonics*, vol. 1, pp. 539–544, Sep 2007.

[134] P. Dombi, A. Hörl, P. Rácz, I. Márton, A. Trügler, J. R. Krenn, and U. Hohenester, "Ultrafast strong-field photoemission from plasmonic nanoparticles," *Nano Letters*, vol. 13, pp. 674–678, Feb 2013.

[135] M. Krüger, C. Lemell, G. Wachter, J. Burgdörfer, and P. Hommelhoff, "Attosecond physics phenomena at nanometric tips," *Journal of Physics B: Atomic, Molecular and Optical Physics*, vol. 51, p. 172001, aug 2018.

[136] K. Yee, "Numerical solution of initial boundary value problems involving maxwell's equations in isotropic media," *IEEE Transactions on Antennas and Propagation*, vol. 14, no. 3, pp. 302–307, 1966.

[137] M. Schenk, M. Krüger, and P. Hommelhoff, "Strong-field above-threshold photoemission from sharp metal tips," *Phys. Rev. Lett.*, vol. 105, p. 257601, Dec 2010.

[138] G. Herink, D. Solli, M. Gulde, and C. Ropers, "Field-driven photoemission from nanostructures quenches the quiver motion," *Nature*, vol. 483, no. 7388, pp. 190–193, 2012.

[139] S. V. Yalunin, G. Herink, D. R. Solli, M. Krüger, P. Hommelhoff, M. Diehn, A. Munk, and C. Ropers, "Field localization and rescattering in tip-enhanced photoemission," *Annalen der Physik*, vol. 525, pp. L12–L18, Feb 2013.

[140] K. E. Echternkamp, G. Herink, S. V. Yalunin, K. Rademann, S. Schäfer, and C. Ropers, "Strong-field photoemission in nanotip near-fields: from quiver to sub-cycle electron dynamics," *Applied Physics B*, vol. 122, p. 80, Mar 2016.

[141] P. Hommelhoff, Y. Sortais, A. Aghajani-Talesh, and M. A. Kasevich, "Field emission tip as a nanometer source of free electron femtosecond pulses," *Phys. Rev. Lett.*, vol. 96, p. 077401, Feb 2006.

[142] R. Bormann, M. Gulde, A. Weismann, S. V. Yalunin, and C. Ropers, "Tip-enhanced strong-field photoemission," *Phys. Rev. Lett.*, vol. 105, p. 147601, Sep 2010.

[143] H. B. Michaelson, "The work function of the elements and its periodicity," *Journal of Applied Physics*, vol. 48, pp. 4729–4733, Nov 1977.

[144] J. Schötz, L. Seiffert, A. Maliakkal, J. Blöchl, D. Zimin, P. Rosenberger, B. Bergues, P. Hommelhoff, F. Krausz, T. Fennel, and M. F. Kling, "Onset of charge interaction in strong-field photoemission from nanometric needle tips," *Nanophotonics*, vol. 10, no. 14, pp. 3769–3775, 2021.

[145] Y. H. Kim, I. A. Ivanov, S. I. Hwang, K. Kim, C. H. Nam, and K. T. Kim, "Attosecond streaking using a rescattered electron in an intense laser field," *Scientific Reports*, vol. 10, p. 22075, Dec 2020.

[146] M. R. Bionta, F. Ritzkowsky, M. Turchetti, Y. Yang, D. Cattozzo Mor, W. P. Putnam, F. X. Kärtner, K. K. Berggren, and P. D. Keathley, "On-chip sampling of optical fields with attosecond resolution," *Nature Photonics*, vol. 15, pp. 456–460, Jun 2021.

[147] R. Trebino and D. J. Kane, "Using phase retrieval to measure the intensity and phase of ultrashort pulses: frequency-resolved optical gating," *J. Opt. Soc. Am. A*, vol. 10, pp. 1101–1111, May 1993.

[148] J. Gagnon, *Attosecond Transient Absorption Spectroscopy.* PhD thesis, Ludwig–Maximilians–Universität, 2010.

[149] J. H. Eberly and K. C. Kulander, "Atomic stabilization by super-intense lasers," *Science*, vol. 262, no. 5137, pp. 1229–1233, 1993.

[150] M. Gavrila, "Atomic stabilization in superintense laser fields," *Journal of Physics B: Atomic, Molecular and Optical Physics*, vol. 35, no. 18, pp. R147–R193, 2002.

[151] L. Medišauskas, U. Saalmann, and J.-M. Rost, "Floquet hamiltonian approach for dynamics in short and intense laser pulses," *Journal of Physics B: Atomic, Molecular and Optical Physics*, vol. 52, no. 1, p. 015602, 2018.

[152] L. C. M. Miranda, "Energy-gap distortion in solids under intense laser fields," *Solid State Communications*, vol. 45, no. 9, pp. 783–785, 1983.

[153] Y. Mizumoto and Y. Kayanuma, "Dynamical collapse of the peierls gap by an intense laser field," *PRB*, vol. 81, p. 233202, June 2010.

[154] N. Tzoar and J. I. Gersten, "Theory of electronic band structure in intense laser fields," *Phys. Rev. B*, vol. 12, pp. 1132–1139, Aug 1975.

[155] F. Faisal and R. Genieser, "Exact solution of the kronig-penney model of 1d crystals in strong laser fields," *Physics Letters A*, vol. 141, no. 5, pp. 297–300, 1989.

[156] M. Holthaus, "The quantum theory of an ideal superlattice responding to far-infrared laser radiation," *Zeitschrift für Physik B Condensed Matter*, vol. 89, no. 2, pp. 251–259, 1992.

[157] F. H. M. Faisal and J. Z. Kamiński, "Floquet-bloch theory of high-harmonic generation in periodic structures," *Phys. Rev. A*, vol. 56, pp. 748–762, Jul 1997.

[158] J. H. Shirley, "Solution of the schrödinger equation with a hamiltonian periodic in time," *Phys. Rev.*, vol. 138, pp. B979–B987, May 1965.

[159] W. C. Henneberger, "Perturbation method for atoms in intense light beams," *PRL*, vol. 21, pp. 838–841, Sept. 1968.

[160] S. Longhi, S. A. R. Horsley, and G. Della Valle, "Scattering of accelerated wave packets," *Phys. Rev. A*, vol. 97, p. 032122, Mar 2018.

[161] R. Bracewell, *The Projection-Slice Theorem*, pp. 493–504. Boston, MA: Springer US, 2003.

[162] G. Taylor, "The phase problem," *Acta Crystallographica Section D*, vol. 59, pp. 1881–1890, Nov 2003.

[163] Y. S. You, D. Reis, and S. Ghimire, "Anisotropic high-harmonic generation in bulk crystals," *Nature Physics*, vol. 13, pp. 345–349, Apr 2017.

[164] C. Corsi, A. Pirri, E. Sali, A. Tortora, and M. Bellini, "Direct interferometric measurement of the atomic dipole phase in high-order harmonic generation," *Phys. Rev. Lett.*, vol. 97, p. 023901, Jul 2006.

[165] D. C. Yost, T. R. Schibli, J. Ye, J. L. Tate, J. Hostetter, M. B. Gaarde, and K. J. Schafer, "Vacuum-ultraviolet frequency combs from below-threshold harmonics," *Nature Physics*, vol. 5, no. 11, pp. 815–820, 2009.

[166] C. Benko, T. K. Allison, A. Cingöz, L. Hua, F. Labaye, D. C. Yost, and J. Ye, "Extreme ultraviolet radiation with coherence time greater than 1 s," *Nature Photonics*, vol. 8, pp. 530–536, Jul 2014.

[167] M. Lewenstein, P. Salières, and A. L'Huillier, "Phase of the atomic polarization in high-order harmonic generation," *Phys. Rev. A*, vol. 52, pp. 4747–4754, Dec 1995.

[168] C. Liu, M. Reduzzi, A. Trabattoni, A. Sunilkumar, A. Dubrouil, F. Calegari, M. Nisoli, and G. Sansone, "Carrier-envelope phase effects of a single attosecond pulse in two-color photoionization," *Phys. Rev. Lett.*, vol. 111, p. 123901, Sep 2013.

[169] G. Sansone, C. Vozzi, S. Stagira, M. Pascolini, L. Poletto, P. Villoresi, G. Tondello, S. De Silvestri, and M. Nisoli, "Observation of carrier-envelope phase phenomena in the multi-optical-cycle regime," *Phys. Rev. Lett.*, vol. 92, p. 113904, Mar 2004.

[170] G. Sansone, E. Benedetti, J.-P. Caumes, S. Stagira, C. Vozzi, M. Pascolini, L. Poletto, P. Villoresi, S. De Silvestri, and M. Nisoli, "Measurement of harmonic phase differences by interference of attosecond light pulses," *Phys. Rev. Lett.*, vol. 94, p. 193903, May 2005.

[171] Y. S. You, M. Wu, Y. Yin, A. Chew, X. Ren, S. Gholam-Mirzaei, D. A. Browne, M. Chini, Z. Chang, K. J. Schafer, M. B. Gaarde, and S. Ghimire, "Laser waveform control of extreme ultraviolet high harmonics from solids," *Optics Letters*, vol. 42, pp. 1816–1819, May 2017.

List of Figures

Acknowledgements

During my PhD journey I've met excellent people not only in professional life but also in personal life. I believe that without them my PhD would have been a harsh and lonely path. Of course, it is not enough to express all my gratitude to them in a single page, but I will try my best.

Most of all, I would like to express my sincere gratitude to Prof. Eleftherios Goulielmakis for supervising my PhD research and for giving me fruitful and insightful guidance. Even a short discussion with him always inspired me to see the problems from another point of view. Furthermore, I'm grateful for his encouragement and trust on all of us, which always motivated us to move forward to reach our goals.

I am grateful to Prof. Ferenc Krausz for giving me the opportunity to work on a big part of my PhD in the labs of his division at Max-Planck-Institute of Quantum optics (MPQ).

I would like to express my thanks to Prof. Jörg Schreiber for taking the effort and the time to be the first referee of my PhD.

I would also like to thank very much the members of the Attoelectronics and now the Extreme photonics group. Dr. Manish Garg worked together with me on most of the research projects presented in this thesis. He always conveyed his knowledge kindly to me. It was great luck for me to work with Dr. Harshit Lakhotia, Dr. Minjie Zhan and Dr. Benedikt Mayer. Harshit always invigorated us with funny jokes even under hard situations, and we fought together to beat the code. Minjie having very precise hands always made experimental implementations smoothly. Ben helped me a lot for extending my view to other fields of research. I really missed the moments with them, from work in the lab to beer party at Garchinger See and Warnemünde!

I want to express my gratefulness to my current colleagues, Santanu Mandal, Zekun Pi, Praful Kumar and Nizar Chaouachi for always being cooperative in the lab and the office. I am really happy to work with them to explore new things. I would also like to thank the my old colleagues, Dr. Antoine Moulet, Dr. Tran Trung Luu and Till Klostermann who gave me great help, when I joined the group. I also acknowledge the excellent cooperation with our collaborators, Shiqi Hu, Prof. Sheng Meng, Dr. Lennart Seiffert and Prof. Thomas Fennel and would like to express my thanks also to the members of the group of Prof. Meiwes-Broer and Dr. Tiggesbäumker for helping us to settle our labs in Rostock.

I sincerely appreciate the great support from our technicians, Hr. Dittrich at Uni. Rostock and Hr. Böswald, Hr. Haas and Hr. Horn at MPQ. I also want to express my

gratefulness to administrative staffs, Fr. Machotzek at Uni. Rostock and Fr. Seidl at MPQ for smooth managing all kinds of administrative issues.

Special thanks to my friends, Hyukjae, Gangsup, Sanae, Youngsun, Sungbae and Eunsuk who always share joy or sorrow whenever/wherever I am and are waiting for me to have a beer at home soon. I really look forward it!

I'm deeply indebted to my mother and parents-in-law and would like to express my deepest love to them. Without their encouragement and support I couldn't have pursued my PhD so far.

I specially thank my love, Jeong Hwa, who makes my life brighter and shares happiness at every single moment of my entire life.

I dedicate this work to my father, in memory of his love.